# An Optimised QPSK-Based Receiver Structure for Possibly Sparse Data Transmission Over Narrowband and Wideband Communication Systems

J. Schoeman

2009

UNIVERSITEIT VAN PRETORIA
UNIVERSITY OF PRETORIA
YUNIBESITHI YA PRETORIA

# AN OPTIMISED QPSK-BASED RECEIVER STRUCTURE FOR POSSIBLY SPARSE DATA TRANSMISSION OVER NARROWBAND AND WIDEBAND COMMUNICATION SYSTEMS

By

**Johan Schoeman**
**(9818583)**

Supervisor: Professor L.P. Linde

Submitted in partial fulfillment of the requirements for the degree

**Master of Engineering (Electronics)**

in the

Department of Electrical, Electronic & Computer Engineering

in the

Faculty of Engineering, Built Environment & Information Technology

UNIVERSITY OF PRETORIA

December 2009

# SUMMARY

---

AN OPTIMISED QPSK-BASED RECEIVER STRUCTURE FOR POSSIBLY SPARSE DATA TRANSMISSION OVER NARROWBAND AND WIDEBAND COMMUNICATION SYSTEMS

by

Johan Schoeman
Supervisor: Professor L.P. Linde
Department of Electrical, Electronic & Computer Engineering
Master of Engineering (Electronics)

---

In this dissertation an in-depth study was conducted into the design, implementation and evaluation of a QPSK-based receiver structure for application in a UMTS WCDMA environment. The novelty of this work lies with the specific receiver architecture aimed to optimise the BER performance when possibly sparse data streams are transmitted. This scenario is a real possibility according to Verdú *et al* [1] and Hagenauer *et al* [2–6]. A novel receiver structure was conceptualised, developed and evaluated in both narrowband and wideband scenarios, where it was found to outperform conventional receivers when a sparse data stream is transmitted.

In order to reach the main conclusions of this study, it was necessary to develop a realistic simulation platform. The developed platform is capable of simulating a communication system meeting the physical layer requirements of the UMTS WCDMA standard. The platform can also perform narrowband simulations. A flexible channel emulator was developed that may be configured to simulate AWGN channel conditions, frequency non-selective fading (either Rayleigh or Rician with a configurable LOS component and Doppler spread), or a full multipath scenario where each path has a configurable LOS component, Doppler spread, path gain and path delay. It is therefore possible to even simulate a complex, yet realistic, COST207-TU channel model. The platform is also capable of simulating MUI. Each interfering user has a unique and independent multipath fading channel, while sharing the same bandwidth. Finally, the entire platform executes all simulations in baseband for improved simulation times.

The research outputs of this work are summarised below:

- A parameter, the sparseness measure, was defined in order to quantify the level by which a data stream differs from an equiprobable data stream.
- A novel source model was proposed and developed to simulate data streams with a specified amount of sparseness.
- An introductory investigation was undertaken to determine the effect of simple FEC techniques on the sparseness of an encoded data stream.
- Novel receiver structures for both narrowband and wideband systems were proposed, developed and evaluated for systems where possibly sparse data streams may be transmitted.
- Analytic expressions were derived to take the effect of sparseness into account in communication systems, including expressions for the joint PDF of a BPSK branch, the optimal decision region of a detector in AWGN conditions as well as the BER performance of a communication system employing the proposed optimal receiver in both AWGN channel conditions as well as in flat fading channel conditions.
- Numerous BER performance curves were obtained comparing the proposed receiver structure with conventional receivers in a variety of channel conditions, including AWGN, frequency non-selective fading and a multipath COST207-TU channel environment, as well as the effect of MUI.

**Keywords:**

**4G, AWGN, BER, CDMA, channel modelling, channelisation codes, COST models, flat fading, MUI, multipath fading, OVSF codes, QPSK, Rake receiver, RRC filter, scrambling codes, sparse data, sparseness measure, UMTS, WCDMA, wireless communication**.

# OPSOMMING

---

’n Geoptimeerde KPSK-gebaseerde Ontvanger Struktuur vir Moontlike Yl Data Versending Oor Noueband en Wyeband Kommunikasiestelsels

deur
Johan Schoeman
Studieleier: Professor L.P. Linde
Departement Elektriese-, Elektroniese- & Rekenaar Ingenieurswese
Meester in Ingenieurswese (Elektronies)

---

In hierdie verhandeling word ’n in-diepte studie gedoen rakende die ontwerp, implementasie en evaluasie van ’n KPSK-gebaseerde ontvanger struktuur wat in ’n UMTS WKVVT omgewing gebruik kan word. Die bydrae van hierdie werk lê in die spesifieke ontvanger argitektuur wat daarop mik om die BFT werksverrigting te optimeer wanneer yl data strome versend word. Hierdie is ’n realistiese moontlikheid volgens Verdú *et al* [1] en Hagenauer *et al* [2–6]. ’n Nuwe ontvanger struktuur is gekonsepsualiseer, ontwikkel en evalueer vir beide noueband en wyeband stelsels, waar dit gevind is dat dit beter werksverrigting lewer as tradisionele ontvangers wanneer yl data strome versend word.

Dit was nodig om ’n realistiese simulasie platform te ontwikkel om die belangrikste gevolgtrekkings van hierdie studie te kan maak. Die ontwikkelde platform is in staat om ’n kommunikasie stelsel te simuleer wat aan die fisiese laag vereistes van die UMTS WKVVT standaard voldoen. Die platform kan ook noueband stelsels simuleer. ’n Aanpasbare kanaal simulator is ontwikkel wat opgestel kan word om SWGR kanaal toestande, plat duining (beide Rayleigh of Ricies met ’n verstelbare siglyn komponent en Doppler verspreiding), sowel as ’n veelvuldige pad omgewing (waar elke unieke pad ’n verstelbare siglyn komponent, Doppler verspreiding, pad wins en pad vertraging het) te emuleer. Dit is selfs moontlik om ’n komplekse, maar steeds realistiese COST207-TU kanaal model te simuleer. Die platform het ook die vermoë om VGS te simuleer. Elke steurende gebruiker het ’n unieke en onafhanklike veelvuldige pad deinende kanaal, terwyl dieselfde bandwydte gedeel word. Laastens, alle simulasies van die platvorm word in basisband uitgevoer wat verkorte simulasie periodes verseker.

Die navorsingsuitsette van hierdie werk kan as volg opgesom word:

- ’n Parameter, die ylheidsmaatstaf, is gedefiniëer om dit moontlik te maak om die vlak waarmee die ylheid van ’n datastroom verskil van ’n ewekansige stroom te versyfer.
- ’n Nuwe bronmodel is voorgestel en ontwikkel om datastrome met ’n spesifieke ylheid te emuleer.
- ’n Inleidende ondersoek is onderneem om vas te stel wat die effek van VFK tegnieke op die ylheid van ’n enkodeerde datastroom is.
- Nuwe ontvanger strukture is voorgestel, ontwikkel en evalueer vir beide noueband en wyeband stelsels waar yl datastrome moontlik versend kan word.
- Analitiese uitdrukkings is afgelei om die effek van ylheid in ag te neem in kommunikasie stelsels. Uitdrukkings vir onder andere die gedeelte WDF van ’n BFVK tak, die optimale beslissingspunt van ’n detektor in SWGR toestande, sowel as die BFT werksverrigting van ’n kommunikasie stelsel wat van die voorgestelde optimale ontvangers gebruik maak, hetsy in SWGR of in plat duinende kanaal toestande.
- Talryke BFT werksverrigting krommes is verkry wat die voorgestelde ontvanger struktuur vergelyk met die konvensionele ontvangers in ’n verskeidenheid kanaal toestande, insluitend SWGR, plat duinende kanale en ’n veelvuldige pad COST207-TU kanaal omgewing, sowel as in die teenwoordigheid van VGS.

**Sleutelwoorde:**

**4G, BFT, COST modelle, draadlose kommunikasie, kanaal modellering, kanalisasie kodes, KDVT, KPSK, mengkodes, OVSF kodes, plat deining, Rake ontvanger, SWGR,UMTS, veelvuldige pad deining, VGS, WGC filter, WKVVT, yl data, ylheidsmaatstaf**.

*To my family and friends.*

*Your support has not gone unnoticed!*

# ACKNOWLEDGEMENT

A number of individuals and institutions have made this study possible. It will be impossible to single out everyone, but I am indebted to them all for their advice and assistance towards the successful completion of this work.

I would like to acknowledge the National Research Foundation (NRF) that has provided financial assistance and created unique opportunities for the duration of this work, as well as the Carl and Emily Fuchs Institute for Microelectronics (CEFIM) that has provided financial support for conferences as well as computing resources. I would like to thank the Director of CEFIM, Professor Monuko du Plessis, who has never hesitated to support me and this work financially, even if it lies outside the direct research field of the institute.

I would like to express my sincere thanks in particular to my superviser, Professor Louis P. Linde, for encouraging me to satisfy my own curiosity when he provided me the freedom to investigate my own topic. His supervision and professional approach has benefited me tremendously, and his teachings has shaped the way I approach research and engineering.

To my research colleagues and friends Jacques van Wyk, Pieter de Villiers, Saurabh Sinha, Paul Greeff and Hans Grobler my sincere thanks for being at my disposal at all times. Your assistance was invaluable, irrespective of whether it was technical or motivational.

A special word of thanks to Tilla Loubser, who assisted with the proofreading of many iterations of this work, as well as providing much needed motivation during times when this work was placed on hold. I would also like to thank Marius Goosen, Hannetjie Nell and Marnus Weststrate for the proofreading that they did.

I would like to thank my family, Marissa Grobler and the Grobler family for the motivation and non-technical support that they have provided while I completed this work. I have often wondered if I would ever finish, and it was you that kept me going.

Finally, I would like to give praise to God Almighty, who has given me the ability and talents to embark on this journey and to finally see it through.

# TABLE OF CONTENTS

# LIST OF FIGURES

# LIST OF TABLES

# LIST OF ABBREVIATIONS

| | |
|---|---|
| 1G | First Generation |
| 2G | Second Generation |
| 3G | Third Generation |
| 4G | Fourth Generation |
| ACF | Autocorrelation Function |
| ADF | Average Duration of Fades |
| AMPS | Advanced Mobile Phone Service |
| ARP | Autoradiopuhelin |
| ATM | Asynchronous Transfer Mode |
| AWGN | Additive White Gaussian Noise |
| BER | Bit Error Ratio/Rate |
| BPSK | Binary Phase Shift Keying |
| C-Netz | Radio Telephone Network C |
| CCF | Cross-Correlation Function |
| CDF | Cumulative Distribution Function |
| CDMA | Code Division Multiple Access |
| CMOS | Complementary Metal-Oxide Semiconductor |
| COST | COperation européenne dans le domaine de la recherche Scientifique et Technique |
| CSS | Complex Spreading Sequences |
| DPCCH | Dedicated Physical Control Channel |
| DPCH | Dedicated Physical Channel |
| DPDCH | Dedicated Physical Data Channels |
| DS/SSMA | Direct Sequence Spread Spectrum Multiple Access |
| EDGE | Enhanced Data Rates for GSM Evolution |
| ESPRIT | European Strategic Program on Research in Information Technology |

| | |
|---|---|
| FDD | Frequency Division Duplex |
| FDMA | Frequency Division Multiple Access |
| FEC | Forward Error Correcting |
| FM | Frequency Modulation |
| GF(2) | Galois Field 2 |
| GPRS | General Packet Radio Service |
| GSM | Global System for Mobile communications |
| HSDPA | Higher Speed Downlink Packet Data Access |
| i.i.d. | Independent and Identically Distributed |
| IC | Integrated Circuit |
| iDEN | Integrated Digital Enhanced Network |
| IEEE | Institute of Electrical and Electronics Engineers |
| IMT-2000 | International Mobile Telecommunications-2000 |
| IPTV | IP Television |
| IS-95 | Interim Standard 95 |
| ISI | Intersymbol Interference |
| ITU | International Telecommunications Union |
| JM | Jakes Method |
| LAN | Local Area Network |
| LCR | Level Crossing Rate |
| LDPC | Low-Density Parity Check |
| LOS | Line of Sight |
| M-PSK | $M$-ary Phase Shift Keying |
| MAP | Maximum A-Posteriori |
| MED | Method of Equal Distances |
| MEDS | Method of Exact Doppler Spread |
| ML | Maximum Likelihood |
| MPA | Message Passing Algorithm |
| MSEM | Mean Square Error Method |
| MUI | Multi-User Interference |
| NMT | Nordic Mobile Telephone |
| OSI | Open System Interconnection |
| OVSF | Orthogonal Variable Spreading Factor |

| | |
|---|---|
| P/S | Parallel-to-Serial |
| PDF | Probability Density Function |
| PRNG | PseudoRandom Number Generators |
| PSD | Power Spectral Density |
| QPSK | Quadrature Phase Shift Keying |
| RRC | Root-Raised Cosine |
| RTMI | Radio Telefono Mobile Integrato |
| S/H | Sample-and-Hold |
| S/P | Serial-to-Parallel |
| SNR | Signal-to-Noise Ratio |
| TACS | Total Access Communication System |
| TDD | Time Division Duplex |
| TDMA | Time Division Multiple Access |
| TFCI | Optional Transport Format Combination Indicator |
| TFI | Transport Format Indicator |
| TPC | Transmit Power Control |
| UMTS | Universal Mobile Telecommunications System |
| UTRA | UMTS Terrestrial Radio Access |
| VoD | Video-on-Demand |
| VoIP | Voice/Video over IP |
| WCDMA | Wideband Code Division Multiple Access |
| WSSUS | Wide-Sense Stationary-Uncorrelated Scattering |

# LIST OF SYMBOLS

| | |
|---|---|
| $\alpha$ | Roll-off factor (minimum bandwidth factor) equal to 0.22 |
| $\alpha_c(t)$ | Instantaneous fading amplitude of the Rician process |
| $\alpha_{fl}$ | Random fading level attenuation |
| $\alpha_{R,i}(t), \alpha_{R,q}(t)$ | In-phase and quadrature output coefficients generated by the complex Rician process |
| $\bar{T}$ | Mean excess delay time |
| $\Delta f_i$ | Frequency spacing between the $f_{z,n}$ components |
| $\eta_s$ | Measure for sparseness on a symbol level |
| $\eta_\alpha$ | Measure for sparseness on an alphabet level |
| $\gamma_b$ | SNR per bit given a random fading level attenuation factor |
| $\overline{\gamma}_b$ | Average SNR per bit given a random fading level attenuation factor |
| $\phi_c(t)$ | Instantaneous fading phase of the Rician process |
| $\rho$ | Amplitude of the LOS component |
| $\sigma_0^2$ | Average transmitted signal power |
| $\sigma_{n(t)}^2$ | Variance of $n(t)$ |
| $\sigma_T$ | RMS delay spread |
| $\tau_l$ | $l^{th}$ excess delay time |
| $\theta_\rho$ | Phase of the LOS component |
| $\theta_{A,i}(t)$ | Angle of arrival of the $i^{th}$ received signal |
| $\theta_{z,n}$ | Random variables uniformly distributed over $[0, 2\pi)$ |
| $\tilde{\sigma}_{T_z}^2$ | Mean power of the deterministic Rician process |
| $\tilde{\xi}(t)$ | Deterministic amplitude envelope of a Rician process |
| $\tilde{\zeta}(t)$ | Deterministic amplitude envelope of a Rayleigh process |
| $\tilde{m}_{T_z}$ | Mean value of the deterministic Rician process |
| $\tilde{r}_{T_iT_q}(\tau)$ | CCF of two deterministic processes, $T_i$ and $T_q$ |
| $\tilde{r}_{T_zT_z}$ | Autocorrelation function of a deterministic Rician process |

| | |
|---|---|
| $\tilde{S}_{T_iT_q}$ | Cross-PSD of two deterministic processes, $T_i$ and $T_q$ |
| $\tilde{S}_{T_z}$ | PSD of a deterministic Rician process |
| $\tilde{T}_z(t)$ | Deterministic Gaussian process |
| $\varepsilon$ | Coherence bandwidth correlation factor |
| $\vartheta(t)$ | Phase of Rayleigh/Rician process |
| $\widehat{\alpha}_l$ | Average channel tap weight of the $l^{th}$ channel path |
| $\widehat{\tau}_k$ | Time delay a received symbol experience due to the receive filters |
| $\widehat{\theta}$ | Estimated phase shift of the received signal |
| $\xi(t)$ | Amplitude envelope of a Rician process |
| $\zeta(t)$ | Amplitude envelope of a Rayleigh process |
| $a_i$ | Source symbol that is least likely to occur |
| $A_k$ | Amplitude of the transmitted data symbol |
| $a_k$ | $k^{th}$ source symbol |
| $B_C$ | Coherence bandwidth |
| $b_h$ | $h^{th}$ source alphabet letter used to construct symbols $a_k$ |
| $b_p(m)$ | Pilot symbols transmitted |
| $B_{T_z}^{(1)}$ | Average Doppler shift/spread |
| $B_{T_z}^{(2)}$ | Doppler spread |
| $c_I, c_Q$ | Codes from an extended very large Kasami set of length 256 |
| $c_R$ | Rician factor that describes the ratio of the power of the LOS component to the sum of the power of all the scattered components |
| $C_{ch,k}$ | $N_k$-chip Welsch channelisation code of the $k^{th}$ user |
| $c_{k,m}(i)$ | Single time varying and user $k$ specific spreading code consisting of a mixed version of $C_{ch,k}$ and $C_{scramb}$ |
| $C_{scramb}$ | Gold code used for scrambling |
| $c_{z,n}$ | Amplitude of the $n^{th}$ component contributing to a Gaussian process |
| $d_{min}$ | Distance between the closest signal points in the constellation |
| $E_b$ | Energy of a bit |
| $E_s$ | Energy of a symbol |
| $f$ | Frequency |
| $f_c$ | Carrier frequency |
| $F_z$ | Periodicity of a deterministic process |
| $f_{-3dB}$ | -3 dB cut-off frequency |

| | |
|---|---|
| $f_\rho$ | Frequency of the LOS component |
| $F_{\xi-}(R_s)$ | CDF of a Rician process |
| $F_{\zeta-}(R_s)$ | CDF of a Rayleigh process |
| $f_{d,i}(t)$ | Doppler shift experienced by the $i^{th}$ multipath component |
| $f_{d,max}(t)$ | Maximum Doppler shift experienced |
| $f_{min}$ | Minimum frequency required to transmit a pulse train at $1/T_s$ symbols per second |
| $f_{z,n}$ | Frequency of the $n^{th}$ component contributing to a Gaussian process |
| $H_s$ | Entropy measure of a source |
| $I_0(x)$ | $0^{th}$ order modified Bessel function of the first kind |
| $J_0$ | $0^{th}$ order Bessel function |
| $L$ | Number of multipath components |
| $m(t)$ | LOS component |
| $M_k$ | Number of data symbols, $x_k(m)$ |
| $m_{n(t)}$ | Mean or expected value of $n(t)$ |
| $N_\xi(R_S)$ | Level crossing rate |
| $N_k$ | User specific spreading factor |
| $N_p$ | Number of pilot symbols |
| $N_z$ | Number of sinusiodal components contributing to a Gaussian process |
| $P(\tau_l)$ | $l^{th}$ received signal power component |
| $p(b^h_{a_i})$ | Probability of occurance of alphabet letter $b_h$ in symbol $a_i$ |
| $P(f)$ | Frequency response of the RRC pulse shaping filter |
| $p(t)$ | Impulse response of the RRC pulse shaping filter |
| $p_\vartheta(\theta, t)$ | PDF of the phase of Rayleigh/Rician process |
| $p_\xi(x)$ | PDF of a Rician process |
| $p_\zeta(x)$ | PDF of a Rayleigh process |
| $P_b$ | Error probability of a bit |
| $P_s$ | Error probability of a symbol |
| $p_{n(t)}(x)$ | PDF of $n(t)$ at $x$ |
| $P_{RC}(f)$ | Frequency response of the raised cosine pulse shaping filter |
| $p_{RC}(t)$ | Impulse response of the raised cosine pulse shaping filter |
| $P_{scale}$ | Power scaling factor for normalisation |
| $r(\tau)$ | Autocorrelation function for the Jakes PSD |

| | |
|---|---|
| $r_d$ | Decision region in a PDF used by detectors |
| $r_k(t)$ | Received signal of the $k^{th}$ user |
| $r_l$ | $l^{th}$ received signal amplitude |
| $R_S$ | Specified RMS power level |
| $r_{k,i}(t), r_{k,q}(t)$ | In-phase and quadrature components of the received signal of the $k^{th}$ user |
| $s_{k,m}(t)$ | $k^{th}$ user specific spreading waveform that corresponds to the $m^{th}$ code segment |
| $s_m(t)$ | Pilot specific spreading waveform that corresponds to the $m^{th}$ code segment |
| $S_{T_i}(f), S_{T_q}(f)$ | In-phase and quadrature components of the PSD at the receiver |
| $S_{T_z}(f)$ | Doppler PSD |
| $T_c$ | Chip time period |
| $T_m$ | Maximum excess delay time |
| $T_p$ | Pilot period of the $k^{th}$ user |
| $T_s$ | Symbol time period |
| $T_s^k$ | Symbol period of the $k^{th}$ user |
| $T_z(t)$ | Stochastic Gaussian process |
| $T_{\xi-}(R_s)$ | Average duration of fades |
| $t_{P_{r,-30dB}}$ | Time when the received power level drops below the -30 dB threshold |
| $t_{P_{r,0}}$ | Time when the first signal component is received |
| $u_k(t)$ | Baseband transmitted downlik signal of the $k^{th}$ user |
| $u_{k,i}(t), u_{k,q}(t)$ | In-phase and quadrature components of the transmitted signal of the $k^{th}$ user |
| $v(t)$ | Mobile speed |
| $x_k(m)$ | Data symbols transmitted |
| $y_{k,i}(t), y_{k,q}(t)$ | Phase corrected versions of RRC matched filter outputs |

# CHAPTER ONE

# INTRODUCTION

> *"Source and channel coding have been treated separately in most cases. It can be observed that most source coding algorithms for voice, audio and images still have correlation in certain bits, because for reasons of delay, non-stationarity and complexity source coding cannot always be done in an optimal way. Transmission errors exactly in these bits usually account for significant errors in the reconstructed source signal. The channel decoder should utilise such a residual correlation."*
>
> JOACHIM HAGENAUER [2]

In the Neanderthal days, homo sapiens proved themselves to be the dominant species on earth in terms of their mental abilities, to such an extend that during the last 30 millennia the modern man has evolved from unintelligible grunting to a rich, multi-cultured species with the ability to communicate in numerous ways. This varies widely from a vast number of verbally spoken and physically signed languages to written languages consisting of anything from simple alphabet letters to complex cyphers and drawings.

A new era in communication dawned after the emergence of written languages, resulting in a feasible way to communicate over large distances, albeit at a very large time penalty (smoke signals employed by the Navaho Indians, flags on masts of ships and reflecting light with mirrors are some exceptions). Despite the time penalty, written messages were the main type of communication prior to the 19$^{th}$ century and was widely accepted by the wealthy, which regularly employed message runners and pigeons to convey important information to distant family, colleagues and friends. Message pigeons were so successful that they were still regularly used during the first World War, even after the emergence of more sophisticated communication techniques prior to that era. Samuel Morse perfected wired telegraphy during the 1840's, followed some decades later by the development of telephony conceived by Alexander Graham Bell. This was followed by the first successful radio transmissions by Guglielmo Marconi during the 1890's. The Age of Electronics dawned during the early $20^{th}$ century when Fleming invented the diode vacuum tube and Pickard created the solid-state point-contact diode. After this, Armstrong developed the super heterodyne receiver and the *Frequency Modulation* (FM) concept. Two decades later Bardeen, Brattain and Shockley received a Nobel prize for the invention of the bipolar transistor, which followed the 1935 patent filed by Heil for the field-effect device. This led to the development of the *Integrated Circuit* (IC) during 1958 by two independent efforts led by Kilby and Noyce/Moore, a concept that was commercialised three years later by Fairchild Semiconductor. During the early 1970's, digital electronic devices emerged and the digital concept bloomed, and digital radio along with it.

Personal wireless communication has emerged from these technologies and have received widespread acceptance, clearly evident from the large growth within the communication sector. Even though it is currently already possible to communicate almost instantly with an individual almost anywhere in the world, the demand for larger bandwidth and a larger user base is ever increasing. These demands challenge telecommunication engineers, as the amount of available frequency spectrum and transmitter power is limited, which resulted in a global effort of various research groups from diverse areas to contribute to the earlier and modern systems.

These problems and others were already emerging in the late 1970's. It was clear that an attempt was necessary to unite the efforts of various hardware and software developers and manufacturers to a specific, standardised framework for a networking architecture that could serve as the foundation for the establishment of a suite of protocols that could be used by international networks. This led to the development of The Basic Reference Model for Open Systems Interconnection, which became widely known as the 7-layer *Open System Interconnection* (OSI) model.

The fundamental challenge of the communication engineer is the error-free transmission of data from some source to the final destination. However, due to practical channel non-idealites, including both linear and non-linear channel effects, the transmitted signal is corrupted, resulting in the introduction of errors. This limits the capacity of the channel to carry information, as first formulated by Shannon [9]. Shannon theorised that the limit of the channel capacity can be determined as a function of transmission bandwidth and the

*Signal-to-Noise Ratio* (SNR) of the *Additive White Gaussian Noise* (AWGN) channel under investigation, and also that this limit may be reached by either increasing the number of transmission symbols in the signal space during modulation, or by increasing the redundancy of the transmitted symbols by means of channel coding. A basic result leading from Shannon's work is the separation theorem, which states that source and channel coding can be treated separately. This means that there exists a separable source and channel coding scheme that allow transmission over the channel with arbitrary low error probability, as long as the entropy of the source is less than the channel capacity. These limits and results are still used to benchmark modern communication systems. Shannon's work inspired various further breakthroughs in telecommunications. *Table* 1.1 lists some of the milestones and contributions of the last six decades.

It is often considered that modern commercial mobile telephony was born on April 3, 1973, when Dr Martin Cooper of Motorola placed a call while walking down the streets of New York City to rival Joel Engel at Bell Labs, regardless of the fact that a successful *Autoradiopuhelin* (ARP) network was launched during 1971 in Finland. Five years later Bell Labs launced a trial *Advanced Mobile Phone Service* (AMPS) commercial cellular network in Chicago. This led to the birth of the *First Generation* (1G) networks like *Nordic Mobile Telephone* (NMT), AMPS, *Total Access Communication System* (TACS), *Radio Telefono Mobile Integrato* (RTMI), *Radio Telephone Network C* (C-Netz), and Radiocom 2000. These were based on analogue transmission and research and development efforts were focused on designing protocols that could take care of handovers.

The *Second Generation* (2G) introduced digital transmission techniques and were deployed in networks such as *Global System for Mobile communications* (GSM), Digital AMPS, *Integrated Digital Enhanced Network* (iDEN) and *Interim Standard 95* (IS-95). These networks were based on multi-user technologies like *Frequency Division Multiple Access* (FDMA), *Time Division Multiple Access* (TDMA) and *Code Division Multiple Access* (CDMA). Even though the first digital cellular call was made in 1990 in the USA, the first commercial network was rolled out in 1991 in Europe. During this time the microelectronic industry also made various breakthroughs in terms of their *Complementary Metal-Oxide Semiconductor* (CMOS) processes. This resulted in ICs with reduced power consumption and increased processing power. Advances in battery technology (for example, the improvement of the Lithium-Ion battery) and denser cellular cell deployment resulted in smaller mobile phones weighing less than 200 grams.

TABLE 1.1: Important contributions in the field of Information and Coding Theory

| Date | Theory developed | Technology developed |
|---|---|---|
| 1948 | Hamming codes<br>Golay codes | |
| 1950 | Reed Muller codes<br>Convolutional codes (Elias)<br>Cyclic codes<br>BCH and Reed-Solomon codes | |
| 1960 | Sequential decoder (Wozencraft & Reiffen)<br>LDPC codes (Gallager)<br>Concatenated codes (Forney)<br>Viterbi decoder<br>Berlekamp-Massey algorithm | IBM 7030 data storage<br>Mariner program (NASA) |
| 1970 | Goppa codes<br>Justensen codes<br>Chase algorithm<br>MAP algorithm (Bahl *et al*)<br>Trellis block codes (Wolf)<br>Trellis coded modulation (Ungerboeck) | Pioneer 10 & 11 (NASA)<br>ARP network (0G)<br>Viking program (NASA)<br>Voyager (NASA) |
| 1980 | SOVA algorithm (Hagenauer) | Compact disc data storage<br>V.32 Modems<br>NMT, AMPS, etc. (1G)<br>1.44M floppy data storage<br>Galileo (NASA) |
| 1990 | Turbo codes (Berrou)<br>Expander Codes (Spielman)<br>Joint source/channel coding (Hagenauer)<br>LDPC codes (MacKay)<br>Space-Time codes (Alamouti) | GSM, IS-95, etc. (2G)<br>V.34 Modems<br>DVD data storage<br>V.90 Modems<br>3G Cellular technology<br>802.11 Wireless technology |
| 2000 | | 802.15 Wireless technology<br>802.16 Wireless technology<br>UMTS, CDMA2000 (3G) |

It was evident by the large segment of mobile telephony in the communication sector that the cellular technology demand would continue to increase. This led to the development of *Third Generation* (3G) systems. However, during this development phase, the 2G networks were improved with 2.5G systems like *General Packet Radio Service* (GPRS), *Enhanced Data Rates for GSM Evolution* (EDGE) and CDMA2000 1x that expanded the 2G services by offering a reduced suite of 3G services.

The standardisation body, *International Mobile Telecommunications-2000* (IMT-2000), approached the development of the 3G networks slightly differently. Rather than standardise on a technology, it was decided to rather standardise on a set of specifications, as the vision of a single, unified worldwide 3G standard based on technology proved impossible. This was due to the start of various research projects not long after the introduction of the 2G networks. During the last years of the $20^{th}$ century, various network providers started testing the different technologies proposed for the 3G networks. This led to the deployment of the first commercial 3G systems at the beginning of the $21^{st}$ century. As expected, most of the GSM network operators adopted *Universal Mobile Telecommunications System* (UMTS) systems, while the IS-95 operators opted for CDMA2000 1xEV-DO systems. The evolution of the basic 2G GSM technology towards the feature rich 3G UMTS technology is illustrated in *Fig.* 1.1.

The design and implementation cost of systems used to evaluate the performance of new techniques is prohibitive and the resultant test bed may be relatively inflexible. Also, considering the significant advances in digital communication systems in a relatively short period of time, simulation can become a powerful tool for the prediction and assessment of system performance [10]. This approach was adopted for the work presented later.

## 1.1 RELATED RESEARCH TOPICS AND LITERATURE

### 1.1.1 Theoretical source models and source generation

Modern binary source modelling is not a topic receiving a lot of attention from the information theory and coding research community, as most researchers find the simple uniformly distributed source models adequate for the generation of statistically independent equiprobable data, or *Independent and Identically Distributed* (i.i.d.) sources. Early work on *PseudoRandom Number Generators* (PRNG) was initialised by Von Neumann [11],

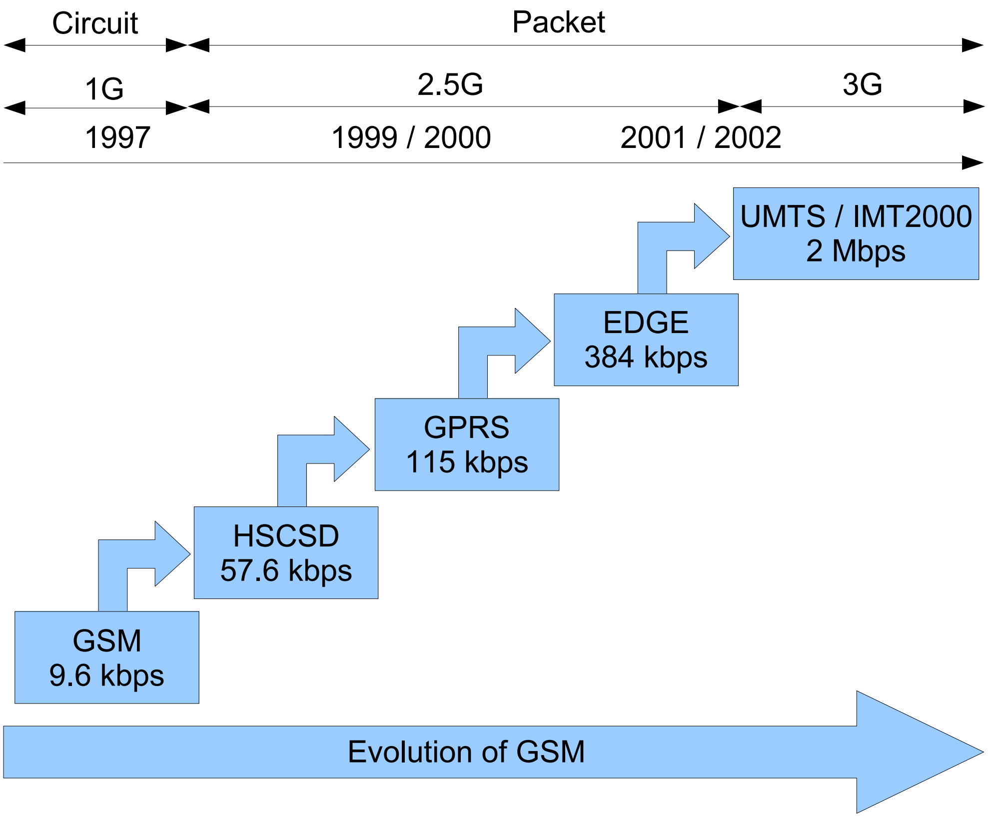

FIGURE 1.1: Evolution of GSM to UMTS

Elias [12] and Peres [13] who shared an approach to generate fair bits by exploiting the symmetries in the source and then considering equally likely events. These techniques, however, do not allow for exact equiprobable bits, as the Elias bound may not be achievable for infinite-memory sources, a problem addressed by Verdú *et al* [14, 15], who proposed an alternate technique allowing for some non-equiprobability in the bits.

The early work of Von Neumann was further followed by the development of various different approaches for PRNG, including linear congruential generators with an application example presented by Wichmann and Hill [16], the lagged Fibonacci generator as used within the Matlab v.5 and higher computational environment [17], the linear feedback shift register approach that is a very popular hardware solution, the Blum-Blum-Shub PRNG presented by Blum *et al* [18] which has popularity within the cryptographic community for its unusually strong security proof, the Fortuna family of secure PRNG [19] employing a generator, an entropy accumulator and a seed file for secure PRNG and the Mersenne twister [20] that is based on the generalised feedback shift register approach, but with a transformation ensuring that the generated numbers are equidistributed in a very large dimensional space. Also of interest is the interval algorithm proposed by Han and Hoshi [21], a simple, yet efficient algorithm based on the successive refinement of partitions of the unit interval $[0; 1)$. Reference to sparse sources were made by Salomon [22].

Recently, however, some of the contributors to the source modelling community have been focussing their attention on two new areas requiring improved models, the first being source models that can be used to successfully model statistically independent streams multiplexed into a single stream, as used extensively for traffic theory. These sources are especially applicable when packet-switching networks are considered. Lu *et al* [23] presented a thorough survey of source modelling techniques for *Asynchronous Transfer Mode* (ATM) networks, including both traditional theories as well as more recent studies that reveal traffic phenomenon not previously included in the models. Petr *et al* [24] evaluated broadband network technologies by multiplexing a constant bit rate voice source, a variable bit rate (but constant packet size) video source, a bursty *Local Area Network* (LAN) data source, and a very bursty image transfer source, while Norris *et al* [25] considered the superposition of variable bit rate sources in an ATM multiplexer.

The second group of researchers started to focus on modelling and analysing the traffic theory related to variable bit rate streams, that could be successfully applied to emulate video streams. Sen *et al* [26] presented work on modelling video sources which have been coded using interframe coding schemes, as well as carrying out buffer queuing analysis for the multiplexing of several such sources. Zhang [27] presented a new technique capable of generating gamma-distributed traffic with arbitrary correlation while retaining the computational efficiency of Gaussian autoregressive models. Garrett and Vetterli [28] investigated the interaction of congestion control with the partitioning of source information into components of varying importance for variable bit-rate packet voice and packet video. Li *et al* [29] investigated the second order effects of a wideband source in high speed networks by characterising it with a multi-state Markov modulated Poisson process, with the numeric results used to identify each individual effect of the source second-order dynamics on both queue length and loss rate, with additional work in the field being done by Anick *et al* [30], Guérin *et al* [31] and Heyman and Lakshman [32].

However, even though the work by Verdú *et al* [14] introduces the notion of allowing an arbitrarily small amount of non-equiprobability in the bits, no sources with a controllable amount of non-equiprobability has been proposed prior to this work.

### 1.1.2 Traditional separation theory and the effect on communication systems

The reader is referred to *Section* 1.2.1 for the bulk of the discussion on the related literature pertaining to the separation theorem, as it is presented as part of the motivation to this study. It is, however, worthwhile to take note of the following. It is well known that practical sources exhibit a certain amount of redundancy. This may be removed with source coders matched for the task, although the success thereof has recently been questioned [1, 4]. Source coding techniques are beyond the scope of this thesis and will not be presented in detail, except to note that 1) the separation of source coding from channel coding needs not result in any loss of performance if the block length is chosen sufficiently large [9], and 2) systems utilising joint source/channel coding techniques in scenarios where the block length is reduced, have been shown to achieve good performance [1, 3, 33–38]. However, as these systems tend to perform better than their separated counterparts in bad channel conditions, it is worth exploiting the redundancy in the source [4] to reduce error propagation and re-transmission requests. Finally, 3) digital transmission of speech, audio, images and video signals often exhibit residual redundancy after source coding due to complexity issues, delay and buffer constraints (resulting in a short block length) and non-ideal quantisation indices. This redundancy remains inside one block or frame as well as in time correlation of subsequent frames [3, 5] and may lead to a sparse data stream. These factors may lead to the transmission of sparse data streams with non-equiprobability in the bits.

### 1.1.3 Mobile channel characteristics and models

Some of the earliest work done regarding mobile channel characterisation, modelling and emulation was that of Rice [39], Clarke [40], Jakes [41] and Van Trees [42], allowing for modern communication engineers to develop simulation systems closely emulating mobile radio links in a very controlled manner. Since then, a multitude of researchers have devoted themselves to the topic. Even though this is a very broad topic, the field may be divided into two areas that hold more relevance to this work. They will be considered next by highlighting recent academic achievements and contributions.

The first area holding relevance is that of mobile radio characterisation. The fundamentals of this area have been presented very well in [43–45], where both temporal and spectral characteristics were discussed. More recent contributions consist of that of Pätzold *et al* [46–50], who have investigated test procedures and performance assessment of mobile fading channel simulators, including a very detailed statistical analysis of Jakes' fading channel simulator. They have also developed various methods to derive Doppler parameters used by Jakes' fading channel simulators and an optimal method for the derivation of deterministic simulation models for mobile radio channels, as well as highlighting problems of Monte Carlo method based simulation models for mobile radio channels. Additional work included channel parameter optimisation, which is required when a practical filter is implemented to approximate the theoretical desired Doppler *Power Spectral Density* (PSD). This is necessary to closely approximate the square root of the Doppler PSD with the magnitude of the implemented filter transfer function, while maintaining a minimal deviation with respect to some error criterion. Numerical optimisation procedures are required to solve this problem. Pop *et al* [51, 52] have also made contributions to Jakes' fading channel simulator model in terms of an in-depth statistical investigation into second order statistics, as well as some limitations to the widely accepted sum-of-sinusoids method.

Furthermore, methods of predicting mobile radio channel characteristics are also investigated, including work by Ekman *et al* [53] investigating linear and quadratic filters to predict channel taps and Dong *et al* [54] who proposed a *European Strategic Program on Research in Information Technology* (ESPRIT)-type algorithm to model and further predict a wideband time-varying channel at different frequencies. However, prediction methods fall mostly outside the scope of this study.

The second area of interest is that of mobile radio channel modelling and emulation. More recent contributions to this area include that of Hoeher [55] who presented a statistical discrete-time model for the *Wide-Sense Stationary-Uncorrelated Scattering* (WSSUS) multipath channel, while Fechtel [56] introduced a novel approach, based on channel orthogonalisation techniques in two inner product spaces, to model and efficiently simulate frequency-selective fading radio channels. Pätzold *et al* [57–60] contributed significantly, including the design of high-speed simulation models by using table look-up techniques, introducing an extended Suzuki model and its statistical properties for land mobile satellite channels as well as a deterministic simulation model for Suzuki processes with application to a shadowed Rayleigh land mobile radio channel. Uyematsu *et al* [61] addressed the problem of simulating a discrete memoryless channel, and proposed two algorithms for channel simulation by using the interval algorithm, while Whillans [62] developed and implemented a FRAMES based baseband channel simulator capable of emulating radio channels based on actual measurements or predefined models. Baddour *et al* [63] investigated autoregressive stochastic models of correlated Rayleigh fading processes and Patel *et al* [64, 65] proposed models with desired statistical properties that also remove some drawbacks of existing models derived by using the discrete line spectrum simulation method.

### 1.1.4 Proposed UMTS platform

The daily addition of thousands of new wireless telephone subscribers have ensured that the wireless digital communication sector is one of the largest growing market sectors today. This does, however, put a large strain on the limited bandwidth available to ensure acceptable service levels to these subscribers. Many multiple access methods have been developed in an effort to increase the number of users per unit bandwidth, including TDMA, FDMA and CDMA methods [43, 44, 66–68]. None of these methods have been shown to be vastly superior to the others, and in many circumstances hybrid systems employ more than one technique, as is the case with the proposed UMTS platform [69].

Not only is it required to provide a service to a huge amount of subscribers, but a vast variety of new network applications are being introduced by network operators to have a competitive advantage. This includes peer-to-peer applications and services [70–72], mobile applications, entertainment and games, multimedia applications (video conferencing, *Video-on-Demand* (VoD), distance learning, *Voice/Video over IP* (VoIP), *IP Television* (IPTV), etc), home automation [73], medical and health care monitoring and medical emergency services [74, 75], surveillance, service evaluation, accessibility, multi-modal interactions and applications, context-aware services and applications, user interfaces for mobile devices, seamless mobility, quad play, e-commerce, m-commerce, location-based services, personalisation, virtual home environments, and field trials and usability.

A lot of focus has been placed on various aspects of next generation systems [76], including the evolution of *Wideband Code Division Multiple Access* (WCDMA) towards *Higher Speed Downlink Packet Data Access* (HSDPA) [77] and challenges and opportunities regarding control and network management [78]. Although the UMTS/WCDMA system is described in sufficient detail in the candidate submission [69], many additional contributions were made describing the system more clearly by Dahlman *et al* [7], as well as system level modelling and simulation of the various links of such systems, performance evaluations, multiplexing of multimedia data and suppression of multi-access interference [79–84]. On a practical level, contributions by Staphorst [85] in terms of a complete mathematical description of a complex baseband QPSK system, allowed for fast simulation.

## 1.2 MOTIVATION AND OBJECTIVES OF THIS STUDY

### 1.2.1 Motivation of this study

The main engineering assumption under scrutiny during this work is the validity of the assumption that equiprobable source models may be used to simulate modern communication systems. A large number of next generation services for UMTS communication systems have been disclosed in *Section* 1.1.4, but many of these may not necessarily be optimally compressed, as there may have been strict time constraints to provide seemingly real-time throughput, or alternatively as in the case of medical data, lossless source codes must be used to ensure data quality. This has a number of implications on the statistics of the data being transmitted, and in turn on the simple i.i.d. source models that are usually employed to simulate these communication systems. Simulation sources very rarely provide for exactly equiprobable bits. If these are required, the Elias upper bound may not be achievable for infinite-memory sources (even if they are stationary and ergodic), because such symmetries need not exist. In general, we can only hope for almost equally-likely events [14]. These implications are not only restricted to the source, but also affect various other subsystems of the communication system, and therefore, serve as main motivation for the study.

1. The statistical distribution of the source is highly dependent on the type of data that is transmitted. It is well known that video, audio and the various types of processed and raw data do not exhibit the same statistical properties and that an optimised source coder for any one of these will not yield optimal results for the others. This leads to the requirement that each type of source requires a matched and optimal source coder. Recent years, however, have seen a large effort into the smooth transformation of current voice/data networks toward a multi-service ubiquitous infrastructure [76, 78]. Such an infrastructure requires that several data sources, that can possibly differ significantly in terms of their statistical properties, are multiplexed into a single data stream. This leads to very unpredictable statistics of the multiplexed stream that is transmitted in the physical layer of the OSI model. This makes it extremely difficult

to find a suitable coder, as the statistics of this stream could very easily change as the type of multiplexed sources (depending on the current application(s) being used) are changed. Another problem that arises at this level is the introduction of sensitive data, an example being a medical application, that is restricted to a lossless codec, clearly leading to non-optimal results if audio and/or video are also multiplexed into this stream. This leads to redundancy that could, depending on the source alphabet and codewords, lead to a non-equiprobable *Cumulative Distribution Function* (CDF) of the alphabet letters within the transmission frame. These data sources may be considered sparse.

2. It is not uncommon that source coding takes place on a higher level in the OSI model, i.e. before the different sources are multiplexed. These types of coders can be better matched to the source and usually yields more promising results than in the previous case, but even under these circumstances practical systems still need to adhere to real-time delay and buffer constraints and suffer from complexity limitations and fixed length quantiser indices. [38, 86–88]. Meeting the requirements of these constraints often lead to reduced complexity and non-optimal source encoding. Often variable bit rate sources are also encoded with constant bit rate coders [28] to satisfy the requirement for low delay and low delay variance. The complexity of the source coders need not necessarily be a problem at the base station or in the downlink channel, as powerful processing units may easily be deployed. There is, however, a practical limitation on the mobile units in terms of processing power and the required power budget associated with more powerful processors when the uplink channel is used. As mentioned above, this could again lead to a non-equiprobable CDF and sparse data streams.

3. For the last number of decades, telecommunication engineers have taken Shannon’s separation theorem very literally and have spent vast research resources on designing source coders that will almost completely remove the redundancy from a source, only to add significant, yet controlled, redundancy again by means of channel coders. After a very convincing argument led by Verdú *et al* [1], Hagenauer *et al* [2–6] have introduced the notion of reducing the coding constraint on the source coders in order to leave some redundancy that could be exploited by a joint source/channel decoder. The CDF of these partially source encoded streams have not been investigated in detail

within the research community, but tentative simulations have shown that there is a degree of non-equiprobability present.

4. The decision region or interval on which a conventional detector bases its decision as to which transmitted symbol has been received, is normally based on the assumption of an equiprobable data stream [44]. Typically this would yield optimal results, unless a non-equiprobable CDF exists, leading to a sparse data stream being transmitted. This leaves room for the improvement of conventional detection theory.

It should be noted that the intent of this work is to investigate uncoded data transmission over a UMTS/WCDMA system for various system, user and/or channel conditions, even if the transmitted sequence is sparse in nature. The fact that an equiprobable data stream will not be assumed, distinguishes this work from others.

### 1.2.2 Objectives of this study

The primary goal of this study was the investigation, the performance evaluation and a comparison of a conventional with a novel *Quadrature Phase Shift Keying* (QPSK)-based receiver structure for a UMTS/WCDMA based platform when possibly sparse data is transmitted. Data degradation was introduced by means of transmission over AWGN and wireless channel environments consisting of either frequency non-selective or frequency selective fading conditions. In order to achieve the primary outcome of this study, several secondary objectives had to be completed.

1. An investigation of the major requirements, specifications and building blocks used to create a realistic UMTS/WCDMA based transmitter (refer to *Chapter* 2), including
    (a) frequency and power requirements, as they influence channel models and transmission filter designs respectively,
    (b) the specifications ensuring the correct design and implementation of the physical channel models, as they need to comply to specific structures ensuring correct synchronisation and timing,
    (c) achieving correct spreading factors and transmission rates as set by the system parameter, and
    (d) implementing the QPSK-based transmitter, ensuring that

    i. the transmitter provides for spreading with variable length channelisation codes enabling multi-user transmission,
    ii. the transmitter provides for spreading with a fixed length scrambling code providing for multi-cell transmission,
    iii. filtering is being done within the specifications of the UMTS/WCDMA standard, and
    iv. quick simulation times are achieved by using a complex baseband equivalent model.

2. An investigation of the major building blocks used to create a realistic UMTS/WCDMA based receiver (refer to *Chapter* 3), including
    (a) a literature study covering conventional complex QPSK-based receivers for both frequency non-selective and frequency selective scenarios, while presenting
        i. the receiver structures for various channel scenarios,
        ii. the mathematical modelling of the received signal, and
        iii. a complete *Bit Error Ratio/Rate* (BER) analysis for various channel scenarios,
    (b) the development of a parameter that may be used to quantify the sparseness of a data stream,
    (c) a comparison of the developed parameter with similar parameters,
    (d) an investigation of the effect that sparseness has on the density functions of bitstreams,
    (e) the development, design and implementation of a source model capable of adjustable sparseness,
    (f) the development of a novel receiver structure capable of adapting to various levels of sparseness of the received data stream,
    (g) the derivation of an analytic expression for the BER performance in AWGN channel conditions,
    (h) the derivation of an analytic expression for the BER performance where the channel experiences Rayleigh fading,

  (i) the implementation of a conventional receiver structure that
    i. is capable of multi-cell detection by means of scrambling codes,
    ii. is capable of multi-user detection by means of channelisation codes,
    iii. is capable of complex baseband operation for faster simulation,
    iv. features the necessary phase correction when complex baseband operation is used,
    v. features the necessary matched filter for band limiting incoming noise and performing waveform correlation, and
    vi. features the necessary synchronisation functions for sampling,
  (j) implementation of a novel receiver structure capable of (i) i. through (i) vi. above, and additionally
    vii. is capable of measuring the sparseness of the received frame,
    viii. uses the measured sparseness level to allow for more accurate detection, and
    ix. enables other subsystems to use the measured sparseness level, which may be of importance when the transition is made to coded systems.

3. An investigation of elementary and statistical properties and parameters used to characterise radio channels, as well as various deterministic models used to simulate radio channels, their properties and their effects on transmitted data (refer to *Appendix* D), including
  (a) the implementation of a baseband AWGN channel model with an automatic calibration feature,
  (b) an in-depth literature study of the various parameters used to characterise channel models, as well as methods to determine these parameters from the measured received data,
  (c) a literature study of the various techniques available to model deterministic channels, as well as the implementation of a channel model that
    i. is capable of simulating a Rayleigh or Rician process for frequency non-selective channels,
    ii. is capable of simulating a wideband Rayleigh or Rician process for frequency selective channels,

        iii. has a high level of reconfigurability, including the carrier frequency, vehicle speed, Rician *Line of Sight* (LOS) parameter, power level of each path and the delay between paths,
        iv. has correct power scaling, and
        v. is compatible with the complex baseband transmitter for faster simulation, and
    (d) investigate and implement various methods to determine the Doppler parameters.

4. The implementation of a complete simulation platform to conduct an extensive simulation study (refer to *Chapter* 4), including

    (a) the use of an object orientated approach to implement and verify all the subsystems as C++ classes,
    (b) the creation of the necessary plain text configuration files to define the various parameters such as *Root-Raised Cosine* (RRC) filter coefficients, the UMTS/WCDMA system parameter, interpolation factors, realistic frequency non-selective and frequency selective configurations, etc. required by the subsystem classes,
    (c) the implementation of complete simulation platforms capable of performing single and multi-user transmission, AWGN noise effects and frequency non-selective as well as frequency selective fading for both conventional and the novel receiver structures in C++,
    (d) the verification and calibration of the complete simulation platforms, as well as various time and frequency domain measurements of the transmitted and received signals used to justify system functionality.
    (e) the use of the performance evaluation platforms to obtain simulated AWGN, frequency non-selective and frequency selective BER results for single and multiple users, as well as for conventional and the optimised receiver structures when using dense and sparse data streams on the *Ipercube* clusters sponsored by *Intel*, as well as the *Alpha* cluster.

# 1.3 CONTRIBUTIONS OF THIS STUDY

## 1.3.1 Novel contributions

This study focused on the effect that sparse data streams have on communication systems, but as it progressed it was necessary to investigate the UMTS/WCDMA physical layer, multi-user CDMA environments, narrowband and wideband systems and the characterisation and the modelling of various types of mobile communication channels. All these aspects culminated in various novel contributions in the fields of mobile communication systems and information theory. Some of these contributions are listed next.

1. A novel complex baseband mathematical model of the transmitted UMTS/WCDMA signal is presented (refer to *Section* 2.3).
2. A highly configurable complex baseband multipath fading channel simulator was developed using the sum-of-sinusoids method. The novelty lies not with the reconfigurability, but in the fact that the simulator can simulate fixed as well as a sinusoidal varying Rician LOS component. Also, the simulator can determine the Doppler parameters with a variety of methods (refer to *Section* D.4.5).
3. A novel complex baseband mathematical model of the received UMTS/WCDMA signal corrupted by AWGN, fading and *Multi-User Interference* (MUI) was presented (refer to *Section* 3.1.1.2).
4. A performance measure, viz. the sparseness measure, analogous to the entropy measure, was developed and can be used to quantify sparseness theoretically as well as in practical systems (refer to *Section* 3.2.1).
5. Source models were developed that are more suitable for simulating sparse data streams as opposed to equiprobable streams. These models were also improved by employing the sparseness measure to reduce the standard deviation of the sparseness in each frame. This reduces the amount of iterations required to compute various statistics accurately (refer to *Appendix* B).
6. A novel comparison was made between the sparseness measure and the entropy measure (refer to *Section* 3.2.3).

7. The effect of sparseness on the density functions of data streams in the presence of AWGN was derived, presented and explained (refer to *Section* 3.2.4).

8. Novel receiver structures capable of employing the sparseness measure to achieve optimal BER performance results were presented for both frequency non-selective and frequency selective fading scenarios (refer to *Section* 3.3.1).

9. An analytic expression used to determine the decision region of a detector was derived in terms of the sparseness measure and the SNR (refer to *Section* 3.3.1.1).

10. Strategies were developed enabling the receiver to practically determine the optimal decision region from the received frame's *Probability Density Function* (PDF) (refer to *Section* 3.3.1.1).

11. An analytic expression was derived for the BER performance of an optimal QPSK-based receiver employing the measure of sparseness in AWGN channel conditions (refer to *Section* 3.3.2.1).

12. An approximate analytic expression was derived for the BER performance of an optimal QPSK-based receiver employing the measure of sparseness in frequency non-selective fading channel conditions (refer to *Section* 3.3.2.2).

13. Novel simulation results were presented for

    (a) analysing the statistical deviation from the norm when a source generator employing feedback and the sparseness measure is employed (refer to *Section* 4.2.1),

    (b) the effect of certain channel coding schemes on the sparseness of the transmitted stream (refer to *Section* 4.3),

    (c) the orthogonality (including the auto- and crosscorrelation) of *Orthogonal Variable Spreading Factor* (OVSF) codes when they are sampled at a rate of more than one sample/chip (refer to *Section* 4.4.5),

    (d) the PDF of an uncoded, narrowband *Binary Phase Shift Keying* (BPSK)/QPSK-branch signal with various levels of sparseness and SNR using an AWGN source (refer to *Section* 4.5.1), and

(e) various BER curves showing the performance of both the conventional and the novel, optimised receiver structure for AWGN, various fading and multi-user examples, etc. (refer to *Section* 4.6.2).

### 1.3.2 Publications emanating from this study

During the course of this research study, the author co-wrote one refereed accredited local journal article, co-wrote and presented five international *Institute of Electrical and Electronics Engineers* (IEEE) conference papers and one local conference paper. The amalgamation of this work presented several relevant concepts, algorithms, analytic performance measures and simulation results that lead from the development of the required simulation building blocks. The following list details the scope of these publications and their relevance to this study in chronological order:

1. *"Performance Evaluation of a Joint Source/Channel Coding Scheme for DS/SSMA Systems Utilizing Complex Spreading Sequences in Multipath Fading Channel Conditions"* co-authored by *Prof. L.P. Linde* and *L. Staphorst* [89] was presented in *Montreal, Quebec, Canada* in May 2003. The paper covered a well-known joint source/channel coding scheme consisting of Huffman encoded data used to generate a state diagram to be decoded by means of a Viterbi algorithm decoder for possible use in future *Fourth Generation* (4G) *Direct Sequence Spread Spectrum Multiple Access* (DS/SSMA) CDMA communication systems. A multi-user *Complex Spreading Sequences* (CSS)-based DS/SSMA CDMA communication system was implemented as test platform for the joint source/channel coding scheme. Simulated BER performances were presented for uncoded, separate source and channel coded as well as joint source/channel coded systems under realistic multipath fading channel conditions.

2. *"Investigation of the Effect of LDPC Coding on the Sparseness of a Data Source in AWGN Channel Conditions"* co-authored by *Prof. L.P. Linde* [90] was presented in *Stellenbosch, South Africa* in September 2004. The paper implements a measure for sparseness in a simple antipodal modulation system employing *Low-Density Parity Check* (LDPC) coding and a *Message Passing Algorithm* (MPA) based decoder in AWGN channel conditions. The effect of the LDPC encoder on the statistics and CDF of the source, as well as the PDF of the received data were investigated. Comparative

results for various levels of sparseness and average SNR were presented, as well as simulation results showing that more detailed source analysis should be done before the assumption of equiprobable input symbols can be justified. Also presented were BER performance graphs for the coded system.

3. *"Performance Investigation of a Sparse Data Compression Technique with AWGN Channel Effects"* co-authored by *Prof. L.P. Linde* [91] was presented in *Gabarone, Botswana* in September 2004. The paper introduced a performance measure for data sources that can be used to evaluate the potential for good compression using a sparse source coding technique, as well as BER bounds in AWGN. Simulation results showed that the performance measure can be effectively used to predict the potential of a source for compression. Comparative PDF and BER results were presented for various sparseness levels in coded and uncoded systems.

4. *"Evaluation of the Effect of Hamming, LDPC and Convolutional Encoding on the Sparseness of a Data Source"* co-authored by *Prof. L.P. Linde* [92] was presented in *Cape Town, South Africa* in May 2005. The paper considered an implementation of the measure for sparseness to serve in a comparative review of various different encoding schemes. The effect that a Hamming encoder, LDPC encoder and a convolutional encoder have on the CDF of the source, as well as the PDF of the received data in AWGN conditions, were simulated and investigated. Comparative results for various levels of source and encoded sparseness were presented, as well as simulation results showing that a detailed source analysis is required before the assumption of equiprobable input symbols can be justified.

5. *"Employing a Measure of Sparseness to Investigate Sparse Data Compression in AWGN Conditions"* co-authored by *Prof. L.P. Linde* [93] appeared in the Transactions of the SAIEE in June 2006. This paper repeated and expanded on earlier work [91] where the algorithm of the sparseness measure was applied in two examples, the first being a sparse source coding technique, while the second example showed the derivation of BER bounds in AWGN for sparse data. Comparative results of sparse source coding and an uncoded system in terms of the introduced performance measure and error propagation in AWGN conditions were presented. Simulation results indicated that the performance measure can be effectively used to predict the potential of a source for compression and to more accurately estimate the decision interval, $r_d$,

for detectors, ranging from $r_d = 0.5493$ ($E_b/N_0 = 0$, $\eta_\alpha = 0.1$) to $r_d = 0.0202$ ($E_b/N_0 = 7$, $\eta_\alpha = 0.4$), with $\eta_\alpha$ the sparseness measure. Comparative PDF and BER results were presented for various sparseness levels in coded and uncoded systems.

6. *"A Novel Approach to Improve Sparse Data Models"* co-authored by *Prof. L.P. Linde* [94] was presented in *Windhoek, Namibia* in September 2007. This paper showed the implementation of the measure of sparseness with a specific feedback mechanism to improve the large standard deviation that current random data sources suffer from. The drawbacks of the current, frequently used random data sources was highlighted and a novel approach was suggested to rectify these disadvantages. Simulation results were presented for various block lengths typically used in 3G UMTS/WCDMA systems, indicating how the standard deviation can be significantly reduced by up to 33% when using an optimal feedback length. The various optimal feedback lengths were also presented, as well as some conclusions regarding communication system simulation.

7. *"Work in Progress - An Optimal UMTS/WCDMA Receiver Structure for Possibly Sparse Data Streams"* co-authored by *Prof. L.P. Linde* [95] was presented in *Pretoria, South Africa* in November 2008. The paper presented a novel, optimal next generation WCDMA receiver structure for situations where data streams exhibiting small or large amounts of sparseness are received. The receiver employs a measure of sparseness, allowing for almost real-time (per timeframe) sparseness estimation to be used in an optimal adaptive estimation technique. The corrected version of the BER performance benchmark was published to replace the erroneous expression presented in [91, 93]. Simulation results indicated the need for sparseness estimation, as well as performance benchmarks of the standard receiver structure to be used as a reference for comparison with results of the optimised receiver.

8. *"A CMOS based multiple-access DSSS transceiver"* authored by *Dr. S. Sinha* and co-authored by *Mr. M. Božanić, Mr. J. Schoeman, Prof M. du Plessis and Prof. L.P. Linde* [96] was presented in *Stellenbosch, South Africa* in April 2009. The paper presented a similar conventional transceiver system as proposed for this work, with the main emphasis being the transistor level CMOS design.

## 1.4 ORGANISATION OF THE DISSERTATION

This chapter was aimed at providing an overview of the history and development of the information and coding theory and the telecommunication system relevant to this study, as well as related research topics and the motivation of this study. The remaining chapters of this dissertation are summarised next and will be used to present a number of important concepts.

*Chapter* 2 gives an overview of the WCDMA *UMTS Terrestrial Radio Access* (UTRA) *Frequency Division Duplex* (FDD) specifications for the physical layer and the general transmitter structure that was implemented and used throughout this study. The specifications presented include the relevant frequency planning, the power requirements, the physical channels, the modulation scheme, various types of spreading codes employed and the filtering methods used.

*Chapter* 3 describes the classic approach to complex QPSK-based WCDMA-UTRA/FDD receiver design for both frequency non-selective and frequency selective scenarios by means of the necessary block diagrams illustrating the building blocks of the receivers, as well as a mathematical model to represent the received signals. The expected performance measures as found in literature are also presented.

The concept of sparseness is introduced and defined in terms of the necessary parameters. An explanation of the concept follows, after which it is related with the entropy measure, a similar parameter frequently encountered in information and communication theory. The effect that this parameter has on the CDF of bitstreams as well as the effect on the PDF when AWGN is introduced, is also examined.

This sparseness measure is then incorporated in novel complex QPSK receiver structures to optimally detect possibly sparse bitstreams. The optimal detection method is discussed and an optimal decision region is derived. The chapter is concluded with the derivation, analysis and discussion of analytic expressions for the BER performance benchmarks of the novel complex QPSK receiver structure when sparseness is taken into account.

*Chapter* 4 gives the results obtained during the simulation study. It was necessary to calibrate the source models in terms of the sparseness of the generated data streams that result from this building block, and the approach and results are discussed. Some initial results are presented to illustrate how coding will influence the sparseness of a data stream.

The results of the complex QPSK transceiver implementation are also evaluated, including time and frequency domain based measurements, synchronisation instances with the help of eye diagrams, narrowband transmission results in both the time and frequency domains and an analysis of the orthogonality of the OVSF codes used when perfectly aligned and also when shifted in time.

The channel models are evaluated next and the presented results include an analysis of the AWGN process, different methods to generate the Doppler parameters, after which the results related to the analysis of the complex Rician process for both frequency non-selective and frequency selective channels are presented.

Finally, a number of BER performance graphs are presented for various scenarios, including uncoded AWGN, frequency non-selective and frequency selective scenarios and results obtained for single user transmission as well as transmission in the presence of MUI.

*Chapter* 5 is used to draw conclusions from the obtained results. As many aspects of the work were not fully investigated and some unanswered questions remain, it was deemed necessary to make suggestions for future research.

In addition to the chapters outlined above, a number of appendices are presented to additionally cover both known and novel topics to clarify subject matter investigated in this topic. *Appendix* A covers some of the protocol signals as specified for the UTRA/FDD platform, while *Appendix* B covers a novel approach to generate data with a specific sparseness. *Appendix* D gives a theoretical discussion on the implemented channel models and various signal degradation effects, including AWGN and various types of signal fading. The appendix starts by investigating elementary properties of Rayleigh and Rician processes and various useful quantifying parameters, after which frequency selective and non-selective channels are defined and discussed. Useful statistical properties are presented, followed by techniques for modelling various types of deterministic fading channels. The appendix is concluded with various methods to determine critical simulation model parameters (viz., the Doppler parameters). Finally, the derivation of the BER performance of a BPSK/QPSK receiver in frequency non-selective channel conditions are presented in *Appendix* E.

# CHAPTER TWO

# WCDMA UTRA/FDD PERFORMANCE EVALUATION PLATFORM

In telecommunication applications, especially with very limited resources as is the case with wireless applications, the physical time/frequency resources are shared by different users accessing the system simultaneously. Traditionally, only three access techniques were implemented, namely FDMA, TDMA and CDMA. However, recent years have seen the emergence of space-time coding, which, although not a full scaled multiple access technique, does increase the number of users within a limited resources environment. Polarisation diversity requires the transmission of data over multiple antennas with different polarisation, but this technique has not received much attention up to date.

Many versions of different mobile communication systems have been implemented in various countries, including GSM, PDC, cdmaOne (IS-95) and US-TDMA (IS-136), to name but a few. Recall that a historical overview and the evolution of GSM towards UMTS have been presented in *Chapter* 1. In the standardisation forums, WCDMA technology has emerged as one of the most widely adopted 3G air interfaces [77]. WCDMA is generally used to refer to both the UTRA/FDD and the UTRA *Time Division Duplex* (TDD) types of operation within the 3GPP. However, the terms UTRA/FDD and UTRA/TDD are used when addressing only one specific type of operation.

The aim of this chapter is to provide the physical link specifications of the transmitters that have been implemented. The transmitter structure is investigated, as well as a mathematical model that may be used to describe the various spreading sequences. The chapter is concluded with the discussion of the required bandlimiting filters. The detailed signalling schemes and protocols governing communication between subsystems in the UTRA/FDD system fall outside the scope of this thesis, but a summary of the operation will be presented in *Appendix* A. The interested reader is referred to [69] for a detailed discussion.

## 2.1 RTT SPECIFICATIONS OF THE UTRA FDD WCDMA PHYSICAL LAYER

### 2.1.1 Frequency planning

The proposed frequency band of operation by the *International Telecommunications Union* (ITU) was accepted on a global scale, with the exception of North America. The uplink was assigned the frequency band of 1920 - 1980 MHz and the downlink 2110 - 2170 MHz. UMTS is based on 5 MHz WCDMA channels with a basic chip rate of 4.096 Mchips/s, corresponding to a bandwidth of approximately 5 MHz. Higher chip rates (8.192 and 16.384 Mchips/s) are also specified. These chip rates are intended for the future evolution of the WCDMA air interface towards even higher data rates (>2 Mb/s). Carriers are separated by a nominal spacing of 5 MHz, although these WCDMA carriers are located on a 200 kHz grid (channel raster). The transmitting and receiving frequencies are separated with a fixed or variable separation [7,8,69].

The wide bandwidth of WCDMA gives an inherent performance gain over previous narrowband cellular systems, since it reduces the effect of fading on the radio signal. In addition, WCDMA uses coherent demodulation in the uplink, a feature that has not previously been implemented in cellular CDMA systems. Additionally, fast power control on the downlink will yield improved performance, especially in indoor and low-speed outdoor environments at low Doppler spread. In total, for a speech service, these improvements are expected to increase the cell capacity of WCDMA by at least a factor of two (3 dB) [7].

### 2.1.2 Power requirements

The transmitter is rated to have a maximum power output as tabulated in *Table* 2.1 [8]. The output power dynamics can be controlled either in an open or closed loop power control fashion. The output power dynamics are given in *Table* 2.2. RF spectrum emissions are determined by the occupied bandwidth. The adjacent channel leakage power ratio for the first and second adjacent channels are 35 dB and 45 dB, respectively, below the in-band

TABLE 2.1: Different power classes and their corresponding maximum power output

| Power Class | Max Power Output |
|---|---|
| 1 | 33 dBm |
| 2 | 27 dBm |
| 3 | 24 dBm |
| 4 | 21 dBm |

power maximum. The transmit intermodulation has a minimum requirement of -35 dBc [8].

TABLE 2.2: Output power dynamics for the uplink and the downlink

| | Uplink | Downlink |
|---|---|---|
| Power control steps | Variable 0.25 - 1.5 dB | Variable 0.25 - 1.5 dB |
| Minimum transmit power | -50 dBm | - |
| Power control cycles per second | 1.6 kHz | 1.6 kHz |
| Power control dynamic range | 80 dB | 30 dB |

The diversity characteristics at the receiver are determined by the time diversity, the multi-path diversity and the antenna diversity. The static reference sensitivity level has a BER of $1 \times 10^{-3}$ at an input power of -110 dBm. The maximum input power has a BER of $1 \times 10^{-3}$ at an input power of -25 dBm. The adjacent channel selectivity has a BER of $1 \times 10^{-3}$ with assigned/adjacent channel power -93/-52 dBm. In-band blocking occurs with a BER of $1 \times 10^{-3}$ for a modulated interferer at -44 dBm, while out-of-band blocking occurs with a BER of $1 \times 10^{-3}$ for a tone interferer at -30/-15 dBm. Inter-modulation should have a BER of $1 \times 10^{-3}$ with 2 interfering signals at -46 dBm. Spurious emissions are tabulated in *Table* 2.3 [8].

TABLE 2.3: Spurious emissions for various frequency bands

| Frequency band | Spurious emission |
|---|---|
| In-band | $<$ -60 dBm / 4.096 MHz |
| 9 kHz to 1 GHz | $<$ -57 dBm / 100 kHz |
| 1 GHz to 12.75 GHz | $<$ -47 dBm / 100 kHz |

## 2.2 THE PHYSICAL CHANNELS

### 2.2.1 Downlink physical channels

The frame structure for the downlink *Dedicated Physical Channel* (DPCH) is illustrated in *Fig.* 2.1. A superframe has a duration of 720 ms, consisting of 72 frames. This results in a basic frame duration of 10 ms. Each frame consists of 15 slots, while each slot can be divided into 2560 chips ($10 \cdot 2^k$ bits, $k = 0...7$). This 10 ms frame corresponds to one power control period.

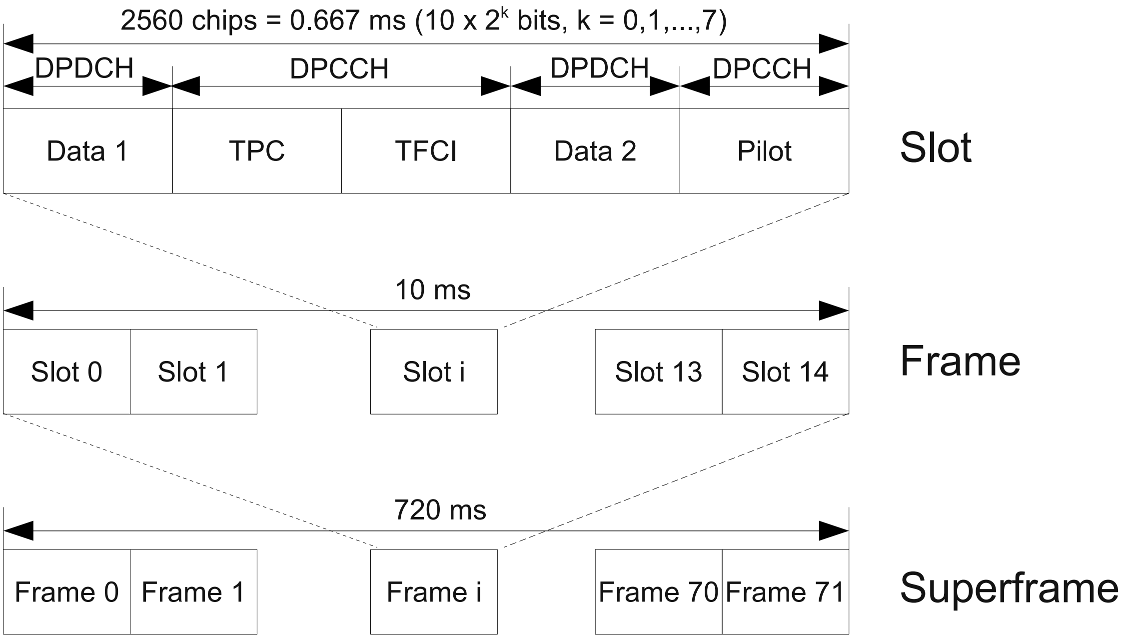

FIGURE 2.1: UTRA FDD downlink frame structure

Layer 2 dedicated data is time-multiplexed with layer 1 control information within each slot. The layer 1 control information consists of known pilot bits for downlink channel estimation, power control commands for uplink closed-loop power control, and a *Transport Format Indicator* (TFI). Dedicated pilot bits are used instead of a common pilot in order to support, for example, the use of adaptive antenna arrays in the base station, also on the downlink. Dedicated pilot bits also allow for more efficient downlink closed-loop power control. The TFI informs the receiver about the instantaneous parameters (block size and number of blocks) of each transport channel multiplexed on the physical channel [7, 69].

### 2.2.2 Uplink physical channels

The frame structure for the uplink DPCH is illustrated in *Fig.* 2.2. A superframe has a duration of 720 ms, consisting of 72 frames. This results in a basic frame duration of 10 ms. Each frame consists of 15 slots. Each slot has a duration of 0.667 ms and can be divided into 2560 chips ($10 \cdot 2^k$ bits, $k = 0...6$). This 10 ms frame corresponds to one power control period.

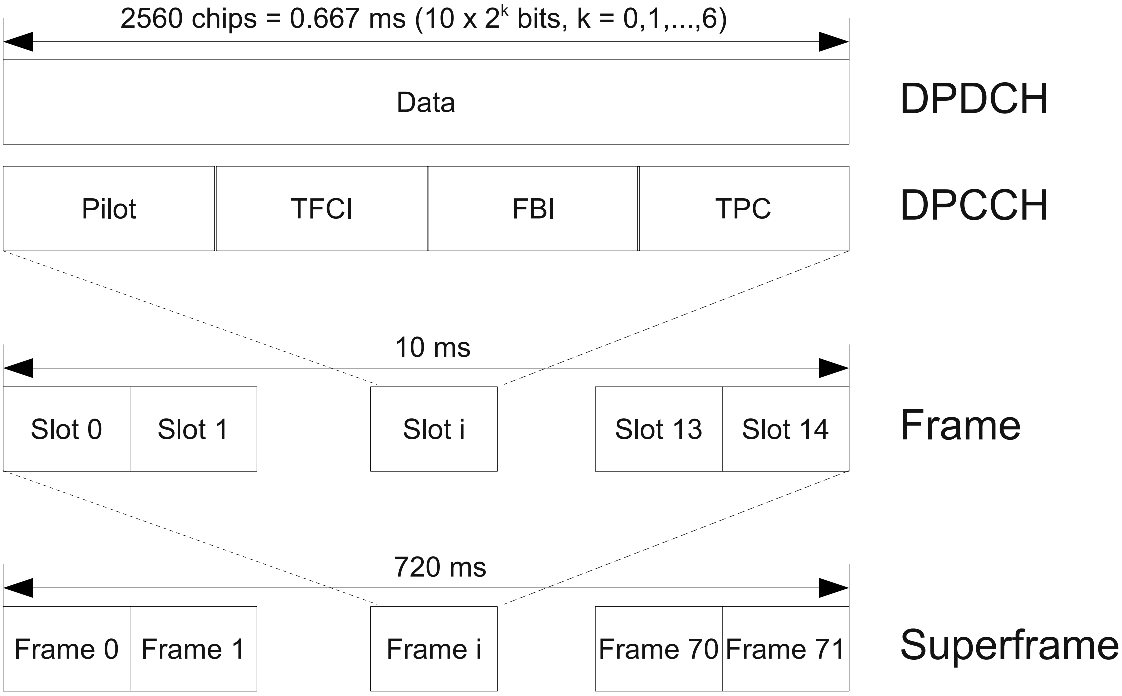

FIGURE 2.2: UTRA FDD uplink frame structure

The uplink dedicated channels can be used for multicode transmission varying from zero up to six parallel *Dedicated Physical Data Channels* (DPDCH) on layer 1, each with a unique channelisation code. On the uplink, layer 2 data and layer 1 control information is transmitted in parallel on different physical channels. The layer 1 control information transmitted on the *Dedicated Physical Control Channel* (DPCCH) consists of several parts. These include the pilot bits to support channel estimation for coherent detection, *Transmit Power Control* (TPC) commands, feedback information on transmit diversity and an *Optional Transport Format Combination Indicator* (TFCI). The TFCI informs the receiver about the instantaneous parameters of the different transport channels multiplexed on the uplink DPDCH, and corresponds to the data transmitted in the same frame [8]. Note that the uplink DPDCH and DPCCH on the same layer 1 connection generally have different values of $k$, which results in different rates and spreading factors [7, 69].

Various design trade-offs for the system parameter, $k$, are summarised in *Table* 2.4

Table 2.4: Trade-off between the system parameter ($k$) and the corresponding symbol rates and spreading factor for the uplink and downlink DPCH

| System parameter | Bits/slot | Bits/frame | Spreading Factor | Symbol Rate ksps | Link direction and channel |
|---|---|---|---|---|---|
| $k$ | $10 \cdot 2^k$ | | $512/2^k$ | | Downlink |
| 0 | 10 | 60/90 | 512 | 7.5 | DPCH |
| 0 | 10 | 30/120 | 512 | 7.5 | DPCH |
| 1 | 20 | 240/60 | 256 | 15 | DPCH |
| 1 | 20 | 210/90 | 256 | 15 | DPCH |
| 1 | 20 | 180/120 | 256 | 15 | DPCH |
| 1 | 20 | 150/150 | 256 | 15 | DPCH |
| 1 | 20 | 120/180 | 256 | 15 | DPCH |
| 2 | 40 | 510/90 | 128 | 30 | DPCH |
| 2 | 40 | 480/120 | 128 | 30 | DPCH |
| 2 | 40 | 450/150 | 128 | 30 | DPCH |
| 2 | 40 | 420/180 | 128 | 30 | DPCH |
| 3 | 80 | 900/300 | 64 | 60 | DPCH |
| 4 | 160 | 2100/300 | 32 | 120 | DPCH |
| 5 | 320 | 4320/480 | 16 | 240 | DPCH |
| 6 | 640 | 9120/480 | 8 | 480 | DPCH |
| 7 | 1280 | 18720/480 | 4 | 960 | DPCH |
| | | | $256/2^k$ | | Uplink |
| 0 | 10 | 150 | 256 | 15 | DPDCH, DPCCH |
| 1 | 20 | 300 | 128 | 30 | DPDCH |
| 2 | 40 | 600 | 64 | 60 | DPDCH |
| 3 | 80 | 1200 | 32 | 120 | DPDCH |
| 4 | 160 | 2400 | 16 | 240 | DPDCH |
| 5 | 320 | 4800 | 8 | 480 | DPDCH |
| 6 | 640 | 9600 | 4 | 960 | DPDCH |

## 2.3 DIGITAL MODULATION

*Fig.* 2.3 illustrates the spreading and modulation of the downlink dedicated physical channel. Data modulation is QPSK-based, that is, a pair of bits is spread to the chip rate using the same channelisation code and subsequently scrambled by a cell-specific real scrambling code. Different physical channels in the same cell use different channelisation codes. Several downlink physical channels can be transmitted in parallel on one connection using different channelisation codes in order to achieve higher channel bit rates (multicode transmission) [7]. The modulating chip rate is 3.84 Mchips/s (3.6864 Mchip/s for multicode transmission).

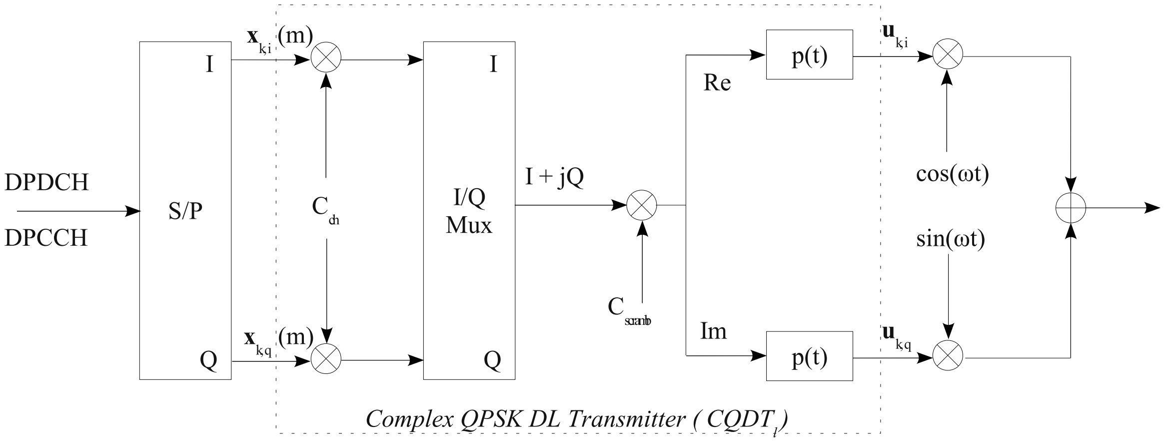

FIGURE 2.3: UTRA FDD downlink spreading and modulation (from [7])

The typical baseband transmitted downlink signal of the $k^{th}$ user may be described mathematically as

$$u_k(t) = \sum_{m=0}^{M_k-1} A_k x_k(m) s_{k,m}(t - mT_s^k) + \sum_{m=0}^{N_p-1} A_p b_p(m) s_m(t - mT_p - (M_k-1)\,T_s^k) \quad (2.1)$$

with $M_k$ (resp. $N_p$) the number of data (resp. pilot) symbols, $x_k(m)$ (resp. $b_p(m)$), $A_k = \sqrt{2E_k}$ the amplitude of the transmitted data symbol, $T_s^k$ (resp. $T_p$) the symbol (resp. pilot) period of the $k^{th}$ user, and $s_{k,m}(t)$ the $k^{th}$ user's (resp. $s_m(t)$ the pilot's) specific spreading waveform that corresponds to the $m^{th}$ code segment, given as

$$\begin{aligned} s_{k,m}(t) &= \tfrac{1}{\sqrt{N_k}} \sum_{i=0}^{N_k-1} C_{ch,k}(i) C_{scramb}(i + mN_k) p(t - iT_c) \\ &= \tfrac{1}{\sqrt{N_k}} \sum_{i=0}^{N_k-1} c_{k,m}(i) p(t - iT_c) \end{aligned} \quad (2.2)$$

with $T_c$ the chip period, $N_k$ the user specific spreading factor, $C_{ch,k}$ an $N_k$-chip Walsh channelisation code and $C_{scramb}$ a Gold code as discussed in *Section* 2.4. These two codes are mixed in a single time varying and user $k$ specific spreading code, $c_{k,m}(i)$. Finally, $p(t)$ is the impulse response of a chip shaping filter as discussed in *Section* 2.5. It is of practical concern to note that

$$\int_{-\infty}^{+\infty} |s_{k,m}(t)|^2 \, dt = 1 \tag{2.3}$$

The transmitted downlink signal may also be written in a complex baseband notation for the $k^{th}$ user, consisting of the in-phase component $u_{k,i}(t)$ and the quadrature component $u_{k,q}(t)$, as

$$\begin{aligned} u_k(t) &= u_{k,i}(t) + j u_{k,q}(t) \\ &= \sum_{m=\{0,2,..\}}^{M_k-1} A_k x_k(m) s_{k,m}(t - mT_s^k) + \sum_{m=\{0,2,..\}}^{N_p-1} A_p b_p(m) s_m(t - mT_p - (M_k - 1)\, T_s^k) \\ &+ j \sum_{m=\{1,3,..\}}^{M_k-1} A_k x_k(m) s_{k,m}(t - mT_s^k) + j \sum_{m=\{1,3,..\}}^{N_p-1} A_p b_p(m) s_m(t - mT_p - (M_k - 1)\, T_s^k) \end{aligned} \tag{2.4}$$

by considering that the *Serial-to-Parallel* (S/P) converter will take two consecutive symbols, $\{x_k(0), x_k(1)\}$, $\{x_k(2), x_k(3)\}$, $\{x_k(4), x_k(5)\}$, etc. as input to be converted to the parallel in-phase stream $\{x_k(0), x_k(2), x_k(4), ...\}$ and the quadrature phase stream $\{x_k(1), x_k(3), x_k(5), ...\}$.

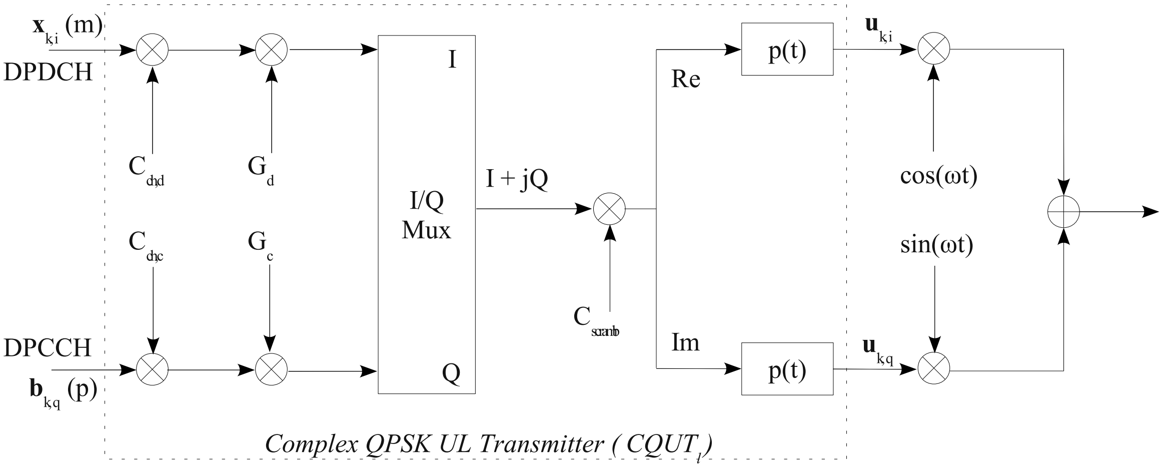

FIGURE 2.4: UTRA FDD uplink spreading and modulation (from [7])

*Fig.* 2.4 illustrates the spreading and modulation for the uplink DPCH. Data modulation is done in such a way that the I and Q branches are used as two independent BPSK channels, resulting in dual channel QPSK. For the case of a single DPDCH, the DPDCH and DPCCH are spread by two different channelisation codes and transmitted on the I and Q branches respectively. If more than one DPDCH is to be transmitted, the additional DPDCHs can be transmitted on either the I or Q branch using additional, unique channelisation codes (multicode transmission). The total spread signal $I + jQ$ is subsequently complex scrambled by a connection-specific complex scrambling code [7, 69].

## 2.4 SPREADING CODES

### 2.4.1 Channelisation codes

The channelisation codes for the downlink, as required in *Fig.* 2.3 for real spreading, are OVSF codes. These codes preserve the orthogonality between the downlink DPDCH/DPCCH channels of different rates and spreading factors.

OVSF codes can be created using a code tree. The different levels in the code tree define channelisation codes of different spreading factor lengths. The choice of codes within the code tree is limited within a cell and a code may be used if, and only if, that code is not a prefix of another. Stated differently, no code on the path from the specific code to the root of the tree and any other code in the sub-tree below the specific code may be used in the same cell. This creates a dependency for the number of available channelisation codes on the rate and spreading factor of each physical channel. The codes for the downlink DPCH are decided by the network and the set of channelisation codes may be changed during an established connection when a change of service or an inter-cell handover occurs [69].

Similar to those of the downlink, the channelisation codes implemented for the uplink shown in *Fig.* 2.4 are OVSF codes, with the same restrictions as that of the downlink codes. Channelisation codes are only valid within one mobile station. A connection requires that a channelisation code is allocated for the uplink DPCCH, and at least one different code is provided for the DPDCH, albeit that the number of codes may be increased as the demand on the number of DPDCHs increase. Since different mobile stations use different uplink scrambling codes, no co-ordination for the uplink channelisation codes are required between different connections, which implies that these codes may be allocated in a pre-defined order, limiting the agreement between the network and mobile station to the number of codes and spreading factor length of the uplink channelisation codes. The exact codes to be used are then implicitly assigned [69].

### 2.4.2 Scrambling codes

There exists 512 unique scrambling codes for the downlink that are divided into 32 groups of 16 codes each. The grouping of the downlink codes is done in such a manner so as to facilitate a fast cell search. Each cell or sector (if antenna segmentation for a cell is done) is assigned with a downlink scrambling code at the initial deployment. The mobile station determines this code during the cell search process.

The scrambling code sequences are constructed as the positionwise modulo 2 sum of 40960 chip segments of two binary $m$-sequences generated by means of two generator polynomials, each of degree 18 [69]. Let $x$ and $y$ be the two independent sequences respectively over *Galois Field 2* (GF(2)). The $x$ sequence is constructed using the primitive polynomial $1 + X^7 + X^{18}$, while the $y$ sequence is constructed using the polynomial $1 + X^5 + X^7 + X^{10} + X^{18}$ for the downlink channel. Similarly for the uplink channel, two generator polynomials of degree 41 are used. The $x$ sequence is constructed using the primitive polynomial $1+X^3+X^{41}$, while the $y$ sequence is constructed using the polynomial $1+X^{20}+X^{41}$. The resulting sequences thus constitute segments of a set of Gold sequences. The scrambling codes are repeated for every 10 ms radio frame.

Either short or long scrambling codes can be used in the uplink. The short scrambling code is a complex code, given by $C_{scramb} = c_I + jc_Q$, with $c_I$ and $c_Q$ being two different codes from the extended very large Kasami set of length 256. The long uplink scrambling code is used when the base station in a cell is not required to perform multi-user detection. The short scrambling code gives direct insight into the choice of long scrambling code to be implemented. Therefore, no explicit allocation of the long scrambling code is needed.

## 2.5 RRC FILTERING

Along with Nyquist and Gaussian filters, RRC filters are among the most popular, bandwidth efficient pulse shaping filters used to combat *Intersymbol Interference* (ISI) in modern digital data transmission systems. RRC filters have been selected by the governing and design bodies for UMTS as the pulse shaping filter of choice with a roll-off factor (minimum bandwidth factor) of $\alpha = 0.22$ in the frequency domain. Let us proceed to evaluate how this parameter is applied to the filter design.

The frequency response of a raised cosine pulse shaping filter is given by [44]

$$P_{RC}(f) = \begin{cases} T_s, & |f| \leq \frac{1-\alpha}{2T_s} \\ \frac{T_S}{2}\left(1+\cos\left[\frac{\pi T_s}{\alpha}\left(f - \frac{1-\alpha}{2T_s}\right)\right]\right), & \frac{1-\alpha}{2T_s} \leq |f| \leq \frac{1+\alpha}{2T_s} \\ 0, & |f| \geq \frac{1+\alpha}{2T_s} \end{cases} \tag{2.5}$$

with $f$ the frequency, $T_s$ the symbol time and $\alpha$ the roll-off factor. The corresponding impulse response (time domain) is obtained by taking the inverse Fourier transform of the frequency response and is given by

$$p_{RC}(t) = \text{sinc}\left(\frac{\pi t}{T_s}\right) \cdot \frac{\cos(\pi\alpha t)/T_s}{1-(2\alpha t/T_s)^2} \tag{2.6}$$

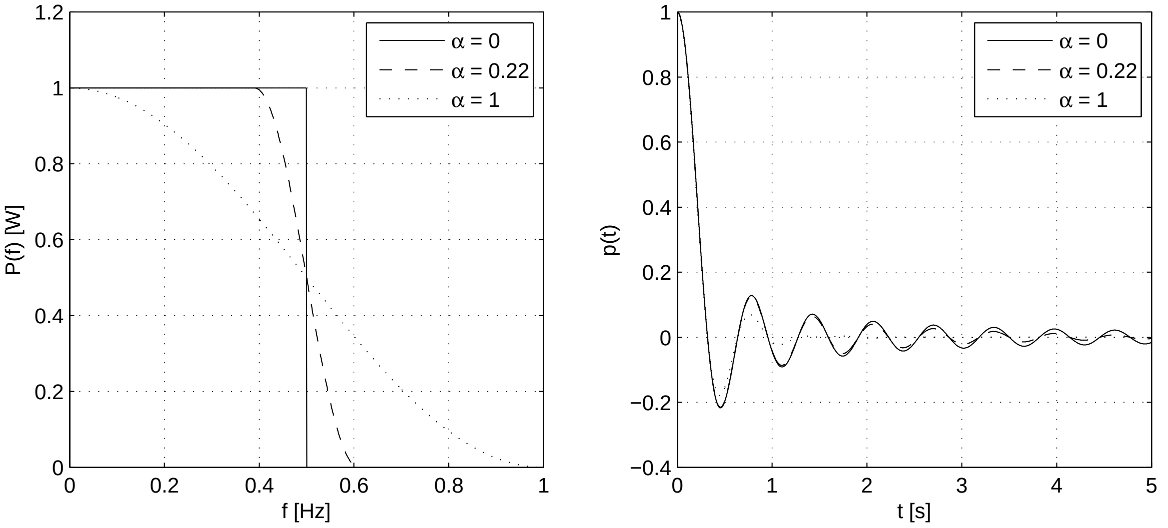

FIGURE 2.5: The normalised a) frequency response and b) impulse response of an RRC filter ($T_s = 1$)

The frequency and impulse responses are illustrated in *Fig.* 2.5. Although $\text{sinc}(0)$ seemingly includes division by zero, L'Hospital's rule indicates that the numeric value of $\text{sinc}(0) = 1$. The minimum bandwidth needed to transmit a pulse train at $1/T_s$ symbols per second is $f_{min} = 1/(2T_s)$ Hz. This requires an ideal filter with a square (brick-wall) low-pass response at $f_{min}$. However, the ideal sinc type impulse response has slowly decaying tails which results in filters that are difficult to implement practically. The addition of excess bandwidth, varied with $\alpha$ as $(1+\alpha)\cdot f_{min}$ Hz, allows for a spectrally less efficient filter with a more manageable impulse response.

In practical systems, the raised cosine frequency response is divided equally between the transmitter and the receiver. Both the receiver and the transmitter contain identical filters whose magnitude response is given by the square root of *Eq.* (2.5), normalised so that the maximum remains $T_s$. The actual implemented frequency response of the RRC pulse shaping filter is given by [97]

$$P\left(f\right)=\begin{cases}\sqrt{T_s}, & |f|\leq\frac{1-\alpha}{2T_s}\\ \sqrt{T_s}\cos\left(\frac{\pi|f|T_s}{2\alpha}-\frac{\pi(1-\alpha)}{4\alpha}\right), & \frac{1-\alpha}{2T_s}\leq|f|\leq\frac{1+\alpha}{2T_s}\\ 0, & |f|\geq\frac{1+\alpha}{2T_s}\end{cases}\tag{2.7}$$

with the impulse response given as

$$p\left(t\right)=\frac{1}{\sqrt{T_s}}\frac{\sin\left(\pi(1-\alpha)\frac{t}{T_s}\right)+\frac{4\alpha t}{T_s}\cos\left(\pi(1+\alpha)\frac{t}{T_s}\right)}{\frac{\pi t}{T_s}\left[1-\left(\frac{4\alpha t}{T_s}\right)^2\right]}\tag{2.8}$$

It should be noted that the symbol time in these equations should represent the shortest time period of the system. Therefore, when a spread spectrum system is to be considered, $T_s$ should be changed to the chip period, $T_c$.

# CHAPTER THREE

# QPSK-BASED WCDMA RECEIVER STRUCTURES

M-*ary Phase Shift Keying* (M-PSK) is perhaps the generic form of modulation most widely utilised in contemporary practice, ranging from voice-band modems to high-speed satellite transmission. A large part of its success lies in the fact that it is elementary with modern processors and signal processing techniques to modulate signals by mapping the digital sequence into an analogue waveform. Also, 4-PSK has been adopted as the base-line technique over BPSK, as the unfiltered QPSK signal occupies only half the spectrum when compared to BPSK with a similar bit error probability, with the only significant penalty being an increased sensitivity to carrier phase synchronisation. This forms part of the motivation for the choice of a QPSK-based modulator in the UMTS/WCDMA physical layer. One such a modulator structure was presented in *Chapter* 2. The communication engineer then has a choice between various different techniques to optimally detect the received waveform, which may have been degraded and corrupted by the physical channel as modelled in *Appendix* D. The optimal receiver consists of two parts, i) the signal demodulator which can be implemented either by means of correlation or matched filtering, and ii) the detector, basing its decision either on the *Maximum A-Posteriori* (MAP) criterion or the *Maximum Likelihood* (ML) criterion, and also either in a symbol-by-symbol fashion for independent symbols or a trellis based fashion over a sequence of symbols when symbol interdependence exists.

This chapter presents an overview of conventional complex wideband QPSK receiver structures and a mathematical model applicable to the UTRA/FDD WCDMA system proposed for both frequency non-selective and frequency selective scenarios. The analytic bit error probabilities for uncoded systems are presented, again for both fading scenarios. The next section entails the discussion of sparse data streams on communication systems and covers topics including a method of measuring sparseness, a comparison of entropy and the measure of sparseness and the effects that sparseness and noise variance have on the joint PDF of bitstreams. In light of this discussion, a novel approach is presented to demodulate a QPSK constellation if a sparse bitstream is transmitted. The chapter is concluded with the analysis of analytic bit error probabilities for various channel conditions.

## 3.1 CONVENTIONAL COMPLEX WIDEBAND QPSK RECEIVERS

This section will investigate traditional means of designing a wideband QPSK receiver for communication systems over a range of communication conditions, including AWGN conditions as well as multipath fading channel conditions typically experienced in mobile communication systems. Analytic BER performance is also investigated as a relevant performance measure used to gauge the effectiveness of such receivers.

### 3.1.1 Complex wideband QPSK receiver structures

As mentioned earlier, a typical receiver structure consists of a demodulator as well as a detector, which may be implemented in a variety of ways depending on the application and situation. A discussion of the choices made for the receiver implementation will follow shortly. Before proceeding, however, it should be noted that the proposed receiver structures are designed to be compatable with the baseband equivalent output of the transmitter and channel models discussed in earlier chapters, therefore negating the effect of high carrier frequencies during simulation. It does, however, include additional complexity in the form of phase correcting subsystems caused by cross-terms due to multiplication of complex numbers.

It is assumed that the received signal, $r_k(t)$, carries information limited over the time duration $0 \leq t \leq T_s$, but also limited to the $M$ signal waverforms $u_m(t)$ with $m = 1, 2, .., M$ of the transmitter. The complex received signal will be in the form of *Eq.* (D.52) measured as the output of either *Fig.* D.10 or *Fig.* D.11 presented in *Appendix* D.6 for a single user, unless it is specifically stated to be a multi-user scenario.

#### 3.1.1.1 Optimal receiver for signals corrupted by frequency non-selective channels with AWGN

A correlation demodulator decomposes the received signal and noise into vectors weighted with orthonormal basis functions. This process enables the receiver to determine the projection of the received vector onto these basis functions and gives an indication of the correlation that exists between the received signal and each basis function over the period, $T_s$. However, the basis functions need to be known at the receiver. It is often much simpler for systems employing filtered waveforms to use the filter as a correlator, as the filtering and correlation functions share many similarities. This method is known as matched filter demodulation and since the filter impulse response of the transmitter is known, it may be used during the demodulation process. For this reason, a raised cosine filter was designed, with the root of the filter used at both the transmitter and receiver (the matched filter) to achieve an effective overall raised cosine response, with the impulse response given by *Eq.* (2.8).

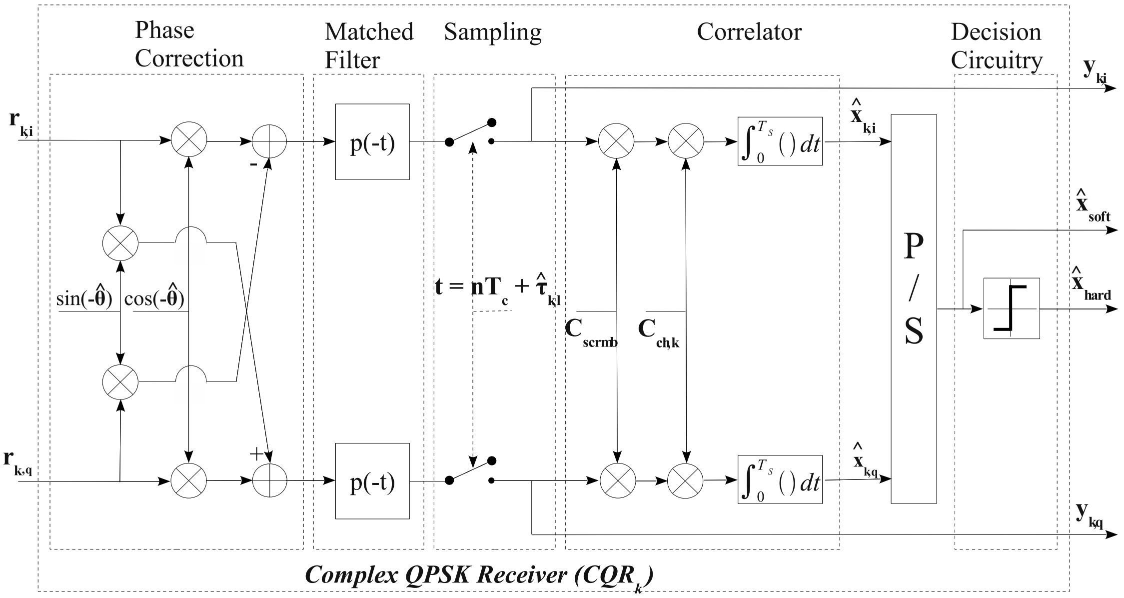

FIGURE 3.1: Complex single path QPSK based receiver for WCDMA applications

A typical complex baseband receiver structure is illustrated in *Fig.* 3.1. As the complex baseband notation introduces additional cross-product terms due to the complex number multiplication process of *Eq.* (D.52), additional phase shift is experienced by the received signal that is corrected by means of the phase correction subsystem as indicated in the figure. The phase-corrected versions of the received signal are both filtered with a RRC matched filter, after which it is sampled at the appropriate time instance, $nT_s + \widehat{\tau_k}$. This yields a signal ready for baseband processing (descrambling and despreading) given as

$$\begin{aligned} y_{k,i}(t) &= \left[\left(r_{k,i}(t)cos(\widehat{\theta}) - r_{k,q}(t)sin(\widehat{\theta})\right) \otimes p^*(t)\right] |_{t=nT_s+\widehat{\tau_k}} \\ y_{k,q}(t) &= \left[\left(r_{k,i}(t)sin(\widehat{\theta}) + r_{k,q}(t)cos(\widehat{\theta})\right) \otimes p^*(t)\right] |_{t=nT_s+\widehat{\tau_k}} \end{aligned} \tag{3.1}$$

with $\widehat{\theta}$ the estimated phase shift introduced by the complex baseband fading channel (an additional phase shift introduced by a receiver lowpass filter to band limit the AWGN can also be incorporated within this parameter) and $\widehat{\tau_k}$ is the time delay a received symbol experiences due to the receiver filters.

The estimated wideband signal may now be processed to its equivalent narrowband signal by first descrambling the signal with the scrambling code, $C_{scramb}$, after which it is despreaded with the channelisation code, $C_{ch,k}$, of the $k^{th}$ user. The narrowband estimation of the transmitted vector is finally multiplexed into a single data stream by means of the *Parallel-to-Serial* (P/S) converter.

#### 3.1.1.2 Optimal receiver for signals corrupted by frequency selective channels with AWGN

The receiver structure discussed earlier is suitable for simpler communication setups where the transmitted signal is only corrupted by a narrowband Rician/Rayleigh process with AWGN. Even though it may be implemented as a receiver for a system experiencing frequency selective fading, it will only receive the portion of the energy within one (corresponding to the selected $\tau_l$) path, rendering it inefficient in its accumulation of received energy. An optimal approach for the case where energy is received via multiple paths was proposed by Price *et al* [98], which was aptly called the Rake receiver, analogous to an ordinary garden rake, for the similar way in which the fingers of the rake correspond to the power-delay profile used to characterise the multipath fading channel and the way multiple signals are received in a tapped delayed line fashion. Rake receiver structures are, therefore, generally used in applications where interference suppression and multipath mitigation are required.

A Rake receiver structure, as illustrated in *Fig.* 3.2 for a complex baseband receiver architecture, corresponds to multiple versions of the flat fading complex QPSK receiver discussed earlier, with each of the $L$ flat fading receivers used to detect the received signal within one of the $L$ distinct paths characterising the multipath channel. This is accomplished

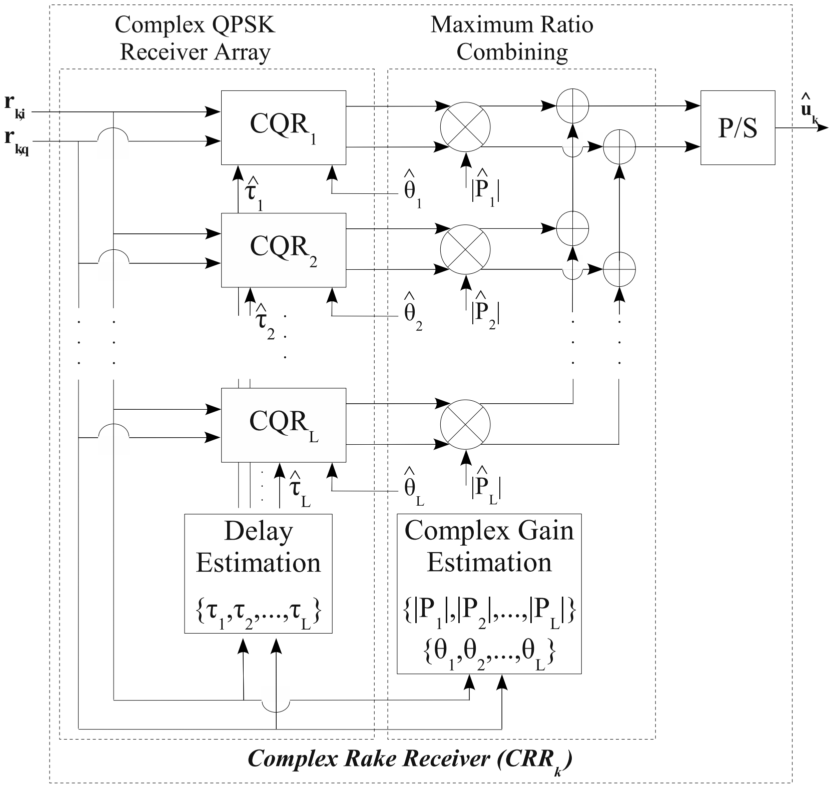

FIGURE 3.2: Complex multipath QPSK based Rake receiver for WCDMA applications

by synchronising the timing of the *Sample-and-Hold* (S/H) circuitry, which (with reference to *Fig.* 3.1) may be controlled with an external time delay parameter, $\tau_l$, for each of the distinct paths within the multipath channel. These values, when perfectly estimated by the delay estimation subsystem, correspond exactly to the time delay parameters of the power-delay profile, as discussed in *Appendix* D.4.3 and *Appendix* D.6, which are often assumed to be known to the receiver when synchronisation techniques are not under investigation. Up to this point, the system may be described mathematically by again investigating the received downlink signal (in this case specifically for a multi-user, multipath environment with AWGN) that is given as

$$\begin{aligned} r(t) &= \underbrace{\sum_{k=1}^{K}\sum_{l=1}^{L}\sum_{m=0}^{M_k-1} A_k\alpha_{k,l}x_k(m)s_{k,m}(t-mT_s^k-\tau_{k,l})}_{S_d(t)} \\ &+ \underbrace{\sum_{l=1}^{L}\sum_{m=0}^{N_p-1} A_p\alpha_{k,l}b_p(m)s_m(t-mT_p-(M_k-1)\,T_s^k-\tau_{k,l})}_{S_p(t)} + n(t) \end{aligned} \tag{3.2}$$

which may be written in the complex baseband notation as

$$\begin{aligned}
r_{k,i}(t) &= u_{k,i}(t)\alpha_{R,k,i}(t) - u_{k,q}(t)\alpha_{R,k,q}(t) + n_i(t) \\
&= \sum_{k=1}^{K}\sum_{l=1}^{L}\left(\begin{array}{c}\underbrace{\sum_{m=\{0,2,..\}}^{M_k-1} A_k x_k(m) s_{k,m}(t-mT_s^k)}_{DPDCH} \\ + \underbrace{\sum_{m=\{0,2,..\}}^{N_p-1} A_p b_p(m) s_m(t-mT_p-(M_k-1)\,T_s^k)}_{DPCCH}\end{array}\right)\alpha_{k,l}(t)\cos\left(\phi_{k,l}(t)\right) \\
&- \sum_{k=1}^{K}\sum_{l=1}^{L}\left(\begin{array}{c}\underbrace{\sum_{m=\{1,3,..\}}^{M_k-1} A_k x_k(m) s_{k,m}(t-mT_s^k)}_{DPDCH} \\ + \underbrace{\sum_{m=\{1,3,..\}}^{N_p-1} A_p b_p(m) s_m(t-mT_p-(M_k-1)\,T_s^k)}_{DPCCH}\end{array}\right)\alpha_{k,l}(t)\sin\left(\phi_{k,l}(t)\right) + n_i(t)
\end{aligned} \tag{3.3}$$

for the in-phase component and

$$\begin{aligned}
r_{k,q}(t) &= u_{k,i}(t)\alpha_{R,k,q}(t) + u_{k,q}(t)\alpha_{R,k,i}(t) + n_q(t) \\
&= \sum_{k=1}^{K}\sum_{l=1}^{L}\left(\begin{array}{c}\underbrace{\sum_{m=\{0,2,..\}}^{M_k-1} A_k x_k(m) s_{k,m}(t-mT_s^k)}_{DPDCH} \\ + \underbrace{\sum_{m=\{0,2,..\}}^{N_p-1} A_p b_p(m) s_m(t-mT_p-(M_k-1)\,T_s^k)}_{DPCCH}\end{array}\right)\alpha_{k,l}(t)\sin\left(\phi_{k,l}(t)\right) \\
&+ \sum_{k=1}^{K}\sum_{l=1}^{L}\left(\begin{array}{c}\underbrace{\sum_{m=\{1,3,..\}}^{M_k-1} A_k x_k(m) s_{k,m}(t-mT_s^k)}_{DPDCH} \\ + \underbrace{\sum_{m=\{1,3,..\}}^{N_p-1} A_p b_p(m) s_m(t-mT_p-(M_k-1)\,T_s^k)}_{DPCCH}\end{array}\right)\alpha_{k,l}(t)\cos\left(\phi_{k,l}(t)\right) + n_q(t)
\end{aligned} \tag{3.4}$$

for the quadrature phase component.

The matched filter outputs of user $k$ are determined by passing the received signal through a bank of filters matched to the delayed versions of $s_{k,n}(t)$ sampled at $nT_s^k + \widehat{\tau}_l$. The filter output for path $l$ is given as

$$\widehat{y}_{k,l}^{n}(t) = \int_{-\infty}^{+\infty} r(t) s_{k,n}^{*}(t - nT_s^k - \widehat{\tau}_l) dt \tag{3.5}$$

As long as the channel exhibits slow fading, the channel tap weights may simply be determined by averaging a number of successive matched filter outputs of the specific channel path. This is accomplished by sending $N_P$ pilot symbols and determining the average of the matched filter as

$$\widehat{\alpha}_{k,l} = \frac{\sum_{n=0}^{N_P-1} \widehat{y}_{k,l}^{n} b_p^{*}(n)}{N_p A_p} \tag{3.6}$$

The $L$ estimated signals are then combined to yield a final output estimation of the transmitted signal. *Fig.* 3.2 illustrates such a receiver structure.

## 3.1.2 Analytic bit error probabilities for uncoded systems

### 3.1.2.1 Communication over AWGN channels

It is well known that the probability of error of an M-PSK system may be determined from the distance between the closest signal points in the constellation, which, for BPSK, is typically given as $d_{min} = 2\sqrt{E_s}|_{E_s=E_b}$. Inspection of the conditional AWGN PDFs superimposed on the signal space then reveals that the error probability of a symbol may be determined in terms of the minimum distance between two signal points as a Gaussian tail integral, which is known to be [43, 44]

$$P_s = Q\left[\sqrt{\frac{d_{min}^2}{2N_0}}\right] \tag{3.7}$$

However, this can be shown to also be the case for any M-PSK system that exhibits sufficient symmetry to ensure that all the minimum distances computed between all possible signal points and their neighbours are equivalent, which is a condition most practical systems adhere to. Now, when considering that the distance between a given signal and one of its nearest neighbours is given as $d_{min} = 2\sqrt{E_s}\sin(\pi/M)$, it may be concluded that the error probability will be lower bounded by

$$P_s \geq Q\left[\sqrt{\frac{2E_s}{N_0}}\sin\left({}^{\pi}\!/_{M}\right)\right] \tag{3.8}$$

If the observation space, $D_i^c$, denoting the union of two half spaces in two dimensions (i.e. one quadrant in a Cartesian plane formed by connecting the four QPSK signal points), is considered, a nearest neighbour decision problem may be defined to yield an upper bound given by

$$P_s \leq 2Q\left[\sqrt{\frac{2E_s}{N_0}}\sin\left({}^{\pi}\!/_{M}\right)\right] \tag{3.9}$$

This is a tight bound of the true error probability to within a factor of 2. Investigation of the error region at high SNR by means of numeric integration would suggest that the upper bound is quite accurate [44, 66].

Finally, by noting that $E_s = E_b \log_2 M$, it may be concluded that the bit error probability of an M-PSK signal is bounded by

$$Q\left[\sqrt{\frac{2E_b}{N_0}(\log_2 M)\sin^2\left({}^{\pi}\!/_{M}\right)}\right] \leq P_b \leq 2Q\left[\sqrt{\frac{2E_b}{N_0}(\log_2 M)\sin^2\left({}^{\pi}\!/_{M}\right)}\right] \tag{3.10}$$

These bounds do not provide for exact bit error probabilities, but they may be determined by means of numeric methods for higher dimensions, as the derivation of the exact solution in such a case is very involved. In the special case of $M = 2$, *Eq.* (3.7) may be used to give the bit error probability of QPSK as

$$P_b = Q\left[\sqrt{\frac{2E_b}{N_0}}\right] \tag{3.11}$$

Care should be taken to ensure that a Grey coding is used when mapping the binary values to the signal points in the constellation.

#### 3.1.2.2 Communication over frequency non-selective channels

This section will present a brief overview on the BER performance of BPSK systems in slowly fading channels. The reader is referred to *Appendix* E for a detailed discussion and a complete derivation of the solution presented next. The steps followed in the proof in *Appendix* E will aid with the derivation presented in *Section* 3.3.2.2 for the BER performance of the proposed structures.

The probability of error, given transmission over a frequency non-selective Rayleigh channel, is given by

$$P_e = \frac{1}{2}\left[1 - \sqrt{\frac{E_b/N_o}{1 + E_b/N_o}}\right] \tag{3.12}$$

The dependence of this function on the average SNR is profound, as a $P_e = 10^{-5}$ may be achieved with a SNR of 9.6 dB for a non-fading channel, compared to approximately 44 dB required for a fading channel. This is due to the basic property of fading channels that the error probability is dependent on infrequent, but long fading events.

## 3.2 THE EFFECT OF SPARSE DATA STREAMS ON COMMUNICATION THEORY

### 3.2.1 A measure of sparseness

Data sources are usually modelled with symbols consisting of letters from a source alphabet and the probability of occurrence of these symbols. These probabilities can then be used to determine the entropy, or the amount of information conveyed by the source in bits per source symbol. The entropy, however, does not necessarily convey insight into the sparseness of the source in a linear manner. Sources are considered sparse if one of the alphabet letters occurs less frequently than the other letters. In order to compare the sparseness of one source with another, we need to introduce a measure for sparseness.

Consider a source with $n$ symbols $a_i \in \{a_0, a_1, ..., a_{n-1}\}$, with $a_i$ constructed with any of $m$ possible alphabet letters $b_h \in \{b_0, b_1, ..., b_{m-1}\}$. Each symbol, $a_i$, has a probability of occurrence given as $Prob[a_i] = p(a_i)$. We define the measure of sparseness for a block of length $l \to \infty$ as the ratio of $p(a_i)$ and $p(a_0), ..., p(a_{n-1})$, with $p(a_i) \leq p(a_j)$ for $j \epsilon [0, n-1]$. This yields a measure for sparseness for symbols given simply by

$$\eta_s = \frac{p(a_i)}{\sum_{k=0}^{n-1} p(a_k)} = \min\left[p(a_0), p(a_1), ..., p(a_{n-1})\right] \quad \forall \;\; a_i \in \{a_0, a_1, ..., a_{n-1}\} \tag{3.13}$$

with $a_i$ the symbol that is least likely to occur. This, however, only gives an indication of the sparseness of a source in terms of the source symbols, $a_i$, and does not take the source alphabet, $b_h$, into account. The sparseness, when measured in terms of $b_h$, might differ significantly from the sparseness when measured for $a_i$. We take this into account by defining the probability of alphabet letter $b_h$ in symbol $a_i$ as $Prob[b^h_{a_i}] = p(b^h_{a_i})$. The measure for sparseness on a letter level, rather than a symbol level, can now be given (when the weighted alphabet letter $b_h$ is least likely to occur over all symbols) as

$$\eta_\alpha = \min\left[\frac{\sum_{k=0}^{n-1} p(a_k)p(b^h_{a_k})}{\sum_{j=0}^{m-1}\sum_{k=0}^{n-1} p(a_k)p(b^j_{a_k})}\right] \quad \forall\ a_i \in \{a_0, a_1, ..., a_{n-1}\}, b_h \in \{b_0, b_1, ..., b_{n-1}\} \tag{3.14}$$

with $\sum_{j=0}^{m-1}\sum_{k=0}^{n-1} p(a_k)p(b^j_{a_k}) = 1$.

This letter level (or bit level, if $m = 2$ for a binary source) measure is more practical, considering that a transmitter will usually send data as a block or frame filled with a string of compressed data letters, rather than data symbols. It is also important to note that an infinite block length is not a practical consideration, but if the block of length $l$ is chosen sufficiently large, $\eta_\alpha$ can be accurately approximated within the frames.

### 3.2.2 Sparseness explained by example

Using the definition above, a binary source alphabet is described by $b_h = \{0, 1\}$. Assume a source with only two symbols, $a_i = \{a_0, a_1\}$. The sparseness measure at a symbol level, $\eta_s$, then indicates the ratio of the number of occurrences of $a_0$ to the sum of the number of occurrences of $a_0$ and $a_1$ in a block of length $l$ as $l \to \infty$, which of course describes the probability of occurrence of $a_0$, given as $P(a_o) = p_0$. Similarly, the probability of occurrence of $a_1$ is given as $P(a_1) = p_1$.

A source is said to be sparse if $p_0 \neq p_1$, and the sparse symbol is the symbol with the lowest probability of occurrence, i.e. $p_1$ is sparse if $p_1 < p_0$. A first source is also considered more sparse than a second source if $\eta_{s,1} < \eta_{s,2}$, i.e. the smaller the measure of sparseness, the larger the sparsity of the source. The symbol level sparseness measure is given as

$$\begin{aligned} \eta_s &= \frac{p(a_i)}{\sum_{k=0}^{n-1} p(a_k)} \\ &= \frac{p_1}{p_0+p_1} \end{aligned} \tag{3.15}$$

with $p_0 + p_1 = 1$, resulting in $\eta_s = p_1$. As $l$ is decreased to a practical, finite length, $\eta_s$ may be approximated by considering how frequently a symbol occurred within the length $l$, or

$$\begin{aligned} \widehat{\eta}_s &= \tfrac{\#a_1}{\#a_0+\#a_1} \\ &= \tfrac{\#a_1}{l} \\ &\approx p_1 \end{aligned} \tag{3.16}$$

with the approximation necessary as the true probability only holds in the limit as $l \rightarrow \infty$.

The various levels at which sparseness may be determined and how it influences bitstreams will be shown next by means of an example. An arbitrary symbol set is given by $a = \{a_0; a_1\} = \{00; 001\}$. It is clear that this symbol sequence will benefit greatly from a suitable source codec, but this is not considered at this stage. Assume that the probability of occurrence of symbol $a_0$ is extremely large, and, following the notation introduced earlier, is given as $p(a_0) = 0.9$. Therefore, $p(a_1) = 1 - p(a_0) = 0.1$. Inspection of the alphabet letters used to construct the symbols reveals that the probability of occurrence of the letter $0$ in symbol $a_0$ is determined as $p(b^0_{a_0}) = 2/2$, and similarly we may find $p(b^1_{a_0}) = 0/2$, $p(b^0_{a_1}) = 2/3$ and $p(b^1_{a_1}) = 1/3$. Having found each alphabet letter's probability of occurrence, we can find the weighted probability of occurrence of each alphabet letter as $p(b^0_{a_n}) = \sum_{k=0}^{1} p(a_k)p(b^0_{a_k}) = 0.9 \cdot 2/2 + 0.1 \cdot 2/3 = 0.967$ and $p(b^1_{a_n}) = \sum_{k=0}^{1} p(a_k)p(b^1_{a_k}) = 0.9 \cdot 0/2 + 0.1 \cdot 1/3 = 0.033$, as this will be required for the calculation of $\eta_\alpha$.

Using these results, it is a simple matter to determine the various different sparseness measures. Firstly, the sparseness may be determined at a symbol level using *Eq.* (3.15), yielding a result of $\eta_s = 0.1/(0.1 + 0.9) = 0.1$. This is an extremely sparse source, but it is to be expected considering the very high probability of occurrence of $a_0$. Secondly, the sparseness may be determined further on an alphabet level using *Eq.* (3.14). However, in order to proceed, we have to recognise that $p(b^1_{a_n}) < p(b^0_{a_n})$. This requires the use of $p(b^1_{a_n})$ as the numerator of *Eq.* (3.14), which leads to $\eta_\alpha = 0.033/(0.967 + 0.033) = 0.033$. This result differs significantly from $\eta_s$, and is explained by considering that the probability of occurrence of the alphabet letter $1$ is very low, as it is weighted with a symbol that is less likely to occur. Notice also from this example that the sparseness level of a bitstream may differ significantly from that of the least likely symbol probability and should, therefore, not be used interchangeably. Unless specifically stated otherwise, this work will assume the sparseness to be determined on an alphabet level, i.e. $\eta_\alpha$.

### 3.2.3 Entropy *vs.* the measure of sparseness

Since sparseness indicates that one symbol occurs less frequently than any other symbol, it is fair to assume that the minimal sparseness, or conversely, a dense data stream, occurs for equiprobable symbols, i.e. $p_i = 1/N$ if $N$ symbols occur, or $p_0 = p_1 = 1/2$ for the binary case, resulting in $\eta_s = 0.5$ as per *Eq.* (3.15). This is the first limit for sparseness, with the second given by $\eta_s = p_a \rightarrow 0$. Sparseness is, therefore, a linear relation $\eta_s = p_a$ limited to the range $0 \leq \eta_s \leq 0.5$.

The sparseness measure may be compared to the entropy measure, which provides us with a measure of information. The entropy is determined as

$$H_s = \sum_{i=0}^{N-1} p(a_i) \log \left(1/p(a_i)\right) \tag{3.17}$$

leading to $H_s \leq \log(N)$ (equality is true for equiprobability) and $H_s = 0$ in the case where no information is transmitted when any symbol has a $p(a_i) = 1$. It is worthwhile to note that the entropy is typically calculated with $\log_2(x)$ with unit bits or $\log_e(x) = \ln(x)$ with unit nats (natural bits).

The following differences are observed.

- The sparseness measure is linear, while the entropy is related to a $\log$ function. This behaviour is analogous to detectors using exponential functions compared to log-likelihood detectors using linear functions.
- Sparseness is limited to $0 \leq \eta_s \leq 0.5$, while entropy is limited to $0 \leq H_s \leq \log(N)$.
- Optimal information transfer occurs when $H_s = \log(N)$ and $\eta_s = 0.5$.
- The sparseness measure may be optimally applied in a scenario where $\eta_s \rightarrow 0$ and $H_s \rightarrow 0$.
- The sparseness measure is used to compensate for the fact that the entropy is non-optimal.

The differences between the sparseness measure and the entropy measure are illustrated in *Fig.* 3.3. The entropy was calculated for a binary source using $\log_2(x)$ for a result with unit bits.

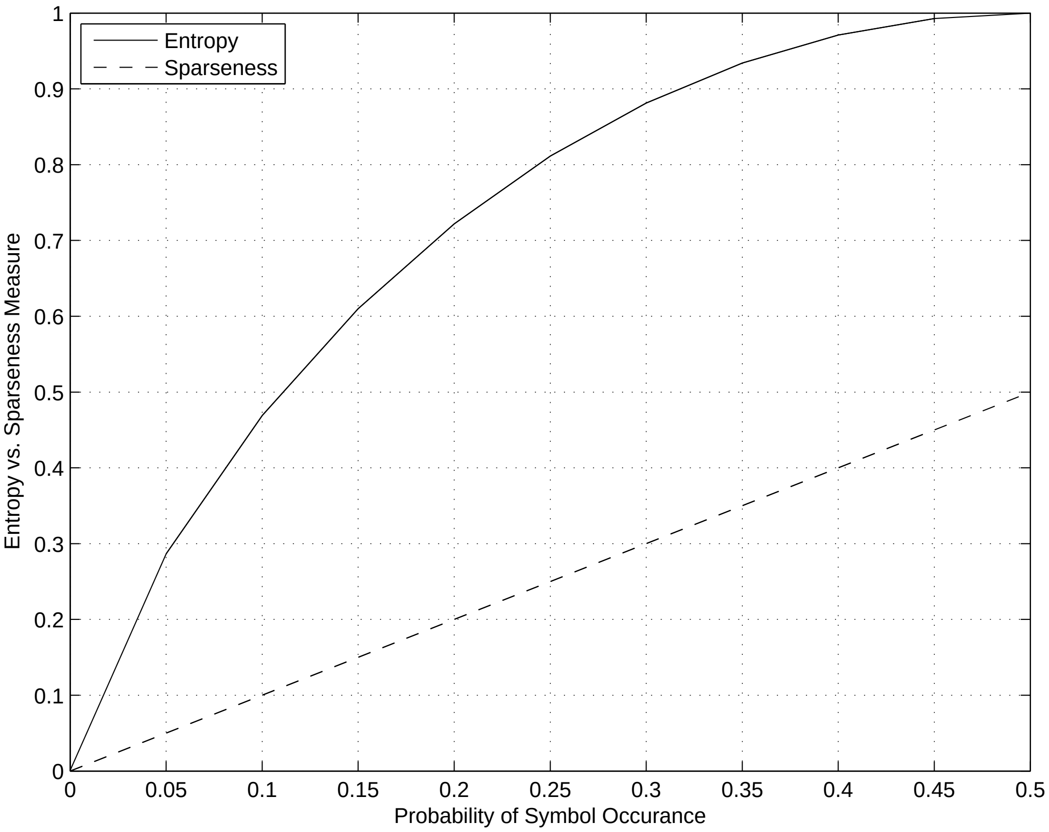

FIGURE 3.3: Comparison of the entropy measure (unit bits) with sparseness for a single binary symbol with varied probability of occurrence.

### 3.2.4 The effect of sparseness and AWGN on the joint PDF of bitstreams

The following section investigates the effect of sparseness on the conditional PDF of a received bitstream. It is assumed that 1) elements $s_i \in \{s_0, ..., s_{n-1}\}$ are independent, 2) a sparse symbol, $s_\alpha$, of sparseness $\eta_\alpha$ exists, and 3) the symbols referred to here correspond to the alphabet letters of *Section* 3.2.1, i.e. $s_i$ correspond to $b_h$. As an example, arbitrarily assume $s_\alpha = s_1$ to be the sparse letter transmitted. The probability of the received letter for an antipodal modulation scheme may be written as a weighted sum of conditional probabilities given by

$$\begin{aligned} p(r) &= \sum_{i=0}^{n-1} \alpha_i p(r|s_i) && (i) \\ p(r) &= \eta_\alpha p(r|s_1) + \sum_{i=0, i\neq 1}^{n-1} \alpha_i p(r|s_i) && (ii) \\ p(r) &= \eta_\alpha p(r|s_1) + (1-\eta_\alpha) p(r|s_0) && (iii) \end{aligned} \tag{3.18}$$

with *Eq.* (3.18) (*i*) the general form where an *a priori* probability, $\alpha_i$, is used as the weighting constant. This is usually assumed to be $\alpha_i = \frac{1}{n}$ for equiprobable inputs. The conditional PDF, $p(r|s_i)$, described by *Eq.* (D.1) may be used for substitution in *Eq.* (3.18). *Eq.* (3.18) *(ii)* represents the case where a sparse symbol, $s_1$, is transmitted. The weighting factor, $\alpha_i$, of that symbol may be represented by the sparseness measure. The motivation for this stems from *Eq.* (3.14), where it was defined that the letter level sparseness is the smallest probability of a letter to occur when weighted with the symbol probabilities. Finally, *Eq.* (3.18) *(iii)* presents the special case for binary transmission. The effect of sparseness on the PDF of the received letter is illustrated in *Fig.* 3.4. It is clear that sparseness does play a role: by increasing the sparseness of one symbol, the probability density increases and the intersection of the two PDFs shifts towards the symbol with the lower probability.

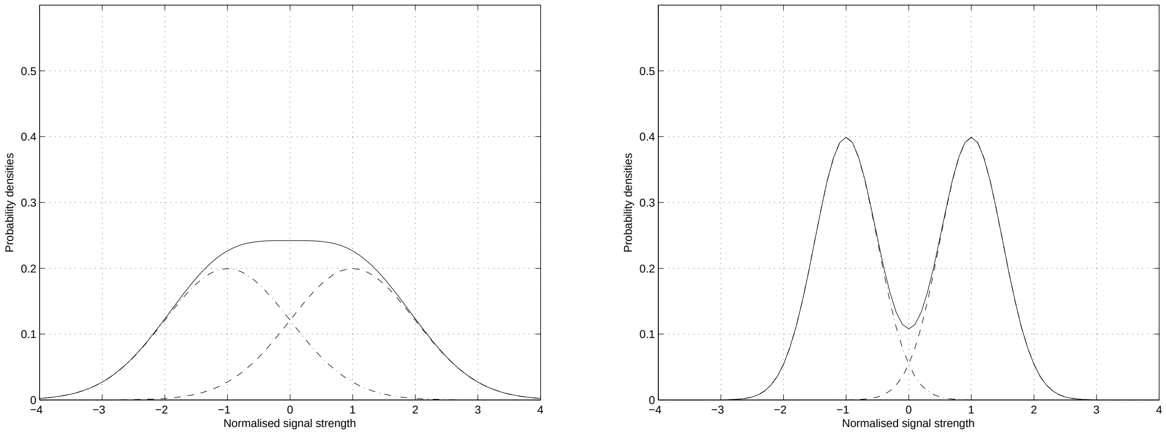

(a) $\sigma = 1$, $\eta_\alpha = 0.5$ (b) $\sigma = 0.5$, $\eta_\alpha = 0.5$

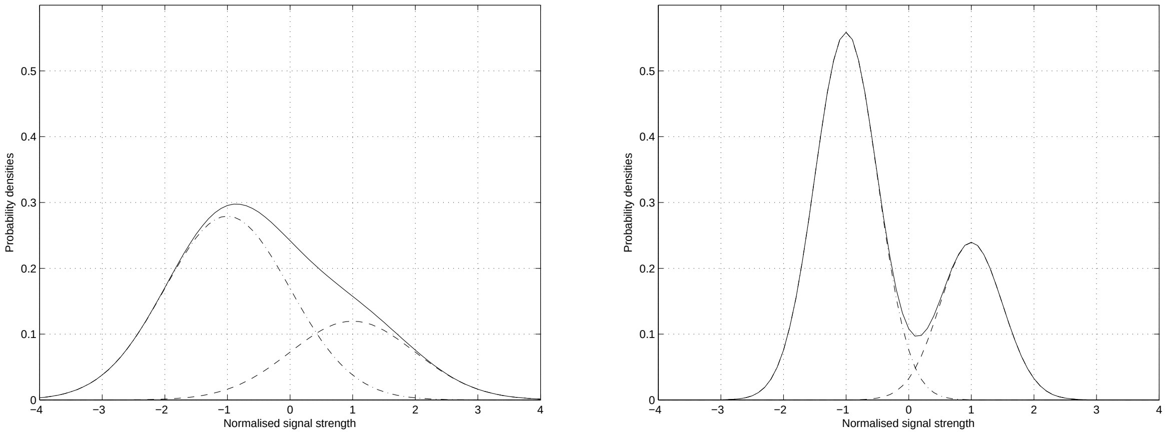

(c) $\sigma = 1$, $\eta_\alpha = 0.3$ (d) $\sigma = 0.5$, $\eta_\alpha = 0.3$

FIGURE 3.4: The effect of sparseness and $\sigma$ on the PDF of the received signal for AWGN.

As will become clear through the course of this study, this movement in the intersection results in a change in the bit error probability, especially so for cases exhibiting large noise variance while the density of the data stream is low (e.g. $\sigma = 1$, $\eta_\alpha = 0.3$). The effect is less obvious for cases where the noise variance is high, but still provides an opportunity to optimise existing receivers.

## 3.3 A NOVEL COMPLEX QPSK RECEIVER STRUCTURE EMPLOYING A MEASURE OF SPARSENESS

Conventional receiver structures have been accepted widely due to the good performance that they offer when compared to the complexity of implementing them. They are, however, designed to function optimally for systems transmitting data at the information limit. This may be a desired property of data streams in communication systems, but it is not necessarily a required system specification or even possible to guarantee such streams in real-time systems.

### 3.3.1 The proposed complex wideband QPSK receiver structures

This section aims to design and analyse modified receiver structures that implement the sparseness measure introduced in *Section* 3.2. Due to the relatively simple way by which the sparseness of a data stream may be estimated, the additional complexity introduced for this receiver structure is close to negligible when compared with the original complexity of the conventional structures. The gains provided vary significantly, depending on the density of the data stream, as will be shown. The same assumptions will be made as for the traditional structures, with the only difference being that the sparseness is either known or can be accurately estimated.

#### 3.3.1.1 The novel optimal receiver for signals corrupted by frequency non-selective channels with AWGN

It should be clear from *Section* 3.2.4 that any BPSK based receiver may be improved if it is able to adapt to the change in sparseness should the sparseness of the data stream change or differ from the typically assumed equiprobable case. One such receiver structure is proposed and presented in *Fig.* 3.5.

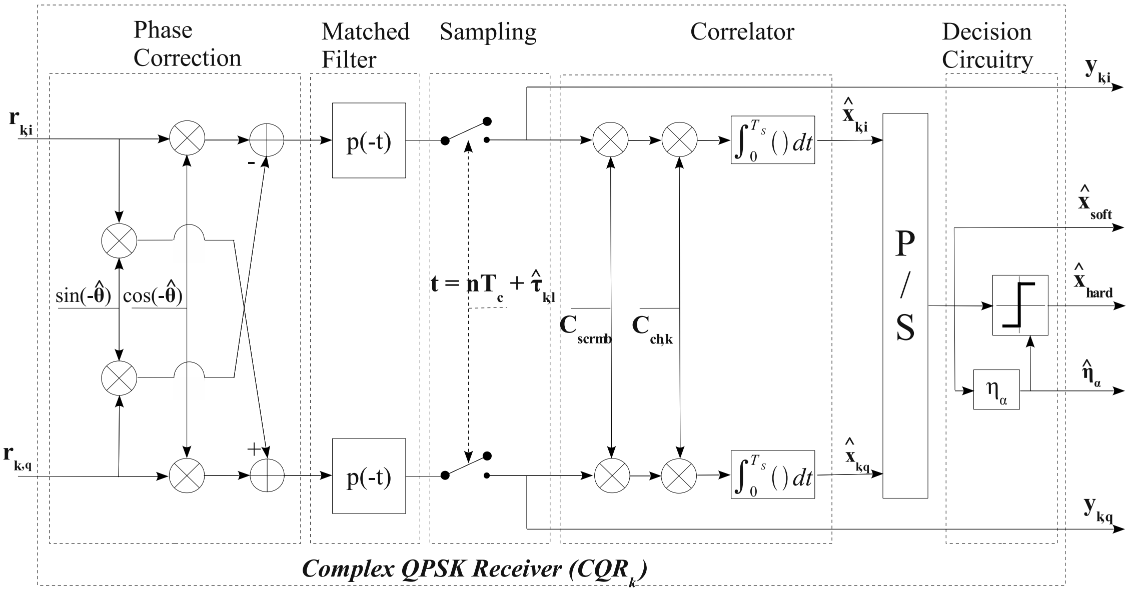

FIGURE 3.5: Complex single path QPSK based receiver for WCDMA applications optimised for possibly sparse data source

The receiver will achieve optimal results when the intersect (refer again to the dashed graphs presented in *Fig.* 3.4, with emphasis on (c)) of the conditional PDFs $p\left(r|s_0\right)$ and $p\left(r|s_1\right)$ are known. This may be determined by setting $p\left(r|s_0\right)$ equal to $p\left(r|s_1\right)$ and solving for $r = r_d$, as

$$\begin{aligned}
p\left(r|s_0\right) &= p\left(r|s_1\right)\\
\frac{(1-\eta_\alpha)}{\sqrt{\pi N_0}} e^{-\left(r_d+\sqrt{E_b}\right)^2 \big/ N_0} &= \frac{\eta_\alpha}{\sqrt{\pi N_0}} e^{-\left(r_d-\sqrt{E_b}\right)^2 \big/ N_0}\\
\frac{(1-\eta_\alpha)}{\eta_\alpha} e^{-\left(r_d+\sqrt{E_b}\right)^2 \big/ N_0} &= e^{-\left(r_d-\sqrt{E_b}\right)^2 \big/ N_0}\\
\ln\left(\frac{1}{\eta_\alpha}-1\right) - \left(r_d+\sqrt{E_b}\right)^2 \Big/ N_0 &= -\left(r_d-\sqrt{E_b}\right)^2 \Big/ N_0\\
\left(r_d+\sqrt{E_b}\right)^2 - \left(r_d-\sqrt{E_b}\right)^2 &= N_0 \ln\left(\frac{1}{\eta_\alpha}-1\right)\\
\left(r_d^2+2r_d\sqrt{E_b}+E_b\right) - \left(r_d^2-2r_d\sqrt{E_b}+E_b\right) &= N_0 \ln\left(\frac{1}{\eta_\alpha}-1\right)\\
4r_d\sqrt{E_b} &= N_0 \ln\left(\frac{1}{\eta_\alpha}-1\right)
\end{aligned}$$

to finally yield, depending on the SNR and the sparseness, the decision region as

$$r_d = \frac{N_0}{4\sqrt{E_b}} \ln\left(\frac{1}{\eta_\alpha}-1\right) \tag{3.19}$$

Various decision intervals are tabulated below for different $E_b/N_0$ and $\eta_\alpha$.

As soon as efficient source coding is introduced, it is found that $\eta_\alpha \to 0.5$, which in turn implies $r_d \to 0$, resulting in a standard binary antipodal system, but as mentioned earlier,

TABLE 3.1: Decision intervals for various SNR and sparseness values.

| $\frac{E_b}{N_0} \setminus \eta_\alpha$ | 0.1 | 0.2 | 0.3 | 0.4 | 0.5 |
|---|---|---|---|---|---|
| 0 | 0.5493 | 0.3466 | 0.2118 | 0.1014 | 0 |
| 3 | 0.2753 | 0.1737 | 0.1062 | 0.0508 | 0 |
| 5 | 0.1737 | 0.1096 | 0.0670 | 0.0321 | 0 |
| 7 | 0.1096 | 0.0692 | 0.0423 | 0.0202 | 0 |

this may not always be plausible or achievable.

A communication system may not necessarily (it may even not be possible to) transmit the SNR and/or a quantised value for the sparseness of the data slot/frame being transmitted. It is typically the responsibility of the receiver to estimate these values. Two strategies are proposed to determine the optimal decision region for the received frame, which may then be used by the decision logic of the circuit to provide an optimal hard output, or a soft output with the additional sparseness level that may be used by probabilistic (or similar) *Forward Error Correcting* (FEC) decoders in coded scenarios. Both strategies will benefit by averaging the PDF of the received letter.

The first strategy is the simpler of the suggested methods, and requires that the minimum value of the probability function must be found. It should be clear that the true minima where the PDF reaches zero are found at the extreme energy level values of $r = -\infty$ and $r = \infty$. These values are obviously of no use and it is, therefore, required to perform the search for the minimum value close to $r = 0$ between the values for $r$ where $s_0$ and $s_1$ are transmitted. Any search method may be used on the averaged values of the PDF to determine the local minimum close to $r = 0$.

The second strategy involves finding the derivative of the averaged PDF. This has been performed analytically in *Eq.* (3.36), but a numeric method will be more practical during the implementation of the system. Given that the derivative of the PDF is considered from $r = -\infty$ at the left towards the right, it is now required to find the value of $r$ corresponding to the point where the derivative changes from negative to positive. Recall that the derivative will be positive and small close to $r = -\infty$, after which it will increase rapidly and then decrease and equal zero at the value for $r$ where $s_0$ is transmitted, after which the derivative will become negative. The next change in the sign of the derivative occurs at the desired decision region. Both these strategies will fail when no minimum exists, as for the case illustrated in *Fig.* 3.4 (a) and (c).

#### 3.3.1.2 The novel optimal receiver for signals corrupted by frequency selective channels with AWGN

Similar to the conventional receivers, the optimal receiver may be implemented by using the tapped delay line approach of a typical Rake receiver, with the major difference being that the proposed receiver will implement the improved complex QPSK receiver proposed for frequency non-selective channels as presented in *Section* 3.3.1.1. Disregarding this one major change, the receiver is similar to conventional Rake receivers and the receiver structure of *Section* 3.1.1.2 applies directly. The inclusion of the modified QPSK receiver, however, allows for the utilisation of the sparseness measure, enabling adaptive behaviour should the density of the transmitted bitstream change, in turn allowing for a modification in the decision region and possibly improved BER performance. The proposed receiver, optimised for data streams that has not been fully source encoded, is illustrated in *Fig.* 3.6.

### 3.3.2 Analytic bit error probabilities for uncoded systems employing a measure of sparseness

#### 3.3.2.1 Communication over AWGN channels

The bounds and bit error probability as presented in *Section* 3.1.2 only hold true for the assumption of equiprobable inputs. The aim of this section is to evaluate the effect of sparseness on the BER performance in AWGN channel conditions. Assume that the assumptions of *Section* 3.2.4 still holds. The PDF of the received signal was given in *Eq.* (3.18) and plotted in *Fig.* 3.4. In order to determine the probability of error of a letter (bit), one needs to integrate from either $-\infty$ or $\infty$ to the decision region identified as the intersect of the two separate PDFs. This has traditionally been considered as $r_d = 0$ for equiprobable inputs, but it should be clear from *Fig.* 3.4 that, for $\eta_\alpha \neq 0.5$, $r_d$ moves toward the sparse symbol.

The probability of receiving the sparse letter $s_1$ in error can be found by integrating the PDF $p\left(r|s_1\right)$ over the range $(-\infty,\, r_d)$, or

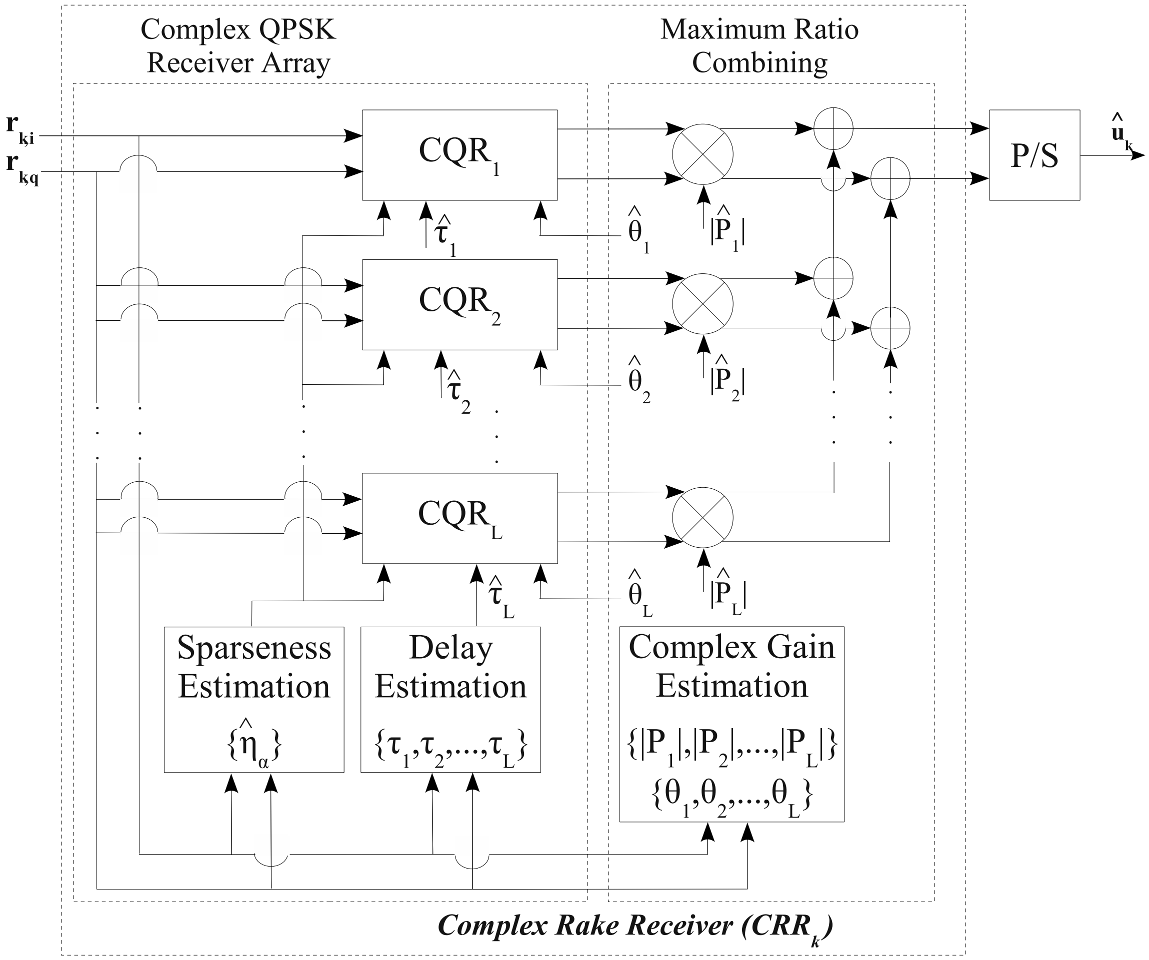

FIGURE 3.6: Complex multipath QPSK based receiver for WCDMA applications optimised for possibly sparse data source

$$\begin{aligned} P_e\left(r|s_1\right) &= \int_{-\infty}^{r=r_d} p\left(r|s_1\right)dr \\ &= \frac{\eta_\alpha}{\sqrt{\pi N_0}} \int_{-\infty}^{r_d} e^{-\left(r-\sqrt{E_b}\right)^2/N_0} dr \end{aligned} \tag{3.20}$$

In order to proceed, a set of variable transformations is defined as

$$\begin{aligned} \frac{\left(r-\sqrt{E_b}\right)^2}{N_0} &= \frac{x^2}{2} \\ \Rightarrow x = \sqrt{\frac{2\left(r-\sqrt{E_b}\right)^2}{N_0}} &= \sqrt{\frac{2}{N_0}}\left(r-\sqrt{E_b}\right) \end{aligned} \tag{3.21}$$

$$\begin{aligned} dx &= \sqrt{\frac{2}{N_0}}dr \\ \Rightarrow dr &= \sqrt{\frac{N_0}{2}}dx \end{aligned} \tag{3.22}$$

which may be used to map *Eq.* (3.20) with the appropriate variables to the standard form required for the error function integral. This yields

$$P_e\left(r|s_1\right) = \frac{\eta_\alpha}{\sqrt{\pi N_0}} \int\limits_{-\infty}^{\sqrt{\frac{2}{N_0}}\left(r_d-\sqrt{E_b}\right)} e^{-x^2/2}\cdot\sqrt{\frac{N_0}{2}}dx \tag{3.23}$$

which may, by noting the symmetry of the function, be rewritten as

$$P_e\left(r|s_1\right) = \frac{\eta_\alpha}{\sqrt{2\pi}} \int\limits_{\sqrt{\frac{2}{N_0}}\left(\sqrt{E_b}-r_d\right)}^{\infty} e^{-x^2/2}dx \tag{3.24}$$

This is in the standard form for the error function integral and can be written in the form of a $Q$-function. By substituting *Eq.* (3.19), the final result is given by

$$\begin{aligned} P_e\left(r|s_1\right) &= \eta_\alpha Q\left(\sqrt{\tfrac{2}{N_0}}\left(\sqrt{E_b}-r_d\right)\right) \\ &= \eta_\alpha Q\left(\sqrt{\tfrac{2E_b}{N_0}}-\sqrt{\tfrac{2}{N_0}}\cdot r_d\right) \\ &= \eta_\alpha Q\left(\sqrt{\tfrac{2E_b}{N_0}}-\sqrt{\tfrac{2}{N_0}}\cdot\tfrac{N_0}{4\sqrt{E_b}}\ln\left(\tfrac{1}{\eta_\alpha}-1\right)\right) \\ &= \eta_\alpha Q\left(\sqrt{\tfrac{2E_b}{N_0}}\underbrace{-\sqrt{\frac{N_0}{8E_b}}\ln\left(\frac{1}{\eta_\alpha}-1\right)}_{\text{effect of sparseness}}\right) \end{aligned} \tag{3.25}$$

Similarly, the result for $P\left(e|s_0\right)$ can be derived by noting that

$$\begin{aligned} P_e\left(r|s_0\right) &= \int\limits_{r_d}^{\infty} p\left(r|s_0\right)dr \\ &= \tfrac{(1-\eta_\alpha)}{\sqrt{\pi N_0}}\int\limits_{r_d}^{\infty} e^{-\left(r+\sqrt{E_b}\right)^2/N_0}dr \end{aligned} \tag{3.26}$$

Again, the variables are transformed according to *Eq.* (3.21) with $(r-E_b)$ replaced by $(r+E_b)$ in order to write $P\left(e|s_0\right)$ in the standard error function integral form as

$$\begin{aligned} P_e\left(r|s_0\right) &= \tfrac{(1-\eta_\alpha)}{\sqrt{\pi N_0}} \int\limits_{\sqrt{\frac{2}{N_0}}\left(r_d+\sqrt{E_b}\right)}^{\infty} e^{-x^2/2}\cdot\sqrt{\tfrac{N_0}{2}}dx \\ &= \tfrac{(1-\eta_\alpha)}{\sqrt{2\pi}} \int\limits_{\sqrt{\frac{2}{N_0}}\left(r_d+\sqrt{E_b}\right)}^{\infty} e^{-x^2/2}dx \end{aligned} \tag{3.27}$$

Rewriting this expression as a $Q$-function and, by substituting *Eq.* (3.19), it is found that

$$\begin{aligned} P_e\left(r|s_0\right) &= \left(1-\eta_\alpha\right) Q\left(\sqrt{\tfrac{2}{N_0}}\left(\sqrt{E_b}+r_d\right)\right) \\ &= \left(1-\eta_\alpha\right) Q\left(\sqrt{\tfrac{2E_b}{N_0}}+\sqrt{\tfrac{2}{N_0}}\cdot r_d\right) \\ &= \left(1-\eta_\alpha\right) Q\left(\sqrt{\tfrac{2E_b}{N_0}}\underbrace{+\sqrt{\frac{N_0}{8E_b}}\ln\left(\frac{1}{\eta_\alpha}-1\right)}_{\text{effect of sparseness}}\right) \end{aligned} \quad (3.28)$$

Finally, by adding $P\left(e|s_0\right)$ and $P\left(e|s_1\right)$, the average probability of error for a received letter, $r$, is found to be

$$P_e(r) = \left(1-\eta_\alpha\right) Q\left(\sqrt{\frac{2E_b}{N_0}}\underbrace{+\sqrt{\frac{N_0}{8E_b}}\ln\left(\frac{1}{\eta_\alpha}-1\right)}_{\text{effect of sparseness}}\right) + \eta_\alpha Q\left(\sqrt{\frac{2E_b}{N_0}}\underbrace{-\sqrt{\frac{N_0}{8E_b}}\ln\left(\frac{1}{\eta_\alpha}-1\right)}_{\text{effect of sparseness}}\right) \quad (3.29)$$

which is recognisable as the standard probability of error for antipodal modulation presented in *Eq.* (3.7) with the additional effect of the sparse data source (measured in terms of the sparseness measure) clearly indicated. Notice that *Eq.* (3.29) reduces to *Eq.* (3.11) if $\eta_\alpha = 0.5$, as all the terms affected by sparseness reduce to zero. This result for the bit error probability also applies directly to QPSK systems, as such a system effectively represents two binary phase-modulated signals in phase quadrature, therefore no crosstalk or interference will occur between the signals on the two quadrature carriers [44]. It should be noted that the symbol error probability of a QPSK system will differ from that of a BPSK system.

Another important observation, which will be required later, is that the error function may be written as a Taylor series, given by

$$erf\left(z\right) = \frac{2}{\sqrt{\pi}}\sum_{n=0}^{\infty}\frac{\left(-1\right)^n z^{2n+1}}{n!\left(2n+1\right)} = \frac{2}{\sqrt{\pi}}\left(z-\frac{z^3}{3}+\frac{z^5}{10}-\frac{z^7}{42}+\frac{z^9}{216}-\cdots\right) \quad (3.30)$$

In order to apply this, we collect and redefine terms to simplify *Eq.* (3.29), after which we rewrite it in a format containing the error function, as

$$\begin{aligned}
P_e\left(\gamma_b\right) &= \left(1-\eta_\alpha\right) Q\left(\sqrt{2\gamma_b}+\sqrt{\tfrac{1}{8\gamma_b}}\ln\left(\tfrac{1}{\eta_\alpha}-1\right)\right)+\eta_\alpha Q\left(\sqrt{2\gamma_b}-\sqrt{\tfrac{1}{8\gamma_b}}\ln\left(\tfrac{1}{\eta_\alpha}-1\right)\right)\\
&= K_1\cdot Q\left(\sqrt{2\gamma_b}+\sqrt{\tfrac{1}{8\gamma_b}}K_3\right)+K_2\cdot Q\left(\sqrt{2\gamma_b}-\sqrt{\tfrac{1}{8\gamma_b}}K_3\right)\\
&= K_1\cdot\tfrac{1}{2}\left[1-erf\left\{\tfrac{\sqrt{2\gamma_b}+\sqrt{\frac{1}{8\gamma_b}}K_3}{\sqrt{2}}\right\}\right]+K_2\cdot\tfrac{1}{2}\left[1-erf\left\{\tfrac{\sqrt{2\gamma_b}-\sqrt{\frac{1}{8\gamma_b}}K_3}{\sqrt{2}}\right\}\right]\\
&= K_1\cdot\tfrac{1}{2}\left[1-erf\left\{\sqrt{\gamma_b}+\tfrac{1}{4}\sqrt{\tfrac{1}{\gamma_b}}K_3\right\}\right]+K_2\cdot\tfrac{1}{2}\left[1-erf\left\{\sqrt{\gamma_b}-\tfrac{1}{4}\sqrt{\tfrac{1}{\gamma_b}}K_3\right\}\right]
\end{aligned} \tag{3.31}$$

This enables the replacement of the error function, allowing for a much simpler linear approximation to the exponential problem experienced when expressing the bit error probability, according to

$$\begin{aligned}
P_e\left(\gamma_b\right) &= K_1\cdot\tfrac{1}{2}\left[1-\tfrac{2}{\sqrt{\pi}}\sum_{n=0}^{\infty}\tfrac{(-1)^n\left(\sqrt{\gamma_b}+\frac{1}{4}\sqrt{\frac{1}{\gamma_b}}K_3\right)^{2n+1}}{n!(2n+1)}\right]\\
&\quad +K_2\cdot\tfrac{1}{2}\left[1-\tfrac{2}{\sqrt{\pi}}\sum_{n=0}^{\infty}\tfrac{(-1)^n\left(\sqrt{\gamma_b}-\frac{1}{4}\sqrt{\frac{1}{\gamma_b}}K_3\right)^{2n+1}}{n!(2n+1)}\right]\\
&\approx K_1\cdot\tfrac{1}{2}\left[1-\tfrac{2}{\sqrt{\pi}}\left(\sqrt{\gamma_b}+\tfrac{1}{4}\sqrt{\tfrac{1}{\gamma_b}}K_3-\tfrac{1}{3}\left(\sqrt{\gamma_b}+\tfrac{1}{4}\sqrt{\tfrac{1}{\gamma_b}}K_3\right)^3+\ldots\right)\right]\\
&\quad +K_2\cdot\tfrac{1}{2}\left[1-\tfrac{2}{\sqrt{\pi}}\left(\sqrt{\gamma_b}-\tfrac{1}{4}\sqrt{\tfrac{1}{\gamma_b}}K_3-\tfrac{1}{3}\left(\sqrt{\gamma_b}-\tfrac{1}{4}\sqrt{\tfrac{1}{\gamma_b}}K_3\right)^3+\ldots\right)\right]
\end{aligned} \tag{3.32}$$

Notice that it is possible to control the order of the approximation by replacing $\infty$ in the summation process with any finite integer. The exact theoretical BER performance achievable is plotted in *Fig.* 3.7 with different levels of sparseness included. Note that the BER performance of a dense stream corresponds exactly to that of a stream with $\eta_\alpha = 0.5$, and the dashed line is therefore not visible in the figure. Also given are various examples of the approximate BER performance of *Eq.* (3.32) in *Fig.* 3.8 through *Fig.* 3.10. It should be noted, however, that the specific Taylor series used to approximate the error function converges very slowly and its usefulness will be limited to low SNR values.

#### 3.3.2.2 Communication over frequency non-selective channels

Similar to the discussion presented in *Section* 3.1.2.2, this section will be dedicated to the analysis of the BER performance of a BPSK system in slowly fading channels. Again it will be assumed that the phase shift that is introduced by the channel can be accurately estimated to allow for coherent detection. Also, it will again be assumed that the fading level attenuation is a random process with a Rayleigh distribution, and $\gamma_b$ will, therefore be

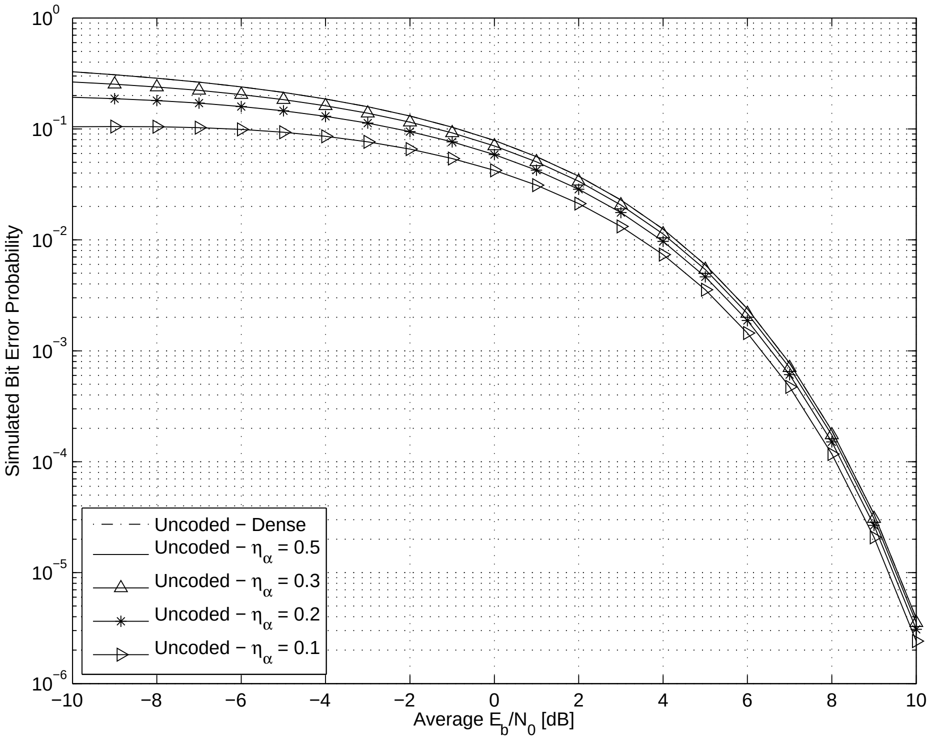

FIGURE 3.7: Theoretical BER performance of a QPSK system with sparseness taken into account

chi-squared-distributed with a PDF given by *Eq.* (E.2). However, in line with the discussion of *Section* 3.3.2.1, it will be assumed that a sparse symbol exists.

It is again necessary to average the PDF of $\gamma_b$ when $\alpha_{fl}$ is random with a specific probability distribution. However, it should be noted that $\gamma_b$ is dependent on the sparseness of the transmitted symbols, as seen in *Eq.* (3.29). The averaging process should now include the effect of sparseness and it is required to solve

$$\begin{aligned}
P_e &= \int\limits_0^\infty P_b\left(e|\gamma_b\right) p\left(\gamma_b\right) d\gamma_b \\
&= \int\limits_a^b f\left(\gamma_b\right) g'\left(\gamma_b\right) d\gamma_b \\
&= \int\limits_0^\infty \left(1-\eta_\alpha\right) Q\left(\sqrt{2\gamma_b} + \sqrt{\tfrac{1}{8\gamma_b}} \ln\left(\tfrac{1}{\eta_\alpha} - 1\right)\right) \tfrac{1}{E_b/N_o} e^{-\gamma_b/(E_b/N_o)} d\gamma_b \\
&+ \int\limits_0^\infty \eta_\alpha Q\left(\sqrt{2\gamma_b} - \sqrt{\tfrac{1}{8\gamma_b}} \ln\left(\tfrac{1}{\eta_\alpha} - 1\right)\right) \tfrac{1}{E_b/N_o} e^{-\gamma_b/(E_b/N_o)} d\gamma_b
\end{aligned} \tag{3.33}$$

with $f(\gamma_b)$ now the bit error probably over AWGN channels with the effect of sparseness included, as given by *Eq.* (3.29). A similar approach as presented in *Section* 3.3.2.1 may be followed to solve the integral by means of an integration by parts process. Unfortunately,

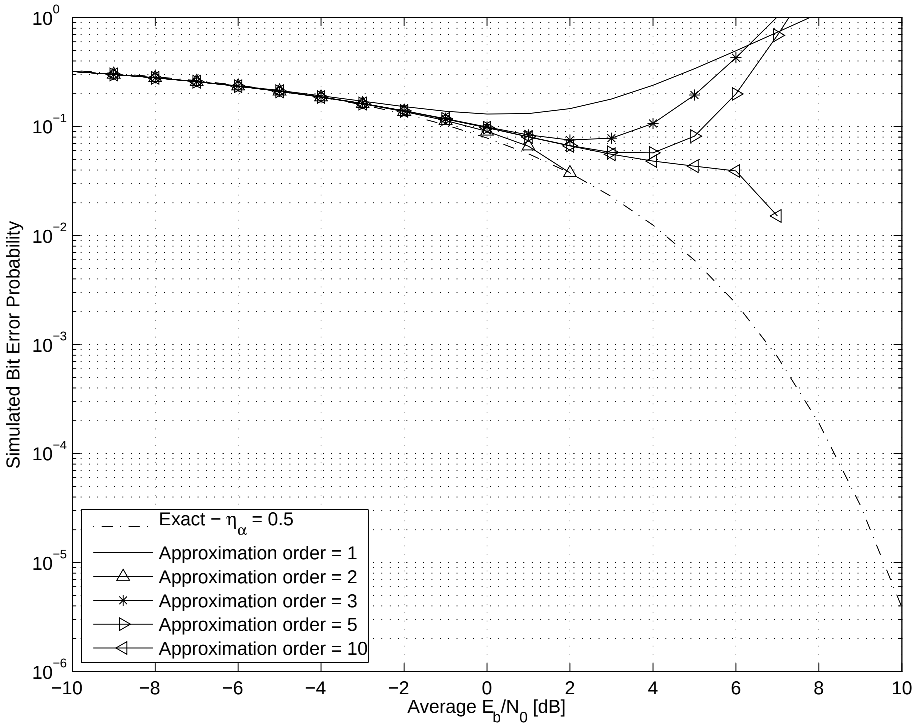

FIGURE 3.8: Theoretical BER performance of a QPSK system with a sparseness of $\eta_\alpha = 0.5$ (dense) given different orders of approximation of the error function

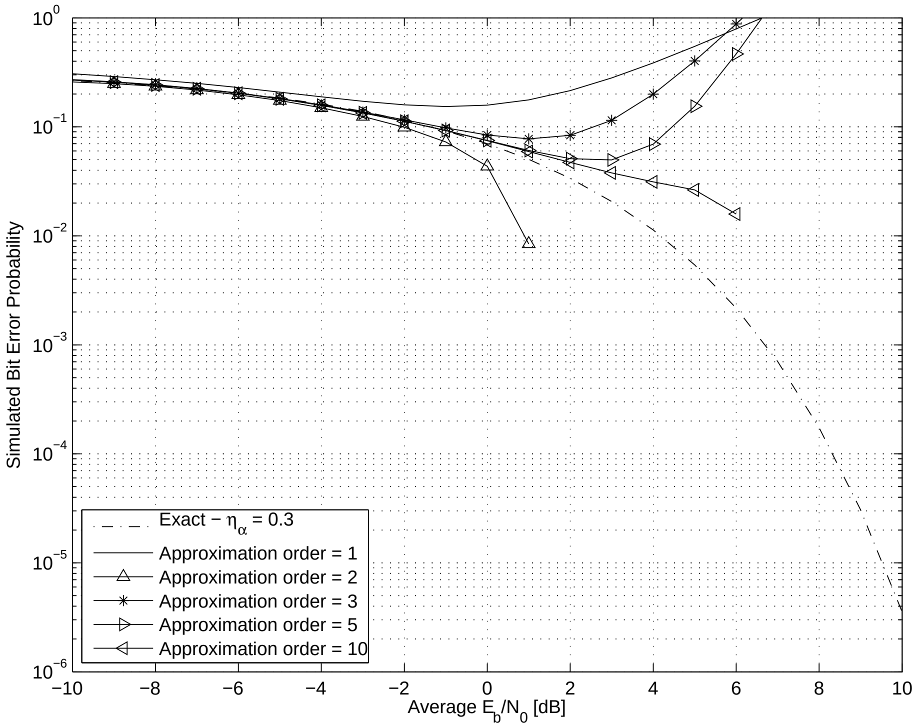

FIGURE 3.9: Theoretical BER performance of a QPSK system with a sparseness of $\eta_\alpha = 0.3$ given different orders of approximation of the error function

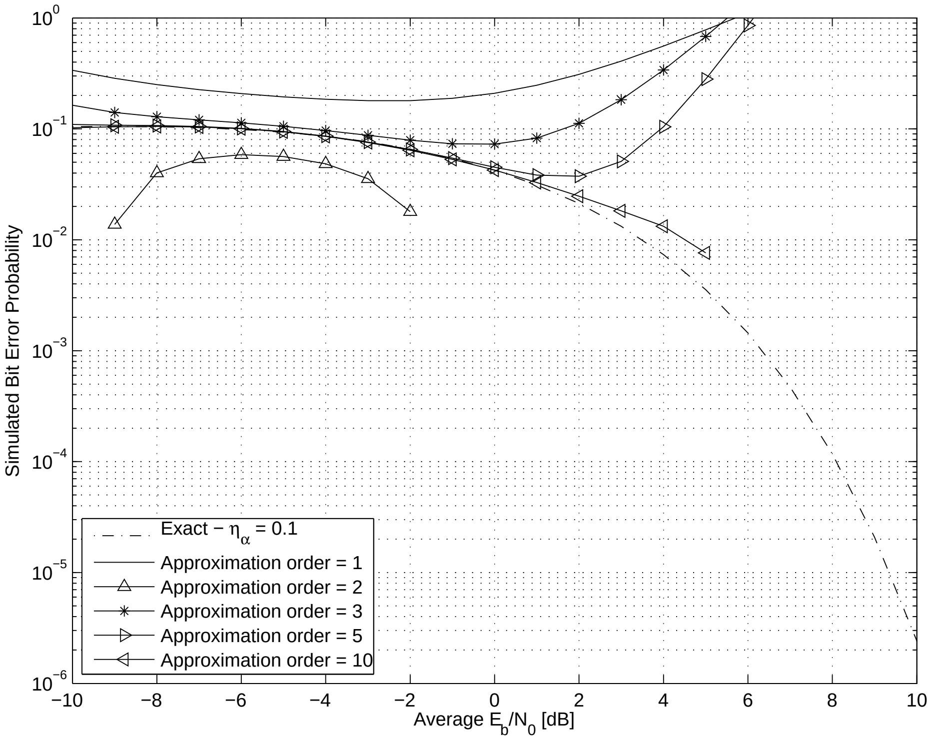

FIGURE 3.10: Theoretical BER performance of a QPSK system with a sparseness of $\eta_\alpha = 0.1$ (extremely sparse) given different orders of approximation of the error function

as the function to be integrated is very involved, a Taylor series is required to solve the integral and, without sufficient terms, the accuracy is compromised. Therefore, a numeric method has also been used to determine the bit error probability as presented at the end of this section. The reader may skip to the closing paragraphs of the section if the exact method by which the approximate closed form solution was derived is not of importance.

The Q-function used to describe the bit error probability of a non-sparse data stream over AWGN channel conditions may be rewritten as

$$\begin{aligned} P_e\left(\gamma_b\right) &= \left(1-\eta_\alpha\right) Q\left(\sqrt{2\gamma_b}+\sqrt{\tfrac{1}{8\gamma_b}\ln\left(\tfrac{1}{\eta_\alpha}-1\right)}\right)+\eta_\alpha Q\left(\sqrt{2\gamma_b}-\sqrt{\tfrac{1}{8\gamma_b}\ln\left(\tfrac{1}{\eta_\alpha}-1\right)}\right) \\ &= K_1\cdot\tfrac{1}{2}\left[1-erf\left\{\sqrt{\gamma_b}+\tfrac{1}{4}\sqrt{\tfrac{1}{\gamma_b}}K_3\right\}\right]+K_2\cdot\tfrac{1}{2}\left[1-erf\left\{\sqrt{\gamma_b}-\tfrac{1}{4}\sqrt{\tfrac{1}{\gamma_b}}K_3\right\}\right] \end{aligned} \tag{3.34}$$

where $K_1$, $K_2$ and $K_3$ are constants defined to simplify further analysis. The integration by parts approach is adopted again and it is necessary to solve

$$P_e = \left[f\left(\gamma_b\right)g\left(\gamma_b\right)\right]_a^b - \int_a^b f'\left(\gamma_b\right)g\left(\gamma_b\right)d\gamma_b \tag{3.35}$$

with $f(\gamma_b)$ given by *Eq.* (3.29), $g(\gamma_b)$ given by *Eq.* (E.6) and finally $g'(\gamma_b)$ is identified from *Eq.* (3.33) as the equivalent expression given by *Eq.* (E.8). The next step in the analysis is to find the derivative of $f(\gamma_b)$, which is done as

$$\begin{aligned}
f'\left(\gamma_b\right) &= \tfrac{\partial}{\partial\gamma_b} P_b\left(e|\gamma_b\right) \\
&= \tfrac{\partial}{\partial\gamma_b}\left(K_1\cdot\tfrac{1}{2}\left[1-erf\left\{\sqrt{\gamma_b}+\tfrac{1}{4}\sqrt{\tfrac{1}{\gamma_b}}K_3\right\}\right]+K_2\cdot\tfrac{1}{2}\left[1-erf\left\{\sqrt{\gamma_b}-\tfrac{1}{4}\sqrt{\tfrac{1}{\gamma_b}}K_3\right\}\right]\right) \\
&= -K_1\cdot\tfrac{1}{2}\cdot\tfrac{\partial}{\partial\gamma_b}\left(erf\left\{\sqrt{\gamma_b}+\tfrac{1}{4}\sqrt{\tfrac{1}{\gamma_b}}K_3\right\}\right)-K_2\cdot\tfrac{1}{2}\cdot\tfrac{\partial}{\partial\gamma_b}\left(erf\left\{\sqrt{\gamma_b}-\tfrac{1}{4}\sqrt{\tfrac{1}{\gamma_b}}K_3\right\}\right) \\
&= -K_1\cdot\tfrac{1}{2}\cdot\tfrac{2}{\pi}\cdot e^{-\left(\sqrt{\gamma_b}+\frac{1}{4}\sqrt{\frac{1}{\gamma_b}}K_3\right)^2}\tfrac{\partial}{\partial\gamma_b}\left(\sqrt{\gamma_b}+\tfrac{1}{4}\sqrt{\tfrac{1}{\gamma_b}}K_3\right) \\
&\quad -K_2\cdot\tfrac{1}{2}\cdot\tfrac{2}{\pi}\cdot e^{-\left(\sqrt{\gamma_b}-\frac{1}{4}\sqrt{\frac{1}{\gamma_b}}K_3\right)^2}\tfrac{\partial}{\partial\gamma_b}\left(\sqrt{\gamma_b}-\tfrac{1}{4}\sqrt{\tfrac{1}{\gamma_b}}K_3\right) \\
&= -\tfrac{K_1}{\pi}\cdot e^{-\left(\gamma_b+\frac{K_3}{2}+\frac{K_3^2}{16}\gamma_b^{-1}\right)}\cdot\left(\tfrac{1}{2}\gamma_b^{-\frac{1}{2}}-\tfrac{K_3}{8}\gamma_b^{-\frac{3}{2}}\right)-\tfrac{K_2}{\pi}\cdot e^{-\left(\gamma_b-\frac{K_3}{2}+\frac{K_3^2}{16}\gamma_b^{-1}\right)}\cdot\left(\tfrac{1}{2}\gamma_b^{-\frac{1}{2}}+\tfrac{K_3}{8}\gamma_b^{-\frac{3}{2}}\right) \\
&= -\tfrac{1}{\pi}\cdot e^{-\left(\gamma_b+\frac{K_3^2}{16}\gamma_b^{-1}\right)}\cdot\left(\tfrac{1}{2}\gamma_b^{-\frac{1}{2}}-\tfrac{K_3}{8}\gamma_b^{-\frac{3}{2}}\right)\cdot K_1\cdot e^{-\left(\frac{K_3}{2}\right)} \\
&\quad -\tfrac{1}{\pi}\cdot e^{-\left(\gamma_b+\frac{K_3^2}{16}\gamma_b^{-1}\right)}\cdot\left(\tfrac{1}{2}\gamma_b^{-\frac{1}{2}}+\tfrac{K_3}{8}\gamma_b^{-\frac{3}{2}}\right)\cdot K_2\cdot e^{\left(\frac{K_3}{2}\right)} \\
&= -\tfrac{1}{2\pi}\cdot\left(K_1\cdot e^{-\left(\frac{K_3}{2}\right)}+K_2\cdot e^{\left(\frac{K_3}{2}\right)}\right)\cdot\gamma_b^{-\frac{1}{2}}\cdot e^{-\left(\gamma_b+\frac{K_3^2}{16}\gamma_b^{-1}\right)} \\
&\quad -\tfrac{K_3}{8\pi}\cdot\left(K_2\cdot e^{\left(\frac{K_3}{2}\right)}-K_1\cdot e^{-\left(\frac{K_3}{2}\right)}\right)\cdot\gamma_b^{-\frac{3}{2}}\cdot e^{-\left(\gamma_b+\frac{K_3^2}{16}\gamma_b^{-1}\right)} \\
&= K_A\cdot\gamma_b^{-\frac{1}{2}}\cdot e^{-\left(\gamma_b+\frac{K_3^2}{16}\gamma_b^{-1}\right)}+K_B\cdot\gamma_b^{-\frac{3}{2}}\cdot e^{-\left(\gamma_b+\frac{K_3^2}{16}\gamma_b^{-1}\right)}
\end{aligned} \tag{3.36}$$

Proceeding with the analysis, the values of the product of $f(\gamma_b)$ and $g(\gamma_b)$ at the integration limits are analysed and with the aid of *Eq.* (3.34), are given by

$$\begin{aligned}
\lim_{\gamma_b\to\infty} f\left(\gamma_b\right)g\left(\gamma_b\right) &= -K_1\cdot\tfrac{1}{2}\left[1-erf\left\{\infty\right\}\right]+K_2\cdot\tfrac{1}{2}\left[1-erf\left\{\infty\right\}\right]\cdot e^{-\infty} \\
&= 0 \\
\lim_{\gamma_b\to 0} f\left(\gamma_b\right)g\left(\gamma_b\right) &= -K_1\cdot\tfrac{1}{2}\left[1-erf\left\{\infty\right\}\right]+K_2\cdot\tfrac{1}{2}\left[1-erf\left\{-\infty\right\}\right]\cdot e^{-0} \\
&= -K_1\cdot\tfrac{1}{2}\left[0\right]+K_2\cdot\tfrac{1}{2}\left[2\right] \\
&= K_2=\eta_\alpha
\end{aligned} \tag{3.37}$$

This result may now be used to find the first term required by the integration by parts process as

$$\begin{aligned}
\left[f\left(\gamma_b\right)g\left(\gamma_b\right)\right]_a^b &= \lim_{\gamma_b\to\infty} f\left(\gamma_b\right)g\left(\gamma_b\right)+\lim_{\gamma_b\to 0} f\left(\gamma_b\right)g\left(\gamma_b\right) \\
&= 0-\left(-\eta_\alpha\right)=\eta_\alpha
\end{aligned} \tag{3.38}$$

This leaves the new integral as the final part to be solved. Substituting *Eq.* (3.36) for $f^{'}(\gamma_b)$ and *Eq.* (E.6) for $g(\gamma_b)$, gives

$$\begin{aligned}
&\int_a^b f^{'}(\gamma_b) g(\gamma_b)\, d\gamma_b \\
&= \int_0^\infty \left( K_A \cdot \gamma_b^{-\frac{1}{2}} \cdot e^{-\left(\gamma_b + \frac{K_3^2}{16}\gamma_b^{-1}\right)} + K_B \cdot \gamma_b^{-\frac{3}{2}} \cdot e^{-\left(\gamma_b + \frac{K_3^2}{16}\gamma_b^{-1}\right)} \right) \cdot e^{-\gamma_b/(E_b/N_o)} d\gamma_b \\
&= \int_0^\infty K_A \cdot \gamma_b^{-\frac{1}{2}} \cdot e^{-\left(\gamma_b + \frac{K_3^2}{16}\gamma_b^{-1} + \frac{\gamma_b}{(E_b/N_o)}\right)} d\gamma_b + \int_0^\infty K_B \cdot \gamma_b^{-\frac{3}{2}} \cdot e^{-\left(\gamma_b + \frac{K_3^2}{16}\gamma_b^{-1} + \frac{\gamma_b}{(E_b/N_o)}\right)} d\gamma_b \\
&= \int_0^\infty K_A \cdot \gamma_b^{-\frac{1}{2}} \cdot e^{-\left(\left[1 + \frac{1}{(E_b/N_o)}\right]\gamma_b + \frac{K_3^2}{16}\gamma_b^{-1}\right)} d\gamma_b + \int_0^\infty K_B \cdot \gamma_b^{-\frac{3}{2}} \cdot e^{-\left(\left[1 + \frac{1}{(E_b/N_o)}\right]\gamma_b + \frac{K_3^2}{16}\gamma_b^{-1}\right)} d\gamma_b \\
&= \int_0^\infty K_A \cdot \gamma_b^{-\frac{1}{2}} \cdot e^{-\left(K_C\gamma_b + K_D\gamma_b^{-1}\right)} d\gamma_b + \int_0^\infty K_B \cdot \gamma_b^{-\frac{3}{2}} \cdot e^{-\left(K_C\gamma_b + K_D\gamma_b^{-1}\right)} d\gamma_b
\end{aligned} \tag{3.39}$$

Neither of these integrals have an analytic solution in a closed form. In order to proceed, it is necessary to note that the exponential function may be rewritten as an equivalent Taylor series expansion, with

$$e^{(-K_C\gamma_b)} = \sum_{n=0}^{\infty} \frac{K_C\left(-\gamma_b\right)^n}{n!} = \sum_{n=0}^{\infty} \frac{\left(-1\right)^n K_C^n \gamma_b^n}{n!} \tag{3.40}$$

$$e^{\left(-K_D\gamma_b^{-1}\right)} = \sum_{n=0}^{\infty} \frac{\left(-1\right)^n K_D^n \gamma_b^{-n}}{n!} \tag{3.41}$$

Considering the two integrals of *Eq.* (3.39) separately, it is found after substitution and collection of terms that

$$\begin{aligned}
\int_0^\infty K_A \cdot \gamma_b^{-\frac{1}{2}} \cdot e^{-\left(K_C\gamma_b + K_D\gamma_b^{-1}\right)} d\gamma_b &= \int_0^\infty K_A \cdot \gamma_b^{-\frac{1}{2}} \sum_{n=0}^{\infty} \frac{(-1)^n K_C^n \gamma_b^n}{n!} \sum_{n=0}^{\infty} \frac{(-1)^n K_D^n \gamma_b^{-n}}{n!} d\gamma_b \\
&= \int_0^\infty K_A \sum_{n=0}^{\infty} \frac{(-1)^n K_C^n \gamma_b^n}{n!} \sum_{n=0}^{\infty} \frac{(-1)^n K_D^n \gamma_b^{-n-\frac{1}{2}}}{n!} d\gamma_b
\end{aligned} \tag{3.42}$$

At this stage it is necessary to approximate the exponential function by selecting a finite number of terms in the summation, thus reducing it to a polynomial function that can be integrated. This is illustrated next in *Eq.* (3.43) by choosing $n = [0, 3]$, although it should be clear that this will not provide an accurate approximation, since Taylor series converges too slowly, and increasing the number of terms increases the complexity significantly.

$$\begin{aligned}
&\sum_{n=0}^{\infty}\frac{(-1)^n K_C^n\gamma_b^n}{n!}\sum_{n=0}^{\infty}\frac{(-1)^n K_D^n\gamma_b^{-n-\frac{1}{2}}}{n!}\approx\sum_{n=0}^{3}\frac{(-1)^n K_C^n\gamma_b^n}{n!}\sum_{n=0}^{\infty}\frac{(-1)^n K_D^n\gamma_b^{-n-\frac{1}{2}}}{n!}\\
&=\left(1-K_C\gamma_b+\frac{K_C^2}{2}\gamma_b^2-\frac{K_C^3}{6}\gamma_b^3\right)\left(\gamma_b^{-\frac{1}{2}}-K_D\gamma_b^{-\frac{3}{2}}+\frac{K_D^2}{2}\gamma_b^{-\frac{5}{2}}-\frac{K_D^3}{6}\gamma_b^{-\frac{7}{2}}\right)\\
&=\left(-\frac{K_D^3}{6}\right)\gamma_b^{-\frac{7}{2}}+\left(\frac{K_D^2}{2}+\frac{K_CK_D^3}{6}\right)\gamma_b^{-\frac{5}{2}}+\left(-K_D-\frac{K_CK_D^2}{2}-\frac{K_C^2K_D^3}{12}\right)\gamma_b^{-\frac{3}{2}}\\
&+\left(1+K_CK_D+\frac{K_C^2K_D^2}{4}+\frac{K_C^3K_D^3}{36}\right)\gamma_b^{-\frac{1}{2}}+\left(-K_C-\frac{K_C^2K_D}{2}-\frac{K_C^3K_D^2}{12}\right)\gamma_b^{\frac{1}{2}}\\
&+\left(\frac{K_C^2}{2}+\frac{K_C^3K_D}{6}\right)\gamma_b^{\frac{3}{2}}+\left(-\frac{K_C^3}{6}\right)\gamma_b^{\frac{5}{2}}
\end{aligned}\tag{3.43}$$

The approximate polynomial may now be integrated to yield

$$\begin{aligned}
&\int_0^{\infty}K_A\cdot\gamma_b^{-\frac{1}{2}}\cdot e^{-\left(K_C\gamma_b+K_D\gamma_b^{-1}\right)}d\gamma_b\\
&=K_A\left[\begin{array}{l}
\left(\frac{K_D^3}{15}\right)\gamma_b^{-\frac{5}{2}}+\left(-\frac{K_D^2}{3}-\frac{K_CK_D^3}{9}\right)\gamma_b^{-\frac{3}{2}}+\left(2K_D+K_CK_D^2+\frac{K_C^2K_D^3}{6}\right)\gamma_b^{-\frac{1}{2}}\\
+\left(2+2K_CK_D+\frac{K_C^2K_D^2}{2}+\frac{K_C^3K_D^3}{18}\right)\gamma_b^{\frac{1}{2}}+\left(-\frac{2K_C}{3}-\frac{K_C^2K_D}{3}-\frac{K_C^3K_D^2}{18}\right)\gamma_b^{\frac{3}{2}}\\
+\left(\frac{K_C^2}{5}+\frac{K_C^3K_D}{15}\right)\gamma_b^{\frac{5}{2}}+\left(-\frac{K_C^3}{21}\right)\gamma_b^{\frac{7}{2}}
\end{array}\right]\Bigg|_0^{\infty}
\end{aligned}\tag{3.44}$$

A similar approach is used to find the second integral of *Eq.* (3.39)

$$\begin{aligned}
\int_0^{\infty}K_B\cdot\gamma_b^{-\frac{3}{2}}\cdot e^{-\left(K_C\gamma_b+K_D\gamma_b^{-1}\right)}d\gamma_b
&=\int_0^{\infty}K_B\cdot\gamma_b^{-\frac{3}{2}}\sum_{n=0}^{\infty}\frac{(-1)^n K_C^n\gamma_b^n}{n!}\sum_{n=0}^{\infty}\frac{(-1)^n K_D^n\gamma_b^{-n}}{n!}d\gamma_b\\
&=\int_0^{\infty}K_B\sum_{n=0}^{\infty}\frac{(-1)^n K_C^n\gamma_b^n}{n!}\sum_{n=0}^{\infty}\frac{(-1)^n K_D^n\gamma_b^{-n-\frac{3}{2}}}{n!}d\gamma_b
\end{aligned}\tag{3.45}$$

which is again approximated as

$$\begin{aligned}
&\sum_{n=0}^{\infty}\frac{(-1)^n K_C^n\gamma_b^n}{n!}\sum_{n=0}^{\infty}\frac{(-1)^n K_D^n\gamma_b^{-n-\frac{3}{2}}}{n!}\approx\sum_{n=0}^{3}\frac{(-1)^n K_C^n\gamma_b^n}{n!}\sum_{n=0}^{\infty}\frac{(-1)^n K_D^n\gamma_b^{-n-\frac{3}{2}}}{n!}\\
&=\left(1-K_C\gamma_b+\frac{K_C^2}{2}\gamma_b^2-\frac{K_C^3}{6}\gamma_b^3\right)\left(\gamma_b^{-\frac{3}{2}}-K_D\gamma_b^{-\frac{5}{2}}+\frac{K_D^2}{2}\gamma_b^{-\frac{7}{2}}-\frac{K_D^3}{6}\gamma_b^{-\frac{9}{2}}\right)\\
&=\left(-\frac{K_D^3}{6}\right)\gamma_b^{-\frac{9}{2}}+\left(\frac{K_D^2}{2}+\frac{K_CK_D^3}{6}\right)\gamma_b^{-\frac{7}{2}}+\left(-K_D-\frac{K_CK_D^2}{2}-\frac{K_C^2K_D^3}{12}\right)\gamma_b^{-\frac{5}{2}}\\
&+\left(1+K_CK_D+\frac{K_C^2K_D^2}{4}+\frac{K_C^3K_D^3}{36}\right)\gamma_b^{-\frac{3}{2}}+\left(-K_C-\frac{K_C^2K_D}{2}-\frac{K_C^3K_D^2}{12}\right)\gamma_b^{-\frac{1}{2}}\\
&+\left(\frac{K_C^2}{2}+\frac{K_C^3K_D}{6}\right)\gamma_b^{\frac{1}{2}}+\left(-\frac{K_C^3}{6}\right)\gamma_b^{\frac{3}{2}}
\end{aligned}\tag{3.46}$$

to yield a polynomial to be integrated, resulting in

$$
\begin{aligned}
&\int_0^\infty K_B \cdot \gamma_b^{-\frac{3}{2}} \cdot e^{-\left(K_C\gamma_b + K_D\gamma_b^{-1}\right)} d\gamma_b \\
&= K_B \left[ \begin{array}{l}
\left(\frac{K_D^3}{21}\right)\gamma_b^{-\frac{7}{2}} + \left(-\frac{K_D^2}{5} - \frac{K_C K_D^3}{15}\right)\gamma_b^{-\frac{5}{2}} + \left(\frac{2K_D}{3} + \frac{K_C K_D^2}{3} + \frac{K_C^2 K_D^3}{18}\right)\gamma_b^{-\frac{3}{2}} \\
+ \left(-2 - 2K_C K_D - \frac{K_C^2 K_D^2}{2} - \frac{K_C^3 K_D^3}{18}\right)\gamma_b^{-\frac{1}{2}} + \left(-2K_C - K_C^2 K_D - \frac{K_C^3 K_D^2}{6}\right)\gamma_b^{\frac{1}{2}} \\
+ \left(\frac{K_C^2}{3} + \frac{K_C^3 K_D}{9}\right)\gamma_b^{\frac{3}{2}} + \left(-\frac{K_C^3}{15}\right)\gamma_b^{\frac{5}{2}}
\end{array} \right]\Bigg|_0^\infty
\end{aligned}
\tag{3.47}
$$

The final approximate bit error probability is obtained by combining *Eq.* (3.38), *Eq.* (3.44) and *Eq.* (3.47), to yield

$$
\begin{aligned}
&P_e = \eta_\alpha \\
&- K_A \left[ \begin{array}{l}
\left(\frac{K_D^3}{15}\right)\gamma_b^{-\frac{5}{2}} + \left(-\frac{K_D^2}{3} - \frac{K_C K_D^3}{9}\right)\gamma_b^{-\frac{3}{2}} + \left(2K_D + K_C K_D^2 + \frac{K_C^2 K_D^3}{6}\right)\gamma_b^{-\frac{1}{2}} \\
+ \left(2 + 2K_C K_D + \frac{K_C^2 K_D^2}{2} + \frac{K_C^3 K_D^3}{18}\right)\gamma_b^{\frac{1}{2}} + \left(-\frac{2K_C}{3} - \frac{K_C^2 K_D}{3} - \frac{K_C^3 K_D^2}{18}\right)\gamma_b^{\frac{3}{2}} \\
+ \left(\frac{K_C^2}{5} + \frac{K_C^3 K_D}{15}\right)\gamma_b^{\frac{5}{2}} + \left(-\frac{K_C^3}{21}\right)\gamma_b^{\frac{7}{2}}
\end{array} \right]\Bigg|_0^\infty \\
&- K_B \left[ \begin{array}{l}
\left(\frac{K_D^3}{21}\right)\gamma_b^{-\frac{7}{2}} + \left(-\frac{K_D^2}{5} - \frac{K_C K_D^3}{15}\right)\gamma_b^{-\frac{5}{2}} + \left(\frac{2K_D}{3} + \frac{K_C K_D^2}{3} + \frac{K_C^2 K_D^3}{18}\right)\gamma_b^{-\frac{3}{2}} \\
+ \left(-2 - 2K_C K_D - \frac{K_C^2 K_D^2}{2} - \frac{K_C^3 K_D^3}{18}\right)\gamma_b^{-\frac{1}{2}} + \left(-2K_C - K_C^2 K_D - \frac{K_C^3 K_D^2}{6}\right)\gamma_b^{\frac{1}{2}} \\
+ \left(\frac{K_C^2}{3} + \frac{K_C^3 K_D}{9}\right)\gamma_b^{\frac{3}{2}} + \left(-\frac{K_C^3}{15}\right)\gamma_b^{\frac{5}{2}}
\end{array} \right]\Bigg|_0^\infty
\end{aligned}
\tag{3.48}
$$

The different techniques presented up to this point to determine the BER performance are plotted in *Fig.* 3.11. It should be noted that the data streams are assumed to be dense for this graph. The closed form analytic solution of *Eq.* (E.11), the original integral of *Eq.* (3.33) solved by means of a numeric method, the combined terms of *Eq.* (3.38) and *Eq.* (3.39) (solved by means of numeric integration) as used in the integration by parts process and finally the approximation of *Eq.* (3.48), are illustrated. It is clear, as mentioned earlier, that the approximation does not hold for very low bit error probabilities, as the Taylor series approximation was only calculated over $n = [0, 3]$. Notice also that the integration by parts approach yields results very close to the exact solution, with only a very small deviation noticeable at a BER of $10^{-2}$. This is expected, as the BER approaches the magnitude of the finite integration intervals required by the implementation of the integrator.

As was found for the AWGN channel case, the sparseness will indeed change the bit error probability achieved at various SNRs. Even though an approximate solution is presented, the BER performance for different levels of sparseness is plotted in *Fig.* 3.12 by means of an integration by parts method. It is again clear that the bit error probability approaches the

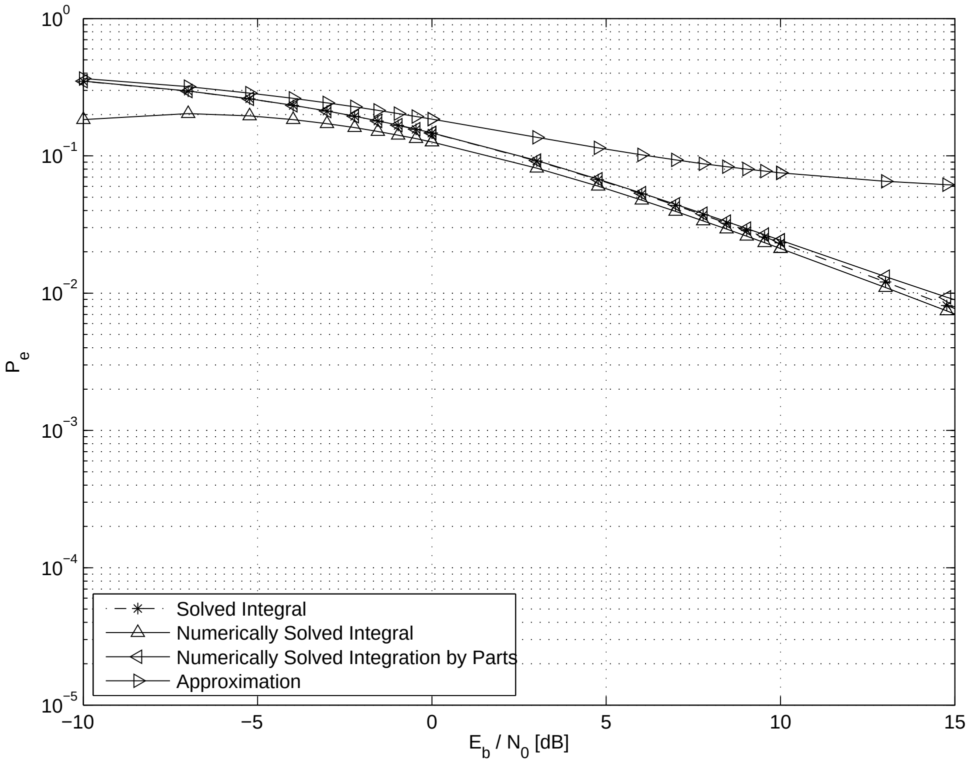

FIGURE 3.11: BER performance for the different techniques presented

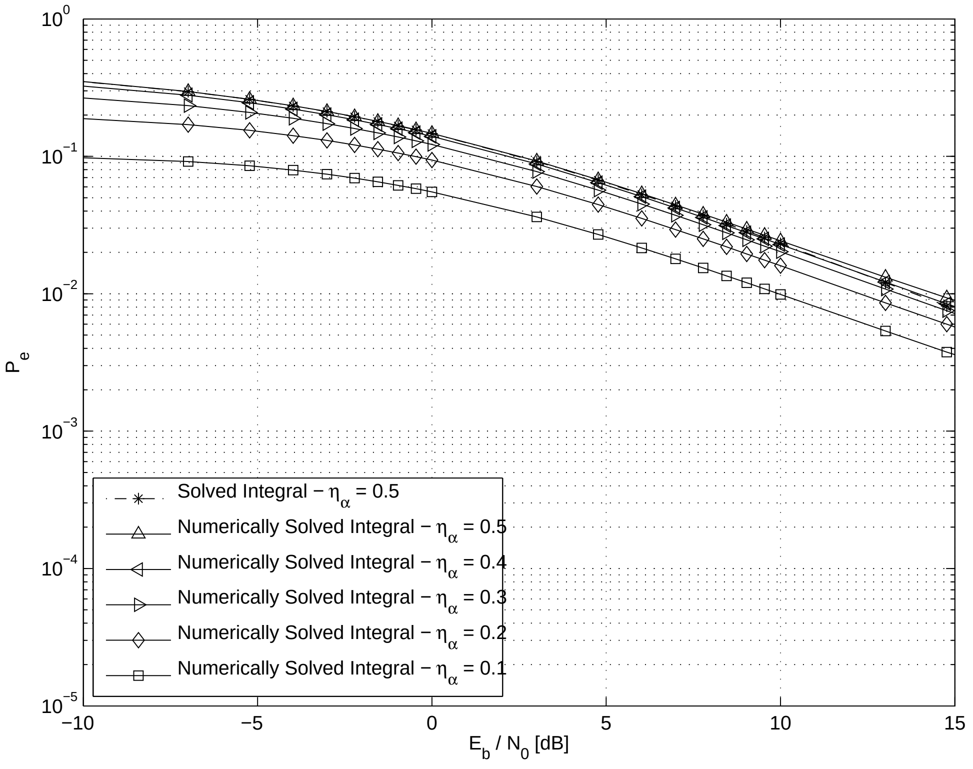

FIGURE 3.12: BER performance for various different sparseness levels

measure of sparseness when the SNR becomes very small, which again means that there exists a certain gain that could be exploited in terms of bit error probability should the sparseness level be known or accurately approximated.

# CHAPTER FOUR

# SIMULATION RESULTS

This chapter commences with an overview of the simulation platform and its capabilities. Integration of the subsystems, as presented in *Chapter* 2 and *Chapter* 3, are highlighted with a functional block diagram. The overview of the platform is concluded by various tables that tabulate the subsystem simulation parameters to indicate the capabilities of the system.

An analysis of a typical and a proposed PRNG, that allows for the adjustment of the sparseness of the generated bitstream, is presented next. Problems of a typical PRNG, that may be alleviated with the proposed model, are investigated and pointed out. This is followed by a short investigation of the effect of some popular FEC encoders on the sparseness of a source bitstream of adjustable sparseness.

*Chapter* 4 continues with a detailed investigation of the UTRA/FDD complex baseband QPSK transmitter. Simulation results, including a time domain analysis, a frequency domain analysis and eye diagrams are used to scrutinise the functionality of the subsystem. OVSF codes are also investigated in terms of the orthogonality of the codes by means of auto- and cross-correlation of perfectly aligned as well as time shifted versions of the codes.

Next, *Chapter* 4 presents the results of the channel models. An AWGN source is implemented and the spectrum is considered, as well as the joint PDF of the received signal for various levels of sparseness. Following the discussion of *Section* D.4.5, the results of the various methods to generate Doppler parameters are presented. This section is concluded with the results of the analysis of the complex Rician process for frequency non-selective and frequency selective channels.

Finally, the chapter is concluded with a large analysis of many BER performance curves for various simulation parameters. These parameters are discussed next.

## 4.1 OVERVIEW OF THE SIMULATION SETUP

A common approach to investigate very large systems is to break it down into smaller parts, or subsystems. This approach has been followed in this study. The critical subsystems to this study included the UTRA/FDD WCDMA transmitter (refer to *Chapter* 2), the channel emulation of AWGN and fading effects (refer to *Appendix* D) and the receiver design, including the effect of sparseness (refer to *Chapter* 3). It was also later found that the design of the PRNG (refer to *Appendix* B) plays a large role in obtaining accurate results while the appropriate statistics converge quickly.

A functional block diagram that aims to clarify the integration of the subsystems as presented in earlier chapters is shown in *Fig.* 4.1. Albeit a very generic diagram of a communication system, many of the subsystems may be configured over a very large span of parameters, each with a range of allowed values. Many of the subsystems may even be configured to be completely removed from the simulation setup if their effect is not desired. The variable parameters of each subsystem of interest are tabulated and discussed next.

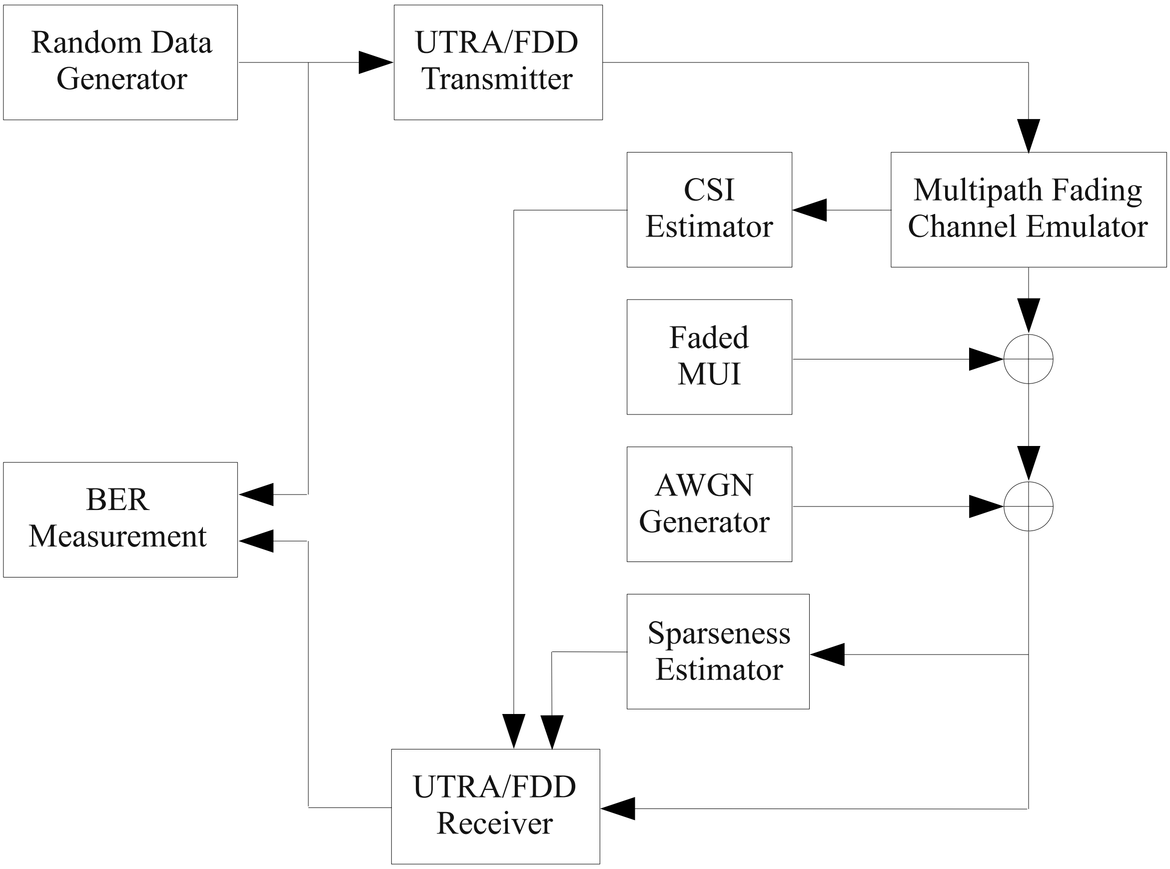

FIGURE 4.1: Block diagram of the general UTRA/FDD WCDMA simulation platform

The UTRA/FDD WCDMA transmitter conforms to the frame structure and modulation architecture required by the UMTS/WCDMA standard that was presented in *Chapter* 2. Simulations were performed with a complex baseband notation, and the transmitter was configured by setting various parameters that influence the final results. These parameters are listed in *Table* 4.1. The generic channel simulator can be configured over a wide range of parameters. Various configuration setups of interest during this study are presented in *Table* 4.2.

An additional study was required to optimise the PRNG in terms of the usage of the sparseness measure as an input parameter after it became obvious that the standard deviation of conventional PRNG bitstream generators are excessively large. An optimised PRNG designed specifically for using sparseness as an input parameter is presented in *Appendix* B. *Table* 4.3 tabulates the specifications of interest when using the PRNG.

Table 4.1: Transmitter/receiver parameters and typical ranges for simulation setups.

| Parameter | Unit | Suggested range | Tested parameter set |
|---|---|---|---|
| *General transmitter/receiver parameters:* | | | |
| System parameter | | [0...7] | [7] (Time domain, Eye diagrams)<br>$[5, 7]$ (Frequency domain)<br>[7] (Narrowband)<br>$[4, 5, 6, 7]$ (OVSF codes)<br>$[5, 7]$ (AWGN, Single user)<br>[7] (Fading, Single user)<br>$[4, 5, 6, 7]$ (Fading, MUI) |
| Carrier frequency | Hz | [0] | [0] (Baseband) |
| Interpolation factor | | [0...32772] | [4] |
| Frame length | s | [0...100] | $[0.1]$ (All transmitter measurements and BER experiments)<br>[10] (Fading channel measurements) |
| Chip rate | Chips/s | $[0...10^7]$ | $[3.84 \times 10^6]$ |

| | | | |
|---|---|---|---|
| Channelisation codes | | | [1, 1, 1, -1] ($k = 7$)<br>[1, 1, 1, -1, 1, -1, 1, -1] ($k = 6$)<br>[1, 1, 1, -1, 1, -1, 1, -1, 1, -1, -1, -1, 1, -1, 1, 1] ($k = 5$)<br>[1, 1, ..., 1, 1] (Narrowband) |
| Scrambling codes | | | Refer to *Section* 2.4.2<br>[1, 1, ..., 1, 1] (Narrowband) |
| Filter order | | $[0...1024]$ | $[33]$ (Wideband)<br>$[127]$ (Narrowband) |
| Filter gain | | $[0...100]$ | $[3.981]$ (Wideband)<br>$[15.842]$ (Narrowband) |
| Filter coefficients | | | Refer to configuration files |
| *Specific receiver parameters:* | | | |
| Sparseness measure | | $[0...0.5]$ | $[0.1, 0.2, 0.3, 0.4, 0.5]$ (BER single user)<br>$[0.1, 0.3, 0.5]$ (BER MUI) |

Table 4.2: Channel parameters required by the channel emulator and typical ranges for channel simulation setups.

| Parameter | Unit | Suggested range | Tested parameter set |
|---|---|---|---|
| *AWGN parameters:* | | | |
| $\mathrm{E}_B/N_0$ | dB | $[-20...50]$ | $[-15, -14, ..., 9, 10]$ (AWGN)<br>$[-15, -14, ..., 14, 15]$ (Fading)<br>$[-15, -14, ..., 14, 15]$ (Multi-user) |
| *Rician process parameters (frequency non-selective):* | | | |
| speed | km/h | $[0...200]$ | $[50, 75, 130]$ |
| $\mathrm{f}_{d,max}$ | Hz | $[0...500]$ | $[91, 141, 241]$ |
| $\sigma_0^2$ | W/W | 1 | 1 |
| $\mathrm{C}_R$ | dB | $[-100...10]$ | $[-100, 0, 6, 9]$ |
| $\rho$ | W/W | $[0...100]$ | $[0, 1.414, 2.822]$ |

| | | | |
|---|---|---|---|
| *Rician process parameters (frequency selective):* | | | |
| Number of paths | | [0...6] | $[0, 1, 3, 6]$ |
| Power tap profile | dB | $[-100...100]$ | -100 (AWGN only) |
| | | | 0 (Flat fading) |
| | | | [-0.139, -15.139, -30.1394] (Exponential decay) |
| | | | [-3, 0, -2, -6, -8, -10] (COST207 TU ) |
| Path delay | $\mu$s | | 0 (AWGN only) |
| | | | 0 (Flat fading) |
| | | | [0, $2.15 \times 10^{-6}$, $4.3 \times 10^{-6}$] $\mu$s (Exponential decay) |
| | | | [0, 0.82, 2.46, 6.55, 9.83, 20.48]*T$_c$ (COST207 TU) |

Table 4.3: Source parameters required by the PRNG and typical ranges for PRNG simulation setups.

| Parameter | Unit | Suggested range | Tested parameter set |
|---|---|---|---|
| *Optimised PRNG parameters:* | | | |
| Block length | | $[150 \cdot 2^k]$ | Refer to *Table* 4.2 for $k$ |
| Sparseness | | $[0.1, 0.2, 0.3, 0.4, 0.5]$ | $[0.1, 0.2, 0.3, 0.4, 0.5]$ (Source Investigation, BER single user) |
| | | | $[0.1, 0.3, 0.5]$ (BER MUI) |
| Feedback percentage | | [0...100] | [15] ($\eta_\alpha = 0.5$, $k = 0$) |
| | | | [2] ($\eta_\alpha = 0.5$, $k = 7$) |
| | | | Complete results in *Section* 4.2.1 |

## 4.2 ANALYSIS OF THE IMPLEMENTED SOURCE MODELS

The source model was applied as a binary PRNG with block lengths equivalent to the specified frame lengths (as defined by [69]) for WCDMA (UMTS). All allowed block lengths were investigated, and include $l = 150$, $l = 300$, $l = 600$, $l = 1200$, $l = 2400$, $l = 4800$, $l = 9600$ and $l = 19200$, depending on the system parameter, $k$. Simulations were executed in such a way that the sparseness parameter was varied over $0.01 < \eta_\alpha < 0.5$, while the feedback parameter was varied over $0 < k/l < 1$.

### 4.2.1 Analysis of the statistical deviation from the norm

Each of the graphs presented in *Fig.* 4.2 through *Fig.* 4.9 shows a three dimensional contour indicating the relationship between the standard deviation, sparseness and feedback length. The contour is sometimes difficult to interpret, so it is also presented as a two dimensional contour of the sparseness versus standard deviation, where the minimum and maximum cases are very clear. The optimal feedback percentage graph for the various levels of sparseness is also superimposed on the two dimensional contour. As an example, the optimal feedback percentage in the case of $k = 0$ for $\eta_\alpha = 0.5$ is 15%, a value difficult to read from the three dimensional contour, as it lies in the back of the optimal valley, but easily obtained from the graph labeled b).

A number of important observations can be made from the results presented in *Fig.* 4.2 through *Fig.* 4.9.

1. The highest standard deviation contour in each of the figures (especially clear in b) of all figures) represents the conventional models with no feedback and occurs for the extreme cases $k/l = 0$ and $k/l = 1$, as neither cases exploit the estimation mechanism of *Eq.* (B.2) in the feedback system. Most of the generally used PRNGs generate equiprobable binary bitstreams with no feedback, which coincides with the highest (worst) standard deviation in all graphs.

2. Comparison of the highest and lowest contours at $\eta_\alpha = 0.5$ (equiprobable case) yields an improved standard deviation of $0.014$ compared to $0.42$ for $l = 150$, $0.008$ compared to $0.285$ for $l = 300$, $0.0061$ compared to $0.0205$ for $l = 600$, $3.5 \times 10^{-3}$ compared to $14.2 \times 10^{-3}$ for $l = 1200$, $2.1 \times 10^{-3}$ compared to $10.2 \times 10^{-3}$ for $l = 2400$, $1.3 \times 10^{-3}$ compared to $7.2 \times 10^{-3}$ for $l = 4800$, $0.6 \times 10^{-3}$ compared to

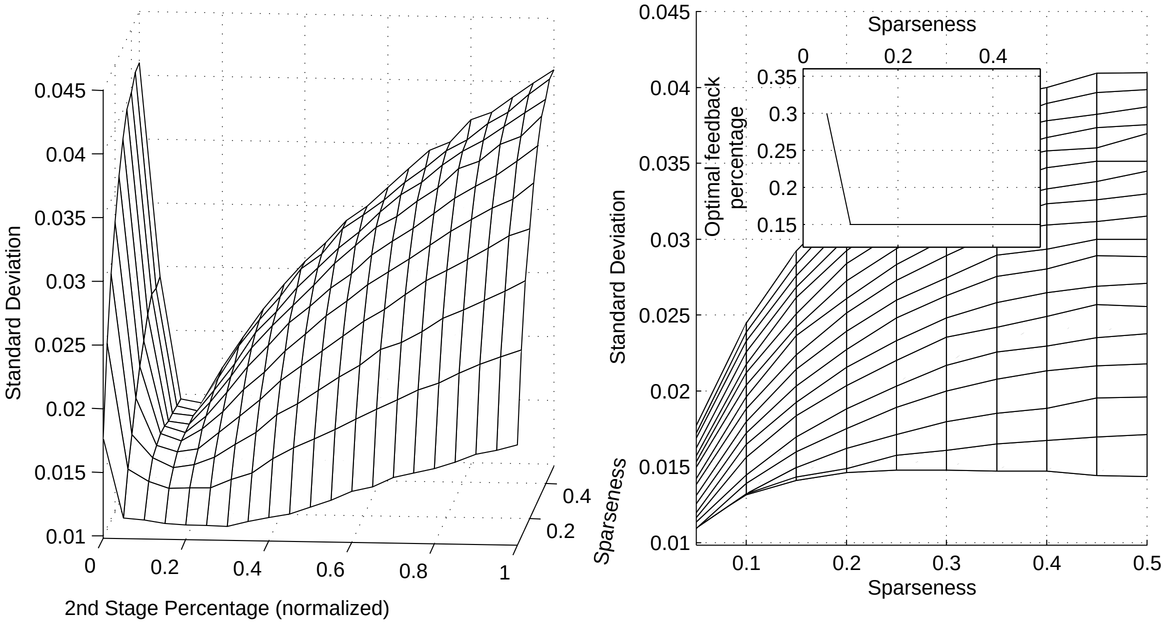

FIGURE 4.2: Standard deviation contour of the source model of length 150 ($k = 0$)

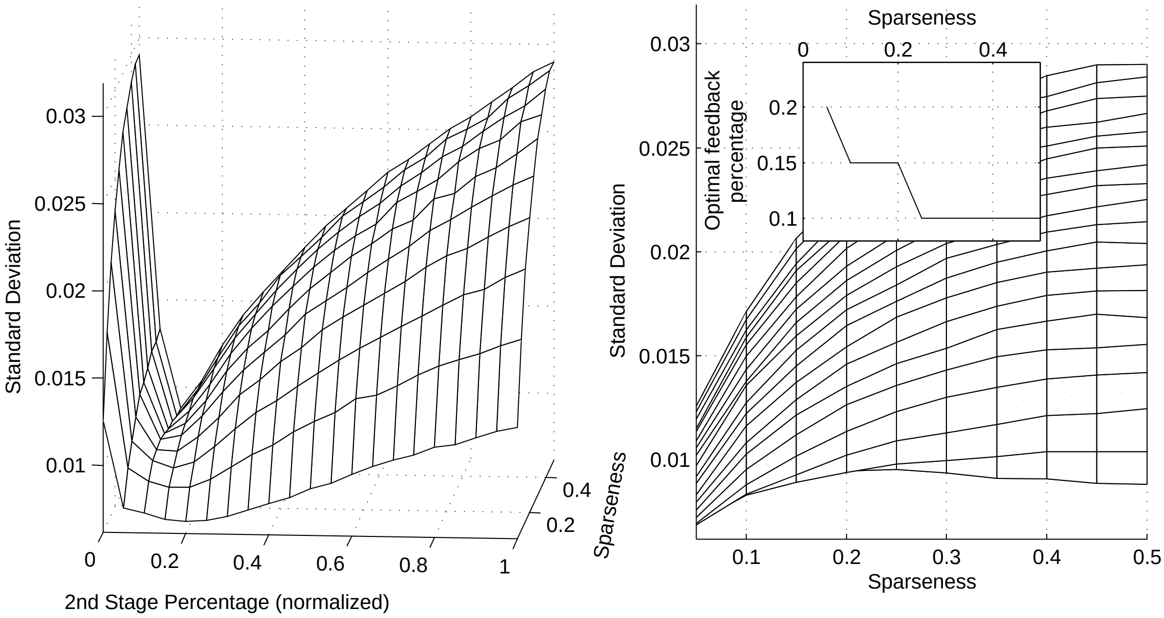

FIGURE 4.3: Standard deviation contour of the source model of length 300 ($k = 1$)

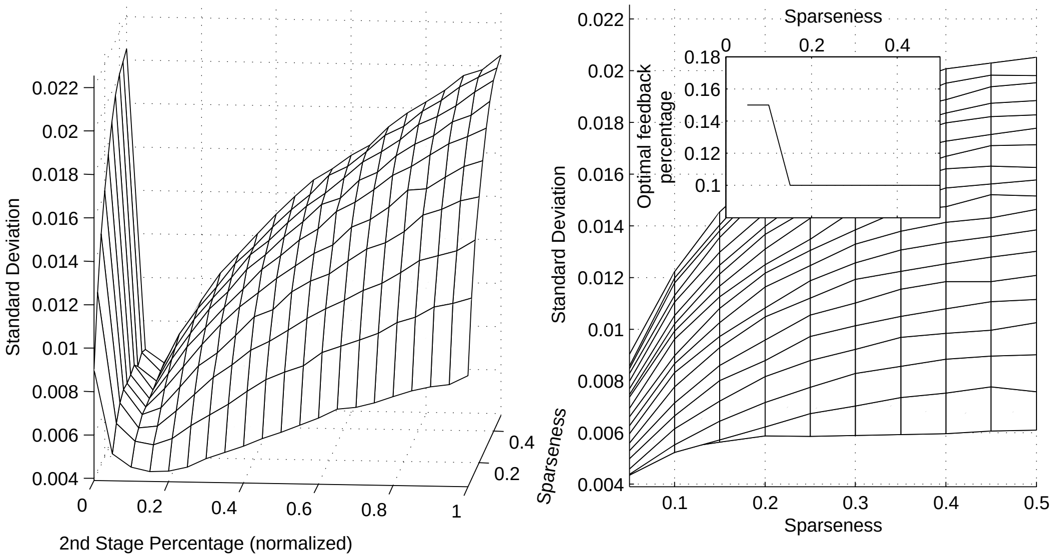

FIGURE 4.4: Standard deviation contour of the source model of length 600 ($k = 2$)

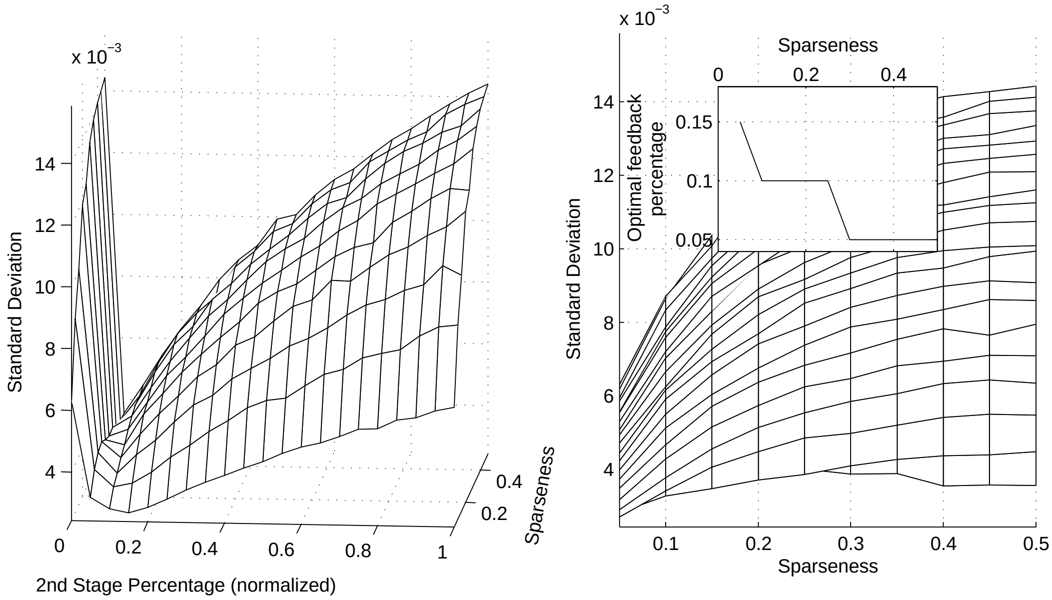

FIGURE 4.5: Standard deviation contour of the source model of length 1200 ($k = 3$)

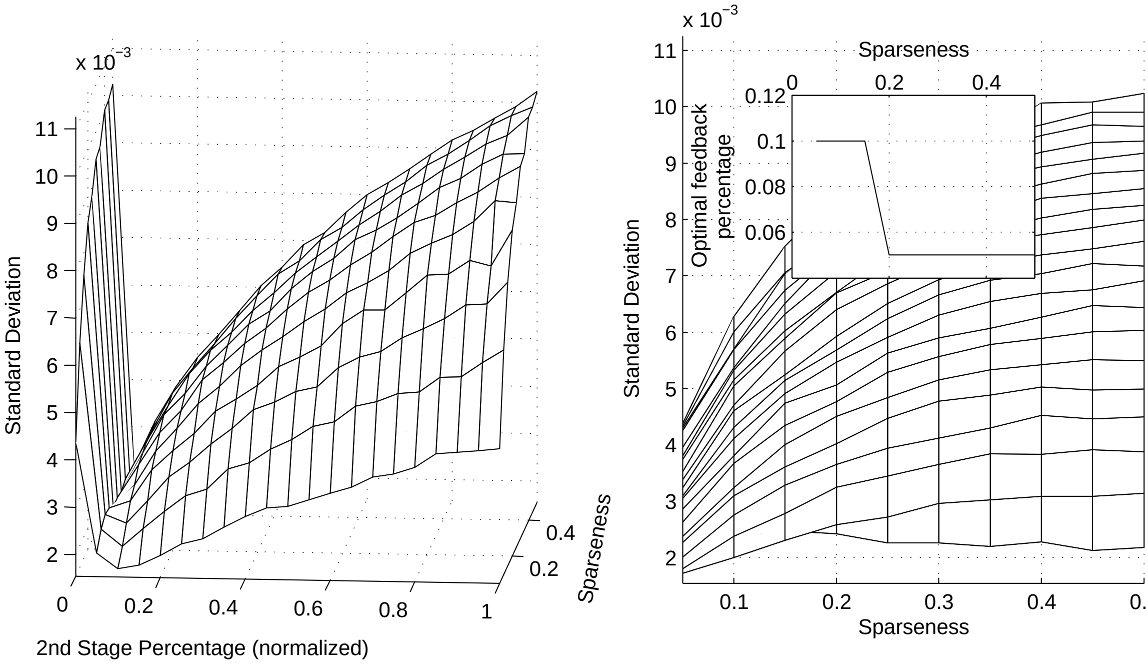

FIGURE 4.6: Standard deviation contour of the source model of length 2400 ($k = 4$)

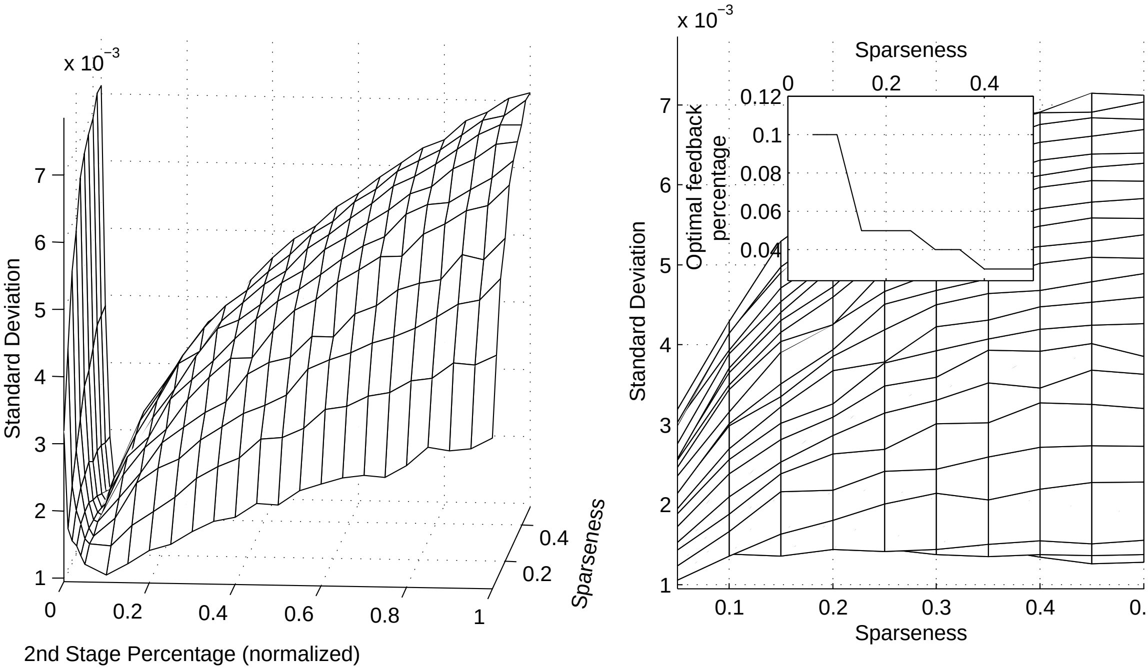

FIGURE 4.7: Standard deviation contour of the source model of length 4800 ($k = 5$)

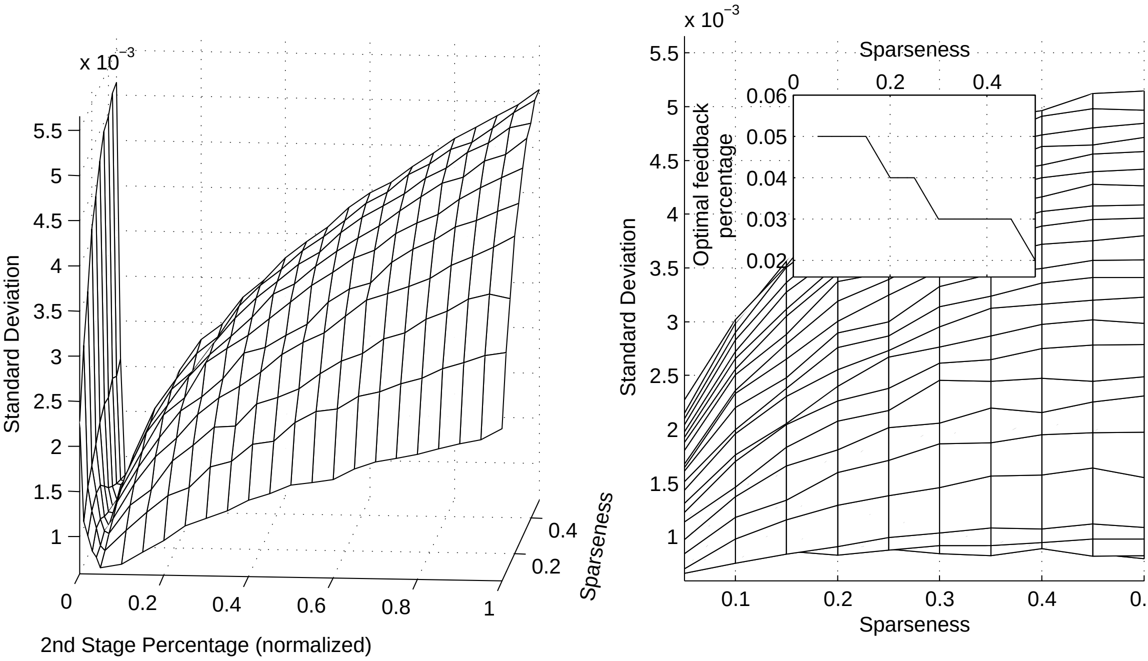

FIGURE 4.8: Standard deviation contour of the source model of length 9600 ($k = 6$)

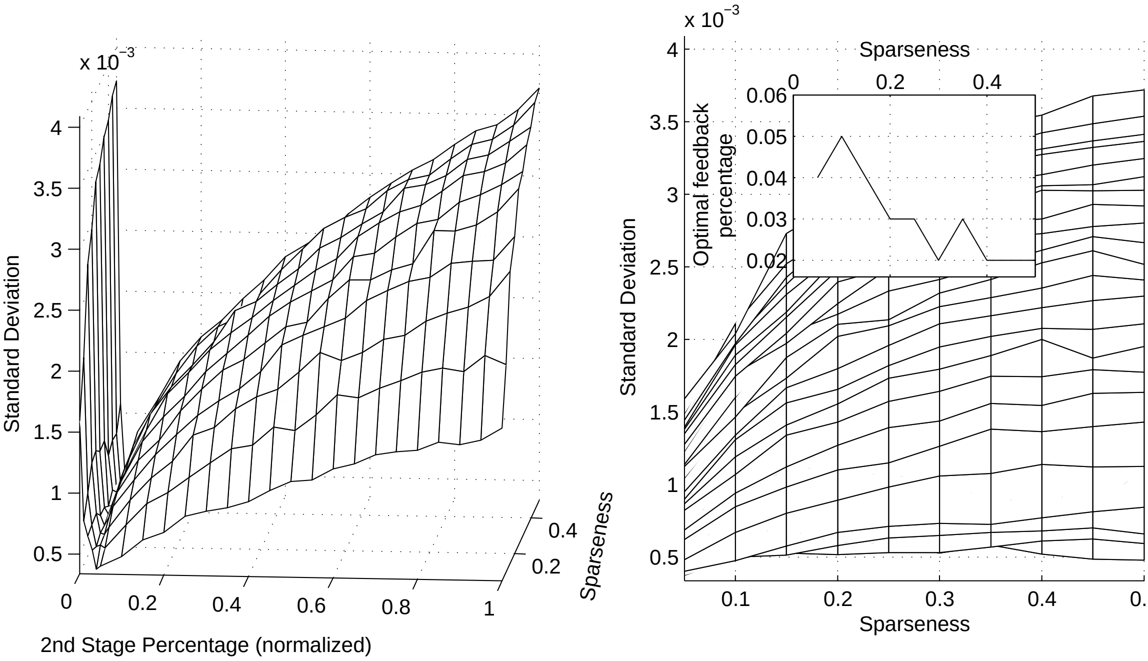

FIGURE 4.9: Standard deviation contour of the source model of length 19200 ($k = 7$)

$5.2 \times 10^{-3}$ for $l = 9600$, and $0.49 \times 10^{-3}$ compared to $3.53 \times 10^{-3}$ for $l = 19200$, or $33.3\%$, $28.1\%$, $29.8\%$, $24.7\%$, $20.6\%$, $18.1\%$ $11.5\%$, and $13.9\%$ for the respective block lengths.

3. Optimal feedback lengths (yielding the lowest standard deviation) for $\eta_\alpha = 0.5$ requires that $k/l$ is set to $15\%$, $10\%$, $10\%$, $5\%$, $5\%$, $3.5\%$, $2\%$ and $2\%$ for the respective block lengths. The overlay figures in all figures b) provide optimal results when $\eta_\alpha \neq 0.5$. It is clear that the optimal $k/l$ parameter reduces as $l$ increases for all $\eta_\alpha$. This corresponds to the valleys of the contours moving left as $l$ increases.

4. The optimal standard deviation for all $\eta_\alpha \gtrsim 0.15$ and all block lengths are approximately constant. As bitstreams with $\eta_\alpha < 0.15$ are extremely sparse and very rare in practical systems, we may generalise that optimal results yield a constant standard deviation, while non-optimal sources yield a declining standard deviation when $\eta_\alpha$ declines.

## 4.3 ANALYSIS OF THE EFFECT OF FEC ENCODING ON SPARSE DATA STREAMS

This subsection aims to introduce the effect that popular FEC encoding techniques have on the density of a bitstream with adjustable sparseness. A more detailed description of the encoders used is presented in *Appendix* C.

The simulation platform consisted of the random number generator in *Fig.* 4.1 that was implemented with the improved model illustrated in *Fig.* B.1 of *Appendix* B. The sparse data source was used with adjustable levels of sparseness while using the optimal feedback percentage. No source coding was performed to maximise the average code length and entropy. A channel coder was used to encode the bitstream by employing a Hamming, LDPC or convolutional encoder, as described in *Appendix* C. Various LDPC block codes were analysed for different block sizes, as well as different code rates. Different convolutional codes were implemented by varying the constraint length, $K$.

A number of important observations can be made from the presented simulation results. As expected, the different LDPC encoding techniques did not cause variations in the results, and only densely encoded results are presented. *Fig.* 4.10 indicates that:

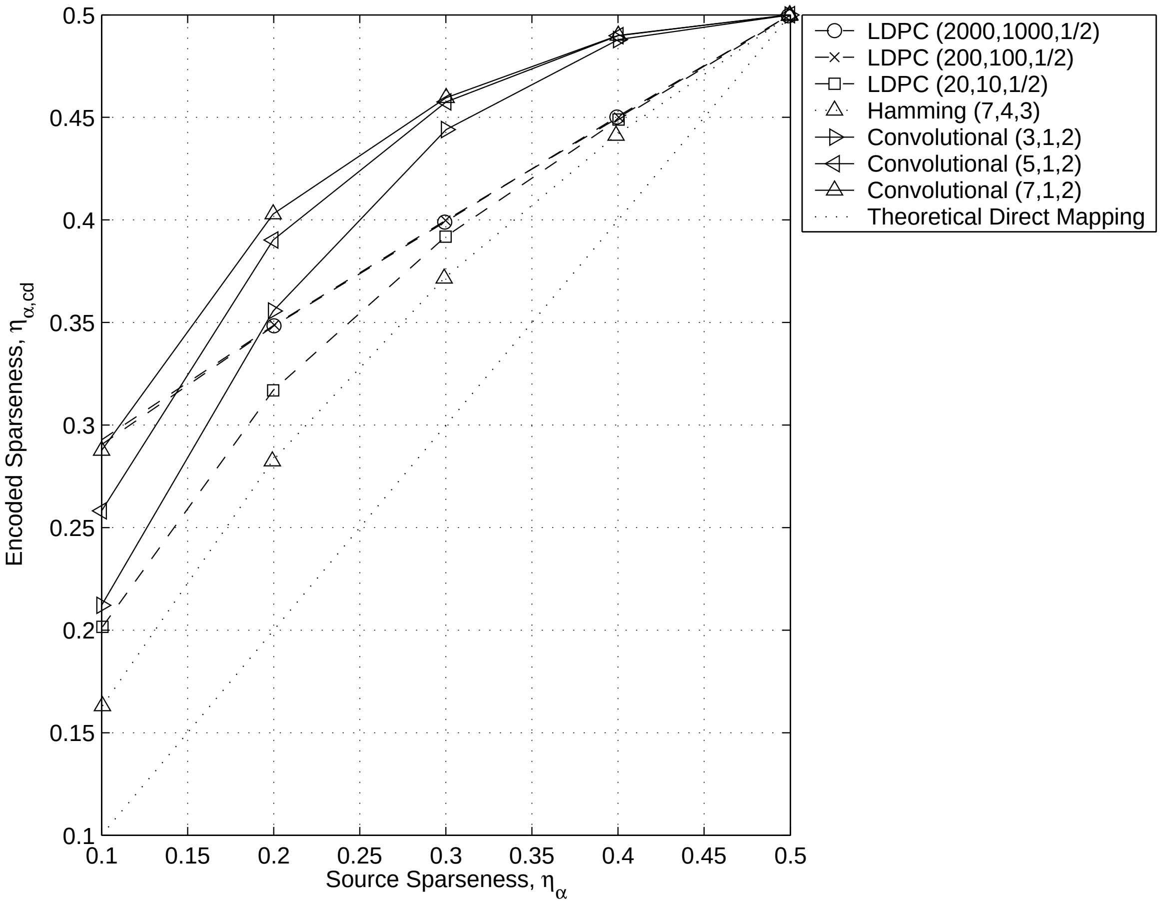

FIGURE 4.10: Encoded sparseness comparison for various half-rate codes.

1. All encoders tend to an encoded sparseness, $\eta_{\alpha,cd}$, of $0.5$ as the source sparseness, $\eta_{\alpha}$, tends to 0.5, indicating that the assumption of equiprobability holds for i.i.d. sources.
2. All encoders have a monotone mapping from $\eta_{\alpha}$ to $\eta_{\alpha,cd}$.
3. An increase in $n$ for block codes tends to transform the mapping of $\eta_{\alpha}$ to $\eta_{\alpha,cd}$ to a linear relationship, indicating that some theoretical linear upper limit exists for $\eta_{\alpha,cd}$ given a linear block encoder.
4. Increasing $k$ to $k > 100$ does not seem to justify the complexity in terms of the advantages the sparseness measure could provide (although this observation does not include improved BER performance).
5. The convolutional encoders transform a sparse data stream to a much denser encoded stream than the investigated block encoder counterparts. It can be seen that the

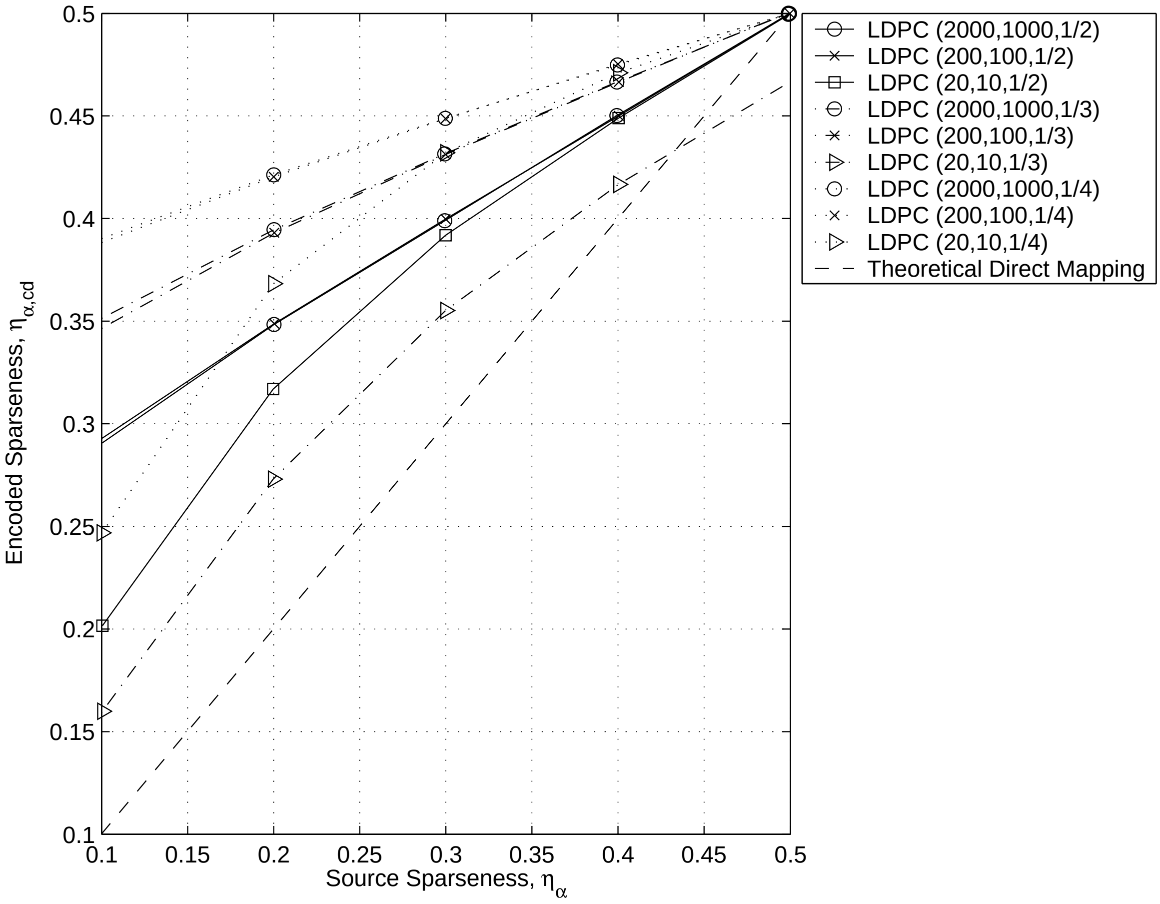

FIGURE 4.11: Encoded sparseness comparison for LDPC codes with various code rates.

simplest convolutional encoder outperforms the best $R_c = 1/2$ LDPC block code at a source sparseness of as little as approximately $\eta_\alpha > 0.19$. This renders various practical advantages, including improved synchronization due to more frequent zero crossings.

6. An increase in $K$ for the convolutional encoders tend to improve the mapping of $\eta_\alpha$ to $\eta_{\alpha,cd}$. The reason for this lies with the particular choice that was made for the function generator $g_2$, since a single sparse letter could potentially generate up to $K$ sparse symbols for a very sparse data source.

Furthermore, *Fig.* 4.11 indicates that

7. previous observations 1, 2, 3 and 4, seem correct for linear LDPC codes with different code rates,

8. increasing the code rate results in an improved mapping of $\eta_\alpha$ to $\eta_{\alpha,cd}$, and
9. the slope that was mentioned in observation 3 decreases with an increase in $n$ (decrease in $R_c = k/n$).

## 4.4 EVALUATION OF THE QPSK TRANSCEIVER IMPLEMENTATION

The following subsections describe results of the general QPSK transceiver structure employed by the UMTS/WCDMA simulation platform for various configurations depending on the system parameter, $k$, as discussed in *Chapter* 2. The RRC filters were configured with $\alpha = 0.22$ and an order of 33. Unless otherwise stated, the UMTS/WCDMA system was simulated with 4 samples per chip, or an oversampling factor of 4. The system was configured in such a way that no AWGN or multiplicative and phase (frequency selective and non-selective fading) noise was introduced, and serves as a back to back setup ensuring that the assumption of perfect synchronisation has been met.

### 4.4.1 Time based analysis of the measured signals

Several time based signals were measured and are presented in *Fig.* 4.12 (a) for both the I-branch and the Q-branch of the QPSK transmitter. It should be clear that the system successfully spreads the data signal with the appropriate spreading sequence, after which the spreaded signal is scrambled with the cell specific scrambling code. Each information bit is upsampled to represent an NRZ signal waveform for the purposes of illustration. However, the filters are pulsed to maintain a close to unity amplitude, i.e. an NRZ chip period with four samples per chip (1, 1, 1, 1) would be passed to the filters as a pulsed chip (0, 0, 0, 1). The output signal of the squared RRC filter is also presented, although it should be noted that the initial delay caused by filter startup has been compensated for.

*Fig.* 4.12 (b) presents results for both the I-branch and the Q-branch of the QPSK receiver, and shows the output of the matched filter (squared RRC filter), which is sampled at the appropriate time and then held constant by the S/H circuitry. The output of the S/H circuit is multiplied with the scrambling code to yield a descrambled output, as presented, which is again multiplied with the user specific spreading code to recover the despreaded signal

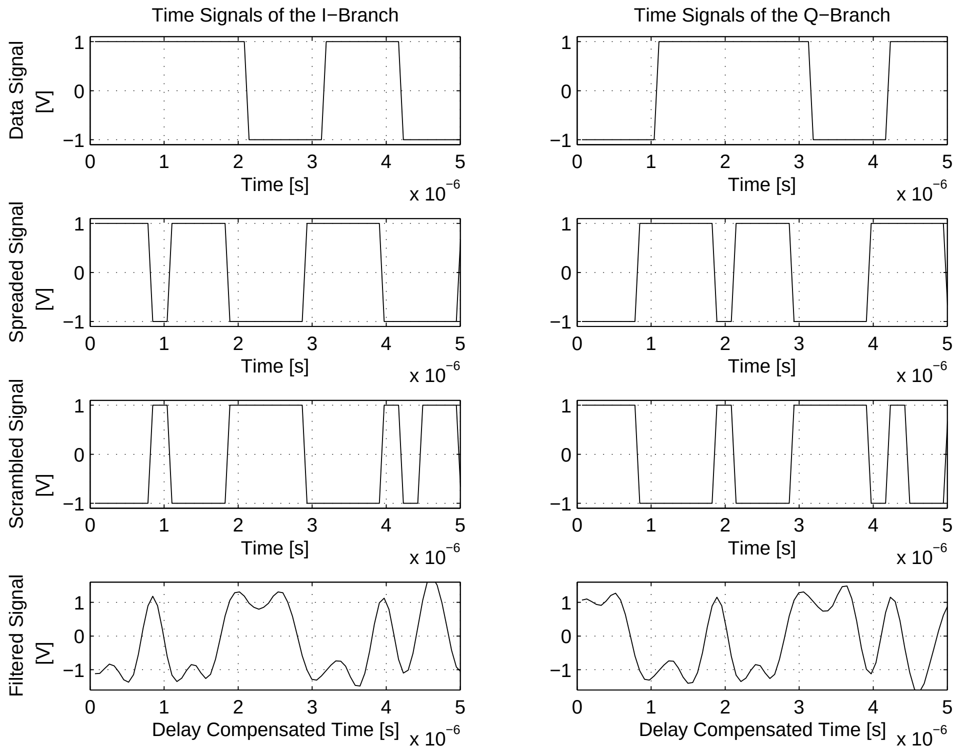

(a) Transmitter signals

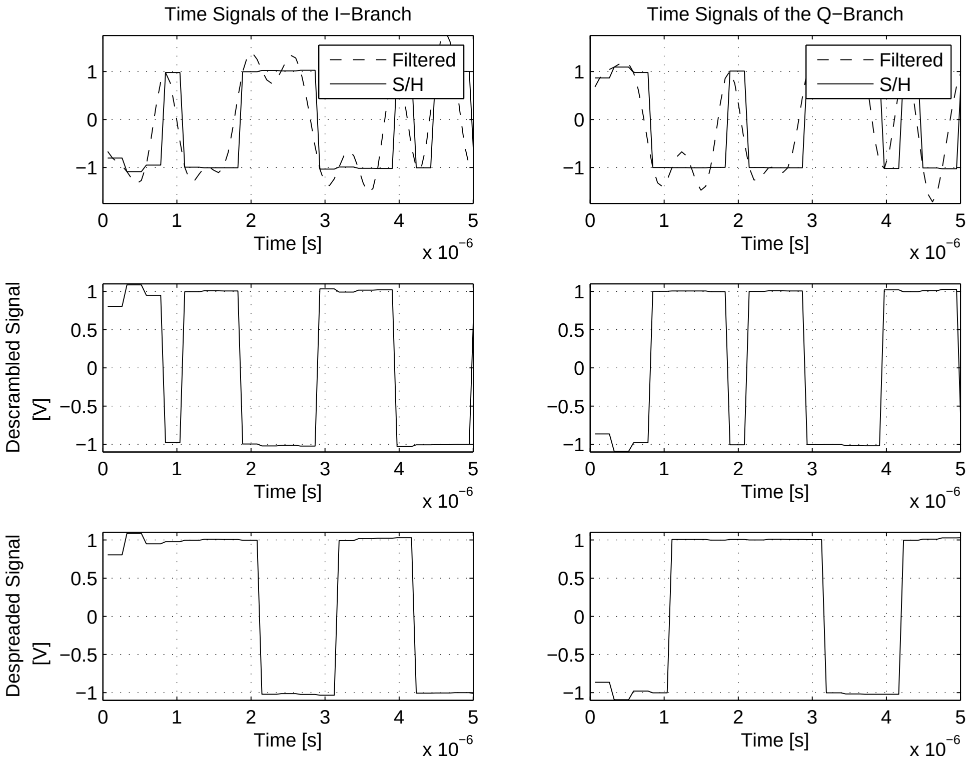

(b) Receiver signals

FIGURE 4.12: Measured timing signals associated with the QPSK transmitter set to a block length of 19200 bits per frame ($k = 7$).

waveform (data signal) similar to the one presented in the top of *Fig.* 4.12 (a). This value may be averaged with integration to provide a soft output for the channel coding subsystems.

### 4.4.2 Eye diagrams of the measured signals

Eye diagrams are often used to test whether a system has the ability to recover data from signals that may be influenced by ISI due to pulse shaping, and to test whether the system is properly synchronised. It indicates to the designer at which appropriate time instance sampling of the pulse shaped/matched filtered signal should take place. It is clear from inspection of the eye diagram of the transmitter presented in *Fig.* 4.16 (a) that there is no appropriate time instance where the signal converges to a single point, and the eye diagram is closed. However, by inspecting *Fig.* 4.16 (b), it is clear that the received signals after matched filtering do converge at points corresponding to samples $[1, 5, 9, ..., 21]$ (or $z \cdot n + 1$, with $n$ an integer index and $z = 4$ the oversampling factor) and that it is possible to recover the signal with no ISI at those instances where the eye diagrams are open.

### 4.4.3 Frequency based analysis of the measured signals

The measured single-sided PSD of the transmitted and filtered received signals as presented in *Fig.* 4.14 correspond very well with the expected theoretical frequency response as given in *Fig.* 2.5. The bandwidth of the I- and Q-branch data streams for the system parameter of value $k = 7$ corresponds to a symbol rate of $960$ ksps, which is spreaded by a spreading factor of $4$, to yield a bandwidth of $3.840$ MHz before filtering. It is worth nothing that the approximate transmitted signal bandwidth after a single RRC filtering stage may be calculated as $(1 + \alpha) \cdot 1/(2T_c) \approx 2.34$ MHz, which is also clear from *Fig.* 4.14. The bandwidth of the I- and Q-branch data streams will reduce, should the system parameter be reduced from $k = 7$. However, the transmission bandwidth will stay fixed, as the spreading factor will increase in reaction to a reduced value of $k$. This concept is illustrated for the case of $k = 5$, where it is clear that the I/Q channel signal bandwidth reduces with a factor of 8. Finally, it is clear that the $33^{rd}$ order square root RRC filter is not quite sufficient to ensure the requirement of 35 and 45 dB suppression below the in-band power maximum for the first and the second adjacent channels. This requirement may easily be met by increasing the filter order to achieve the additional 5 dB suppression, but due to the increased simulation time, it was decided to implement a lower filter order.

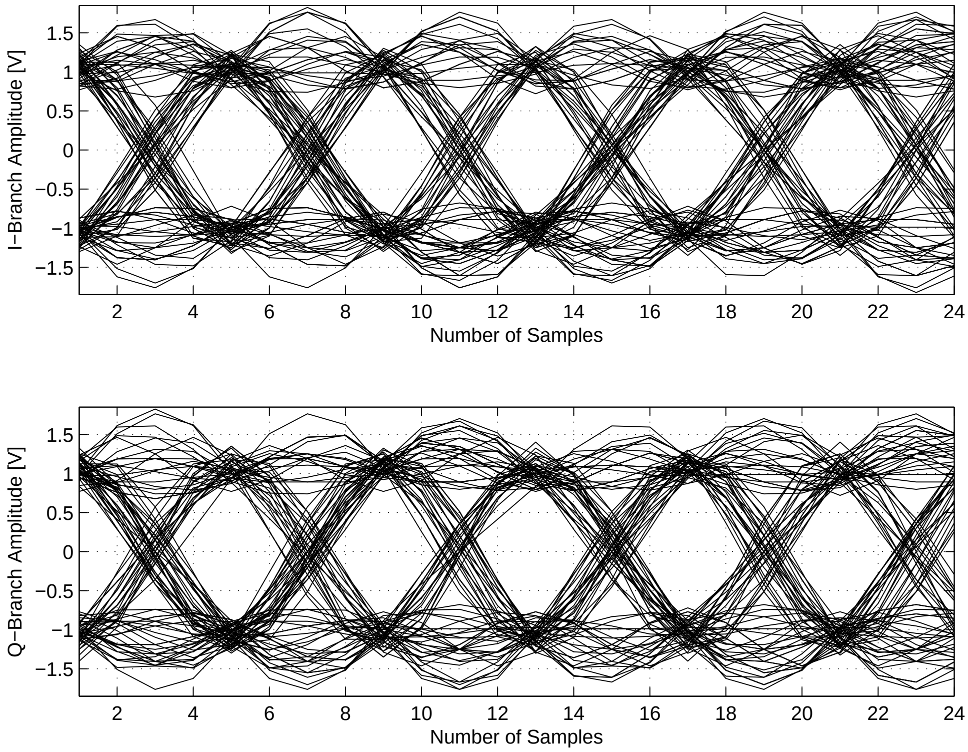

(a) Transmitter signals

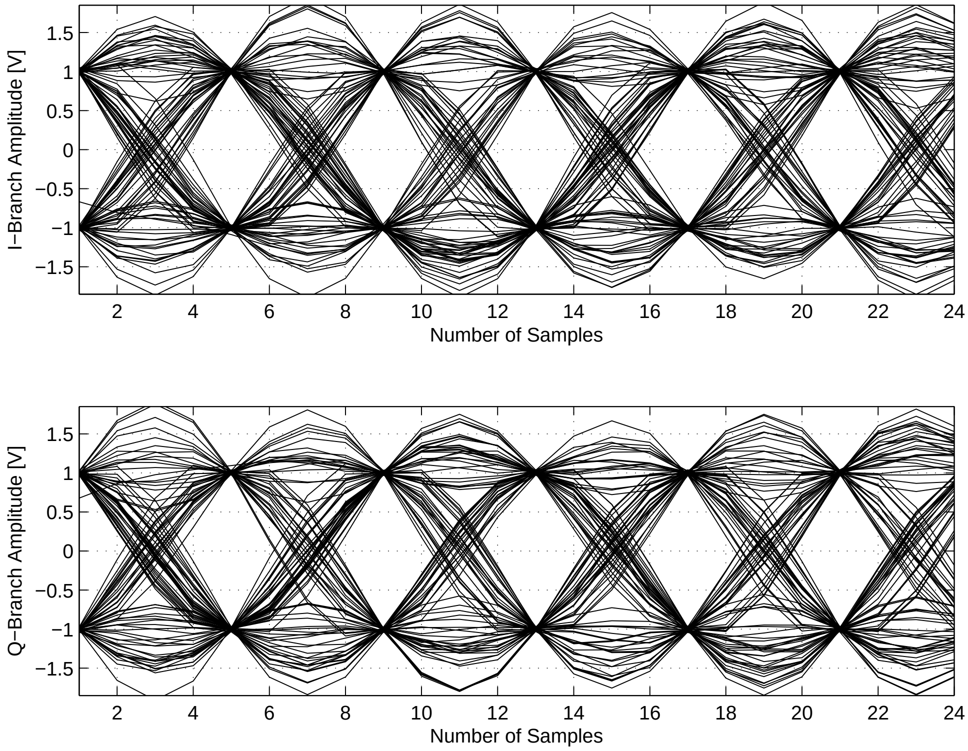

(b) Receiver signals

FIGURE 4.13: Measured eye diagrams of the RRC pulse shaping filter ($\alpha = 0.22$) for the QPSK transceiver set to a block length of 19200 bits per frame ($k = 7$).

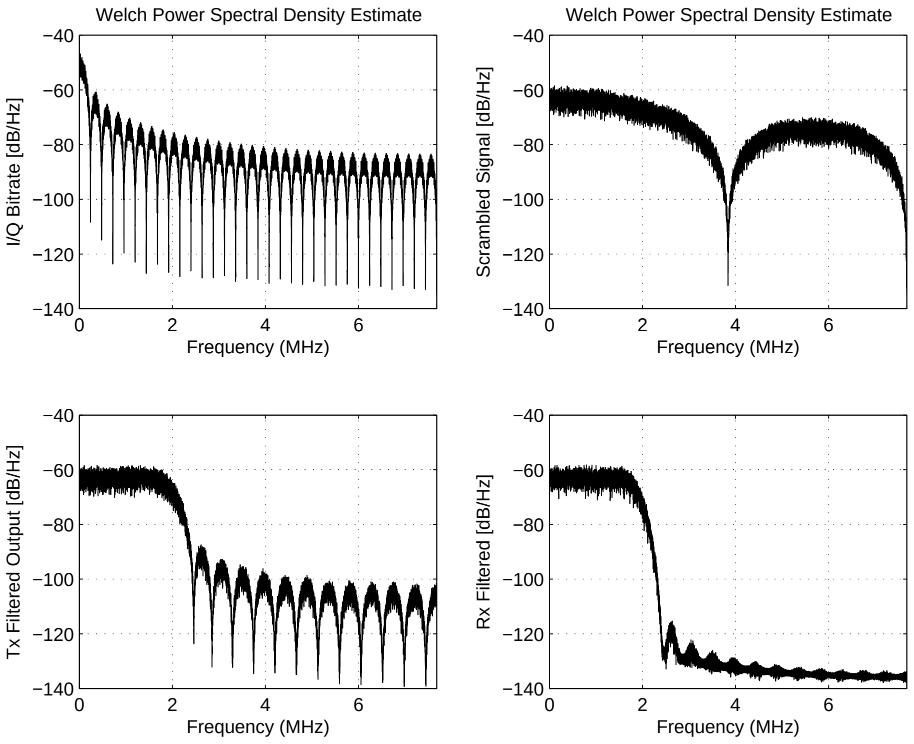

(a) $k = 5$, spreading factor of 16, data rate of 480 kbps / user

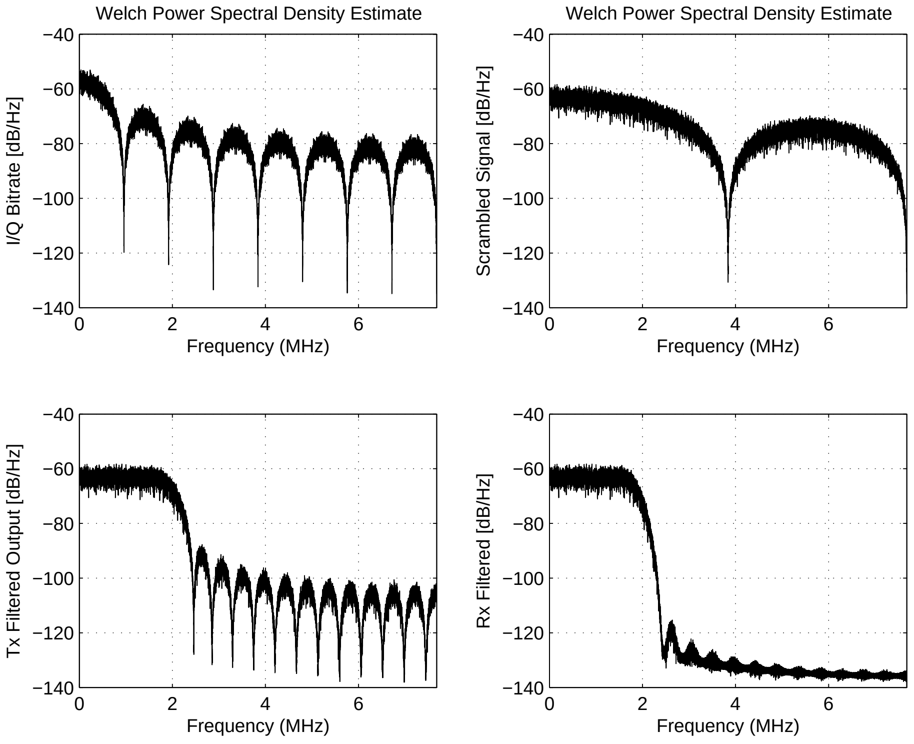

(b) $k = 7$, spreading factor of 4, data rate of 1.92 Mbps / user

FIGURE 4.14: Single-sided PSD for various signals of the QPSK transceiver employing a RRC transmitter and receiver (matched) filter ($\alpha = 0.22$) configured for different system parameters.

### 4.4.4 Analysis of the platform when configured for narrowband transmission

The UTRA WCDMA transceiver may easily be configured as a narrowband QPSK transceiver by setting the channelisation code to an all ones vector $C_{ch} = [1, ..., 1]$ of length $512/2^k$ (the spreading factor for the downlink), and the scrambling code to an all ones vector $C_{scramb} = [1, ..., 1]$ of length $(10 \cdot 2^k \cdot 15)/2 \cdot 512/2^k$ with $(10 \cdot 2^k \cdot 15)/2$ the number of bits per frame per I/Q branch and $512/2^k$ the spreading factor for the downlink. *Fig.* 4.15 through *Fig.* 4.17 illustrate the measured results that may be compared with the wideband results presented in *Fig.* 4.12 through *Fig.* 4.14. It is clear that the transmission bandwidth presented here, approximately equal to $585$ kHz, is smaller than that of the wideband transceiver as expected. Also notice that the eye diagrams at the receiver are open on every $16^{th}$ sample, which differs from the results presented in *Section* 4.4.2 with a factor of $4$, which is associated with the spreading factor of $512/2^7 = 4$ for the simulation setup. This is important from a practical perspective, as the receiver uses this information to sample and hold the received data at the appropriate time instances. Should the sampling rate be similar to the wideband scenario (i.e. too fast), an incorrect quantised (almost) sinusoidal signal would be obtained. Finally, it should be noted that a higher filter order of $129$ is required to ensure that the ISI is reduced to an insignificant amount. A good approximation for the required impulse response length of RRC filters is given as $4 \times 512^k \cdot T_{chip}/2T_s + 1$, where the corner frequency of the filter is $512/2^k$ times smaller than $2/T_{chip}$ for the narrowband system, thus requiring a larger impulse response length (filter order).

### 4.4.5 Analysis of the orthogonality of the OVSF codes

The ability of any CDMA system to reject MUI depends heavily on the selection of the appropriate family of spreading codes and the orthogonality of the underlying codes within the family. As discussed in *Section* 2.4, UMTS/WCDMA has standardised to OVSF codes to be used as the channel codes to distinguish between different DPDCH, and not specifically users only, as a single user may be assigned with several DPDCH if they are available. OVSF codes are well known for their superior orthogonality properties when synchronised, which is a plausible scenario in the downlink. These codes, however, are used in an asynchronous fashion as well during uplink operation. This section briefly analyses the characteristics of these codes within a multi-user environment by means of a truncated periodic autocorrelation

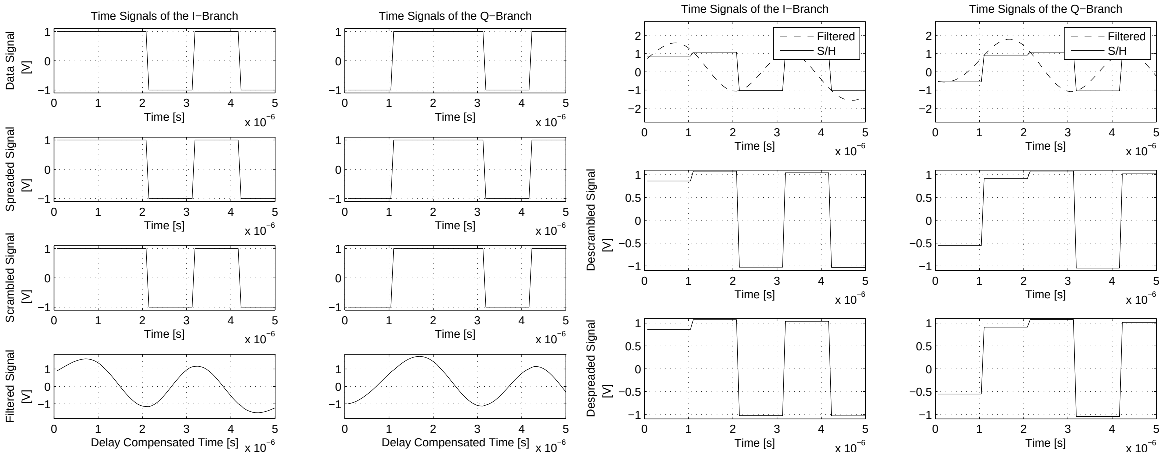

(a) Transmitter signals (b) Receiver signals

FIGURE 4.15: Timing signals associated with the QPSK transmitter configured for narrowband transmission set to a block length of 19200 bits per frame ($k = 7$).

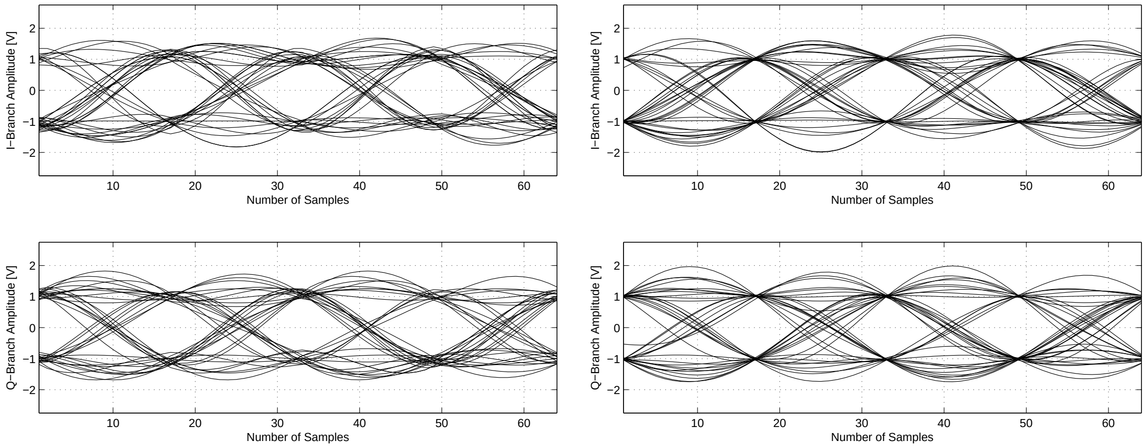

(a) Transmitter signals (b) Receiver signals

FIGURE 4.16: Measured eye diagrams of the RRC pulse shaping filter ($\alpha = 0.22$) for the narrowband QPSK transceiver set to a block length of 19200 bits per frame ($k = 7$).

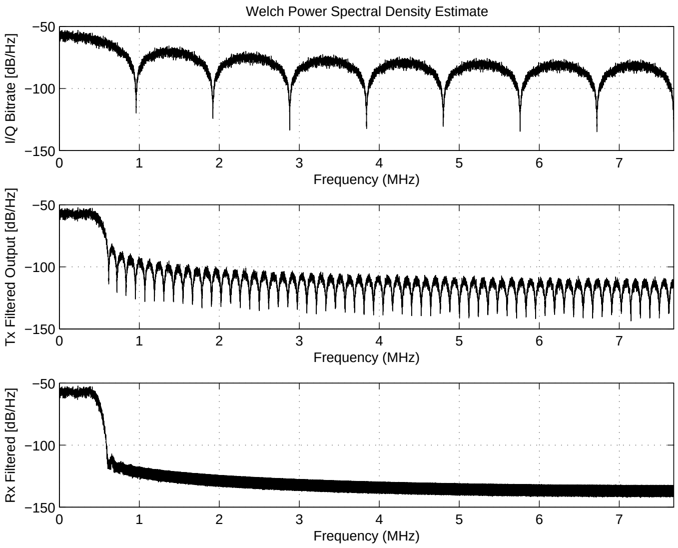

FIGURE 4.17: Single-sided PSD for various signals of the QPSK transceiver configured for narrowband transmission at 19200 bits per frame ($k = 7$)

and the cross-correlation of the codes.

*Fig.* 4.18 shows the autocorrelation of each of the codes within the different system setups, primarily determined by the system parameter, $k$. As expected, each of the unique codes has a normalised peak at the same time instance, again indicating the strict requirement of having a very good synchronisation method. It is interesting to note that the autocorrelation characteristics of the code set $k = 7$ repeat itself exactly as the autocorrelation characteristics of the first $512/2^k = 4$ codes in the code set $k = 6$, while the last 4 codes display new autocorrelation characteristics. Likewise, with $k = 6$, the autocorrelation characteristics of the $512/2^k = 8$ codes repeat itself exactly as the first 8 autocorrelation characteristics of set $k = 5$, with the last 8 autocorrelation characteristics again previously unobserved. This process repeats up to $k = 1$.

MUI is primarily determined by the cross-correlation that exists between different codes within a code family. *Fig.* 4.19 shows the maximum cross-correlation that exists between a single code and all the others for various system setups. Maximum values indicate that the cross-correlation between the code and itself (i.e. an autocorrelation) was determined. As expected for a perfectly synchronised system (1 sample/chip case), the OVSF exhibits perfect autocorrelation with zero cross-correlation. However, these codes do not exhibit perfect cross-correlation properties when they have more than 1 sample/chip, as one code has the potential of being slightly shifted in time with reference to the other code, a scenario perfectly plausible for a practical uplink. *Fig.* 4.19 exhibits the worst case measurement, or

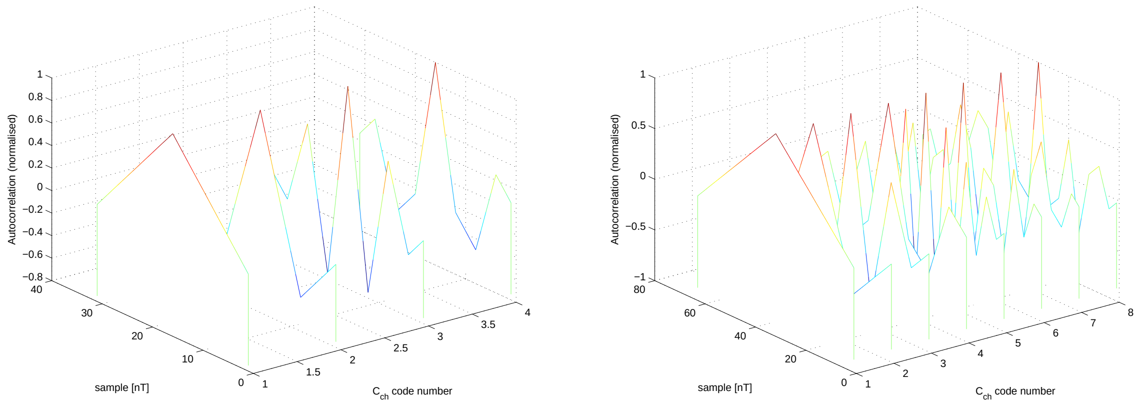

(a) Autocorrelation with $k = 7$ (b) Autocorrelation with $k = 6$

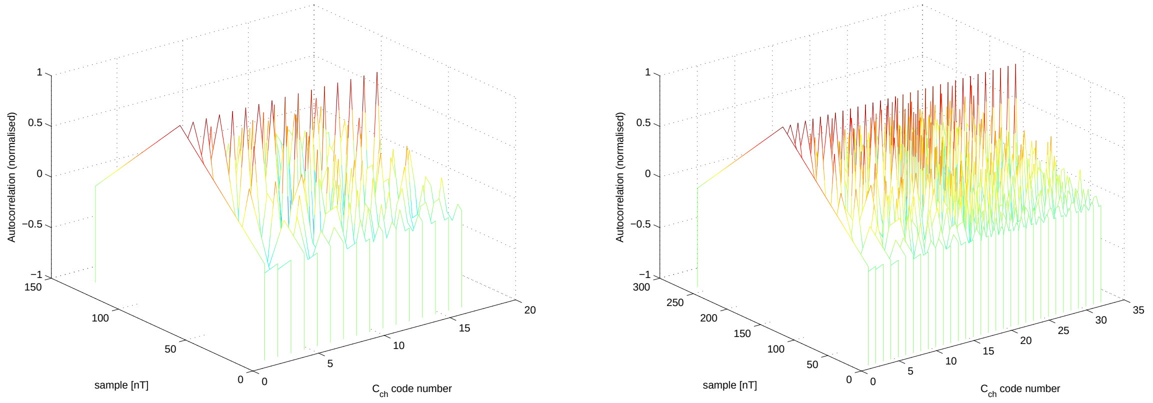

(c) Autocorrelation with $k = 5$ (d) Autocorrelation with $k = 4$

FIGURE 4.18: Measured periodic autocorrelation for various sets of OVSF codes with 4 samples/chip.

the maximum possible cross-correlation. A system configured with $k = 7$ will exhibit an amount of cross-correlation between codes $C_{ch,2}$ and $C_{ch,4}$, while a system configured with $k = 6$ will exhibit the same amount of cross-correlation between codes $C_{ch,3}$ and $C_{ch,7}$, as well as some additional cross-correlation between other codes. The large cross-correlation may be attributed to the fact that the two codes would have been identical, were it not for a shift of one bit position. This process repeats itself as $k$ decreases. A final observation is that there exists good code combinations that have zero cross-correlation regardless of the relative time shift between them. Notice from *Fig.* 4.19 d) that every second cross-correlation performed returned a zero result. Again, this result repeats itself as $k$ decreases. It is, therefore, imperative for asynchronous systems employing OVSF codes to closely manage the process of code selection from the available family of codes.

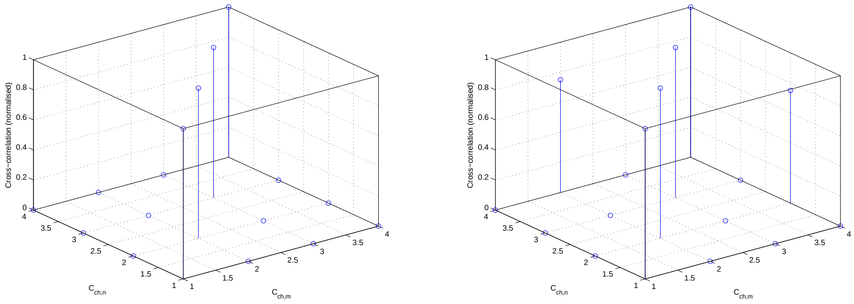

(a) Cross-correlation with $k = 7$ and 1 samples/chip

(b) Cross-correlation with $k = 7$ and 4 samples/chip

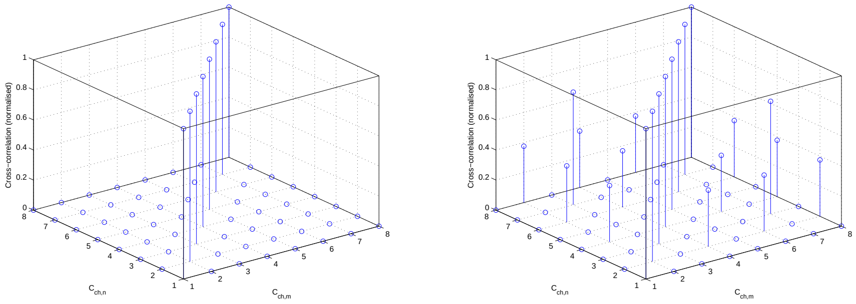

(c) Cross-correlation with $k = 6$ and 1 samples/chip

(d) Cross-correlation with $k = 6$ and 4 samples/chip

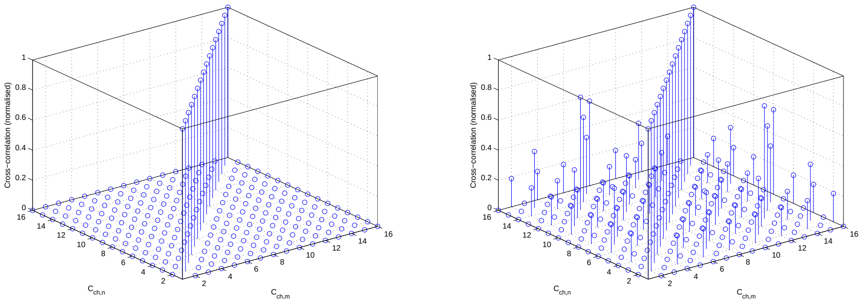

(e) Cross-correlation with $k = 5$ and 1 samples/chip

(f) Cross-correlation with $k = 5$ and 4 samples/chip

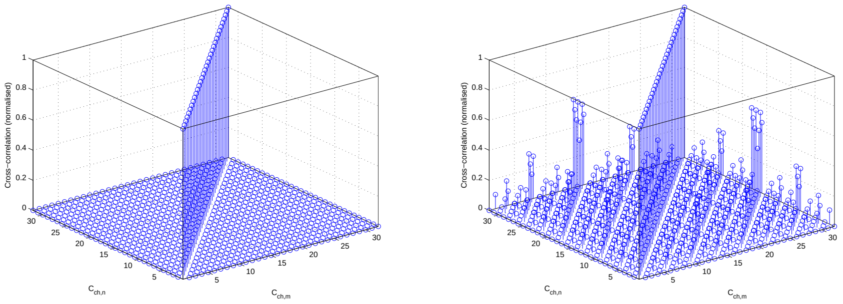

(g) Cross-correlation with $k = 4$ and 1 samples/chip

(h) Cross-correlation with $k = 4$ and 4 samples/chip

FIGURE 4.19: Measured maximum periodic cross-correlation for various sets of OVSF codes for synchronous and asynchronous setups.

## 4.5 ANALYSIS OF THE IMPLEMENTED CHANNEL MODELS

The following subsections describe the experimental setup and the results obtained to illustrate the various adjustable channel parameters as listed in *Table* 4.2 of the simulator platform and their effect on the wireless transmission channel. The main emphasis of the experiments was to ensure that the models are properly calibrated according to the theoretical models as described in *Appendix* D and that the first and second order statistics of the simulated deterministic processes closely correspond to that of the associated stochastic processes.

### 4.5.1 Analysis of the AWGN process

*Fig.* 4.20 illustrates the PSD of the transmitted signal (as illustrated in *Fig.* 4.14) with a controlled amount of AWGN added. The experiment was performed with the UMTS/WCDMA transceiver configured with a system parameter, $k = 7$, while the SNR was adjusted in 5 dB increments over a large range of $E_b/N_0 = [0, 50]$ dB, although only some of these results are illustrated. It is clear from the figures that the noise is indeed scaled appropriately according to the input $E_b/N_0$ parameter, and that the matched filter bandlimits the out-of-band noise spectral power entering the system. It was observed that the second spectral component of the matched filtered signal approached -115 dB/Hz as the SNR was increased to $E_b/N_0 \approx 30$ dB.

*Fig.* 4.21 illustrates various different scenarios for an antipodal modulation scheme such as BPSK or each branch of the QPSK transmitter when the sparseness of the data source and the amount of noise power are adjusted independently. It is well known that the PDF of the noise (normal distribution) will be superimposed on the PDF of the data source (discrete binomial distribution), with the decision region of the detector determined by the intersect of the two symbols' independent Gaussian PDFs, normally assumed as $r_d = 0$. This is especially clear from the equiprobable cases illustrated in *Fig.* 4.21 e) and f), while a) through d) show that non-optimal results will be achieved if the equiprobable assumption is made.

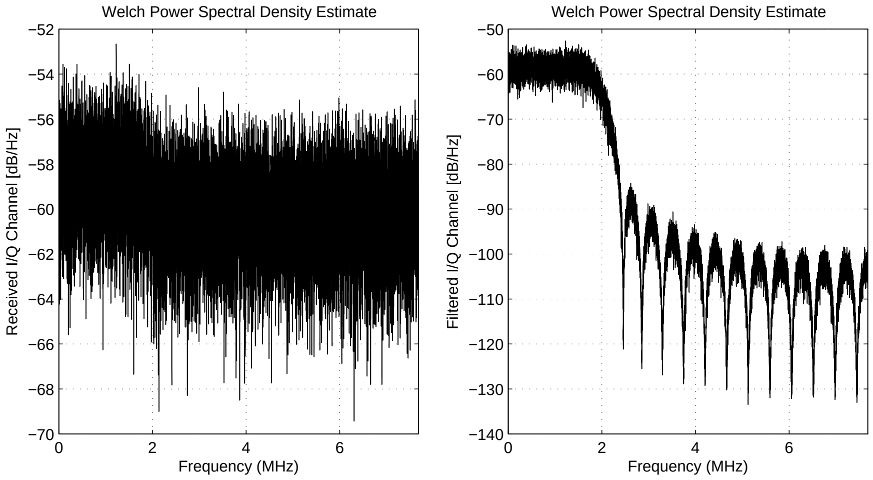

(a) $E_b/N_0 = 0$ dB

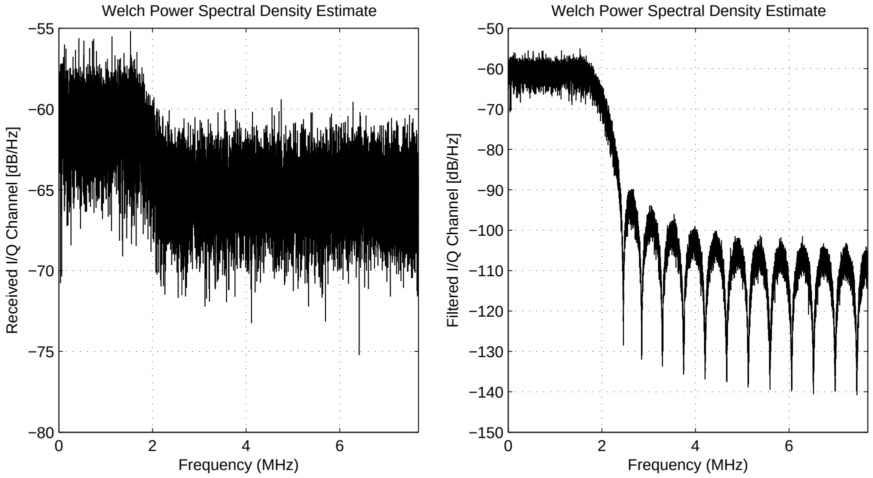

(b) $E_b/N_0 = 5$ dB

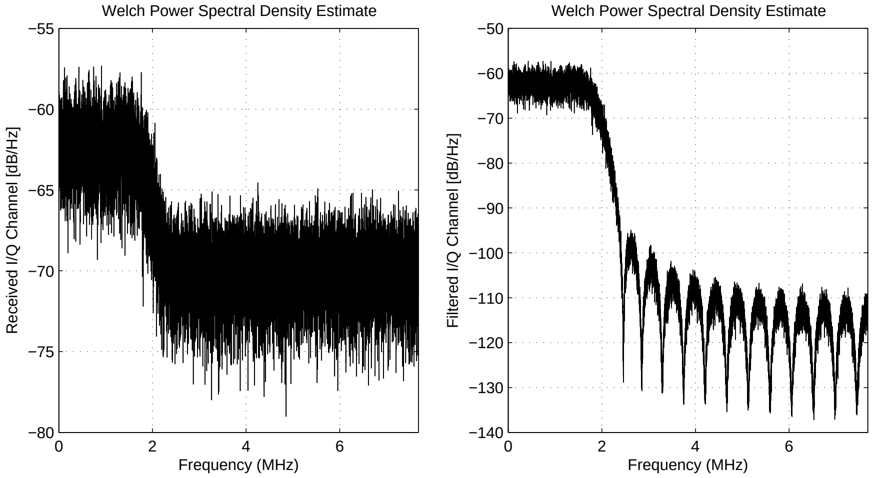

(c) $E_b/N_0 = 10$ dB

FIGURE 4.20: PSD of the received and matched filtered wideband QPSK-branch signals with various levels of SNR using an AWGN source.

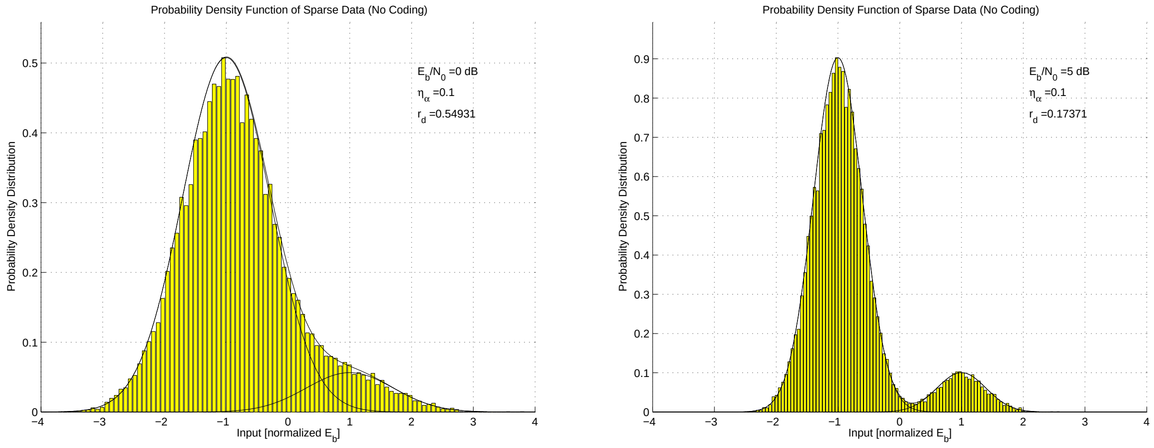

(a) $\eta_\alpha = 0.1$ (extremely sparse), $E_b/N_0 = 0$ dB

(b) $\eta_\alpha = 0.1$ (extremely sparse), $E_b/N_0 = 5$ dB

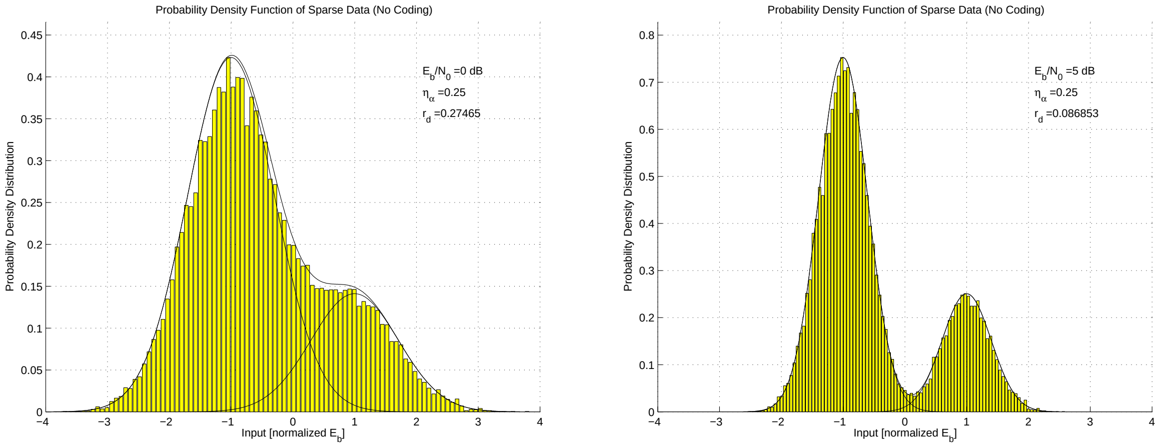

(c) $\eta_\alpha = 0.25$ (highly sparse), $E_b/N_0 = 0$ dB

(d) $\eta_\alpha = 0.25$ (highly sparse), $E_b/N_0 = 5$ dB

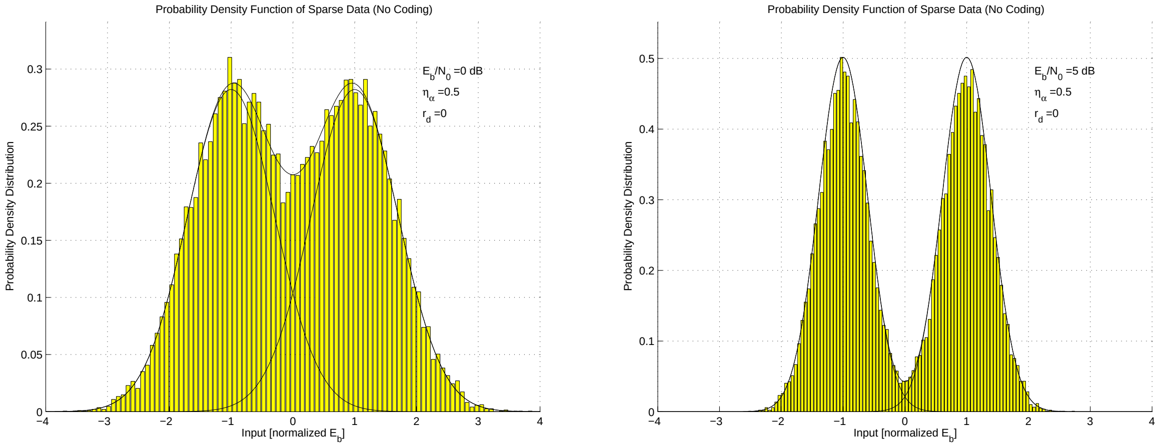

(e) $\eta_\alpha = 0.5$ (equiprobable), $E_b/N_0 = 0$ dB

(f) $\eta_\alpha = 0.5$ (equiprobable), $E_b/N_0 = 5$ dB

FIGURE 4.21: PDF of an uncoded, narrowband BPSK/QPSK-branch signal with various levels of sparseness and SNR using an AWGN source.

From *Fig.* 4.21, a number of novel observations can be made.

- The decision intervals, $r_d$, for non-equiprobable inputs are larger than zero when $s_1$ is sparse compared to $s_{-1}$, and tend to increase when $\eta_\alpha$ is decreased. It is clear that the decision region lies between zero and the sparse symbol, and not necessarily at $r_d = 0$.

- The decision intervals, $r_d$, for non-equiprobable inputs are larger than zero when $s_1$ is sparse compared to $s_{-1}$, and tend to increase when $E_b/N_0$ is decreased.

- For a specific symbol (either $s_{-1}$ or $s_1$), the area under that symbol's PDF has to remain constant (and equal to the maximum probability of 1, therefore the magnitude (scaled with $1/\sqrt{2\pi\sigma_n^2}$) will increase as $E_b/N_0$ increases (or $1/N_0 = 1/2\sigma_n^2$ increases), since $\sigma_n$ (that essentially governs the width of the PDF) decreases when the signal power is kept constant. The magnitude approaches $\eta_\alpha$ as $E_b/N_0$ becomes large.

### 4.5.2 Analysis of the methods to generate the Doppler parameters

The various methods as discussed in *Appendix* D.4.5, that are used to determine the Doppler parameters required by the Rician process when using the sum-of-sinusoids method, were implemented. *Fig.* 4.22 through *Fig.* 4.25 show the calculated PSD and *Autocorrelation Function* (ACF) of the different methods. The PSD is measured as a line spectrum, with the $f_{z,n}{}^{th}$ component density given by $\frac{c_{z,n}^2}{4}[\delta(f \pm f_{z.n})]$ according to *Eq.* (D.37). The Rician process was configured throughout the experiments with $N = 16$ oscillators.

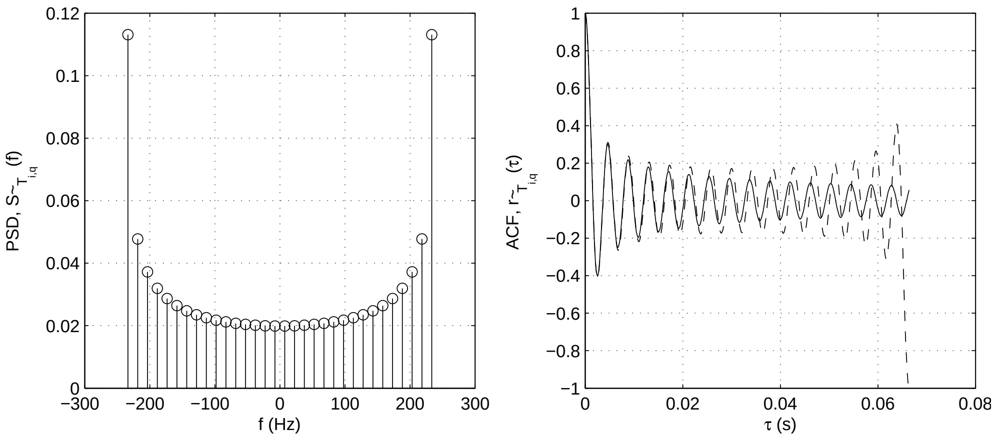

FIGURE 4.22: a) PSD, $\tilde{S}_{Ti,q}(f)$ and b) ACF, $\tilde{r}_{Ti,q}(\tau)$ for the MED ($N_i = 16$ , $f_{d,max} = 241$ Hz, $\sigma_0^2 = 1$).

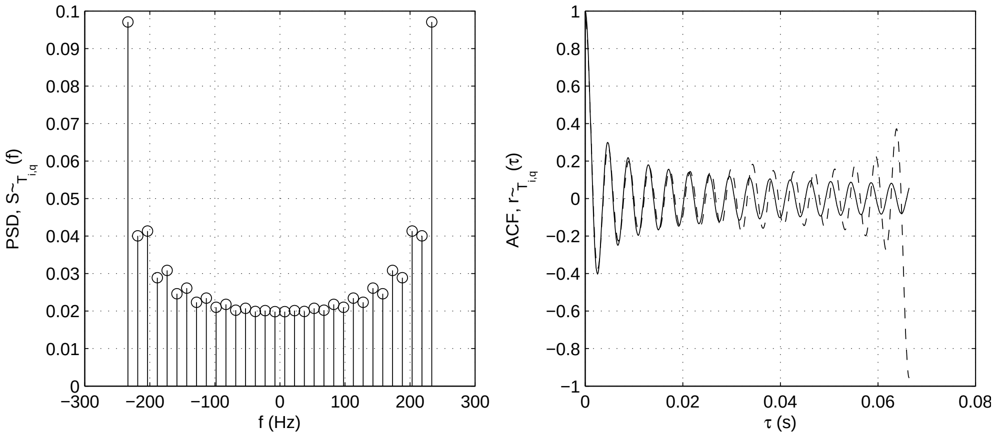

FIGURE 4.23: a) PSD, $\tilde{S}_{Ti,q}(f)$ and b) ACF, $\tilde{r}_{Ti,q}(\tau)$ for the MSEM ($N_i = 16$ , $f_{d,max} = 241$ Hz, $\sigma_0^2 = 1$).

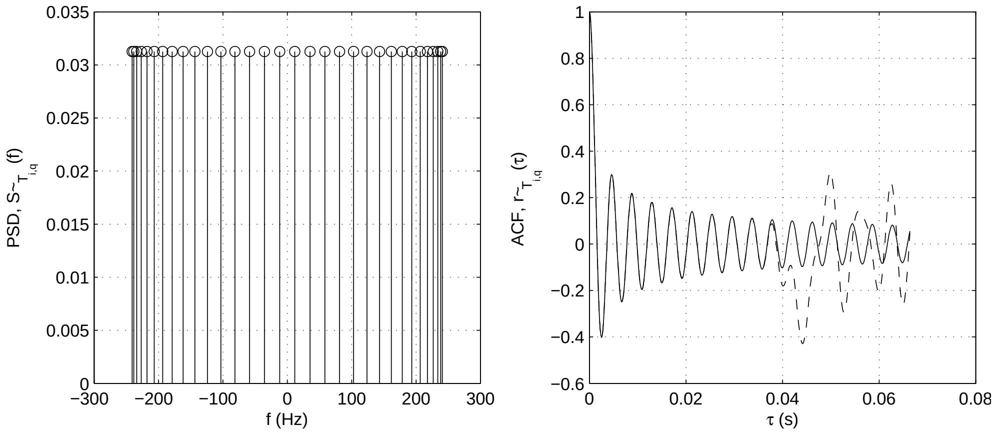

FIGURE 4.24: a) PSD, $\tilde{S}_{Ti,q}(f)$ and b) ACF, $\tilde{r}_{Ti,q}(\tau)$ for the MEDS ($N_i = 16$ , $f_{d,max} = 241$ Hz, $\sigma_0^2 = 1$).

A number of observations can be made from the results.

- It is clear that the MEDS and the MSEM use equal and constant spacing between the frequency components and that the resulting PSD closely resembles the theoretical Jakes' PSD as presented in *Fig.* D.1.

- At first glance, it does not seem as if the PSD of the MEDS and the JM share the same shape as the proposed theoretical requirement of *Fig.* D.1. However, it should be noted that there exists a higher density of spectral components closer to $\pm f_{d,max}$ than to the center of the graph. If the density graph is to be integrated, the resulting spectral power will still share the same shape as a theoretically integrated Jakes PSD.

- The obtained ACF closely follows the theoretical function in the range $0 \leq \tau \leq \tau_{max}$,

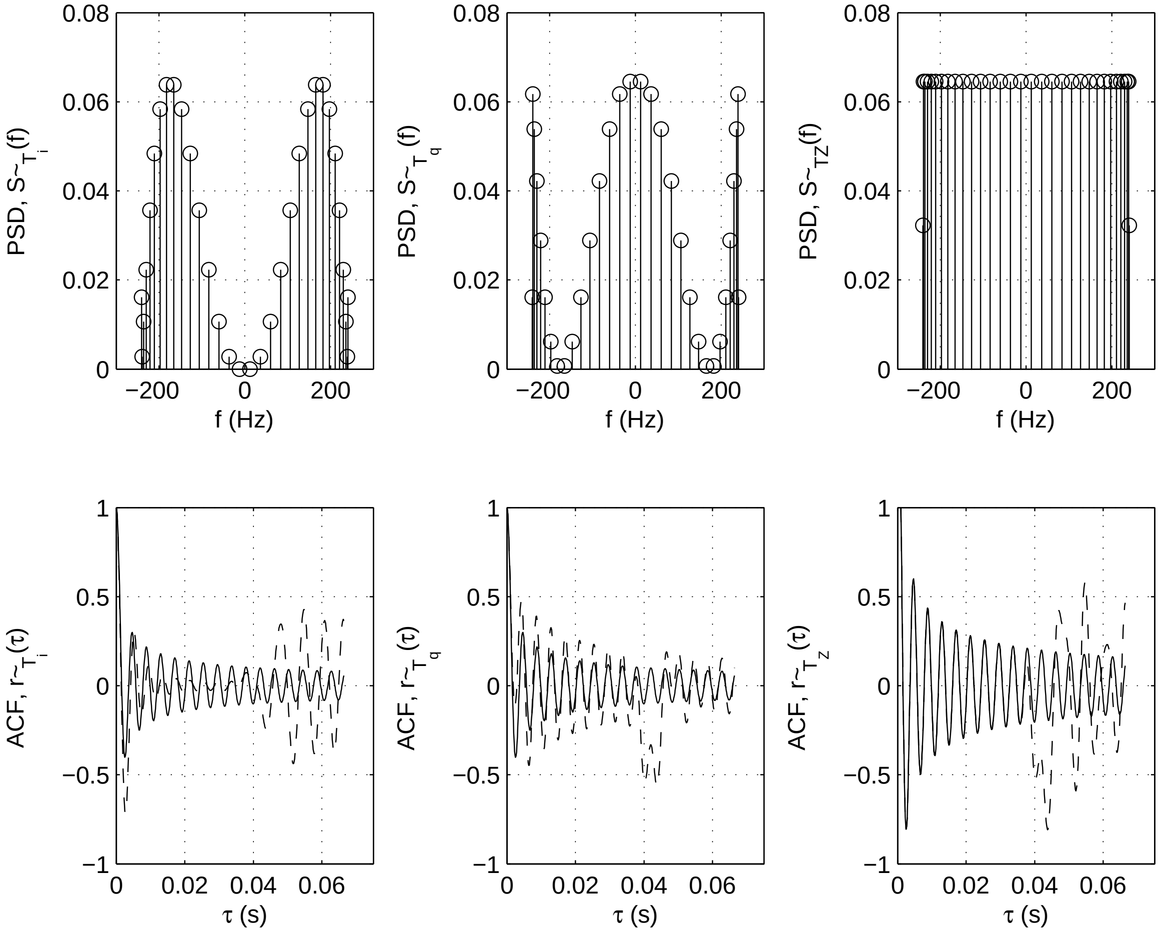

FIGURE 4.25: a) PSD, $\tilde{S}_{Ti,q}(f)$ and b) ACF, $\tilde{r}_{Ti,q}(\tau)$ for the JM ($N_i = 16$ , $f_{d,max} = 241$ Hz, $\sigma_0^2 = 1$).

with $\tau_{max} = N_I/(2f_{d,max}) = 33.2$ ms for $N_i = 16$ and $f_{d,max} = 241$ Hz for all cases.

- The measured autocorrelation at $\tau = 0$ s is $\tilde{r}_{T_Z} = 1$ for all methods and this value corresponds to the mean power of the process, or $\tilde{\sigma}^2_{T_Z} = 1$, an observation also clear from *Fig.* 4.27 a).

### 4.5.3 Analysis of the complex Rician process for frequency non-selective channels

The following subsection performs various first and second order statistical analyses of the complex Rician process specifically for frequency non-selective channels and focusses on the results obtained by varying the mobile speed/Doppler spread and/or the ratio of the LOS component and the scattered components, $C_R$ (or the related parameter $\rho$, when $\sigma_0^2 = 1$ is assumed). The typical values of the adjustable parameters used during the experiments are summarised in *Table* 4.2. It should be clear from *Section* 4.5.2 that any of the methods may be used for the generation of the complex Rician process, but it is worthwhile to note that the JM was selected due to its popularity within the research community, which should simplify a comparison with published results.

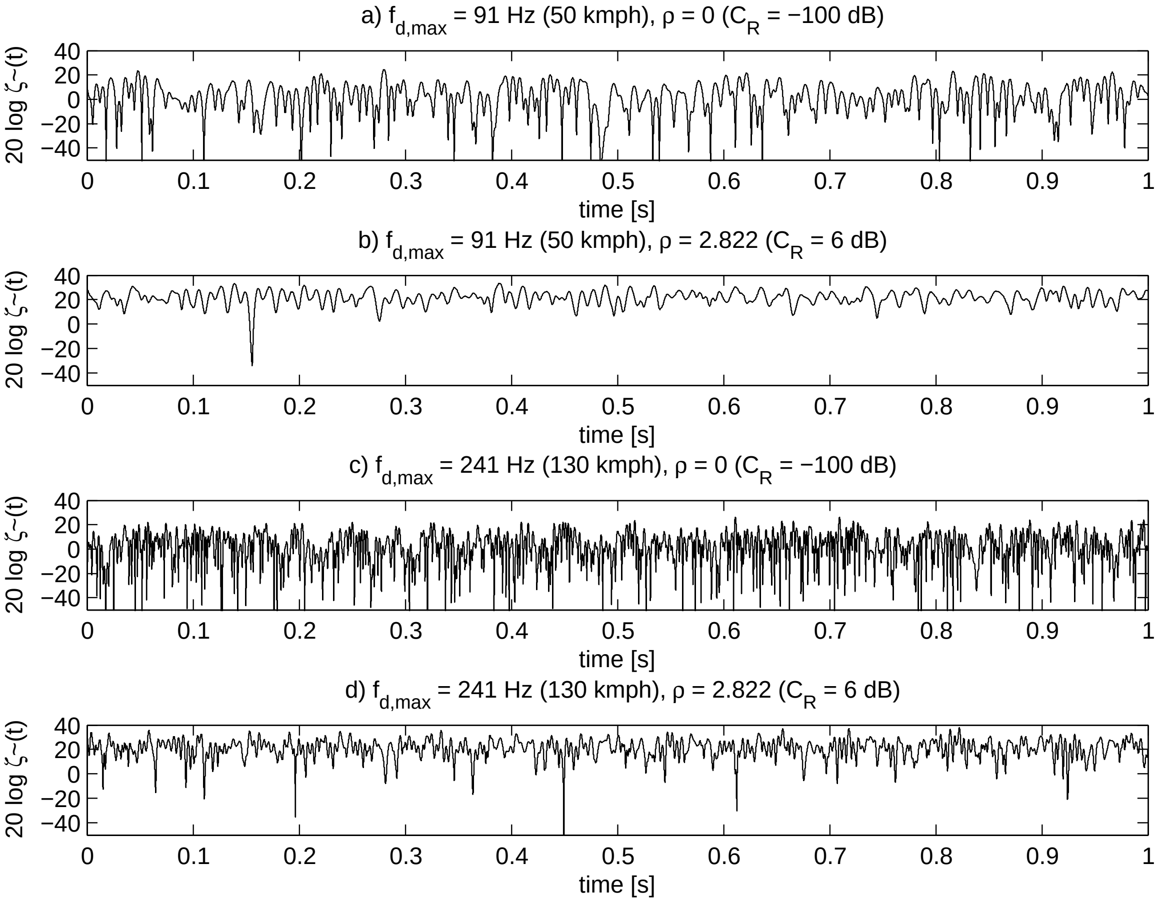

FIGURE 4.26: The measured envelope of the Rician process over 100 frames configured with $\sigma_0^2 = 1$, a) $f_{d,max} = 91$ Hz and $\rho = 0$, b) $f_{d,max} = 91$ Hz and $\rho = 2.822$, c) $f_{d,max} = 241$ Hz and $\rho = 0$, and d) $f_{d,max} = 241$ Hz and $\rho = 2.822$.

*Section* D.4.2 discusses the generation of a complex Rician process from two independent coloured Gaussian processes according to *Eq.* (D.30). The simulation model of *Fig.* D.8 was implemented and the output of the process was measured and used to determine the envelope according to *Eq.* (D.31). The resulting envelope versus time is illustrated in *Fig.* 4.26 for combinations of the minimum/maximum mobile speeds and minimum/maximum LOS component power as investigated in this study. It is observed that heavier shadowing occurs in the event that no LOS component ($C_R \rightarrow -\infty$) exists compared to a large LOS component

($C_R = 6$ dB), resulting in deeper fades. The converse also holds true, with lighter shadowing in the cases of $C_R = 6$ dB. It is also shown that the amount of fades increases, while the fading duration decreases, when the mobile speed, and therefore the Doppler frequency, is increased. These results are further investigated in the following experiments.

The influence of various parameters on the magnitude/phase PDFs (a first order statistic) of the Rician processes were investigated. In all cases it was assumed that the LOS component does not change within a frame period, and $f_\rho = 0$ and $\theta_\rho = 0$ was assumed, resulting in $m(t) = \rho = \sqrt{2\sigma_0^2 \cdot 10^{(C_R/10)}}$. This assumption results in a strict-sense stationary process, as the process becomes independent of time.

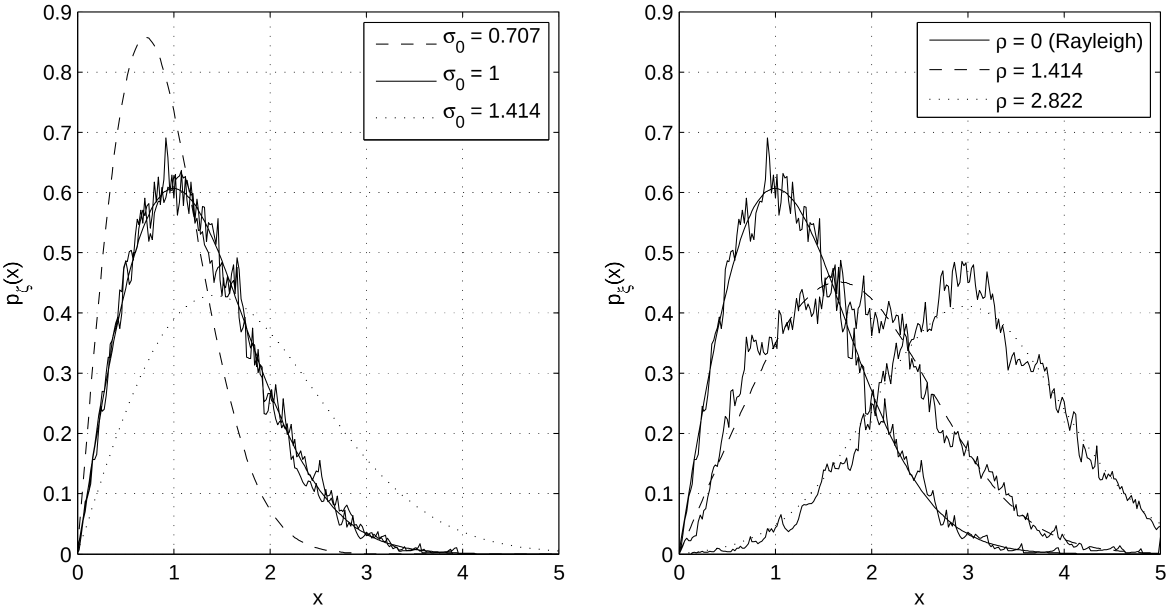

FIGURE 4.27: The PDF of the respective envelopes of a) a Rayleigh process with $\sigma_0^2 = 1$ and b) a Rician process with various $\rho$ levels ($\sigma_0^2 = 1$).

*Fig.* 4.27 a) shows the measured PDF of the magnitude of a Rician process with $\rho = 0$, i.e. a Rayleigh process, with $\sigma_0^2 = 1$. The simulation was performed with $f_{d,max} = 91$ Hz and repeated with $f_{d,max} = 241$ Hz. It is clear that the measured results closely follow the theoretical result presented in *Section* D.3.1, and that the magnitudes of the envelopes are almost identical and independent of the Doppler spread (as expected from *Eq.* (D.15)). The influence of the LOS component, $C_R$, was investigated next and the results are illustrated in *Fig.* 4.27 b) with $\sigma_0^2 = 1$ and $f_{d,max} = 91$ Hz (although the selected value of $f_{d,max}$ clearly has no effect). Again the results closely correspond to the theoretical results and it can be seen that $p_\xi(x) \to p_\zeta(x)$ for $\rho = 0$, and $p_\xi(x)$ tends to a Gaussian distribution as $\rho \approx 2.8$ ($C_R = 6$ dB).

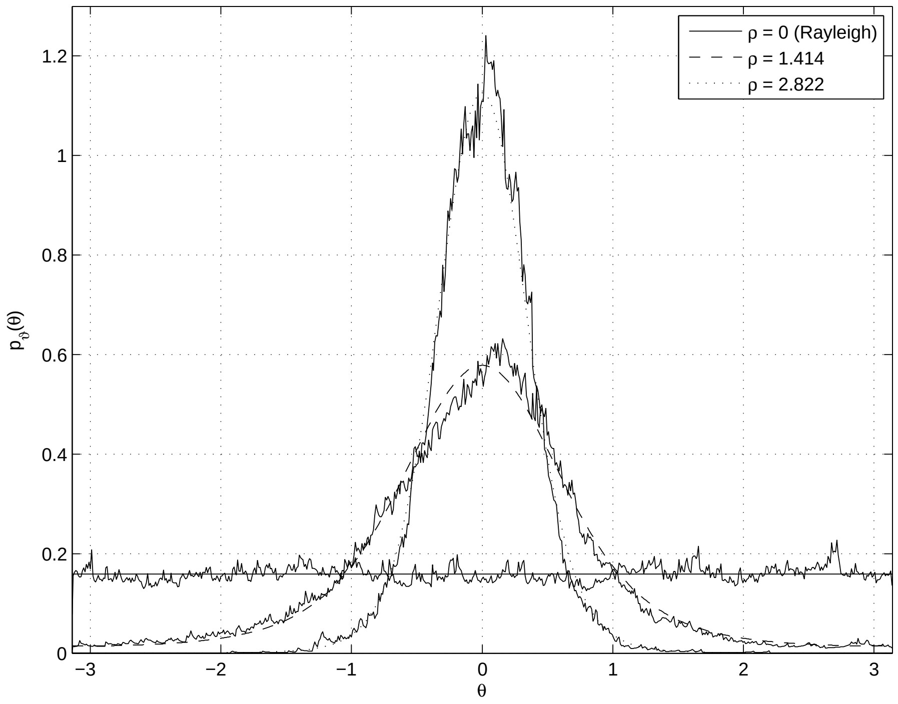

FIGURE 4.28: The PDF of the phase $p_\vartheta(\theta)$ of Rayleigh and Rician processes ($\sigma_0^2 = 1$, $f_\rho = 0$ and $\theta_\rho = 0$).

Similar to the case for the magnitudes above, the PDFs of the phase of the complex Rician processes were analysed. The results are presented in *Fig.* 4.28 as the LOS component is varied from $\rho = 0$ to $\rho = 2.822$. Again the results follow the theoretical values very closely and it is clear that the uniform distribution of $\rho = 0$ changes to a Gaussian distribution that tends to an impulse at $\theta = 0$ as $\rho \to \infty$.

Even though the analysis thus far is sufficient for BER performance measures, some second order statistical properties were investigated as well. Recall from *Fig.* 4.26 that it was observed that the amount of deep fades increased as the Doppler spread increased. The formal measure for this phenomena is the *Level Crossing Rate* (LCR), as discussed in *Section* D.3.2.

The LCR was determined according to *Eq.* (D.21) for the measured results of the magnitude PDF of the Rician process. *Fig.* 4.29 a) illustrates the dependence of the LCR on the mobile speed and Doppler spread. All the results were normalised with the maximum Doppler spread of $f_{d,max} = 241$ Hz, although this is not strictly necessary. It is clear from

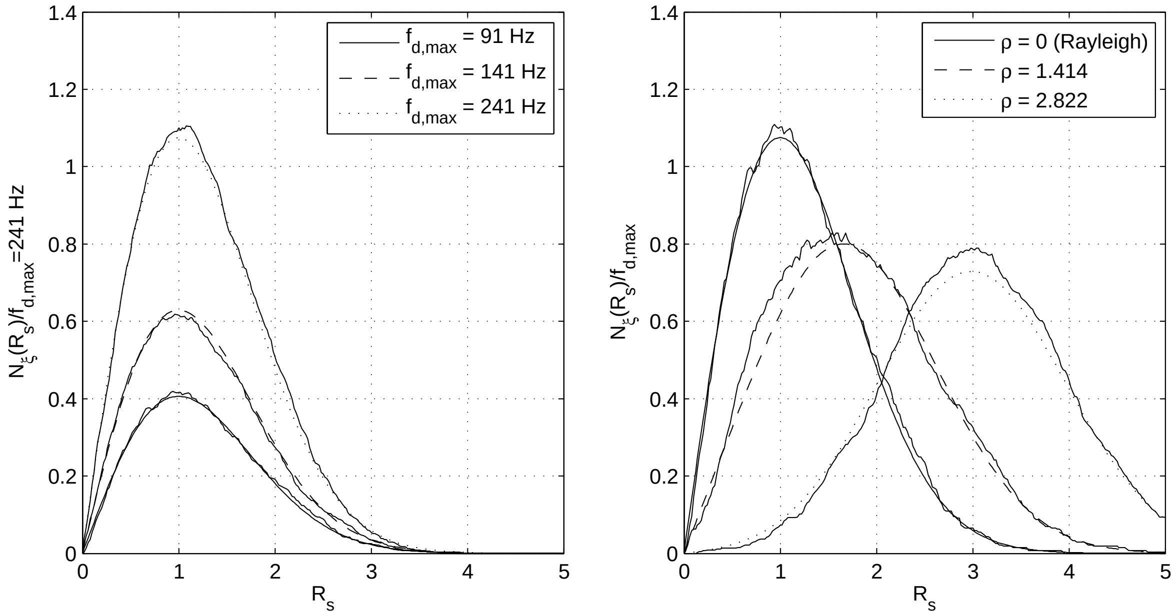

FIGURE 4.29: The measured level crossing rate for a Rician process as a) $f_{d,max}$ is varied and normalised with $f_{d,max} = 241$ Hz ($f_\rho = 0$ and $\theta_\rho = 0$) and b) $\rho$ is varied and normalised with $f_{d,max} = 91$ Hz ($f_{d,max} = 91$ Hz, $f_\rho = 0$ and $\theta_\rho = 0$).

these graphs that the highest LCR is observed for $f_{d,max} = 241$ Hz, but that the dependence for all different $f_{d,max}$ is a straightforward linear one. Recall that the LCR is dependent on $p_\xi(x)$, a parameter independent of $f_{d,max}$, as observed earlier. This means that the LCR is a fixed value scaled with $\sqrt{\beta/2\pi}$, which is linearly dependent on $f_{d,max}$ (refer to *Eq.* (D.20)). This may be better explained with an example: the maximum normalised LCR is observed from *Fig.* 4.29 a) at $R_S = 1$ for $f_{d,max} = 241$ Hz as $N_\xi(1)/241 \approx 1.07$. The corresponding $N_\xi(1)/241$ at $f_{d,max} = 91$ Hz may be calculated as $N_\xi(1)/241 \times 91/241 \approx 0.4$. In other words, this channel will experience level crossings at $R_S = 1$ at a rate of 96.4 crossings per second for an $f_{d,max}$ of 91 Hz, and 257.9 crossings per second if $f_{d,max}$ increases to 241 Hz.

The dependence of the LCR on $p_\xi(x)$ is very clear when examining *Fig.* 4.29 b), a result measured while the dependence of the Doppler spread is removed. It is clear that the results follow those of the magnitude PDF of *Fig.* 4.27 b) very closely, with the only difference being one of scaling, as discussed.

A final experiment was performed to measure the *Average Duration of Fades* (ADF) at a specific level for various LOS scenarios. The relevant measure was presented in *Eq.* (D.23). The measured results were again plotted on the theoretical curves, and follow the expected

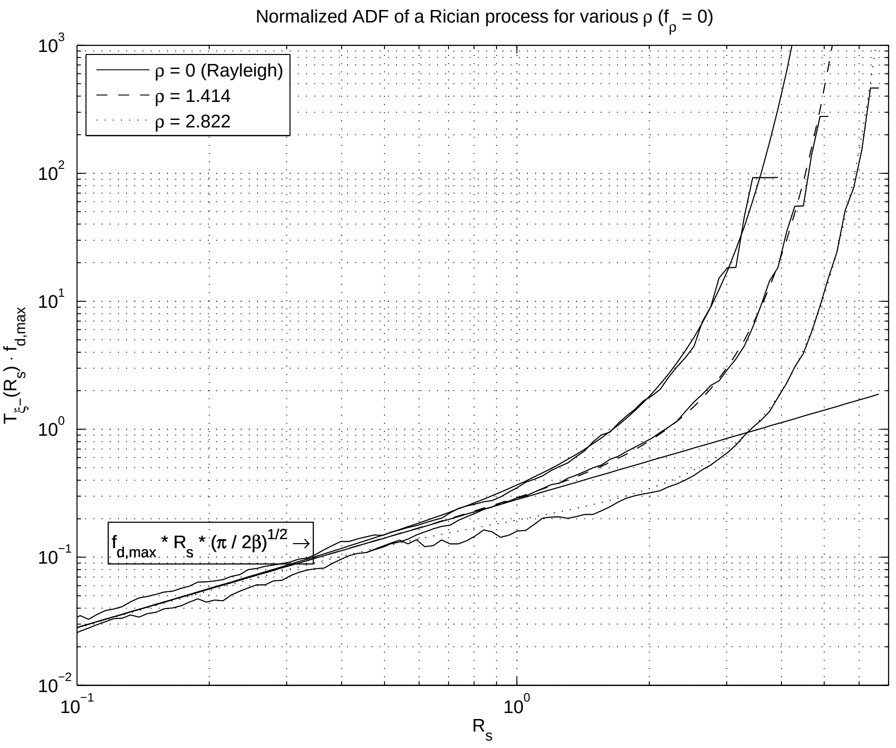

FIGURE 4.30: The measured ADF of a Rician process for various values of $\rho$ ($f_{d,max} = 91$ Hz and $\sigma_0^2 = 1$).

values very closely. Note that the linear approximation of *Eq.* (D.25) holds very well for cases where $\rho R_S/\sigma_0^2 << 1$.

### 4.5.4 Analysis of the complex Rician process for frequency selective channels

The following subsection discusses the various tests performed to quantify the behaviour of the frequency selective channel as described in *Section* D.4.3. Various different channel models were implemented and the different parameters are summarised in *Table* 4.2.

It is of importance to quantify the behaviour of the frequency selective channel to a very narrow pulse, as the channel impulse response gives a very good indication of the amount of received signal power available from each of the multiple paths, as well as necessary timing information required by diversity techniques. During the first test, various different channel models were excited with a narrow pulse in an effort to measure the impulse response of the channel. The results are presented in *Fig.* 4.31. It is clear that the exponential decay profile does not spread the energy evenly between the various multiple paths and that most of the

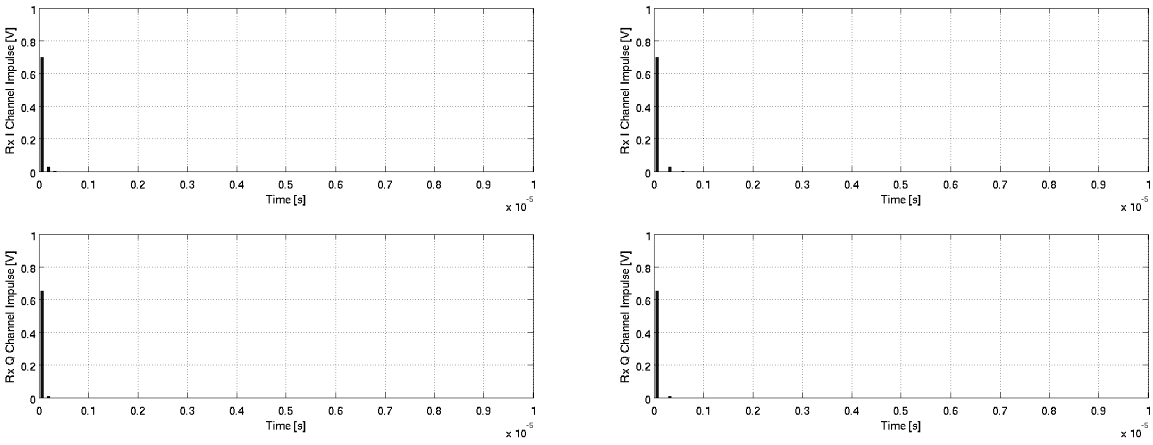

(a) Exponential decaying profile with $L = 3, T_m = 0.2\mu$s

(b) Exponential decaying profile with $L = 3$, $T_m = 0.5\mu$s

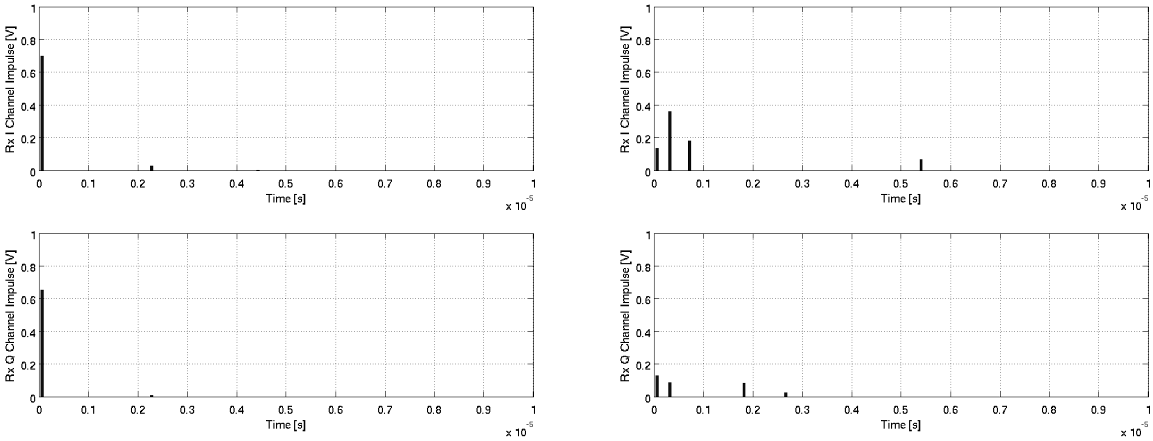

(c) Exponential decaying profile with $L = 3, T_m = 4.3\mu$s

(d) COST (TU) profile with $L = 6, T_m = 5.4\mu$s

FIGURE 4.31: Measured received signal strength when various MPF channels are excited with a narrow pulse.

energy is contained within the first path. It is expected that this profile will not yield very different BER performance graphs compared to a slowly fading Rician channel, and that diversity techniques will provide for very little gain. The proposed *COperation européenne dans le domaine de la recherche Scientifique et Technique* (COST) 207 (TU) model, however, has no significant single path containing most of the energy, but rather significant energy spread over 3 paths. This will severely limit the BER performance, unless receiver diversity techniques are employed.

## 4.6 ANALYSIS OF BER PERFORMANCE OF THE UMTS/WCDMA PLATFORM

### 4.6.1 Analysis of BER performance of a conventional uncoded system

The BER performance graphs for various uncoded system setups are presented next. These graphs aim to convince the reader that the system is well calibrated with reference to known theoretical BER performance curves. Typically, the effect of only a single performance dependent parameter was investigated at a time.

Typical simulation parameters for the platform were provided in *Section* 4.1 (specifically *Table* 4.1 through *Table* 4.3). Although it is possible to configure for narrowband transceivers, the emphasis for the remainder of this study is placed on wideband transmission. Calibration results are presented for AWGN, frequency non-selective and frequency selective single user scenarios, after which these simulations are re-evaluated for multi-user scenarios.

#### 4.6.1.1 BER performance results for AWGN channel conditions

The first test performed was the calibration process required where the noise variance is scaled appropriately to achieve a desired BER performance at a specific signal power. System calibration for the proposed platform posed some difficulty, seeing as a single system with the capability of varying the period of a single bit (dependent on the system parameter, $k$, or by selecting a narrowband configuration) varies the bit power as $E_b = A^2T$. In order to achieve a fair comparison between various different bit power values, the system measures an average bit power using an adjustable number of bits during the averaging operation. This also presents fair results whether unfiltered or filtered transmission is done, since a small amount of bit power will be lost to the filtering process in the vicinity of the transition from the passband to the stopband of the filter, as is the case with the required roll-off of $\alpha = 0.22$. Once the average bit energy is known, the required noise variance is calculated from the desired $E_b/N_0$ using *Eq.* (D.51) and is then generated. The user is referred to *Appendix* D.5 for a detailed discussion on variance scaling. *Fig.* 4.32 shows the simulated BER preformance of an uncoded complex UMTS/WCDMA QPSK-based transceiver system (refer to *Section* 2.3) in AWGN (refer to *Section* D.1), which compares exactly with *Eq.* (3.11) after a relatively small amount of averaging. The results remain consistent, even when the bit power is changed as the system parameter changes from $k = 7$ to $k = 5$, as well as for the case where narrowband transmission is selected.

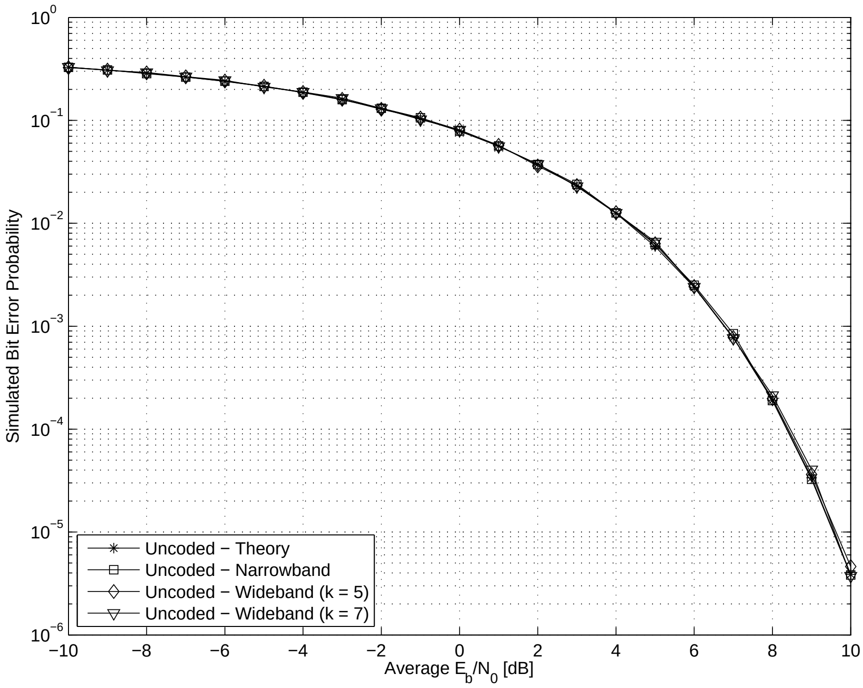

FIGURE 4.32: The measured bit error probability rate of various configurations of the narrowband and wideband UMTS/WCDMA transceiver in AWGN channel conditions (single user case).

#### 4.6.1.2 BER performance results for frequency non-selective channel conditions

The BER performance of various scenarios of slowly fading channels with either Rayleigh or Rician statistics are presented next. *Table* 4.2 lists the various allowed configuration parameters. All simulations are configured to correspond to an uncoded system with only a single user transmitting. *Fig.* 4.33 illustrates the effect that the LOS component has on the BER performance, varying from an almost Rayleigh distribution ($C_R = -100 \approx -\infty$ dB) to a fairly strong LOS component of $C_R = 9$ dB. The platform is further configured to emulate a system with a relative velocity difference of 50 km/h between the mobile and base station units, corresponding to a maximum Doppler frequency of $f_{d,max} = 91$ Hz. Also indicated on the figure are the two theoretical benchmarks for AWGN BER performance as well as slow Rayleigh flat fading conditions, as given by *Eq.* (3.11) and *Eq.* (E.11) respectively. These represent the lower and upper bounds of the uncoded system's possible BER performance. Similarly, *Fig.* 4.34 illustrates equivalent results for the case of a relative velocity difference of 130 km/h between the mobile and base station units, corresponding to a maximum Doppler frequency of $f_{d,max} = 241$ Hz. Considering that no major difference can be observed from these results, it will be assumed that $f_{d,max} = 241$ Hz for the remainder of this study, unless otherwise indicated.

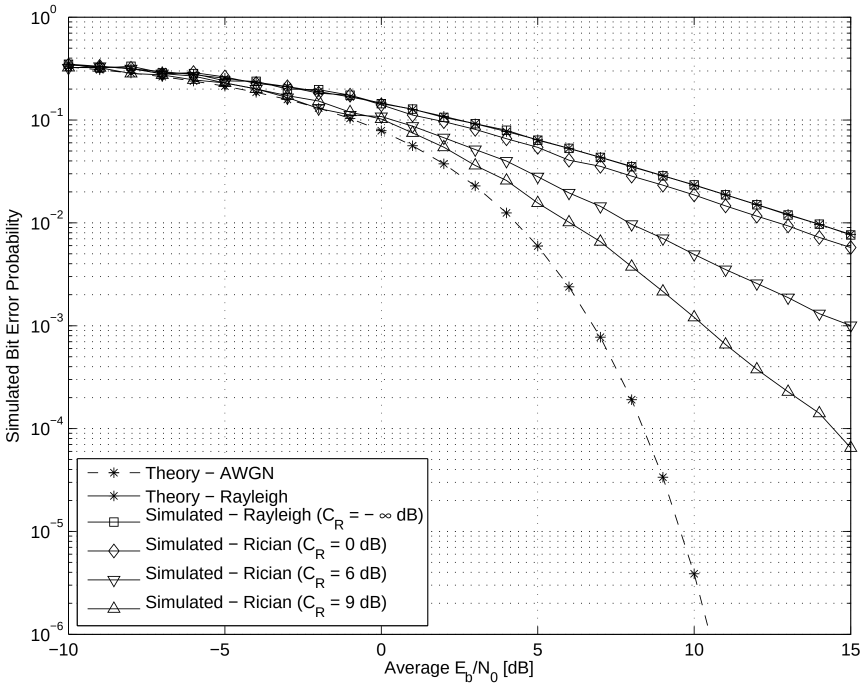

FIGURE 4.33: The measured bit error probability rate of various configurations of the narrowband and wideband UMTS/WCDMA transceiver in a slowly fading channel at a velocity of 50 km/h (single user case).

#### 4.6.1.3 BER performance results for frequency selective channel conditions

The BER performance of various multipath fading channels are presented next. *Table* 4.2 again lists the various allowed configuration parameters. All simulations are configured to correspond to an uncoded system with only a single user employing a Rake receiver structure. *Fig.* 4.35 illustrates the BER performance of the simulation platform when configured for a three path fading channel with an exponential delay profile varying from a delay spread of $T_m = 0.2$ $\mu$s to $T_m = 200$ $\mu$s. Also indicated is the BER performance of a single tap Rake receiver in a more practical reduced six path COST207 for non-hilly terrestrial urban model with delay spread of $T_m = 5.6$ $\mu$s, as well as a 3-tap Rake receiver exploiting most of the available multipath diversity. This, again, indicates the flexibility of the simulation platform in terms of the channel configuration capabilities.

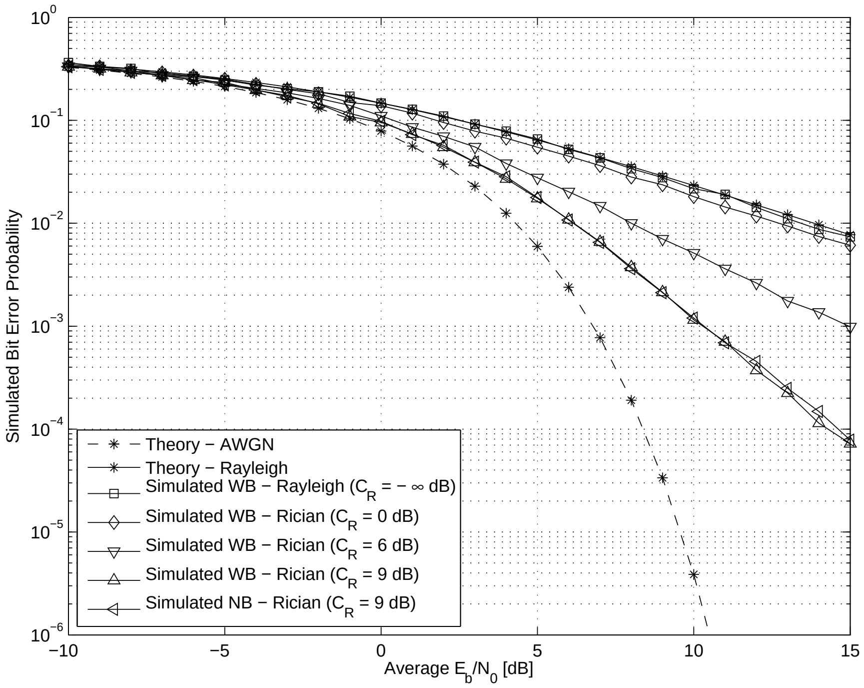

FIGURE 4.34: The measured bit error probability rate of various configurations of the narrowband and wideband UMTS/WCDMA transceiver in a slowly fading channel at a velocity of 130 km/h (single user case).

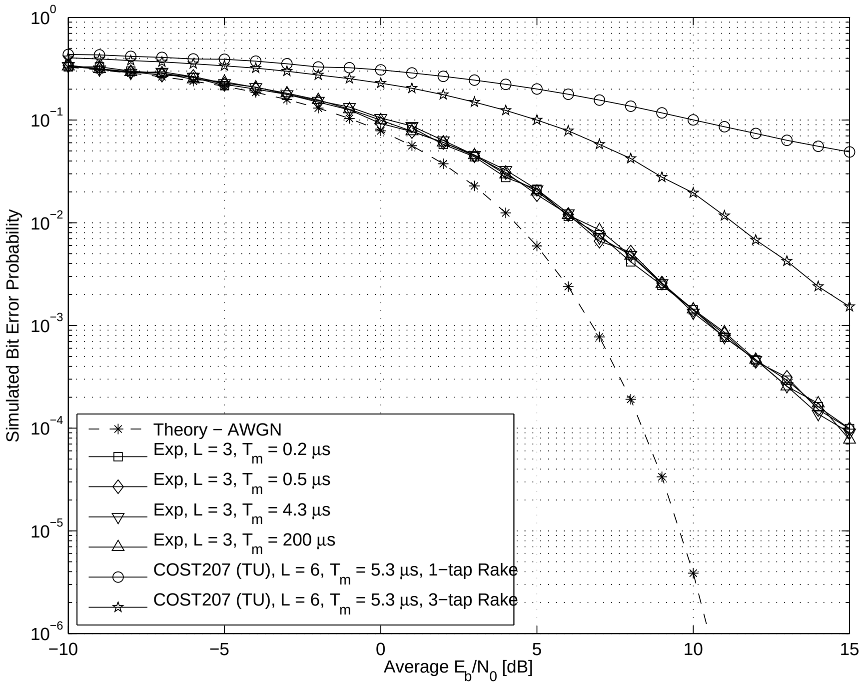

FIGURE 4.35: The measured bit error probability rate of various configurations of the wideband UMTS/WCDMA transceiver in a multipath fading channel at a velocity of 130 km/h (single user case).

#### 4.6.1.4 BER performance results for multi-user conditions

This section presents BER performance results in the presence of multiple user transmission. The simulation setup for this section is very similar to that of *Section* 4.6.1.3 where a complete multipath fading scenario is considered, with the major difference being the addition of controlled MUI. *Fig.* 4.36 through *Fig.* 4.39 illustrates different simulation conditions where the platform was configured with the system parameter equal to $k = 7$, $k = 5$ and $k = 4$ respectively. Single user transmission was considered in all scenarios as a lower bound benchmark, after which additional interfering users were added up to the limit as allowed by the available amount of OVSF codes for each scenario of $k$.

It is interesting to note that these simulations were performed with an interpolation factor of 4, corresponding to 4 samples per chip (similar to the results as presented in *Fig.* 4.18). Also, it was never assumed that the users will transmit with their various frames perfectly aligned as would be the case for a downlink scenario. A random time offset was deliberately assigned for each transmitter ensuring misaligned transmission, specifically to investigate the effect that this has on the BER performance due to the cross-correlation (refer to *Fig.* 4.19) that exist between codes in an OVSF family under these conditions.

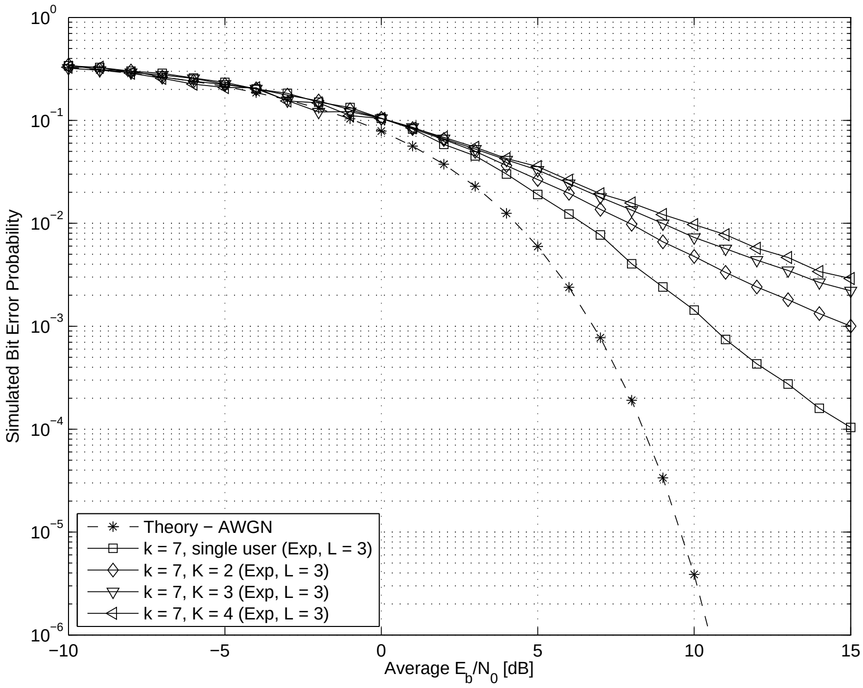

FIGURE 4.36: The measured bit error probability rate of a single user in multi-user conditions with the wideband UMTS/WCDMA transceiver configured for the uplink with $k = 7$ in a multipath fading channel at a velocity of 130 km/h.

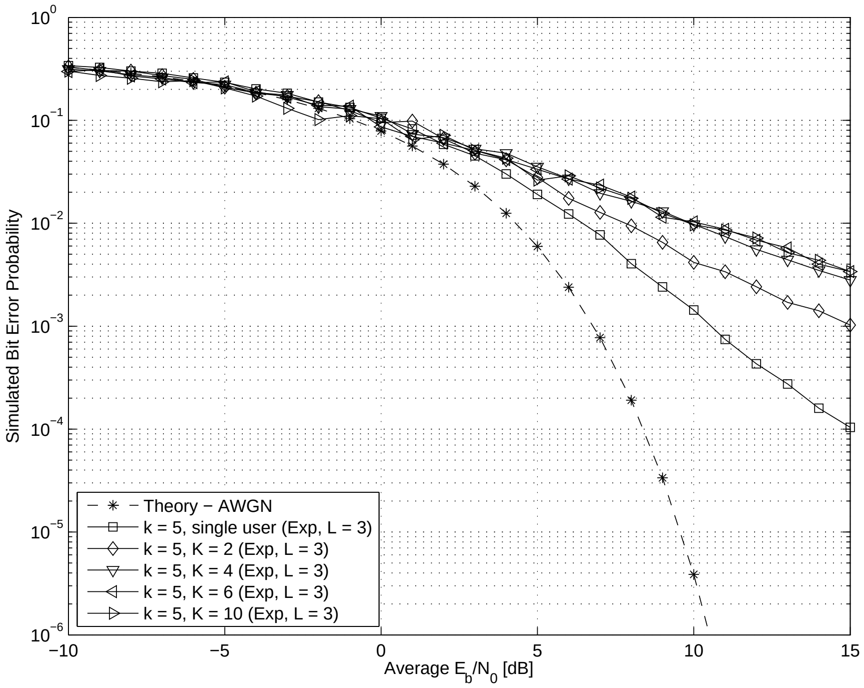

FIGURE 4.37: The measured bit error probability rate of a single user in multi-user conditions with the wideband UMTS/WCDMA transceiver configured for the uplink with $k = 5$ in a multipath fading channel at a velocity of 130 km/h.

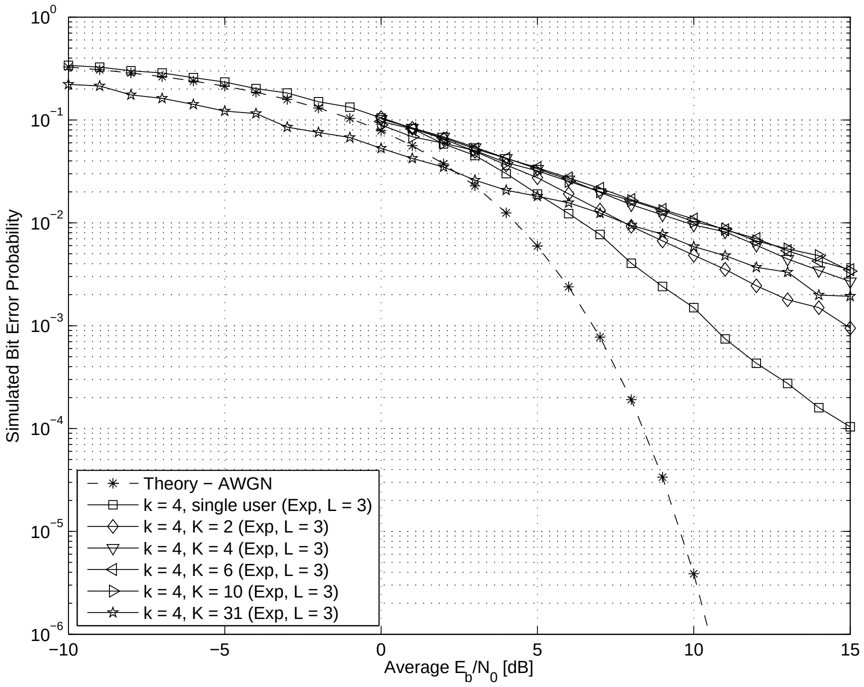

FIGURE 4.38: The measured bit error probability rate of a single user in multi-user conditions with the wideband UMTS/WCDMA transceiver configured for the uplink with $k = 4$ in a multipath fading channel at a velocity of 130 km/h.

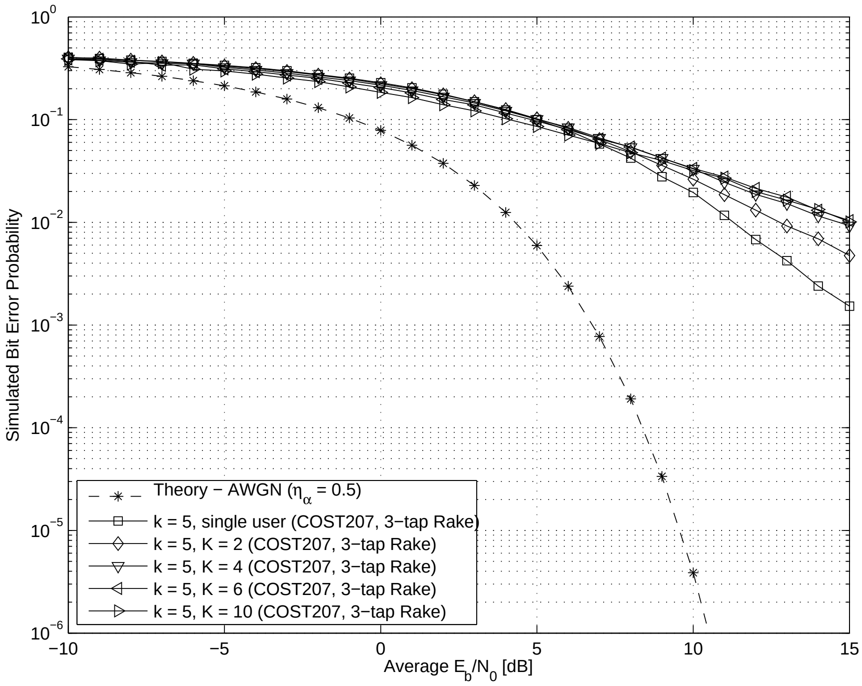

FIGURE 4.39: The measured bit error probability rate of a single user in multi-user conditions with the wideband UMTS/WCDMA transceiver configured for the uplink with $k = 5$ in a COST207 multipath fading channel at a velocity of 130 km/h.

#### 4.6.1.5 Discussion of results for conventional receiver structures

A number of important observations can be made based on the results presented in *Section* 4.6.1.1 through *Section* 4.6.1.4 for the narrowband and wideband uncoded communication systems under the various channel conditions.

1. Observations based on the simulation results for AWGN channel conditions:

    - The simulation results as illustrated in *Fig.* 4.32 closely follow the theoretical result of *Eq.* (3.11). It is clear that the deviation is insignificant. This may be attributed to the fact that each transmitted frame is used to exactly measure the bit power, from which the noise variance may be derived. This allows for perfect $E_b/N_0$ calibration, even in scenarios where narrowband and wideband streams are filtered and when various spreading factors may be transmitted over the same link, as for the proposed UMTS/WCDMA platform.

2. Observations based on the simulation results for frequency non-selective channel conditions:

  - The simulation results as illustrated in *Fig.* 4.33 closely follow the theoretical result of *Eq.* (E.11), which also holds true for the results presented in *Fig.* 4.34. It is, therefore, clear that even at a relative velocity of 130 km/h between the mobile unit and the base station no significant deviation exists between the simulated and theoretical results. This is explained by noting that even at the largest simulated Doppler spread of $f_{d,max} = 241$ Hz, the assumption that the fading amplitude is essentially flat over an entire chip period holds. This is true considering that the coherence time is approximately $T_{coh} = 9/(16\pi \times 241) = 742.9$ $\mu$s for a classic Doppler spread where the arrival azimuthal angle of the propagation paths have a normal distribution. The value is larger than the burst time of $625$ $\mu$s associated with the UTRA/WCDMA platform.
  - Only a very small difference is observed between *Fig.* 4.33 and *Fig.* 4.34 for the cases corresponding to a Doppler spread of $91$ Hz and $241$ Hz. This is attributed to the fact that in both cases the coherence time is significantly larger than the burst time of $625$ $\mu$s associated with the UTRA/WCDMA platform.

3. Observations based on the simulation results for frequency selective channel conditions as presented in *Fig.* 4.35:

  - It is clear that the single tap Rake receiver and the three-tap Rake receiver provide very similar results when the exponential delay profile is considered. This is explained by considering the power profile of the delayed taps as presented in *Table* 4.2. Notice that the second and third components correspond to a very small contribution of the transmitted power. If 1 W is transmitted, the received energy corresponding to the first path would be 0.9684 W, while the second and third paths would contribute 0.0306 W and 0.00096841 W respectively, indicating that these paths do not greatly influence the results. A tentative gain of only $10\ \log_{10}(1/0.9684) = 0.139$ dB may be expected by employing a diversity technique.
  - It is clear that the BER performance of specifically the exponential delay profile is not strongly dependent on the various delay spreads that were simulated. This is again contributed to the specific power distribution of the profile, as the second and third paths cause very little intersymbol interference when their power is compared to that of the first path.

- A single tap Rake receiver achieves very poor BER performance for COST207-TU channel conditions. This is due to the fact that only the -3 dB path is resolved, while many additional paths exist that carry significant portions of the transmitted power.
- The three-tap Rake receiver outperforms the receiver structure that does not employ diversity techniques as expected, especially for the case where the COST207-TU multipath fading channel model is employed.
- It is clear that the BER performance is worse in the more realistic COST207-TU channel than with the exponential decay profile.

4. Observations based on the simulation results for multipath fading channel conditions in the presence of MUI:

    - In the case of the highest allowed system parameter, $k = 7$, only four unique spreading codes are defined. *Fig.* 4.36 illustrates single user transmission as a reference, as well as the sequential incrementation of interfering users transmitting in the same band. It is clear that the BER performance decreases with each additional user.
    - A reduction of the system parameter, $k$, increases the number of available codes to choose from and, along with that, the number of users that may access the system. *Fig.* 4.37 illustrates the BER performance for the case of $k = 5$, where sixteen unique codes are available. It is again clear that the BER performance dramatically decreases by the addition of the first few users. It is interesting to note that the BER performance saturates quickly at the worst case scenario, and any amount of interferes in the range of four to ten has very little influence on further BER performance degredation.
    - Similar observations can be made for the results presented in *Fig.* 4.38. Decreasing the system parameter to $k = 4$ again doubles the amount of allowed users. Shown in the results is a case where 31 of the possible 32 codes were used. It is interesting to note that the BER performance actually increased. This may be attributed to the fact that such a large amount of additive interferes tend to a normal distribution according to the central limit theorem, or that perhaps the all ones codeword has a DC contribution to the mean value.

- BER performance of the system is worse when the COST207-TU channel model is employed when compared to the simpler exponential decay profile. This is to be expected, as the channel has more multiple paths that are not all resolved within the Rake receiver structure.

### 4.6.2 Analysis of BER performance of a novel uncoded system utilising the sparseness measure

*Section* 4.6.1 presented various BER performance measures for traditional receiver systems without the capability of utilising the potential gains provided by knowledge of the sparseness of a datastream. This section aims to present a novel, comparative study detailing the effect of sparseness on the scenarios presented earlier, again for both single and multi-user transmission in various channel conditions.

#### 4.6.2.1 BER performance results for AWGN channel conditions

The proposed receiver was tested in the same calibrated AWGN channel conditions that were used for the traditional receiver structure, as discussed in *Section* 4.6.1.1. The sparseness of the datastream was calibrated in the range $\eta_\alpha = [0.1, 0.5]$ in increments of $0.1$. Only a single user uncoded scenario with a system parameter of $k = 7$ was considered. *Fig.* 4.40 shows the simulated BER performance of an uncoded complex UMTS/WCDMA QPSK-based transceiver system in AWGN (refer to *Section* 3.3.2.1), which compares exactly with the theoretical results as derived and given by *Eq.* (3.29) and plotted in *Fig.* 3.7.

#### 4.6.2.2 BER performance results for frequency non-selective channel conditions

The experimental setup as discussed in *Section* 4.6.1.2 was again used to obtain the results presented in this section. The main difference, as to be expected, was that the sparseness level of the bitstream was varied over the range $\eta_\alpha = [0.1, 0.5]$ in increments of $0.1$. Simulation results are presented in *Fig.* 4.41 through *Fig.* 4.43 for various values of $C_R$. Also indicated on the figures are the two theoretical benchmarks for AWGN BER performance as well as slow Rayleigh flat fading conditions. However, it is suggested that *Eq.* (3.29) with $\eta_\alpha = 0.1$ represents the lower bound, while *Eq.* (E.11) is still used to represent the upper bound of the uncoded system's possible BER performance.

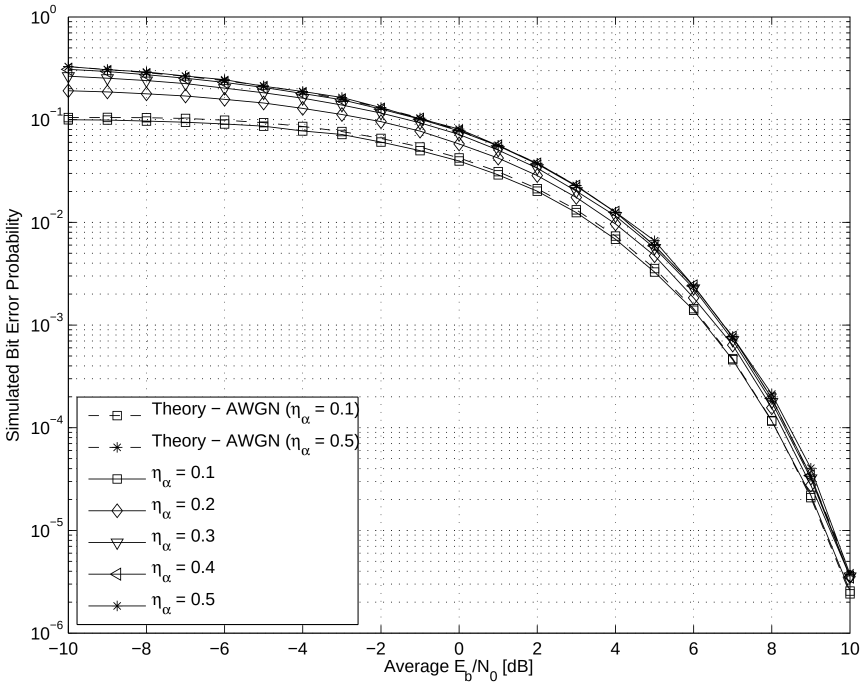

FIGURE 4.40: The measured bit error probability rate of the wideband UMTS/WCDMA transceiver in AWGN channel conditions (single user case) for various sparseness configurations.

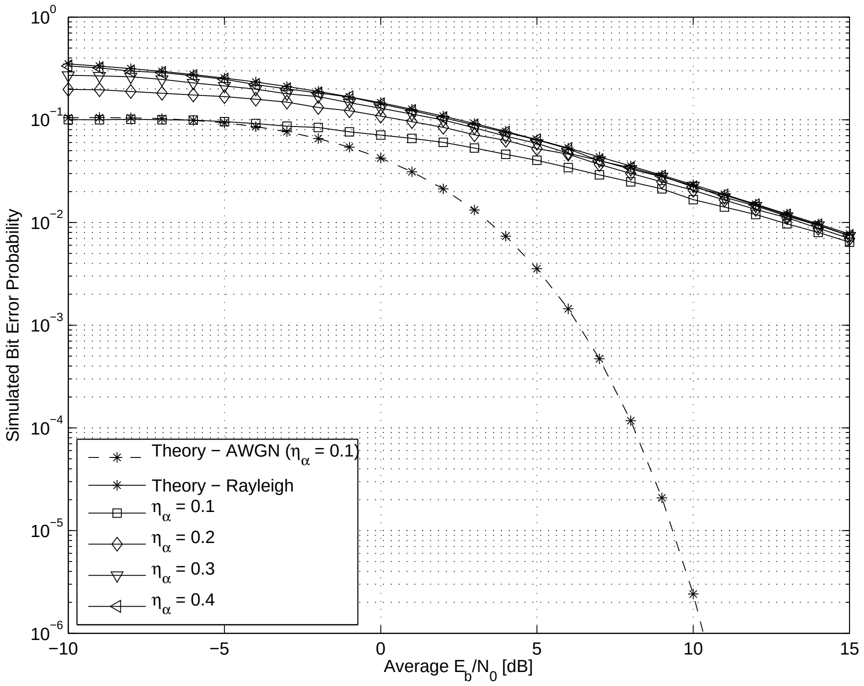

FIGURE 4.41: The measured bit error probability rate of various sparseness levels of the narrowband and wideband UMTS/WCDMA transceiver in a slowly Rayleigh fading channel at a velocity of 130 km/h with $C_R = -\infty$ dB (single user case).

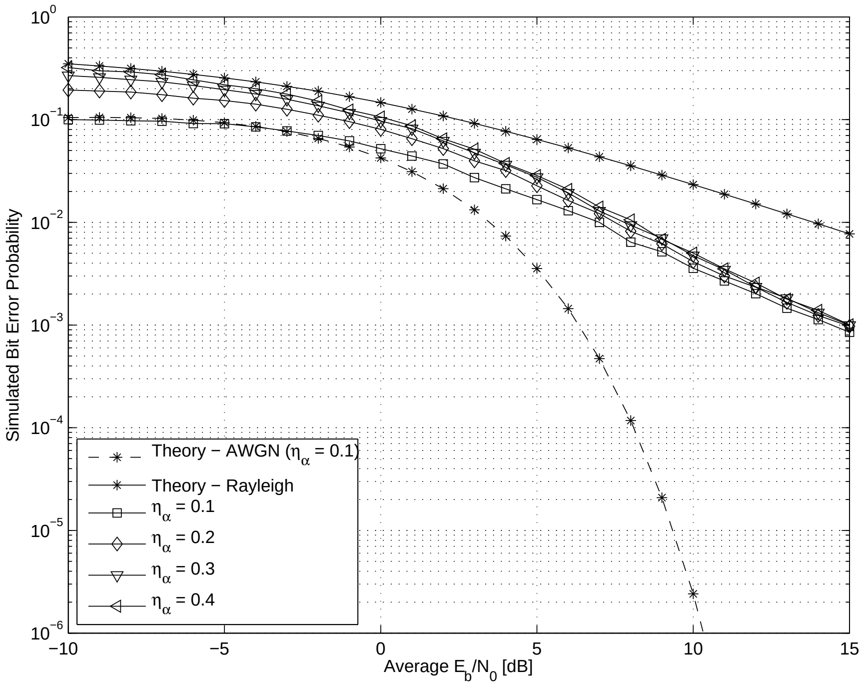

FIGURE 4.42: The measured bit error probability rate of various sparseness levels of the narrowband and wideband UMTS/WCDMA transceiver in a slowly fading Rician channel at a velocity of 130 km/h with $C_R = 6$ dB (single user case).

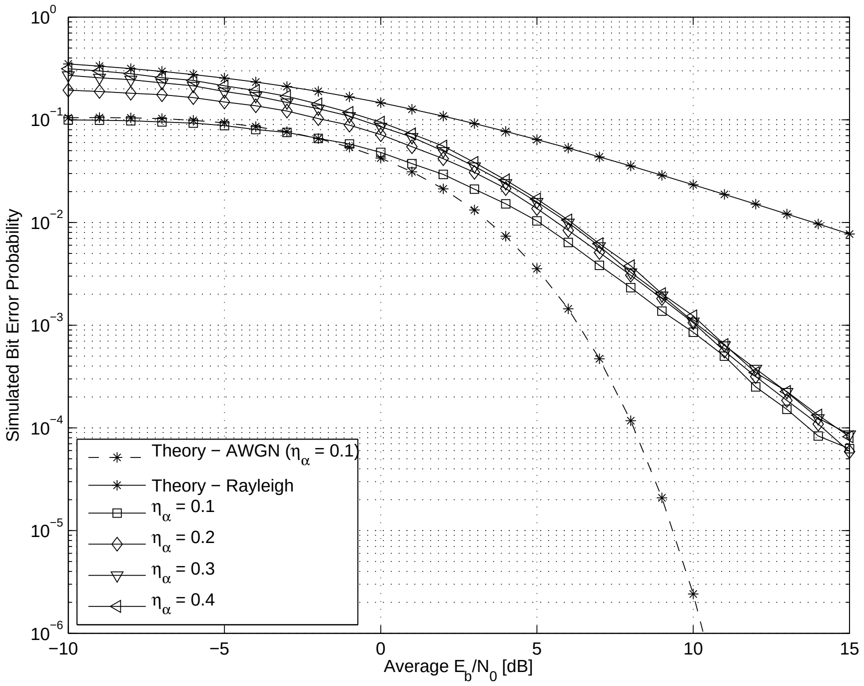

FIGURE 4.43: The measured bit error probability rate of various sparseness levels of the narrowband and wideband UMTS/WCDMA transceiver in a slowly fading Rician channel at a velocity of 130 km/h with $C_R = 9$ dB (single user case).

#### 4.6.2.3 BER performance results for frequency selective channel conditions

The simulation setup presented in *Section* 4.6.1.3 was repeated here while the sparseness level was varied over $\eta_\alpha = \{0.1, 0.3, 0.5\}$. The simulated results of an exponential decaying profile were found, but these are very similar to the results presented in *Fig.* 4.43 and will therefore not be repeated here. The similarity is due to the fact that very little additional energy is transmitted in the second and third paths, leaving very little multipath diversity for the Rake receiver to resolve.

System performance was further investigated by means of a more practical COST207-TU channel configuration that offers a much clearer indication of the receiver's capabilities. Simulation results are presented in *Fig.* 4.44 for a receiver when configured with no diversity, while *Fig.* 4.45 presents simulation results with a three-tap Rake receiver. Note that the results are valid even though the system parameter is not consistent, as this does not influence the results for single user transmission with the implemented calibration scheme.

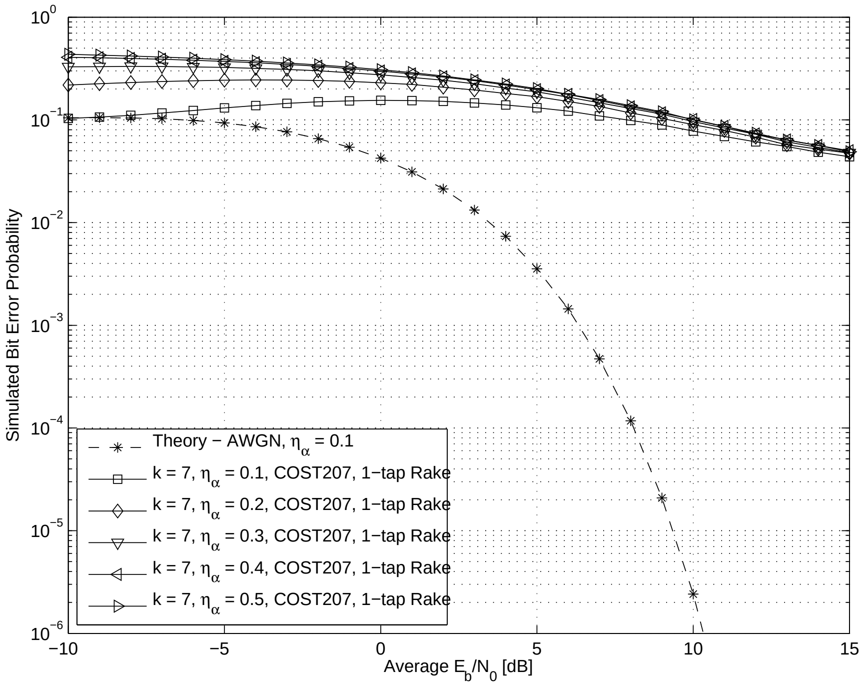

FIGURE 4.44: The measured bit error probability rate of the wideband UMTS/WCDMA transceiver with no diversity in a COST207-TU multipath fading channel at a velocity of 130 km/h (single user case) for various levels of sparseness.

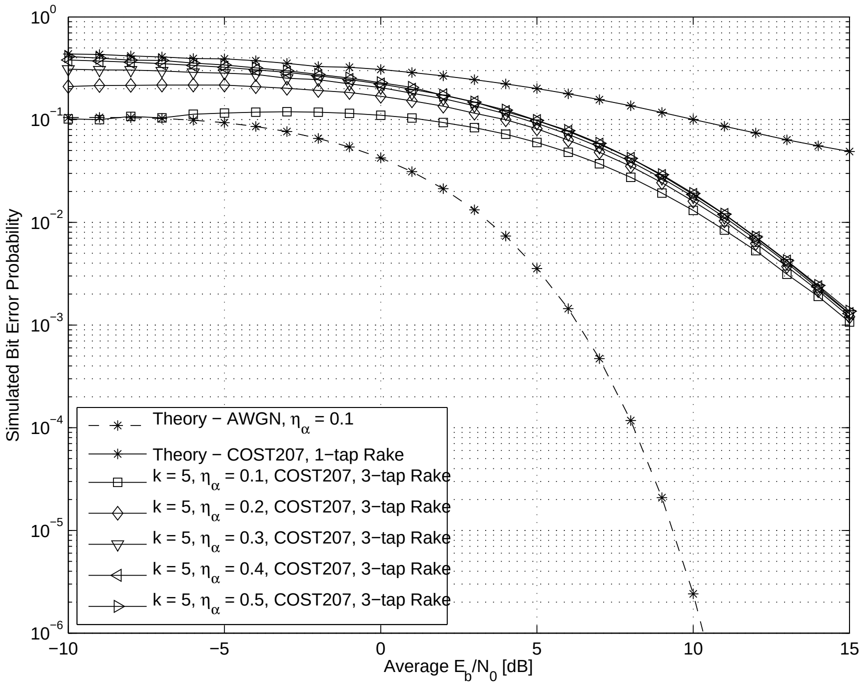

FIGURE 4.45: The measured bit error probability rate of the wideband 3-tap Rake UMTS/WCDMA transceiver in a COST207-TU multipath fading channel at a velocity of 130 km/h (single user case) for various levels of sparseness.

#### 4.6.2.4 BER performance results for multi-user conditions

This section presents BER performance results achieved by a single user in the presence of multiple user transmissions. The system suffers from complete multipath fading, with different fading profiles investigated separately. The setup is similar to that of *Section* 4.6.1.4, with the major exception again that the sparseness level is adjusted between $\eta_\alpha = \{0.1, 0.3, 0.5\}$. *Fig.* 4.46 through *Fig.* 4.49 illustrate different simulation results where the platform was configured with the system parameter equal to $k = 7$ and $k = 5$ for different sparseness levels. Single user transmission was considered in all scenarios as a lower bound benchmark, after which additional interfering users were added up to the limit as allowed by the available amount of OVSF codes for each scenario of $k$. Each user experienced unique multipath fading with the channel emulator configured with an exponential decay profile.

*Fig.* 4.50 and *Fig.* 4.51 once again show the BER performance simulation results of a multi-user communication system similar to the one described above, with the simulation platform configured for COST207-TU channel conditions. Only the three-tap Rake receiver structure was considered due to its obvious improved BER performance.

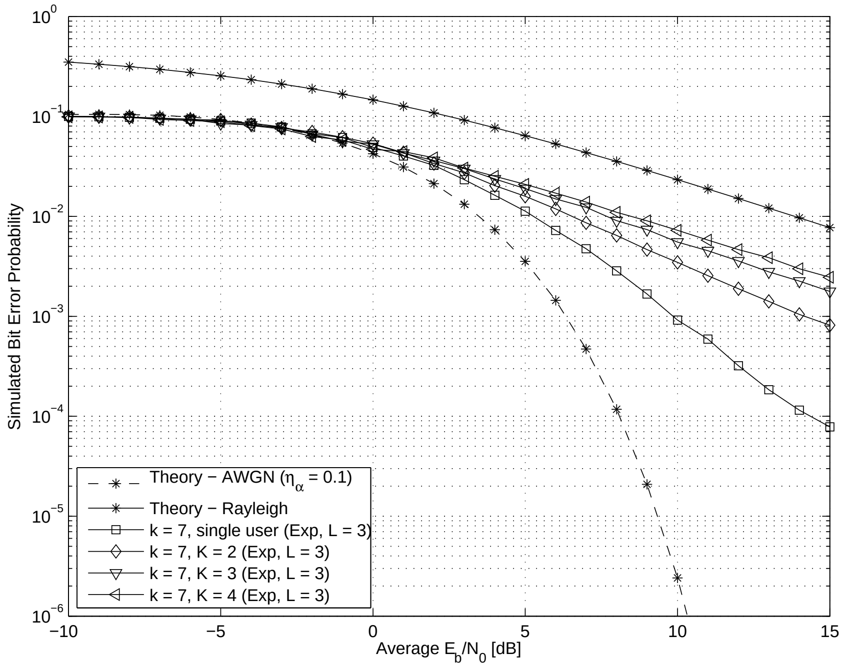

FIGURE 4.46: The measured bit error probability rate of a single user transmitting at $\eta_\alpha = 0.1$ in multi-user conditions with the wideband UMTS/WCDMA transceiver configured for the uplink with $k = 7$ in a multipath fading channel (exponential profile) at a velocity of 130 km/h and $C_R = 9$ dB.

#### 4.6.2.5 Discussion of results for the proposed receiver structure

The final section of this chapter is dedicated to a number of interesting observations that can be made based on the novel results presented in *Section* 4.6.2.1 through *Section* 4.6.2.4 for the narrowband and wideband uncoded communication systems under the various channel conditions.

1. Observations based on the simulation results for AWGN channel conditions as illustrated in *Fig.* 4.40:

    - The dense datastream, for the case where $\eta_\alpha = 0.5$, compares exactly with results presented earlier in *Fig.* 4.32. This shows that the proposed receiver provides equivalent results to a traditional receiver when a datastream is truly equiprobable. It is clear that the proposed receiver will not perform poorer than the benchmark performance as set by traditional receiver structures.

    - The proposed receiver adapts to knowledge of the sparseness of datastreams and increases BER performance in all scenarios when compared to results obtained from traditional receiver structures.

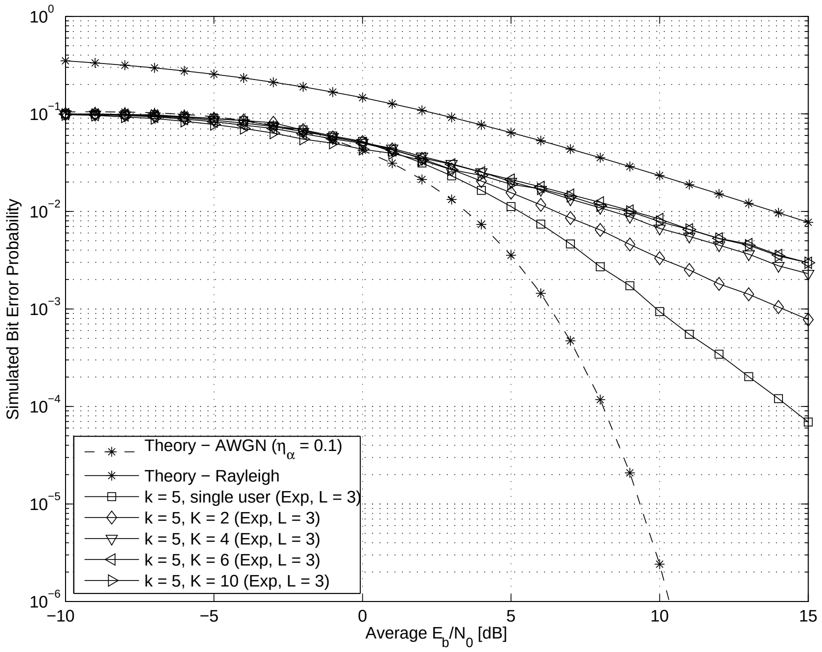

FIGURE 4.47: The measured bit error probability rate of a single user transmitting at $\eta_\alpha = 0.1$ in multi-user conditions with the wideband UMTS/WCDMA transceiver configured for the uplink with $k = 5$ in a multipath fading channel (exponential profile) at a velocity of 130 km/h and $C_R = 9$ dB.

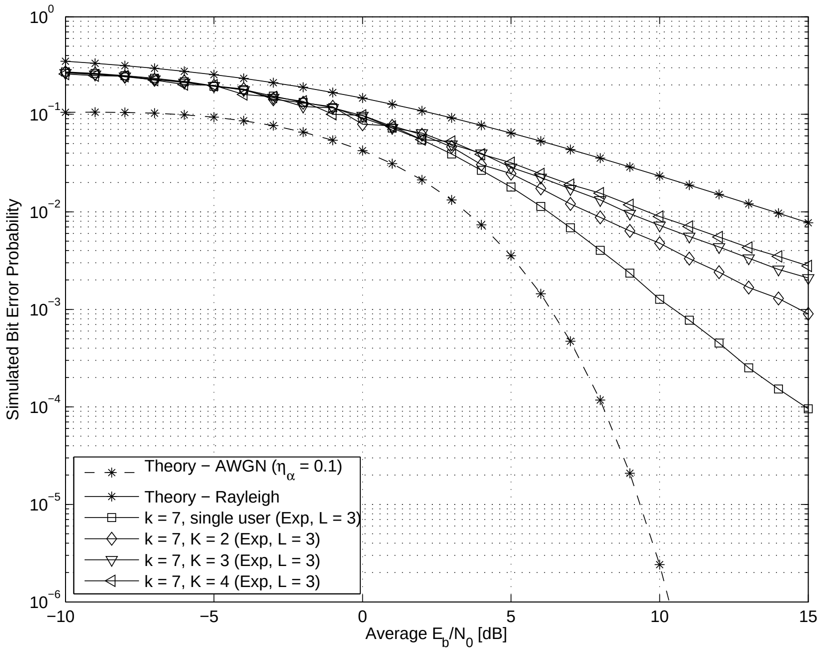

FIGURE 4.48: The measured bit error probability rate of a single user transmitting at $\eta_\alpha = 0.3$ in multi-user conditions with the wideband UMTS/WCDMA transceiver configured for the uplink with $k = 7$ in a multipath fading channel (exponential profile) at a velocity of 130 km/h and $C_R = 9$ dB.

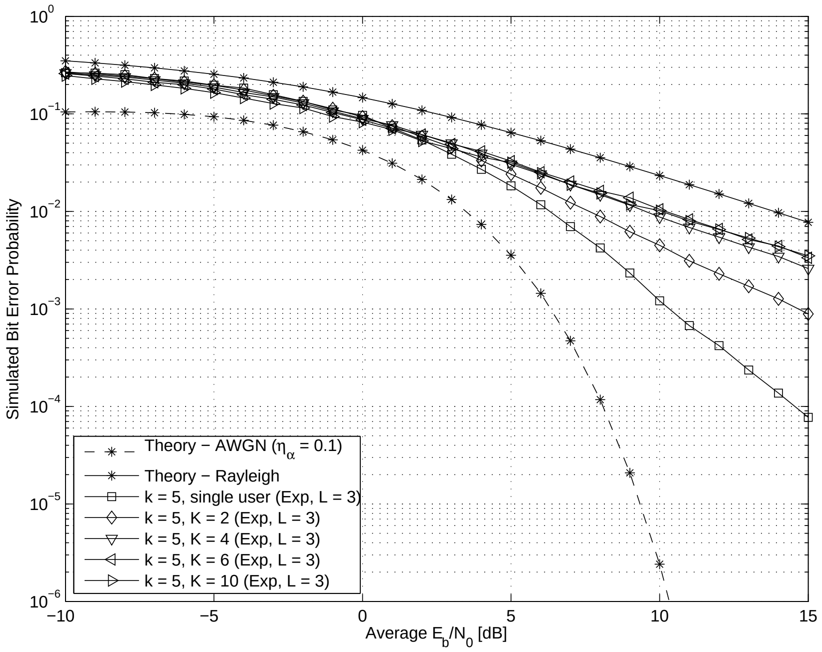

FIGURE 4.49: The measured bit error probability rate of a single user transmitting at $\eta_\alpha = 0.3$ in multi-user conditions with the wideband UMTS/WCDMA transceiver configured for the uplink with $k = 5$ in a multipath fading channel (exponential profile) at a velocity of 130 km/h and $C_R = 9$ dB.

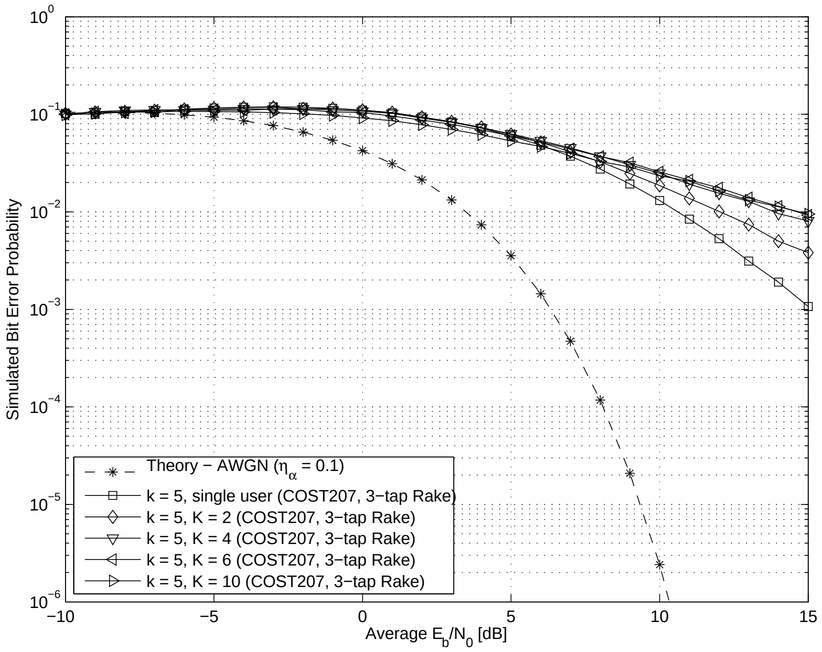

FIGURE 4.50: The measured bit error probability rate of a single user transmitting at $\eta_\alpha = 0.1$ in multi-user conditions with the wideband UMTS/WCDMA transceiver configured for the uplink with $k = 5$ in a multipath fading channel (COST207) at a velocity of 130 km/h and $C_R = 9$ dB.

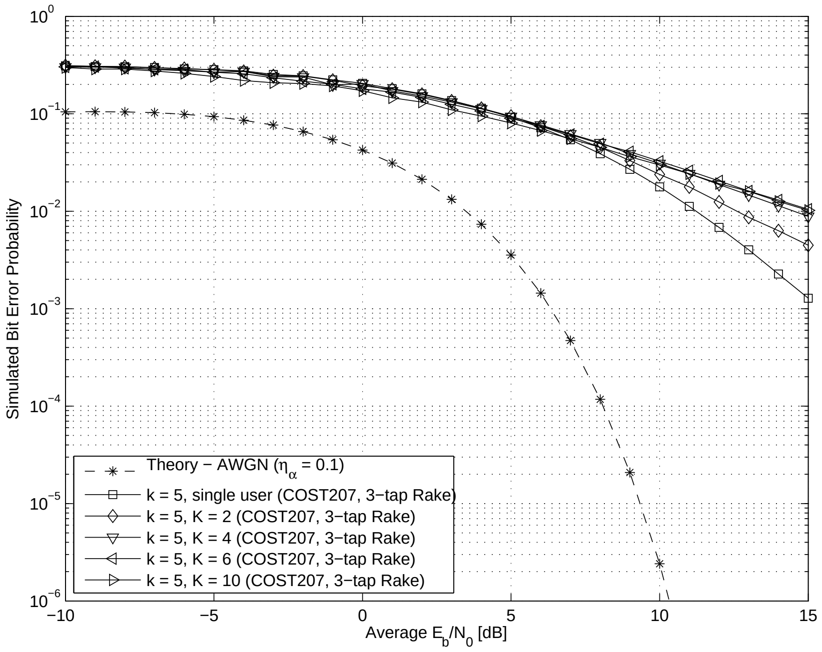

FIGURE 4.51: The measured bit error probability rate of a single user transmitting at $\eta_\alpha = 0.3$ in multi-user conditions with the wideband UMTS/WCDMA transceiver configured for the uplink with $k = 5$ in a multipath fading channel (COST207) at a velocity of 130 km/h and $C_R = 9$ dB.

- The level of improvement depends both on the sparseness level and $E_b/N_0$. This is clear from the illustrated results, but the attentive reader may have noticed this from the highlighted terms in *Eq.* (3.29). Notice that the improvement in BER performance is drastic for very low $E_b/N_0$ values, especially for cases that coincide with low sparseness levels as well, but is much less noticeable for high $E_b/N_0$ values.
- The BER curve indicates that the probability of erroneous transmission tends towards the value of the sparseness of the bitstream (rather than 0.5), that is $P_e \rightarrow \eta_\alpha$ when $E_b/N_0$ becomes small (or strongly negative when measured in dB). This suggests that a new lower bound exists that can be achieved by systems employing the measure of sparseness in conditions where the sparseness level of a datastream deviates from $\eta_\alpha = 0.5$.

2. Observations based on the simulation results for frequency non-selective channel conditions:

   - Earlier observations presented in *Section* 4.6.1.5 still holds for all the considered scenarios with $\eta_\alpha = 0.5$.

- The simulation results as illustrated in *Fig.* 4.41 follow the theoretical result of *Eq.* (3.48) at lower $E_b/N_0$ values. The fairly large deviation at higher $E_b/N_0$ values may be attributed to the fact that the analytical expression is a crude, low order approximation of the integral presented in *Eq.* (3.33). A more accurate numeric solution of *Eq.* (3.33) indicates that the simulation results follow the theoretical results of *Fig.* 3.12 quite closely.
- It is again observed that the BER improvement depends both on the sparseness level and $E_b/N_0$. The improvement in BER performance is drastic for very low $E_b/N_0$ values, especially for cases that coincide with low sparseness levels as well, but is much less noticeable for high $E_b/N_0$ values.
- It is again observed that $P_e \rightarrow \eta_\alpha$ when $E_b/N_0$ becomes small (or strongly negative when measured in dB), suggesting that a new lower bound exists that may be exploited by systems employing the measure of sparseness in conditions where the sparseness level of a datastream deviates from $\eta_\alpha = 0.5$.

3. Observations based on the simulation results for frequency selective channel conditions as presented in *Fig.* 4.35:

    - Earlier observations presented in *Section* 4.6.1.5 still holds for all the considered scenarios with $\eta_\alpha = 0.5$.
    - Similar to previous observations it is again apparent that the BER improvement depends both on the sparseness level and $E_b/N_0$. The improvement in BER performance is drastic for very low $E_b/N_0$ values, especially for cases that coincide with low sparseness levels as well, but is much less noticable for high $E_b/N_0$ values.
    - Similar to previous observations it is again apparent that $P_e \rightarrow \eta_\alpha$ when $E_b/N_0$ becomes small (or strongly negative when measured in dB), suggesting that a new lower bound exists that may be exploited by systems employing the measure of sparseness in conditions where the sparseness level of a datastream deviates from $\eta_\alpha = 0.5$.
    - It is clear that BER performance is better for an exponential decaying power profile simulation setup than for a more practical COST207-TU channel test

platform when all other parameters are equivalent. This is expected, as the power content is distributed over six paths of which only three paths are resolved.

4. Observations based on the simulation results for multipath fading channel conditions in the presence of MUI:

   - Earlier observations presented in *Section* 4.6.1.5 still holds for all the considered scenarios if the datastream is configured with $\eta_\alpha = 0.5$.
   - It is again observed that $P_e \rightarrow \eta_\alpha$ when $E_b/N_0$ becomes small (or strongly negative when measured in dB), suggesting that a new lower bound exists that may be exploited by systems employing the measure of sparseness in conditions where the sparseness level of a datastream deviates from $\eta_\alpha = 0.5$.
   - It is again observed that the BER improvement depends both on the sparseness level and $E_b/N_0$. The improvement in BER performance is drastic for very low $E_b/N_0$ values, especially for cases that coincide with low sparseness levels as well, but is much less noticeable for high $E_b/N_0$ values.

# CHAPTER FIVE

# CONCLUSIONS AND FUTURE RESEARCH

This chapter provides a summary of the major conclusions that may be drawn from the body of work completed during this study. Even though the emphasis will be on conclusions from the novel parts of the work, some conclusions are made that may already be known to the relevant research communities. Following the conclusions, some topics that were not addressed during this study are suggested for future research.

## 5.1 CONCLUSION

The most important and summarising conclusion to be drawn from this study regards the superiority of the proposed improved receiver structures when dealing with possibly sparse datastreams. It is clear from the BER performance graphs of the various scenarios investigated that all the communication system setups considered, when transmitting possibly sparse data, will benefit from utilising one of the proposed improved receiver structures. The gains achieved will be dependent on both the sparseness and the current SNR.

The following subsections aim to provide conclusions to investigations regarding the major subsystems as presented in earlier chapters, as well as some of the appendices to follow.

### 5.1.1 Implemented source models

The following conclusions are based on the simulation results and discussion as presented in *Section* 4.2 for the source model as discussed in *Appendix* B.

1. Over the years many engineers simulating telecommunication systems have been content to use simple PRNG limited to a GF(2) to generate random binary data streams, with the mindset that results will converge to some average value with sufficient iteration, especially with the increased processing power available. However, simulation results have shown that these traditional sources have a very large standard deviation, meaning that the expected results may take longer to converge to the expected value. This provides a feasible opportunity to explore different data source models to improve the standard deviation.

2. Optimal feedback lengths exist and have been calculated by simulation where the minimum standard deviation may be achieved with the proposed and implemented method. The current proposed model is not optimal and suggestions are made later in this chapter to improve this model even further.

3. It is important to note that the complexity of the proposed improved data source is larger than that of traditional sources. This model is, however, an improvement over traditional models when

   (a) it is imperative to simulate data with accurately controlled amounts of sparseness, and

   (b) in complex equiprobable simulations where the total simulation time is significantly larger than the time to generate data with either the traditional or improved data source models. Here the improvement lies in the fact that the number of iterations required for the results to converge will reduce, rather than optimising each iteration to decrease simulation time of many iterations (even though this is still suggested).

### 5.1.2 Effect of FEC encoding on sparse data streams

The following conclusions are based on the simulation results and discussion as presented in *Section* 4.3 for the simple FEC encoders discussed in *Appendix* C.

1. It has been shown via simulation that the sparseness of an encoded data stream does in fact differ from the sparseness of the source and that the sparseness of the encoded stream tends to be less sparse (conversely more dense) than the sparseness of the

original data source. This holds true for the small number of encoders considered in this study.

2. It has been found that the convolutional encoder makes the sparse stream significantly denser than a similarly complex block encoder, especially when the constraint length is increased. This is mostly due to the choice of generator polynomials used.

3. It is also clear that the encoded sparseness tends to become linearly mapped for block codes of increased $n$, and that the slope of such a linear mapping decreases with a decrease in code rate.

### 5.1.3 UMTS/WCDMA transmitter and receiver structures

The UMTS/WCDMA platform utilised QPSK-based wideband transmitter and receiver structures. These structures were discussed in detail in *Chapter* 2 and *Chapter* 3. The following conclusions can be drawn from the simulation results and discussions of *Section* 4.4.

1. The timing diagrams indicate that the transmitter successfully performs a S/P conversion, employs both channelisation and scrambling spreading and filters the data stream with the required RRC filter, while the receiver is capable of extracting the original transmitted data perfectly when tested without the presence of noise.

2. The eye diagrams indicate that the system does indeed exhibit timing instances where the ISI is minimised. It may therefore be concluded that the system may (as it does) extract the original data during these time instances once clock recovery has been performed and the system is synchronised to both the carrier and the spreading sequences.

3. The spectrum indicates that the RRC filter does indeed filter the spreading sequences and bandlimits the signal to the required value as specified by $\alpha = 0.22$. It is also clear that the system parameter functions according to specifications and that the transmitted data rate before spreading is indeed controlled according to the requirements.

4. The ACF as well as the CCF of the OVSF (channelisation) codes indicate that the best performance is achieved when the system is perfectly synchronised, but that these codes do in fact have a cross-correlation when they are upsampled while not perfectly

aligned. BER performance curves, however, suggest that even if misaligned, these codes still perform well in a multi-user environment.

### 5.1.4 Channel model verification

The implemented channel model is a direct implementation of the mathematical model that was presented in *Section* D.6. The following conclusions may be drawn.

1. The channel simulator was designed to be very flexible and generic in the way that it may be configured to perform fading channel simulations. Each path exhibits frequency non-selective behaviour with a selectable Rician factor and Doppler spread. It is important to note that the simulator performs these functions in baseband, eliminating the need for high frequency carrier waves during simulations.

2. Each of the paths may be configured with a unique power gain as well as a time delay value, enabling the ability to configure the simulator for most practical gain delay profiles as required by the various models existing in literature.

3. A number of conclusions can be drawn specifically from the simulated channel measurements, as presented in *Section* 4.5:

    (a) The AWGN channel simulator generates PDF results consistent with the theoretical derivations presented in *Eq.* (D.1) for the equiprobable case, as well as those presented in *Eq.* (3.18) for the case where sparse data streams are transmitted.

    (b) It is clear that the decision interval for non-equiprobable data streams may deviate from the typical assumed $r_d = 0$ value and also that it tends towards the sparse symbol, with an increase in the amount of deviation when the sparseness measure decreases. This closely corresponds to the dependence of $r_d$ on $\eta_\alpha$ as theoretically derived in *Eq.* (3.19).

    (c) It is clear that the decision interval for non-equiprobable data streams may deviate from the typically assumed $r_d = 0$ value and that it tends towards the sparse symbol, with an increase in the amount of deviation when the SNR decreases. This closely corresponds to the dependence of $r_d$ on $E_b/N_0$ as theoretically derived in *Eq.* (3.19).

(d) Various different ways of computing the values to generate a specific Doppler spread was presented in *Section* D.4.5, with the results of the PSD and ACF of the respective methods indicating that it corresponds well to the theoretical values.

(e) A statistical analysis of the various processes was presented in *Section* D.3 and the simulated results correspond very well with the expected theoretical models. This applies to both the first order statistics, including the PDF of the respective envelopes and phases of the Rayleigh and Rician processes, as well as the second order statistics, including the LCR under various conditions as well as the ADF.

(f) It is clear that the simulator generates a complex baseband equivalent channel model of any multipath fading channel configuration, including the popular COST models.

### 5.1.5 BER performance of the UMTS/WCDMA platform

A theoretical analysis of the BER performance of an uncoded BPSK/QPSK-based modulation system was presented in *Section* 3.1.2 and *Section* 3.3.2 for both the traditional equiprobable case as well as the case where sparseness is considered. The uncoded BER performance results were presented and discussed in *Section* 4.6. The following conclusions may be drawn from the results.

1. The simulation platform functions as expected and compares well with the theoretical analysis of an uncoded system presented in literature for the equiprobable case as well as with the derived performance measures for a non-equiprobable case. This holds true for AWGN, frequency non-selective as well as frequency selective fading conditions.

2. It is clear that the self-calibrating feature of the AWGN channel scales correctly with various values of the system parameter, $k$, where essentially the value of $E_b$ is changed with a change in $k$. This calls for a recalibration of $N_0$ to achieve the desired $E_b/N_0$ value. This is also useful when simulating an adaptive or general system that either employs filtered or unfiltered data streams, and/or filtered or unfiltered spreading sequences, since some bit energy is lost to the filtering process.

3. The BER performance curves are dependent on the selected channel configuration. As expected, BER performance decreases when the channel is varied from exhibiting

AWGN channel conditions only to a frequency non-selective channel. BER performance again decreases when the channel is changed to a frequency selective channel configuration, especially when switching from an exponential decay multipath profile to a COST207-TU channel setup.

4. The BER performance curves are dependent on the number of transmitting users selected. As expected, BER performance decreases when the number of users transmitting in the same frequency band is increased. It is clear that the BER performance quickly tends to the worst case scenario curve for many users when OVSF codes are used.

5. In general, it was found that the novel receiver structures outperformed or at least matched (whenever the assumption of equiprobability holds) the conventional receiver structures in any channel environment. The small amount of additional complexity of these receiver structures is easily warranted when considering the improvement in BER performance for highly sparse scenarios.

6. It is clear that use of the novel receiver structures improves the BER performance for sparse data streams, especially at low values of $E_b/N_0$. It is still recommended to use FEC and/or interleaving techniques to improve the BER performance at high $E_b/N_0$ values.

7. Sparse data streams could potentially be utilised in joint source/channel decoder systems to improve BER performance, similar to FEC decoders. In such cases, the proposed receiver structures would easily outperform the conventional structures.

## 5.2 FUTURE RESEARCH

The following subsections present some of the questions raised by this study that were not answered in sufficient detail or have not been addressed at all. Many of these topics may be selected for investigation in future research.

### 5.2.1 Source model improvements

The following questions and topics arose from the simulation results and conclusions based on the proposed improved source model presented in *Appendix* B.

1. Investigation of the effect of multiple feedback paths for the proposed improved source model is still required.
2. Alternative architectures for source generators may be investigated and designed to improve the standard deviation, while also improving the computational complexity.
3. An in depth study of the first and second (and possibly higher) order statistical properties of the implemented source, as well as the newly suggested source with multiple feedback paths and/or an improved architecture, may be performed.

### 5.2.2 Effect of sparseness on modulation systems

The following questions and topics arose from the simulation results and conclusions that were based on the implemented UMTS/WCDMA platform, specifically regarding the modulation scheme.

1. The effect of sparseness on complete M-PSK narrowband and wideband systems has yet to be gauged.
2. The effect of sparseness on QAM systems is still unknown and may be studied.
3. A study may be done regarding the effect of sparseness on continuous wave modulation schemes, which may include FM, chirp like signals and MSK (including variants like GMSK) systems.
4. The effect of sparseness on adaptive/hybrid systems employing multiple modulation schemes, e.g. CDMA EV-DO, may be determined.
5. Further, a complete study may be performed on the effect of sparseness on OFDM modulated systems.
6. The effect, if any, that interleaving may have on communication systems employing receivers capable of using the sparseness measure to optimise detection may be determined and studied.

### 5.2.3 Effect of sparseness on coded systems

The following questions and topics arose from the simulation results and conclusions that were based on the implemented UMTS/WCDMA platform, specifically regarding the effect of coding.

1. Study the effect that sparseness has on simple and/or advanced FEC systems employing block codes. The investigation could include topics such as:
    (a) the effect that sparse data has on the encoded stream to be transmitted,
    (b) potential strengths and weaknesses of the codes and how well they are suited for encoding sparse data streams,
    (c) how good codes may be designed and optimised to improve BER performance results specifically for sparse data streams,
    (d) improving decoding methods by providing more accurate a-priori information based on the estimated sparseness measure, and
    (e) an analysis and simulation study on the effect of sparseness on BER performance for coded systems.
2. Complete a study of the effect that sparseness has on simple and/or advanced FEC systems using convolutional codes. The study may be conducted with a similar approach as (a) through (e) above.
3. Study complex FEC systems employing concatenated block/convolutional codes and the effect that sparseness has on such systems. The study may be conducted with a similar approach as (a) through (e) above, and may additionally include
    (f) a comparison of serial and parallel concatenated codes and their respective response to sparse data streams, and
    (g) an optimisation of the decoder structures for concatenated coding schemes by providing more accurate a-priori information
4. Performance evaluation of joint source/channel coded systems when the sparseness measure is employed. This study may be conducted with a similar approach as (a) through (e) above, and may additionally include

    (f) a comparison of different source and channel coding schemes to be used in the joint coding scheme.

5. A study of the effect of code puncturing on the sparseness of the coded streams, as well as an investigation of whether puncturing profiles exist to optimise BER performance of systems transmitting possibly sparse streams.

6. A study of the controllability of the sparseness of data streams when different source coding techniques are employed.

# REFERENCES

[1] S. Vembu, S. Verdú, and Y. Steinberg, "The source-channel separation theorem revisited," *IEEE Transactions on Information Theory*, vol. 41, no. 1, pp. 44–54, January 1995.

[2] J. Hagenauer, "Source-controlled channel decoding," in *IEEE International Symposium on Information Theory*, 27 June-1 July 1994 1994, p. 165.

[3] ——, "Source-controlled channel decoding," *IEEE Transactions on Communications*, vol. 43, no. 9, pp. 2449–2457, Sep 1995.

[4] G. Buch, F. Burkert, J. Hagenauer, and B. Kukla, "To compress or not to compress?" in *GLOBECOM '96: Communications: The Key to Global Prosperity*, November 1996, pp. 198 – 203.

[5] T. Hindelang, J. Hagenauer, and S. Heinen, "Source-controlled channel decoding: estimation of correlated parameters," in *ITG-Fachbericht, Conference Source and Channel Coding*, 2000.

[6] B. Hochward and K. Zeger, "Tradeoff between source and channel coding," *IEEE Transactions on Information Theory*, vol. 43, no. 5, pp. 1412–24, September 1997.

[7] E. Dahlman, B. Gudmundson, M. Nilsson, and J. Skold, "UMTS/IMT-2000 Based on Wideband CDMA," *IEEE Communications Magazine*, pp. 70–80, September 1998.

[8] K. V. Ravi, "Third Generation (3G) mobile systems: IMT2000 Standardisation and Transceiver Structure," May, 2000, http://www.nus.edu.sg/ cwcravi.

[9] C. Shannon, "A mathematical theory of communication," *Bell Syst. Technol*, vol. 27, 1948.

[10] M. Jeruchim, P. Balaban, and K. Shanmugan, *Simulation of Communication Systems*, ser. Applications of communications theory, R. Lucky, Ed. Plenum, 1992.

[11] J. von Neumann, "Various techniques used in connection with random digits," *Applied Mathematics Series*, no. 12, pp. 36–38, 1951.

[12] P. Elias, "The efficient construction of an unbiased random sequence," *Ann. Math. Statist.*, vol. 43, pp. 865–870, 1972.

[13] Y. Peres, “Iterating non Neumanns procedure for extracting random bits,” *Ann. Statist.*, vol. 20, no. I, pp. 590–597, 1992.

[14] S. Vembu and S. Verdú, “Generating random bits from an arbitrary source: fundamental limits,” *IEEE Transactions on Information Theory*, vol. 41, no. 5, pp. 1322–1332, September 1995.

[15] T. S. Han and S. Verdú, “Approximation theory of output statistics,” *IEEE Transactions on Information Theory*, vol. 39, no. 3, pp. 752–772, May 1993.

[16] B. Wichmann and D. Hill, “Building a random number generator,” *Byte*, pp. 127–128, March 1987.

[17] C. Moler, “Numerical Computing with MATLAB,” Electronic edition: The MathWorks, Inc., 2004, http://www.mathworks.com/moler.

[18] L. Blum, M. Blum, and M. Shub, “A simple unpredictable pseudo-random number generator,” *SIAM Journal on Computing*, vol. 15, pp. 364–383, May 1986.

[19] N. Ferguson and B. Schneier, *Practical Cryptography*. Wiley, 2003.

[20] M. Matsumoto and T. Nishimura, “Mersenne twister: A 623-dimensionally equidistributed uniform pseudorandom number generator,” *ACM Transactions on Modeling and Computer Simulations (TOMACS)*, vol. 8, no. 1, pp. 3–30, January 1998.

[21] T. Han and M. Hoshi, “Interval algorithm for random number generation,” *IEEE Transactions on Information Theory*, vol. 43, no. 2, pp. 599–611, March 1997.

[22] D. Salomon, *Data compression: the complete reference*. New York, Springer, 1998.

[23] Y.-Q. Lu, D. W. Petr, and V. S. Frost, “Survey of Source Modeling Techniques for ATM Networks,” Univiersity of Kansas, Tech. Rep. TISL-10230-1, September 1993.

[24] D. W. Petr, V. S. Frost, A. Demirtjis, and C. Braun, “Evaluation of Broadband Networking Technologies: Phase II Report,” Univiersity of Kansas, Tech. Rep. TISL-9750-4, July 1993.

[25] I. Norros, J. Roberts, A. Simonian, and J. Virtamo, “The superposition of variable bit rate sources in an ATM multiplexer,” *IEEE Journal on Selected Areas in Communications*, vol. 9, no. 3, pp. 378–387, April 1991.

[26] P. Sen, B. Maglaris, N.-E. Rikli, and D. Anastassiou, “Models for packet switching of variable-bit-rate video sources,” *IEEE Journal on Selected Areas in Communications*, vol. 7, no. 5, pp. 865 – 869, June 1989.

[27] Q. Zhang, “A general AR-based technique for the generation of arbitrary gamma VBR video traffic in ATM networks,” *IEEE Transactions on Circuits and Systems for Video Technology*, vol. 9, no. 7, pp. 1130 – 1137, October 1999.

[28] M. W. Garrett and M. Vetterli, “Joint source/channel coding of statistically multiplexed real-time services on packet networks,” *IEEE/ACM Transactions on Networking*, vol. 1, no. 1, pp. 71–80, February 1993.

[29] H. D. Sheng and S. Q. Li, “Second order effect of binary sources on characteristics of queue and loss rate,” *IEEE Transactions on Communications*, vol. 42, no. 234, pp. 1162–1173, February-April 1994.

[30] D. Anick, D. Mitra, and M. M. Sondhi, “Stochastic theory of a data handling system with multiple sources,” in *ICC ’80; International Conference on Communications, Seattle, Wash., June 8-12, 1980, Conference Record. Volume 1. (A81-32276 14-32) New York, Institute of Electrical and Electronics Engineers, Inc., 1980, p. 13.1.1-13.1.5.*, 1980, pp. 13–+.

[31] R. Guérin, H. Ahmadi, and M. Naghshineh, “Equivalent capacity and its application to bandwidth allocation in high-speed networks,” *IEEE Journal on Selected Areas in Communications*, vol. 9, no. 7, pp. 968–981, September 1991.

[32] D. P. Heyman and T. V. Lakshman, “Source models for VBR broadcast-video traffic,” *IEEE/ACM Transactions on Networking*, vol. 4, no. 1, pp. 40 – 48, February 1996.

[33] M. Park and D.J. Miller, “Decoding entropy-coded symbols over noisy channel by MPA sequence estimation for asynchronous HMMs,” *32nd Annual Conference on Information Sciences and Systems*, June 1998.

[34] J. Wen and J.D. Villasenor, “Utilizing soft information in decoding of variable length codes,” *Proc. 1999 IEEE Data Compression Conference*, March 1999.

[35] N. Demir and K. Sayood, “Joint source/channel coding for variable length codes,” *Proc. 1999 IEEE Data Compression Conference*, March 1999.

[36] K. Lakovic, J. Villasenor and R Wesel, “Robust joint Huffman and convolutional decoding.”

[37] L. Staphorst, J. Schoeman, and L. Linde, “Performance evaluation of a joint source/channel coding scheme for DS/SSMA systems utilizing complex spreading sequences in multipath fading channel conditions.” IEEE CCECE2003, May 2003.

[38] S. B. Zahir Azami, P. Duhamel and O. Rioul, “Joint source-channel codig: panorama of methods,” in *Proceedings of CNES Workshop on Data Compression*, November 1996.

[39] S. Rice, “Statistical properties of a sine wave plus random noise,” *Bell System Technical*, vol. 27 (1), pp. 109–157, January 1948.

[40] R. Clarke, “A statistical theory of mobile radio reception,” *Bell System Technical Journal*, pp. 957–1000, July-August 1968.

[41] W. Jakes, *Microwave Mobile Communications*. New York: Wiley and Sons, 1974.

[42] H. van Trees, “Analog communication over randomly-time-varying channels,” *IEEE Transactions on Information Theory*, vol. 12, no. 1, pp. 51 – 63, January 1966.

[43] T. Rappaport, *Wireless Communications - Principles and Practice*, 2nd ed., ser. Prentice Hall Communications Engineering and Emerging Technologies. Upper Saddle River, NJ 07458: Prentice Hall, 2002, vol. 1.

[44] J. G. Proakis, *Digital Communications*, international edition ed., ser. Electrical Engineering Series. McGraw-Hill International Series, 2001, vol. 4.

[45] B. Sklar, “Rayleigh fading channels in mobile digital communication systems Part I: Characterization,” *IEEE Communications Magazine*, vol. 35, no. 7, pp. 90 – 100, July 1997.

[46] M. Pätzold and F. Laue, “The performance of deterministic Rayleigh fading channel simulators with respect to the bit error probability,” in *IEEE 51st Vehicular Technology Conference Proceedings*, vol. 3, May 2000, pp. 1998 – 2003.

[47] M. Pätzold, “On the stationarity and ergodicity of fading channel simulators basing on Rice’s sum-of-sinusoids,” in *14th IEEE Proceedings on Personal, Indoor and Mobile Radio Communications*, vol. 2, September 2003, pp. 1521 – 1525.

[48] M. Pätzold and D. Kim, “Test procedures and performance assessment of mobile fading channel simulators,” in *IEEE 59th Vehicular Technology Conference*, vol. 1, May 2004, pp. 254 – 260.

[49] M. Pätzold and F. Laue, “Statistical properties of Jakes’ fading channel simulator,” in *48th IEEE Vehicular Technology Conference*, vol. 2, May 1998, pp. 712 – 718.

[50] M. Pätzold, F. Laue, U. Killat, and Y. Li, “A new and optimal method for the derivation of deterministic simulation models for mobile radio channels,” in *IEEE 46th Vehicular Technology Conference: ’Mobile Technology for the Human Race’*, vol. 3, 28 April-1 May 1996, pp. 1423 – 1427.

[51] M. Pop and N. Beaulieu, “Statistical investigation of sum-of-sinusoids fading channel simulators,” in *IEEE Global Telecommunications Conference*, vol. 1A, 1999, pp. 419 – 426.

[52] ——, “Limitations of sum-of-sinusoids fading channel simulators,” *IEEE Transactions on Communications*, vol. 49, no. 4, pp. 699 – 708, April 2001.

[53] T. Ekman, G. Kubin, M. Sternad, and A. Ahlen, “Quadratic and linear filters for radio channel prediction,” in *IEEE Vehicular Technology Conference*, vol. 1, September 1999, pp. 146 – 150.

[54] L. Dong, G. Xu, and H. Ling, “Prediction of fast fading mobile radio channels in wideband communication systems,” in *IEEE Global Telecommunications Conference*, vol. 6, November 2001, pp. 3287 – 3291.

[55] P. Hoeher, “A statistical discrete-time model for the WSSUS multipath channel,” *IEEE Transactions on Vehicular Technology*, vol. 41, no. 4, pp. 461 – 468, November 1992.

[56] S. Fechtel, “A novel approach to modeling and efficient simulation of frequency-selective fading radio channels,” *IEEE Journal on Selected Areas in Communications*, vol. 11, no. 3, pp. 422 – 431, April 1993.

[57] M. Pätzold, F. Laue, and R. Garcia, “Design of high-speed simulation models for mobile fading channels by using table look-up techniques,” *IEEE Transactions on Vehicular Technology*, vol. 49, no. 4, pp. 1178 – 1190, July 2000.

[58] M. Pätzold, F. Laue, and U. Killat, “An extended Suzuki model for land mobile satellite channels and its statistical properties,” *IEEE Transactions on Vehicular Technology*, vol. 47, pp. 617 – 630, 1998.

[59] ——, “A deterministic digital simulation model for Suzuki processes with application to a shadowed Rayleigh land mobile radio channel,” *IEEE Transactions on Vehicular Technology*, vol. 45, pp. 318 – 331, 1996.

[60] ——, “A deterministic model for a shadowed Rayleigh land mobile radio channel,” in *5th IEEE International Symposium on Personal, Indoor and Mobile Radio Communications, 1994. Wireless Networks - Catching the Mobile Future*, vol. 4, 18 - 23 September 1994, pp. 1202 – 1210.

[61] T. Uyematsu and F. Kanaya, “Channel simulation by interval algorithm,” in *Proceedings of the 1999 IEEE Information Theory and Communications Workshop, 1999*.

[62] N. Whillans, “The development of a baseband channel emulator for use in the evaluation of the FRAMES demonstrator,” in *IEEE Vehicular Technology Conference*, vol. 1, September 1999, pp. 161 – 165.

[63] K. Baddour and N. Beaulieu, “Autoregressive modeling for fading channel simulation,” *IEEE Transactions on Wireless Communications*, vol. 4, no. 4, pp. 1650 – 1662, July 2005.

[64] C. Patel and T. Stuber, G.L and; Pratt, “Comparative analysis of statistical models for the simulation of Rayleigh faded cellular channels,” *IEEE Transactions on Communications*, vol. 53, no. 6, pp. 1017 – 1026, June 2005.

[65] ——, “Simulation of Rayleigh-faded mobile-to-mobile communication channels,” *IEEE Transactions on Communications*, vol. 53, no. 11, pp. 1876 – 1884, November 2005.

[66] S. G. Wilson, *Digital Modulation and Coding*. Prentice-Hall, Inc., 1996, vol. 1.

[67] S. Haykin, *Communication systems*, 4th ed., 2000.

[68] K. Feher, *Wireless Digital Communications*. Prentice Hall, 1995.

[69] *The ETSI UMTS terrestrial radio access (UTRA) ITU-R RTT candidate submission*, ETSI, June 1998.

[70] C. Lindemann and O. Waldhorst, “A distributed search service for peer-to-peer file sharing in mobile applications,” in *Peer-to-Peer Computing, 2002. (P2P 2002). Proceedings. Second International Conference on*, 2002, pp. 73– 80.

[71] S.-L. Tsao and C.-C. Lin, “Design and evaluation of UMTS-WLAN interworking strategies,” in *Vehicular Technology Conference, 2002. Proceedings. VTC 2002-Fall. 2002 IEEE 56th*, vol. 2, 2002, pp. 777–781.

[72] T. Hopfeld, K. Tutschku, F. Andersen, H. de Meer, and J. Oberender, “Simulative performance evaluation of a mobile peer-to-peer file-sharing system,” in *Next Generation Internet Networks, 2005*, 18-20 April 2005, pp. 281–287.

[73] T. Ruohonen, J. Seppälä, M. Salmenpera, and H. Koivisto, “Secure autoconfiguration of field equipment in mobile automation system,” Tampere University of Technology, Institute of Automation and Control, Tech. Rep., 2004, http://ae.tut.fi/research/AIN/Publications/.

[74] J. R. Gállego, A. Hernández-Solana, M. Canales, J. Lafuente, A. Valdovinos, and J. Fernández-Navajas, “Performance analysis of multiplexed medical data transmission for mobile emergency care over the UMTS channel,” *IEEE Transactions on Information Technology in Biomedicine*, vol. 9, no. 1, pp. 13–22, March 2005.

[75] O. Boric-Lubeke and V. Lubecke, “Wireless house calls: using communications technology for health care and monitoring,” *Microwave Magazine, IEEE*, pp. 43–48, Sept 2002.

[76] D. C. Dowden, R. D. Gitlin, and R. L. Martin, “Next-generation networks,” *Bell Labs Tech J*, vol. 3, no. 4, pp. 3–14, 1998.

[77] S. Parkvall, E. Dahlman, P. Frenger, P. Beming, and M. Persson, “The evolution of WCDMA towards higher speed downlink packet data access,” in *VTC ’01*. IEEE, 2001, pp. 2287–2291.

[78] A. R. Modarressi and S. Mohan, “Control and management in next-generation networks: challenges and opportunities,” *Communications Magazine, IEEE*, vol. 38, no. 10, pp. 94–102, Oct. 2000.

[79] R. Patachaianand and K. Sandrasegaran, “System-level modeling and simulation of uplink WCDMA,” in *Fifth International Conference on Information Technology: New Generations*, Apr. 2008, pp. 1071–1076.

[80] A. Toskala, H. Holma, and P. Muszynski, “ETSI WCDMA for UMTS,” in *IEEE 5th International Symposium on Spread Spectrum Techniques and Applications*, vol. 2, Sept. 1998, pp. 616–620.

[81] O. Fratu, S. Halunga, and D. Vizireanu, “Downlink simulation for an UMTS/WCDMA cell,” in *5th International Conference on Telecommunications in Modern Satellite, Cable and Broadcasting Service*, vol. 1, Sept. 2001, pp. 137–140.

[82] K. Waheed, K. Desai, and F. Salem, “Adaptive RAKE-blind source recovery algorithms for 3GPP UMTS/WCDMA downlink receivers,” in *5th International Conference on Telecommunications in Modern Satellite, Cable and Broadcasting Service*, vol. 1, Oct. 2003, pp. 634–639.

[83] S. Baey, M. Dumas, and M.-C. Dumas, “Cooperative strategy for efficient multiplexing of multimedia traffic in the uplink of the UMTS WCDMA,” in *Wireless Communications and Networking Conference*, vol. 4, March 2004, pp. 2207–2213.

[84] S. Sharma and S. Naseem Ahmad, “Suppression of multiple access interference (MAI) in wideband code division multiple access (WCDMA),” in *International Conference on Wireless and Optical Communications Networks*, July 2007, pp. 1–6.

[85] L. Staphorst, “Viterbi decoded linear block codes for narrowband and wideband wireless communication over mobile fading channels,” Master’s thesis, University of Pretoria, Lynnwood Road, Pretoria, South Africa (ZA), July 2005.

[86] J. Lim and D. L. Neuhoff, “Joint and tandem source-channel coding with delay constraints,” in *IEEE International Conference on Acoustics, Speech, and Signal Processing (ICASSP ’01)*, 2001.

[87] N. Görtz, “Delay-constrained coding and transmission of continuous-amplitude sources,” Institute for Communications Engineering, Munich University of Technology. [Online]. Available: http://www.lnt.ei.tum.de/mitarbeiter/goertz/jwcc02.pdf

[88] N. Görtz and U. Heute, “Joint source-channel decoding with iterative algorithms,” in *Proceedings of EUSIPCO-2000*, vol. 1, Tampere, Finland, September 2000, pp. 425–428.

[89] J. Schoeman, L. Linde, and L. Staphorst, “Performance evaluation of a joint source/channel coding scheme for DS/SSMA systems utilizing complex spreading sequences in multipath fading channel conditions,” in *Proceedings, IEEE CCECE 2003*, May 2003, pp. 1679 – 1682.

[90] J. Schoeman and L. Linde, “Investigation of the effect of LDPC coding on the sparseness of a data source in AWGN channel conditions,” in *SATNAC 2004*, September 2004.

[91] ——, “Performance investigation of a sparse data compression technique with AWGN channel effects,” in *Proceedings, IEEE AFRICON (7th) 2004*, September 2004, pp. 275 – 278.

[92] ——, “Evaluation of the effect of Hamming, LDPC and convolutional encoding on the sparseness of a data source,” in *Proceedings, IEEE ICT 2005*, May 2005.

[93] ——, “Employing a measure of sparseness to investigate sparse data compression in AWGN conditions,” *Transactions of the South African Institute of Electrical Engineers (Africon ’04 Special Issue 1 : Towards Next Generation Wireless Communication Systems)*, pp. 157–161, June 2006.

[94] ——, “A novel approach to improve sparse data models,” in *Proceedings, IEEE AFRICON (8th) 2007*, September 2007, pp. 1 – 5.

[95] ——, “Work in Progress - An optimal UMTS/WCDMA receiver structure for possibly sparse data streams,” in *Proceedings, IEEE BROADCOM 2008*, Nobember 2008, pp. 117 – 119.

[96] S. Sinha, M. Božanić, J. Schoeman, M. du Plessis, and L. Linde, “A CMOS based multiple-access DSSS transceiver,” in *SACSST 2009*, September 2009.

[97] M. Rice, *Digital Communications: a discrete-time approach*, International ed. Prentice Hall, 2008.

[98] R. Price and P. Green, “A Communication Technique for Multipath Channels,” in *Proceedings of the IRE*. IEEE, March 1958, pp. 555–570.

[99] T. Uyematsu and F. Kanaya, “Almost sure convergence theorems of rate of coin tosses for random number generation by interval algorithm,” in *IEEE International Symposium on Information Theory, 2000. Proceedings.*, June 2000, p. 457.

[100] P. L’Ecuyer, “Software for Uniform Random Number Generation: Distinguishing the Good and the Bad,” in *Proceedings, 2001 Winter Simulation Conference*, 2001, pp. 98 – 105.

[101] D. J. C. MacKay, “Good error correcting codes based on very sparse matrices,” 1997, submitted to IEEE transactions on Information Theory. Available from `http://wol.ra.phy.cam.ac.uk/`.

[102] J. G. Proakis, *Digital Communications*, 4th ed., 2001.

[103] R. G. Gallager, “Low-density parity-check codes,” Ph.D. dissertation, Cambridge, MA, 1963.

[104] D. J. C. MacKay and R. M. Neal, “Near Shannon limit performance of low density parity check codes,” *Electronics Letters*, vol. 32, pp. 1645–1646, 1996, reprinted with printing errors corrected in vol. 33, pp. 457-458.

[105] M. Pätzold, *Mobile Fading Channels*. Wiley and Sons, 2002.

[106] F. Swarts and H. C. Ferreira, “Markov characterization of channels with soft decision outputs,” *IEEE Transactions on Communications*, vol. 41, no. 5, pp. 678 – 682, May 1993.

[107] E. Lutz and E. Plöchinger, “Generating Rice processes with given spectral properties,” *IEEE Transactions on Vehicular Technology*, vol. 34, no. 4, pp. 178 – 181, November 1985.

[108] Y. R. Zheng and C. Xiao, “Simulation models with correct statistical properties for Rayleigh fading channels,” *IEEE Transactions on Communications*, vol. 51, no. 6, pp. 920 – 928, June 2003.

[109] M. Pop and N. Beaulieu, “Design of wide-sense stationary sum-of-sinusoids fading channel simulators,” in *IEEE International Conference on Communications*, vol. 2, 28 April-2 May 2002, pp. 709 – 716.

[110] K. Shanmugan, *Digital and Analogue Communication Systems*. Wiley, 1985.

[111] R. Coates, G. Janacek, and K. Lever, “Monte Carlo simulation and random number generation,” *IEEE JSAC*, vol. 6, no. 1, pp. 55–66, January 1988.

[112] S. Swanepoel, “A time spread diversity technique with integrated coding and interference cancellation,” Master’s thesis, University of Pretoria, Lynnwood Road, Pretoria, Gauteng, South Africa (ZA), 2002.

# APPENDIX A

# SUMMARY OF THE UTRA/FDD PLATFORM PROTOCOL

The IMT-2000 family of 3G systems includes support for three types of core network technology:

- GSM based, using mobile application part protocols on top of SS7 protocols for signalling
- ANSI-41 based (IS-634 protocols for signalling)
- Internet Protocol based (in future, to be specified)

As for any protocol, the protocol supporting the IMT-2000 WCDMA standard may be broken into various layers of the ISO's OSI model. The channels in the three lower layers are designated differently based on the functions they perform [8]:

- Physical channels (L1 PHY) are defined in the physical layer. A physical channel is characterised by the *code*, *frequency* and in the reverse link the *relative phase (I/Q)* when operating in the FDD mode, while, for the TDD mode, it is also characterised by a *timeslot*. The physical channel specifications are discussed in more detail in *Section* 2.1
- Transport channels (L1 PHY/L2 MAC) are characterised by how the information is transferred over the radio interface. The transport channels may be categorised into two groups, the *dedicated channels* (only one type called the dedicated channel (DCH) for uplink and downlink control information), where the UEs are identified by the physical channel, i.e. code and frequency; and the *common channels*, where there is

a need for inband identification of UEs when they are addressed in particular. There exists six different common channels:

  - Broadcast channel (BCH) (D/L), used to broadcast system- and cell-specific information.
  - Forward access channel (FACH) (D/L), used to carry control information to a UE when the system knows the location cell of the UE. FACH may also carry short user packets.
  - Paging channel (PCH) (D/L), used to carry control information to an UE when the system does not know the location cell of the UE (transmitted over the entire cell).
  - Random access channel (RACH) (U/L), used to carry control information from the UE. It may also carry short user packets.
  - Common packet channel (CPCH) (U/L), used for bursty data traffic. It is associated with a dedicated channel in the downlink which provides power control for the uplink CPCH.
  - Downlink shared channel (DSCH) (D/L), shared by several UEs.

- Logical channels (L2 MAC) are characterised by the type of information that is transferred and offers different logical channels to (L2 LAC).

The radio interface protocol is illustrated in *Fig.* A.1, while the protocol architecture is illustrated in *Fig.* A.2.

The physical layer provides the following services to the upper layers [8]:

- FEC encoding and decoding of transport channels
- Error detection
- Macrodiversity distribution/combining and soft handover execution
- Multiplexing/demultiplexing of transport channels and of coded composite transport channels
- Mapping of coded composite transport channels on physical channels

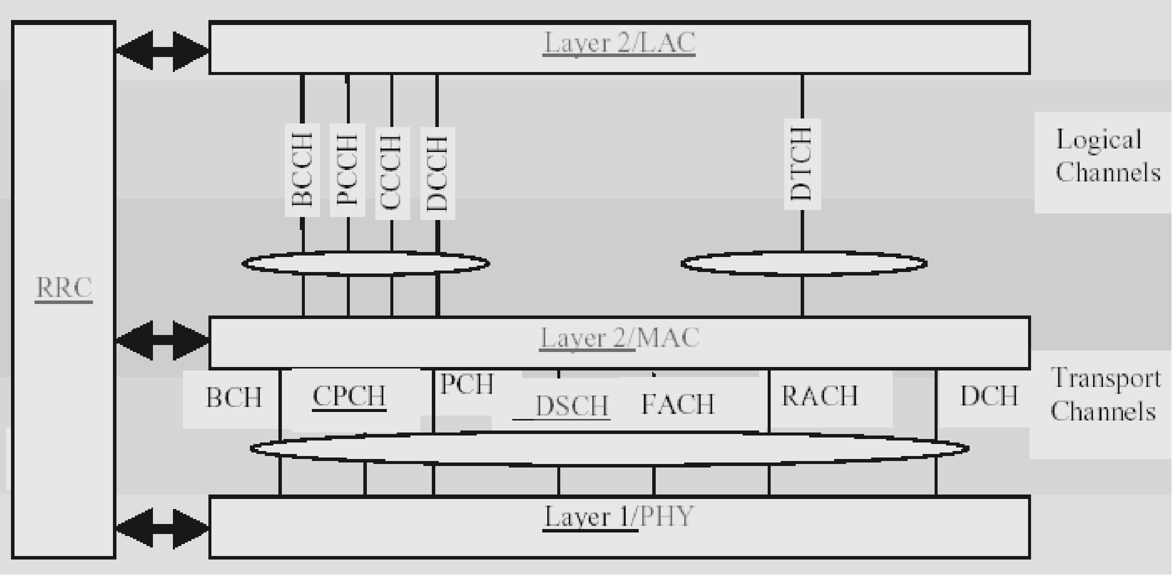

FIGURE A.1: IMT-2000 radio interface protocol (from [8] )

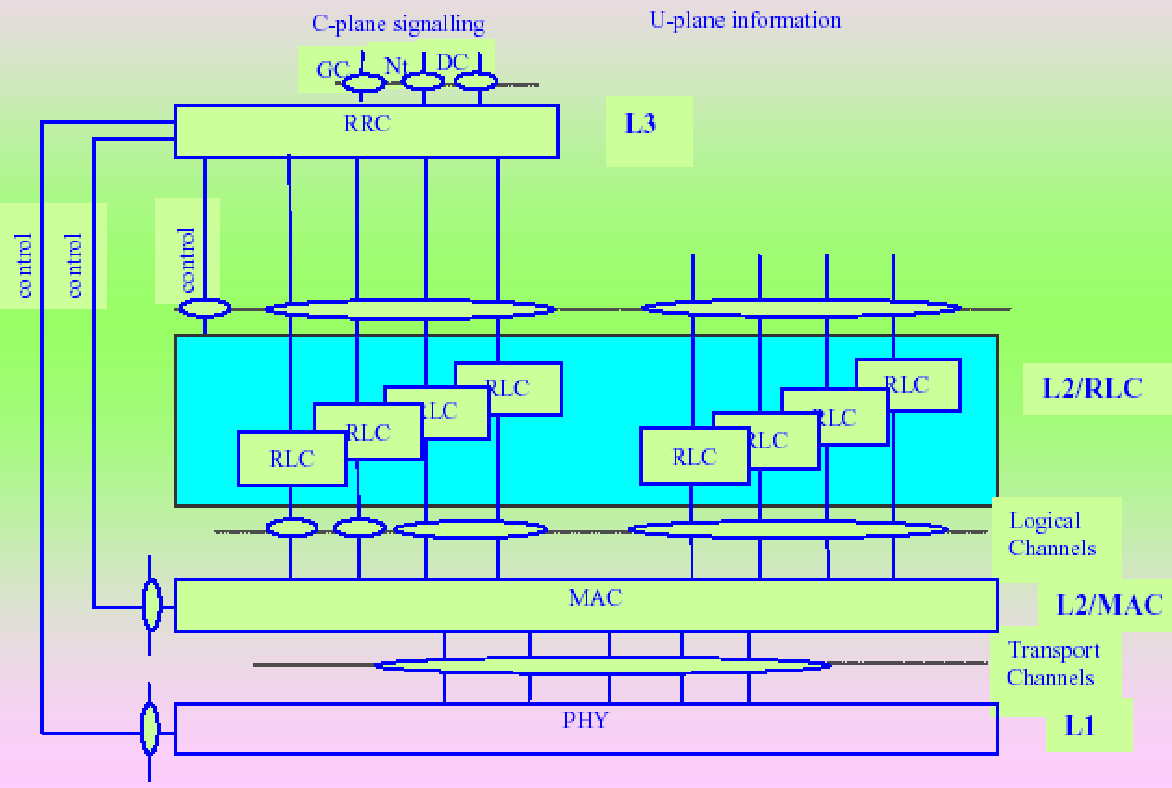

FIGURE A.2: IMT-2000 protocol architecture (L1 and L2) (from [8] )

- Modulation/demodulation and spreading/despreading of physical channels
- Frequency and time (chip, bit, slot, frame) synchronisation
- Closed-loop power control

- Power weighting and combining of physical channels
- RF processing
- Rate matching (data multiplexed on DCH)
- Radio characteristics measurements including FER, SIR, Interference Power, etc.

More specific details of the signalling, scheduling and protocols can be found in UTRA technical specifications [69].

# APPENDIX B

# NOVEL APPROACHES TO GENERATING SPARSE DATA SOURCES

## B.1 THE PROPOSED IMPROVED DATA SOURCE

Modern binary source modelling is not a topic receiving a flourish of attention from the research community, since most researchers find the simple uniformly distributed source models adequate for generating statistically i.i.d. variables. Recently, some techniques have been proposed [14–16, 21, 99] for the generation of pseudorandom data that may be used for such sources. None of these sources, however, focuses specifically on controlling the amount of sparseness. This lead to the development of a more optimal pseudorandom data source model able to emulate specific sparseness levels as required by various experimental setups.

The most widely used pseudorandom number generators are based on linear recurrences of the form

$$x_i = (a_1 x_{i-1} + \ldots + a_k x_{i-k}) \mod n \tag{B.1}$$

with the modulus $n$ and the order, $k$ positive integers of the recurrence with maximal period length $\rho = n^k - 1$ [100]. Pseudorandom binary bits are easily generated by letting $n = 2$, and since the output is uniformly distributed, the resultant output is equiprobable. In order to overcome this, $n$ may be increased and the resultant number may be compared to a certain subranges, $[0, m-1)$, $[m, n)$ within the range , $[0, n)$. Each output, $x_i$, will only fall within one of the subranges, and a specific subrange may be mapped to a binary $0$ or $1$ value. A clever choice of the ratio $m/n$ will ensure a weighted binary cumulative

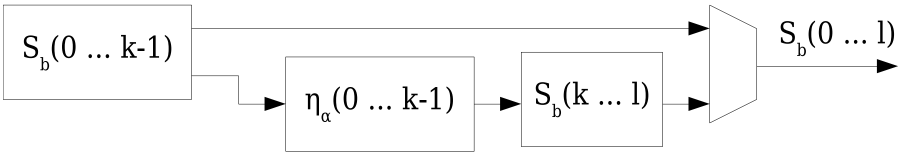

FIGURE B.1: Block diagram of an improved sparse data source

distribution function. This has been the approach for [90, 91]. However, it has been found that the standard deviation of the sparseness parameter in a large sample space of $S_b(0 \cdots l)$ is very large, resulting in many frames having $\widehat{\eta}_\alpha >> \eta_\alpha$ and $\widehat{\eta}_\alpha << \eta_\alpha$.

*Fig.* B.1 shows the block diagram of one possible source model that may be used to generate data streams or blocks for block length, $l$, with a measured sparseness, $\widehat{\eta}_\alpha$, very close to the original specified sparseness, $\eta_\alpha$ with a significantly reduced standard deviation. The output data block, $S(0 \cdots l)$, is a multiplexed stream of $S(0 \cdots k-1)$ and $S(k \cdots l)$ which is ideally suited to model sparse data sources in applications that requires such, as regularly required by simulation setups in *Chapter* 4, without the drawbacks of the unmodified range/bin approach above.

Rather than generating $S(0 \cdots l)$, a shorter data block, $S(0 \cdots k-1)$, is generated. This allows us to measure the sparseness of $S(0 \cdots k-1)$, as discussed in *Section* 3.2.1. When $\widehat{\eta}_\alpha(0 \cdots k-1)$ deviates from the expected sparseness, $\eta_\alpha$, we may modify the sparseness control of $S(k \cdots l)$ to change $\widehat{\eta}_\alpha(k \cdots l)$ in a weighted fashion by modifying the subranges to $[0, m_{new}-1),\ [m_{new}, n)$, with $m_{new}$ determined as

$$m_{new} = n \times \left[\eta_\alpha \times l - (\widehat{\eta}_\alpha(0 \cdots k-1) \times k)\right] / (l-k) \tag{B.2}$$

with all parameters defined earlier. It should be clear that, when $\widehat{\eta}_\alpha(0 \cdots k-1) > \eta_\alpha$, $m_{new}$ decreases in order to decrease $\widehat{\eta}_\alpha(k \cdots l)$, which results in $\widehat{\eta}_\alpha(0 \cdots l) < \widehat{\eta}_\alpha(0 \cdots k-1)$. The proposed model, therefore, aims to decrease the sparseness of $S(k \cdots l)$ in an attempt to reduce the total sparseness, $\widehat{\eta}_\alpha(0 \cdots l)$. Likewise, $\widehat{\eta}_\alpha(0 \cdots k-1) < \eta_\alpha$ results in $\widehat{\eta}_\alpha(0 \cdots l) > \widehat{\eta}_\alpha(0 \cdots k-1)$.

# APPENDIX C

# FEC ENCODER DESCRIPTIONS

Although somewhat outside the scope of the main body of work, it was considered interesting to begin an investigation into the effect that FEC encoders have on the sparseness of a bitstream. This was by no means investigated fully, but does provide motivation for this study as well as a number of interesting future research topics (refer to *Section* 5.2.3). Some popular, yet randomly selected FEC encoding methods are discussed next, with the results presented in *Section* 4.3.

## C.1 BLOCK ENCODING

A linear block code is best described by an $(n, k)$ binary generator matrix, $\mathbf{G^T}$. It is convenient to define the $(n-k, n)$ parity check matrix, $\mathbf{H}$, such that $\mathbf{HG^T} = \mathbf{0}$. Encoding a $k$-bit input vector, $\mathrm{s}$, using either $\mathbf{G^T}$ or $\mathbf{H}$, yields an $n$-bit vector given by $\mathbf{x} = \mathbf{G^T} \cdot \mathrm{s}$. All arithmetic operations are restricted to GF(2). System performance is increased by allowing $N \rightarrow \infty$ [101] [102].

### C.1.1 Hamming encoding

A binary Hamming encoder with properties $(n, k) = (2^m - 1, 2^m - (1 + m))$ is implemented with $m = 3$, yielding a $(7, 3)$ block code [102]. No two columns of the parity check matrix, $\mathbf{H}$, are identical, which implies linear independance.

### C.1.2 LDPC encoding

The creation of an LDPC generator and parity check matrix pair has been described in detail by Gallager [103] and optimised by MacKay [101]. Neal *et al.* [104] proceeded to optimise the encoding process by partitioning $\mathbf{H}$ into $[\mathbf{A}|\mathbf{B}]$ with dimensions $M \times M$ and $M \times N$. The parity check bits can then be found by determining $\mathbf{c} = \mathbf{A}^{-1}\mathbf{B}\mathbf{s}$, which can be approached in three different ways. Dense encoding predetermines $\mathbf{A}^{-1}\mathbf{B}$, which is multiplied by $\mathbf{s}$ to find $\mathbf{c}$. Mixed encoding exploits the sparseness of $\mathbf{B}$ by computing $\mathbf{z} = \mathbf{B}\mathbf{s}$, after which $\mathbf{c} = \mathbf{A}^{-1}\mathbf{z}$ is determined. Finally, sparse encoding determines $\mathbf{z} = \mathbf{B}\mathbf{s}$, then solves $\mathbf{y}$ in $\mathbf{L}\mathbf{y} = \mathbf{z}$ by forward substitution with $\mathbf{L}$ the lower triangle and finally solves $\mathbf{c}$ in $\mathbf{U}\mathbf{c} = \mathbf{y}$ by backward substitution, where $\mathbf{U}$ is the upper triangle.

## C.2 CONVOLUTIONAL ENCODING

A very simple convolutional encoder was implemented with a $K = 3$ length shift register (constraint length), by shifting $k = 1$ bit at a time into the encoder, and using $n = 2$ bits as output obtained with function generators $g_1 = [101]$ and $g_2 = [111]$. The code is, therefore, classified as a $(3, 1, 2)$ convolutional code with code rate $R_c = 1/2$. As alternatives, a $(5, 1, 2)$ code was generated with function generators $g_1 = [10001]$ and $g_2 = [11111]$ and a $(7, 1, 2)$ code was generated with function generators $g_1 = [1000001]$ and $g_2 = [1111111]$. Notice that $g_2$ feeds back the same bit repeatedly, and is selected as the all ones vector on purpose in an attempt to increase the density of a sparse stream when a sparse one is used a number of times to generate multiple ones at the output.

# APPENDIX D

# THEORETICAL JUSTIFICATION OF THE CHANNEL MODELS

> *"Nature is seldom kind. One of the most appealing uses for radio-telephone systems – communication with people on the move – must overcome radio transition problems so difficult they challenge the imagination."*
>
> W.C. JAKES [41]

The mobile radio channel is the transmission path between the transmitter and the receiver and can vary from the simplest LOS scenario to another that is severely obstructed by buildings, mountains, foliage and/or other large structures. The radio link is required to be effective in a variety of environments which include urban, suburban, rural and indoor areas. The velocity of the mobile unit may vary from stationary to fast, which also has an effect on performance. Several effects including reflection, diffraction, scattering and attenuation, combine to make reliable and accurate detection of digital data under these conditions very difficult. This has motivated the development of equalisation and diversity techniques, including the Rake receiver architecture, as well as power control, strong FEC codes and interleaving techniques capable of partially compensating for the signal distortion produced by the mobile channel. The aforementioned effects will be studied for a variety of different channel types in this appendix. Longer term amplitude fading, also referred to as shadow fading, is a type of fading that is slow when compared with the fading due to scattering and is not considered further, except to note that it will alter the SNR at the receiver. This type of fading is generally modelled by a Log-Normal statistical amplitude distribution. Interested readers are referred to [43].

This appendix presents an overview of various types of channel effects, including additive noise and fading effects. In order to obtain a deeper understanding of fading channels, both Rayleigh and Rician processes are investigated and useful fading channel parameters, as well as properties of these processes, are considered. The stochastic processes presented are used to create a deterministic channel model, which is then shown to be useful in both a frequency non-selective and a frequency selective emulation model. A detailed survey on the various methods to determine the Doppler parameters is also presented. The appendix is concluded with practical complex baseband simulation models.

## D.1 ADDITIVE WHITE GAUSSIAN NOISE

A common benchmark for assessing the performance of digital communication systems is the addition of Gaussian noise to the signal prior to the receiver filter and detection. This may sound like a trivial exercise, but there are a number of important considerations to take into account to ensure that accurate observations can be made.

Noise is any unwanted signal present in the communication system that inhibits error free transmission. There are many different sources of noise, some of which include other electrical systems, natural sources such as the cosmos, lighting and the random motion of charged particles in wires. The latter may be justified by evaluating the physics of electron motion in conductors and semi-conductors that are used to realise the hardware. This random motion of charged particles gives rise to thermal noise and is present in all electrical systems. The generated noise is additive in nature, and is normally distributed with the PDF given by

$$p_{n(t)}\left(x\right) = \frac{1}{\sqrt{2\pi\sigma^2_{n(t)}}} \exp\left[-\left(x - m_{n(t)}\right)^2 \Big/ 2\sigma^2_{n(t)}\right], \quad x \,\epsilon\, \mathbb{R} \tag{D.1}$$

where $m_{n(t)} \,\epsilon\, \mathbb{R}$ denotes the mean or expected value given by $E[n(t)]$ and $\sigma^2_{n(t)} \,\epsilon\, (0,\infty)$ the variance given by $\text{Var}\{n(t)\} = E[n(t)^2] - m^2_{n(t)}$ of the Gaussian distributed random process. This function is essentially flat at room temperature for frequencies varying from DC to $f = 10^{12}$ Hz. This noise has a constant PSD over all frequencies of interest for practical communication systems. Usually $n(t)$ can easily be generated with $m_{n(t)} = 0$ and $\sigma^2_{n(t)} = 1$. This is the standard normal distribution and can be denoted as $n(t) \backsim N(0,1)$. In *Appendix* D.5 a technique is discussed that shows how such a noise source may be modified to properly scale the variance using important benchmarking parameters as input.

# D.2 ELEMENTARY PROPERTIES OF THE RAYLEIGH AND RICIAN PROCESSES

It is possible to distinguish between different types of fading based on grossly quantified multipath channel parameters measured in 1) the time domain (symbol time, maximum excess delay time, mean excess delay time and rms delay spread) which is typically useful for frequency selective channels, that results from multipath propagation and, 2) the frequency domain (average Doppler shift and Doppler spread) which is typically useful for frequency non-selective channels caused by a relative difference in velocity between the transmitter and receiver. The definitions of these parameters are presented next.

## D.2.1 Useful fading channel parameters

### D.2.1.1 Time domain parameters

The following parameters are calculated by using a multipath intensity profile of the channel. A multipath signal intensity profile may be plotted over time by measuring the received signal power after the channel has been excited by either an impulse or a wideband signal. Typical wireless channels will propagate the signal via various different paths (with each path having a different length), resulting in the reception of various different time delayed signals with decaying (due to large scale fading effects) signal power.

- The **symbol time**, $T_s$, is said to be the time duration of a symbol. It should, however, be noted that this symbol duration is not to be confused with the symbol rate of the source, but is rather chosen as the time duration of a single chip in the event of spreading, or the bit duration of a single bit if a modulation scheme with a dimensionality of higher than one is selected (i.e. the symbol will be passed through a S/P converter). The symbol time is, therefore, the shortest signal duration before the signal is modulated onto a carrier.

- A signal power level may be arbitrarily selected below the maximum power level; then the **maximum excess delay time**, $T_m$, is said to be the time difference between the first received signal power and the time when the received signal power drops below the selected signal power level [43, 45]. A typical value for this signal drop is -30 dB relative to the strongest signal component, resulting in $T_m = t_{P_{r,0}} - t_{P_{r,-30dB}}$, with $t_{P_{r,0}}$

the time when the first signal component was received and $t_{P_{r,-30dB}}$ the time when the received power level dropped below the -30 dB threshold. It is worthwhile to note that typically $P_{r,0}$ is not equal to $P_{r,max}$, and similarly $t_{P_{r,0}} \neq t_{P_{r,max}}$, as the maximum signal component may be preceded by a number of non-minimum phase precursor multipath components.

- The **mean excess delay time** is the first moment of the power delay profile and is given by [43]

$$\bar{T} = \frac{\sum_{l=1}^{L} r_l^2 \left(\tau_l - \tau_0\right)}{\sum_{l=1}^{L} r_l^2} = \frac{\sum_{l=1}^{L} P\left(\tau_l\right)\left(\tau_l - \tau_0\right)}{\sum_{l=1}^{L} P\left(\tau_l\right)} \tag{D.2}$$

  with $r_l$ the $l^{th}$ received signal amplitude, $\tau_l$ the $l^{th}$ excess delay time, $\tau_0$ the time at which the first received signal is detected and $P(\tau_l)$ the $l^{th}$ received signal power component.

- The **rms delay spread** is the square root of the second central moment of the power delay profile and is given by [43]

$$\sigma_T = \sqrt{\bar{T^2} - \left(\bar{T}\right)^2} \tag{D.3}$$

  with

$$\bar{T^2} = \frac{\sum_{l=1}^{L} r_l^2 \left(\tau_l - \tau_0\right)^2}{\sum_{l=1}^{L} r_l^2} = \frac{\sum_{l=1}^{L} P\left(\tau_l\right)\left(\tau_l - \tau_0\right)^2}{\sum_{l=1}^{L} P\left(\tau_l\right)} \tag{D.4}$$

  This parameter is usually more relevant to designers than the maximum excess delay spread, as the multipath intensity profile of channels with the same value of $T_m$ may differ significantly.

It is possible to distinguish between two distinct scenarios in the time domain when comparing the symbol time with the maximum excess delay. The first case arises whenever the duration of the received multipath components extends beyond the original symbol time, or $T_m > T_s$. The channel is said to experience frequency selective fading and the received signal will suffer from ISI distortion, pulse mutilation and an irreducible BER. However, many of the multipath components are resolvable and distortion can be mitigated by means of various diversity techniques. The second case arises whenever all the received multipath components arrive within a single symbol duration, or $T_s > T_m$. This channel is said to experience frequency non-selective or flat fading and can experience a significant loss in SNR whenever the unresolvable phasor components add up destructively. The most effective way of combating flat fading is to employ an FEC coding scheme or to introduce some form of signal diversity in order to improve the SNR.

#### D.2.1.2 Frequency domain parameters

The following parameters are calculated by using the spaced-frequency correlation function (Fourier transform of the multipath intensity profile) of the channel.

- The **coherence bandwidth**, $B_C$, is the range of frequencies over which the channel will pass the spectral components with approximately equal gain and linear phase, i.e. the channel may be considered to behave like a lowpass filter with the passband being the coherence bandwidth. The coherence bandwidth is proportional to the reciprocal of the excess delay time and the rms delay spread, although the relationship is a function of the exact multipath structure. The coherence bandwidth, in Hz, for a channel is regularly approximated by

$$B_C = \frac{1}{\varepsilon \sigma_\tau} \tag{D.5}$$

  with $\varepsilon = 50$ when a high correlation of 90% and $\varepsilon = 5$ when a moderate correlation of larger than 50% is required over the channel bandwidth [43, 45].

The following parameters are calculated by using the Doppler PSD of the channel.

- The **average Doppler shift/spread**, $B_{T_z}^{(1)}, z = i, q$, gives the average frequency shift or spread that a carrier signal experiences during transmission. It is calculated as the first moment of the Doppler PSD and is given, in Hz, by [105]

$$B_{T_z}^{(1)} = \frac{\int_{-\infty}^{\infty} f S_{T_z}(f)\, df}{\int_{-\infty}^{\infty} S_{T_z}(f)\, df} \tag{D.6}$$

for $z = i, q$, with $S_{T_z}(f)$ the appropriate Doppler PSD, which can be either a Jakes or Gausian PSD as defined in *Eq.* (D.10) and *Eq.* (D.12).

- The **Doppler spread**, $B^{(2)}_{T_z}, z = i, q$, is defined as the square root of the second central moment of the Doppler PSD and is given by [105]

$$B^{(2)}_{T_z} = \sqrt{\frac{\int_{-\infty}^{\infty} \left(f - B^{(1)}_{T_z}\right)^2 S_{T_z}\left(f\right) df}{\int_{-\infty}^{\infty} S_{T_z}\left(f\right) df}} \tag{D.7}$$

with all the parameters as defined earlier.

An important special case exists when the Doppler PSD $S_{T_i}$ and $S_{T_q}$ are identical and symmetrical. It can be shown that the average Doppler shift and the Doppler spread may be expressed under these assumptions as [105]

$$\begin{aligned} B^{(1)}_{T_i} &= B^{(1)}_{T_q} = B^{(1)}_{T} = 0 \\ B^{(2)}_{T_i} &= B^{(2)}_{T_q} = B^{(2)}_{T} = \begin{cases} \frac{f_{d,max}}{\sqrt{2}}, & \text{Jakes PSD} \\ \frac{f_{-3dB}}{\sqrt{2\ln 2}}, & \text{Gaussian PSD} \end{cases} \end{aligned} \tag{D.8}$$

Analogous to the delay spread parameters in the time domain, the coherence bandwidth is used to characterise the channel in the frequency domain. If the bandwidth of a transmitted signal is smaller than the coherence bandwidth, i.e. $B_S < B_C$, the channel exhibits frequency non-selective or flat fading where all frequencies of interest fade with approximately the same amount. If the bandwidth of the transmitted signal is large compared to the coherence bandwidth, i.e. $B_S > B_C$, the channel will exhibit frequency selective or wideband fading and significant ISI will be introduced. This is due to channel gain and phase variations across the spectrum of the transmitted signal as time progresses.

### D.2.2 Frequency non-selective fading

Frequency non-selective or flat fading occurs whenever $T_s > T_m$ and $B_S < B_C$, and is observed whenever the receiver and/or base station experience a motion relative to each other. A random process model of the received power of random interfering waves is required to simulate the effect of flat fading between a fixed and mobile transceiver pair. An incident wave is characterised by its amplitude, phase shift and direction. Each incident wave at the receiver antenna undergoes a Doppler shift due to the motion of the receiver. This results in an increase in frequency if the receiver is advancing into the approaching wavefront and a decrease in frequency if the receiver is moving away from the wavefront. The Doppler shift experienced by the $i^{th}$ multipath component is given by

$$f_{d,i}(t) = \frac{v(t)}{\lambda}\cos(\theta_{A,i}(t)) = \frac{v(t)f_c}{c}\cos(\theta_{A,i}(t)) \tag{D.9}$$

with $\theta_{A,i}(t)$ the angle of arrival of the $i^{th}$ received signal, $v(t)$ the velocity of the mobile unit in m/s, $f_c$ the carrier frequency in Hz and $c$ the speed of light in free space. A simple conclusion is that for $f_{d,max}(t) = f_{d,i}(t) \mid_{\theta_{A,i}(t)=0}$, a maximum Doppler shift will be experienced.

Each arriving wave at the receiver may be considered as complex valued with an in-phase component, $T_i$, and a quadrature phase component, $T_q$, that are independent stationary Gaussian processes. Assuming that the angles of arrival at an omnidirectional receiver are uniformly distributed throughout $[0, 2\pi)$ radians and that the antenna power gain is constant (i.e. a vertical monopole antenna), Clarke [40] determined that the PSD, $S(f) = S_{T_i}(f) + S_{T_q}(f)$, of the in-phase and quadrature components at the receiver is defined as

$$S_{T_i}(f) = S_{T_q}(f) = \begin{cases} \frac{\sigma_0^2}{\pi f_{d,max}\sqrt{1-\left(\frac{f-f_c}{f_{d,max}}\right)^2}} & |f-f_c| \leq f_{d,max} \\ 0 & |f-f_c| > f_{d,max} \end{cases} \tag{D.10}$$

with $\sigma_0^2$ the average transmitted signal power. The normalised Jakes PSD is illustrated in *Fig.* D.1. A full derivation of the Jakes PSD is presented in Appendix A of [105]. In the event that both vertical and horizontal components are received, the resulting Jakes PSD is similar to (D.10), without the poles at $f = \pm f_{d,max}$. A similar model may be derived for communication between two mobile units (satellite communication serves as an example), but this scenario falls outside the scope of this study.

The inverse Fourier transform of $S_{T_i}(f)$ results in the ACF for the Jakes PSD, given by $r(\tau) = r_{T_i}(\tau) + r_{T_q}(\tau)$, with

$$r_{T_i}(\tau) = r_{T_q}(\tau) = \sigma_0^2 J_0(2\pi f_{d,max}\tau) \tag{D.11}$$

where $J_0$ is the zeroth-order Bessel function of the first kind [41, 105]. The normalised Jakes ACF is illustrated in *Fig.* D.1. It is clear that the inverse Fourier transform of the

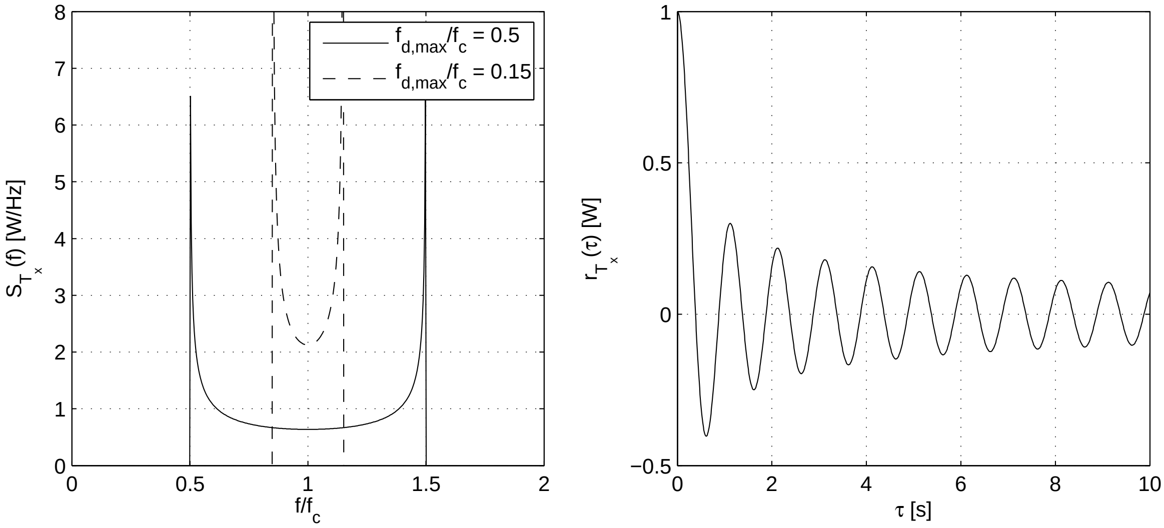

FIGURE D.1: The normalised Jakes functions with $\sigma_0^2 = 1$: a) the PSD for different ratios of $f_{d,max}$ and $f_c$ and b) the ACF normalised to $f_{d,max} = 1$

Doppler PSD, therefore, results in a spaced-time correlation function of the original Doppler power spectrum.

### D.2.3 Frequency selective fading

Frequency selective or channel ISI fading occurs whenever $T_m > T_s$ and $B_C < B_S$, and is observed whenever the same attenuated and phase shifted signal is received via various different paths by the receiver.

It regularly occurs for frequency selective channels that the shape of the Doppler PSD deviates from that of the Jakes PSD for far field echoes. The reason for this is that, unlike the original assumption that the angles of arrival at an omnidirectional receiver are uniformly distributed throughout $[0, 2\pi)$ radians, the far field echoes mostly dominate from a certain direction. This causes the Doppler PSD to have an approximately Gaussian shape and is generally shifted from the origin of the frequency plane. The complex components that add up to give the Gaussian PSD are given by [105]

$$S_{T_i}(f) = S_{T_q}(f) = \frac{\sigma_0^2}{f_c}\sqrt{\frac{\ln 2}{\pi}} \exp\left[-\ln 2\left(\frac{f - f_c}{f_{-3dB}}\right)^2\right] \tag{D.12}$$

with $f_{-3dB}$ the -3 dB cut-off frequency. The normalised Gaussian PSD is illustrated in *Fig.* D.2.

A similar result to the one presented in *Section* D.2.2 for *Eq.* (D.11) is obtained when the

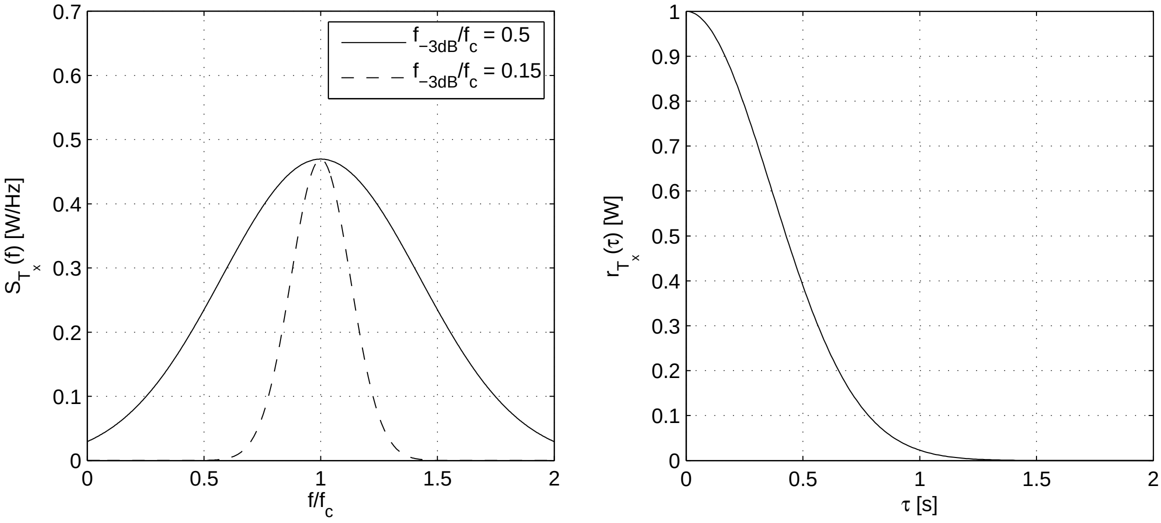

Figure D.2: The normalised Gaussian functions with $\sigma_0^2 = 1$: a) the PSD for different ratios of $f_{-3dB}$ and $f_c$ and b) the ACF normalised to $f_{-3dB} = 1$

inverse Fourier transform of the Gaussian PSD is taken, resulting in the complex components of the Gaussian ACF given by [105]

$$r_{T_i}(\tau) = r_{T_q}(\tau) = \sigma_0^2 \exp\left[-\pi \frac{f_{-3dB}}{\sqrt{\ln 2}}\tau^2\right] \tag{D.13}$$

The normalised Gaussian ACF is illustrated in *Fig.* D.2. Again we find that the inverse Fourier transform of the Doppler PSD results in a spaced-time correlation function of the original Doppler power spectrum.

However, a dual process to the relationship between the spaced-time correlation functions of the Doppler power spectra exists. The Fourier transform of the multipath intensity profile may be calculated as well, resulting in a spaced-frequency correlation function. This is a useful parameter, as it indicates the frequency response of the channel, and is typically used in conjunction with the calculated coherence bandwidth of *Eq.* (D.5).

## D.3 Statistical Properties of the Rayleigh and Rician Processes

Now that most of the useful elementary properties of the fading channels and their corresponding effects on signals have been clarified, we may proceed to the statistical domain where these channels can be characterised by various useful statistical means.

### D.3.1 PDF of the amplitude and phase

The received signal may consist of multiple reflective rays and a significant LOS component. The significance of this component is measured with the Rician factor, $c_R$, that describes the ratio of the power of the LOS component, $m(t) = \rho e^{j(2\pi f_\rho t + \theta_\rho)}$, to the sum of the power of all the scattered components and is given (in dB) by

$$c_R = 10 \log_{10} \left( \frac{\rho^2}{2\sigma_0^2} \right) \tag{D.14}$$

where $\rho$ denotes the amplitude of the LOS component and $\sigma_0^2$ the power of the scattered components, which is equivalent to the power of the real valued Gaussian random process.

In general, the amplitude envelope of a Rician process, $\xi(t)$, yields a PDF, $p_\xi(x)$, given by [43, 105]

$$p_\xi(x) = \begin{cases} \frac{x}{\sigma_0^2} I_0\left(\frac{x\rho}{\sigma_0^2}\right) \exp\left[-\frac{x^2+\rho^2}{2\sigma_0^2}\right], & x \geq 0 \\ 0, & x < 0 \end{cases} \tag{D.15}$$

with $I_0(\cdot)$ the $0^{th}$ order modified Bessel function of the first kind. It should be clear that $p_\xi(x)$ depends on $\rho$ and $\sigma_0^2$, but is independent of the exact shape of the Doppler PSD.

In the event that the LOS component diminishes, or for $\rho \to 0 \Rightarrow c_R \to 0$, the Rician process $\xi(t)$ reduces to a simpler Rayleigh process $\zeta(t)$, with the PDF given by

$$p_\zeta(x) = \begin{cases} \frac{x}{\sigma_0^2} \exp\left[-\frac{x^2}{2\sigma_0^2}\right], & x \geq 0 \\ 0, & x < 0 \end{cases} \tag{D.16}$$

The PDFs of $p_\xi(x)$ and $p_\zeta(x)$ for various scenarios are illustrated in *Fig.* D.3.

It is also possible to derive the PDF, $p_\vartheta(\theta, t)$, of the phase $\vartheta(t)$, as for the case of the amplitude envelope of the received signal. It is given by the following relation [58]

$$\begin{aligned} p_\vartheta(\theta, t) = \frac{\exp\left(-\frac{\rho^2}{2\sigma_0^2}\right)}{2\pi} \Bigg\{ & 1 + \frac{\rho}{\sigma_0}\sqrt{\frac{\pi}{2}} \cos(\theta - 2\pi f_\rho t - \theta_\rho) \exp\left(\frac{\rho^2 \cos^2(\theta - 2\pi f_\rho t - \theta_\rho)}{2\sigma_0^2}\right) \\ & \cdot \left[1 + erf\left(\frac{\rho \cos(\theta - 2\pi f_\rho t - \theta_\rho)}{\sqrt{2\sigma_0^2}}\right)\right], \qquad -\pi < \theta \leq \pi \end{aligned} \tag{D.17}$$

where $erf(\cdot)$ denotes the error function, $f_\rho$ the Doppler frequency of the LOS component and $\theta_\rho$ a fixed phase reference of the LOS component. It is worthwhile to note that the time dependence of $p_\vartheta(\theta, t)$ is due to $f_\rho$. Therefore, $p_\vartheta(\theta, t)$ only becomes truly strict-sense stationary, i.e. $p_\vartheta(\theta)$, when $f_\rho = 0$, while $\rho \neq 0$.

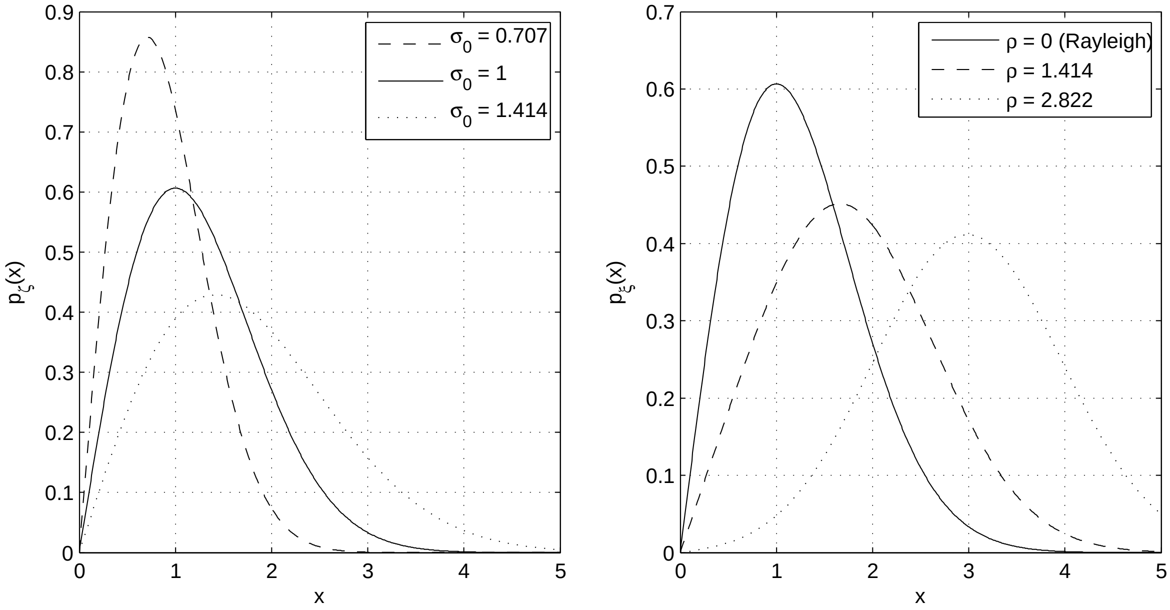

FIGURE D.3: The PDF of the respective envelopes of a) a Rayleigh process with various $\sigma_0^2$ levels and b) a Rician process with various $\rho$ levels ($\sigma_0^2 = 1$)

As $\rho \rightarrow 0$, it follows that $\xi(t) \rightarrow \zeta(t)$ and a uniform distribution is obtained, as given by

$$p_\vartheta(\theta) = \frac{1}{2\pi}, \qquad -\pi < \theta \leq \pi \tag{D.18}$$

Finally, it should be noted that, as $\rho \rightarrow \infty$, $p_\vartheta(\theta) \rightarrow \delta(\theta - 2\pi f_\rho t - \theta_\rho)$. The PDF of the phase, $p_\vartheta(\theta)$ is illustrated in *Fig.* D.4 for various values of $\rho$.

### D.3.2 Level crossing rate and average duration of fades

Additional statistics of the Rician envelope that are of interest include the LCR, $N_\xi(R_S)$, and the ADF, $T_{\xi_-}(R_s)$, as they are used to relate the time rate of change of the received signal to the signal level and velocity of the mobile, which is useful when designing diversity techniques. It is assumed that the two underlying Gaussian processes are independent and uncorrelated (zero cross-correlation), and that their ACFs are identical.

The **LCR**, defined as the expected rate at which the Rayleigh fading envelope, normalised to the local rms signal level, crosses a specified level, $R_s$, in a positive-going direction (with unit crossings/s), is given by [58]

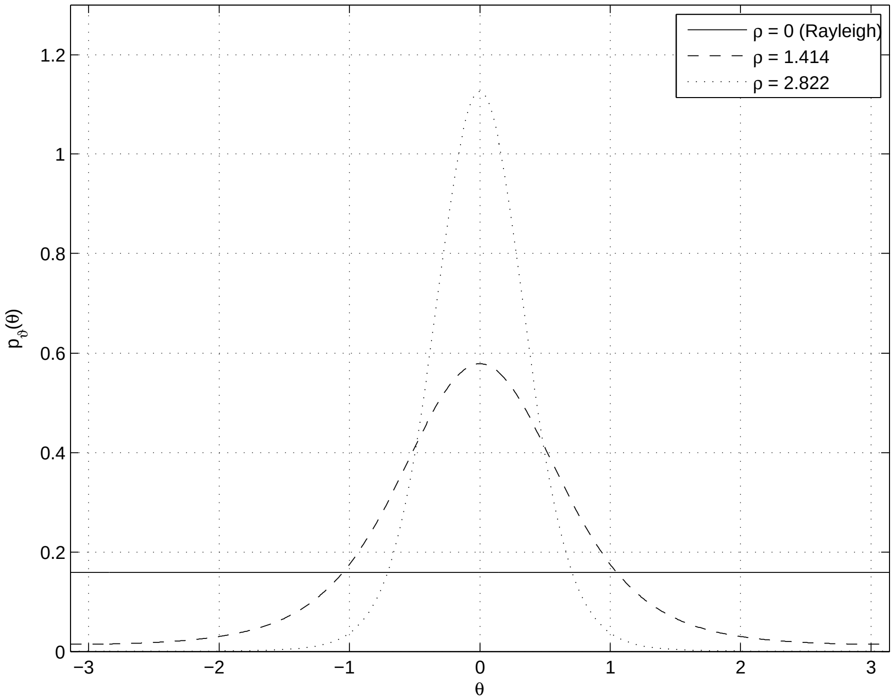

FIGURE D.4: The PDF of the phase $p_\vartheta\left(\theta\right)$ of Rayleigh and Rician processes ($\sigma_0^2 = 1$, $f_\rho = 0$ and $\theta_\rho = 0$)

$$\begin{gathered}N_\xi\left(R_s\right) = \tfrac{R_s\sqrt{2\beta}}{\pi^{3/2}\sigma_0^2}\exp\left(-\tfrac{R_s^2-\rho^2}{2\sigma_0^2}\right)\int\limits_0^{\pi/2}\cosh\left(\tfrac{R_s\rho}{\sigma_0^2}\cos\theta\right)\\ \left\{\exp\left[-\left(c_\alpha\rho\sin\theta\right)^2\right]+\sqrt{\pi}c_\alpha\rho\sin\left(\theta\right)\cdot erf\left(c_\alpha\rho\sin\theta\right)\right\}d\theta,\quad R_s\geq 0\end{gathered} \tag{D.19}$$

with $c_\alpha = 2\pi f_\rho/\sqrt{2\beta}$ and $\beta = \beta_i = \beta_q = -\ddot{r}_{T\,z}(0),\ z = i, q$. It can be shown that for the Jakes and Gaussian PSD, $\beta$ can be determined as [105]

$$\beta = \begin{cases} 2\left(\pi f_{d,max}\sigma_0\right)^2, & \text{Jakes PSD} \\ 2\left(\pi f_{-3dB}\sigma_0\right)^2\big/\ln 2, & \text{Gaussian PSD} \end{cases} \tag{D.20}$$

As $c_\alpha$ is a function of $f_\rho$, the Doppler frequency of the LOS component influences $N_\xi(R_S)$. However, if $f_\rho = 0 \Rightarrow c_\alpha = 0$, the LCR reduces to

$$N_\xi\left(R_s\right) = \sqrt{\frac{\beta}{2\pi}}\cdot p_\xi\left(R_s\right),\quad R_s \geq 0 \tag{D.21}$$

with $p_\xi\left(R_s\right)$ the PDF of the amplitude envelope given in *Eq.* (D.15).

Finally, as $\rho \rightarrow 0$, it follows that $\xi(t) \rightarrow \zeta(t)$, resulting in the LCR of the Rayleigh process described by

$$N_\zeta\left(R_s\right) = \sqrt{\frac{\beta}{2\pi}} \cdot p_\zeta\left(R_s\right), \quad R_s \geq 0 \tag{D.22}$$

The influence of the parameters $f_{d,max}$ and $\rho$ on the LCR normalised with $f_{d,max}$ is shown in *Fig.* D.5.

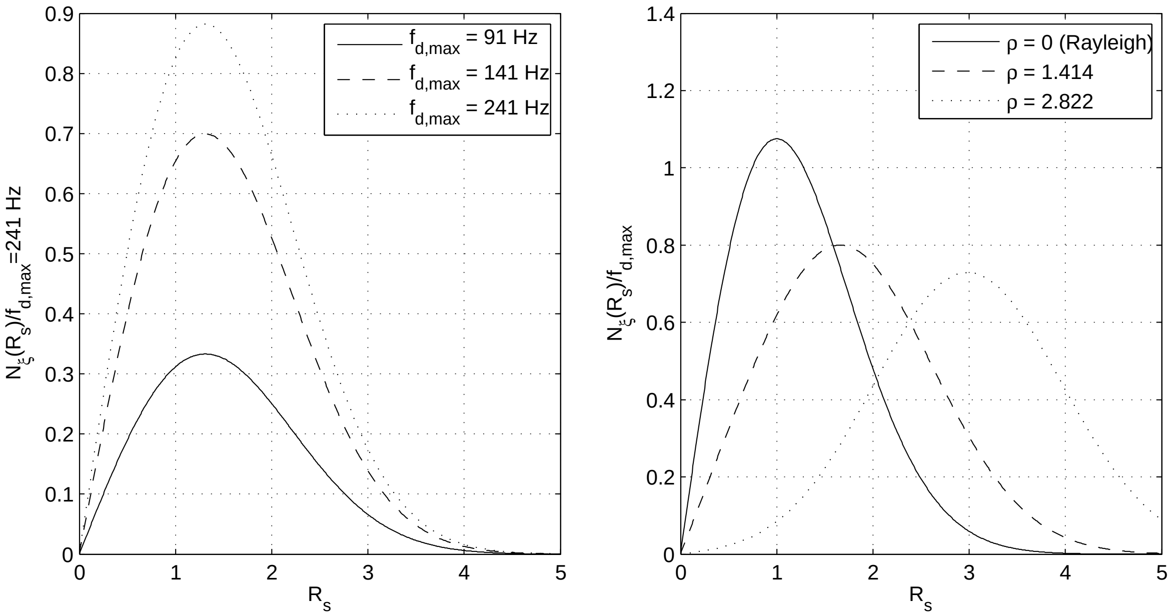

FIGURE D.5: The effect on the LCR for a Rician process as a) $f_{d,max}$ is varied and normalised with $f_{d,max} = 241$ Hz ($f_\rho = 0$ and $\theta_\rho = 0$) and b) $\rho$ is varied and normalised with $f_{d,max} = 91$ Hz ($f_{d,max} = 91$ Hz, $f_\rho = 0$ and $\theta_\rho = 0$)

The **ADF** is defined as the average period of time for which the channel amplitude is below a specified level, $R_s$, and is expressed as

$$\begin{aligned} \mathrm{T}_{\xi-}\left(R_s\right) &= \tfrac{F_{\xi-}\left(R_s\right)}{N_\xi\left(R_s\right)} \\ &= \sqrt{\tfrac{\beta}{2\pi}} \cdot \frac{\exp\left(\frac{R_s^2}{2\sigma_0^2}\right)}{R_s I_0\left(\frac{R_s\rho}{\sigma_0^2}\right)} \int\limits_0^{R_s} x \cdot \exp\left(-\tfrac{x^2}{2\sigma_0^2}\right) I_0\left(\tfrac{x\rho}{\sigma_0^2}\right) dx, \quad R_s \geq 0 \end{aligned} \tag{D.23}$$

$$\mathrm{T}_{\zeta-}\left(R_s\right) = \frac{F_{\zeta-}\left(R_s\right)}{N_\zeta\left(R_s\right)} = \sqrt{\frac{\beta}{2\pi}} \cdot \frac{\sigma_0^2}{R_s}\left[\exp\left(\frac{R_s^2}{2\sigma_0^2}\right) - 1\right], \quad R_s \geq 0 \tag{D.24}$$

for the Rician and Rayleigh processes respectively, with $F_{\xi-}(R_s) = P(\xi(t) \leq R_s)$ and $F_{\zeta-}(R_s) = P(\zeta(t) \leq R_s)$ the CDFs of the respective processes.

Finally, for low fading levels, i.e. for $R_s \ll 1$, a linear approximation for the ADF for both processes can be given as [105]

$$\mathrm{T}_{\xi-}\left(R_s\right) \approx \mathrm{T}_{\zeta-}\left(R_s\right) \approx R_s\sqrt{\frac{\beta}{2\pi}}, \quad R_s \geq 0 \tag{D.25}$$

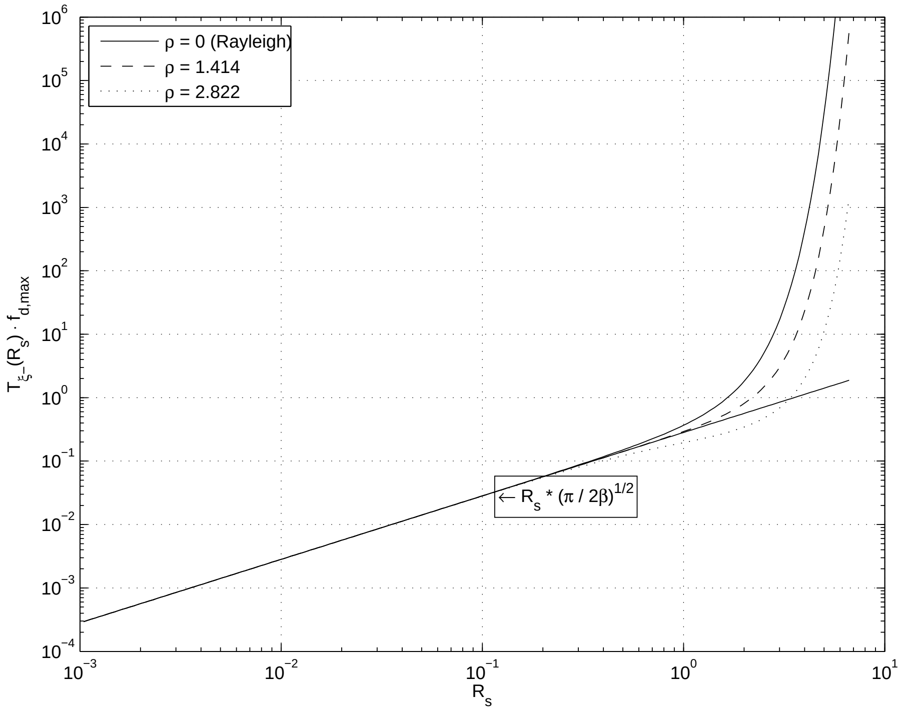

FIGURE D.6: The ADF of a Rician process for various values of $\rho$ ($f_{d,max} = 91$ Hz and $\sigma_0^2 = 1$)

The ADF for a Rician process as given in *Eq.* (D.23) is illustrated in *Fig.* D.6 for various levels of $\rho$. Notice that the normalised version (i.e. a version multiplied with $f_{d,max}$) of the linear approximation of *Eq.* (D.25) is also indicated; it is clear that the approximation holds true as long as $R_s$ is sufficiently small.

## D.4 DETERMINISTIC CHANNEL MODELLING

### D.4.1 Generating a coloured Gaussian process

Two fundamental methods are regularly used for the modelling of a coloured Gaussian random process: the filter method and the sum-of-sinusoids method. This study will focus on the latter, and filter methods are briefly introduced for completeness. It should be noted that hidden Markov models exist with good results [106], but that this type of model has not been widely adopted.

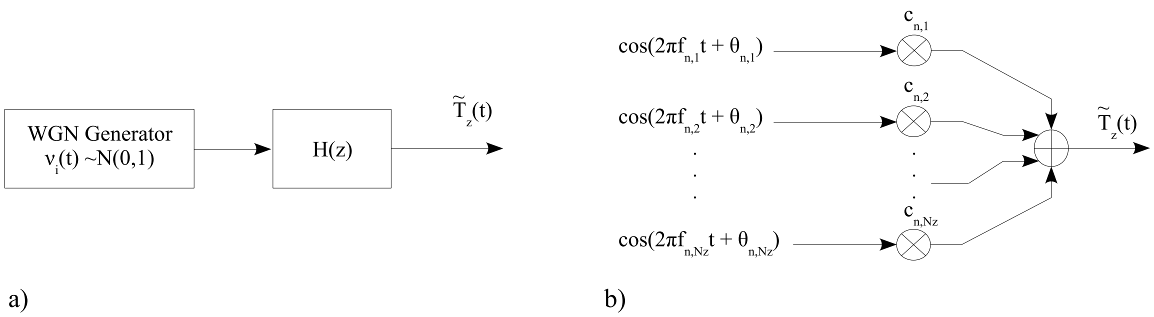

FIGURE D.7: Reference models for generating a deterministic coloured Gaussian process using a) the filter method and b) the sum-of-sinusoids method

#### D.4.1.1 Filter methods

When using the filter method, it is frequently assumed that an ideal filter is used and that the transfer function, $H_i(f)$ can be fitted to any given frequency response with arbitrary precision. A zero mean AWGN input, $\nu_i(t) \backsim N(0,1)$ will result in a zero mean output where the absolute value matches the square of the absolute value of the transfer function, resulting in $S_i(f) = |H_i(f)|^2$. This is illustrated in *Fig.* D.7.

In a simulation environment, the transfer functions for such filters are usually represented in the $z$-domain as

$$H_i(z) = A_i \frac{\prod_{n=1}^{N_i/2} \left(z - \rho_{i,n} e^{j\varphi_{i,n}}\right)\left(z - \rho_{i,n} e^{j\varphi_{i,n}}\right)}{\prod_{n=1}^{N_i/2} \left(z - \rho_{\infty,n} e^{j\varphi_{\infty,n}}\right)\left(z - \rho_{\infty,n} e^{j\varphi_{\infty,n}}\right)} \tag{D.26}$$

with $N_0$ the filter order and $A_0$ a scaling constant to ensure that the mean output power of the filter is equal to $\sigma_0^2$.

It should, however, be immediately clear that the assumption of an ideal filter is unpractical, as it would require $N_0 \to \infty$. This problem may be overcome by reducing the complexity of the implemented FIR/IIR filter and matching the magnitude function of the filter as closely as possible to the square root of the required Doppler PSD. This, however, yields a new problem of optimising the filter coefficients. This challenge has been addressed by various authors [56, 85, 107].

It is worth noting that a decrease in $N_0$ leads to a lower filter quality factor, $Q$, resulting in less attenuation in the frequency range $f_{d,max} \leq f \leq \infty$. However, as the magnitude of the theoretical model in this frequency range is 0 dB, we can safely assume that a decrease in

$N_0$ would result in additional frequency spreading that yields results more pessimistic than the theoretical models [85]. These pessimistic results, however, do not have to be interpreted as unrealistic, as they correspond more closely to a worst case scenario that is regularly encountered when determining a signal power budget.

#### D.4.1.2 Sum-of-sinusoids methods

The sum-of-sinusoids or Rician method [41, 105] is based on the principle of the superposition of an infinite number of weighted sinusoids with frequencies spaced at equal distances and random phases. A stochastic Gaussian process $T_z(t)$ can then be generated as illustrated in *Fig.* D.7 and described mathematically as

$$T_z\left(t\right) = \lim_{N_z \to \infty} \sum_{n=1}^{N_z} c_{z,n} \cos\left(2\pi f_{z,n} t + \theta_{z,n}\right) \tag{D.27}$$

with

$$\begin{aligned} c_{z,n} &= 2\sqrt{\Delta f_z S_{T_z}\left(f_{z,n}\right)} \\ f_{z,n} &= n \cdot \Delta f_z \end{aligned} \tag{D.28}$$

where the phases $\theta_{z,n}$ are random variables uniformly distributed over $[0, 2\pi)$ and $\Delta f_i$ is chosen in such a way that $f_{z,n}$ covers the entire frequency range up to $f_{d,max}$.

It is not possible to generate the ideal stochastic process on a computer platform. It is, however, plausible to reduce the number of harmonics to a finite value, resulting in a new stochastic process. However, as the random phases of this stochastic process are generated with a PRNG taken as the realisation (i.e. the outcomes) of this process, it becomes obvious that the now limited stochastic process of *Eq.* (D.27) becomes a deterministic process $\tilde{T}_z\left(t\right)$ described by

$$\tilde{T}_z\left(t\right) = \sum_{n=1}^{N_z} c_{z,n} \cos\left(2\pi f_{z,n} t + \theta_{z,n}\right) \tag{D.29}$$

Note that an appropriate choice of the (Doppler) parameters $c_{z,n}$, $f_{z,n}$ and $\theta_{z,n}$ as discussed in *Section* D.4.5, will approximate the statistical properties of $T_z(t)$ very closely for $\tilde{T}_z\left(t\right)$, even for a discrete-time simulation model where $t$ is replaced with $t = k_i T_s$, where $k_i$ represents an integer valued time index and $T_s$ the sampling interval. In order to achieve this approximation, a trade off is made between the realisation complexity (in this case the choice of $N_z$), which should be kept as low as possible, while achieving the correct statistical properties that is achieved by keeping $N_z$ sufficiently large. A good choice in general is $N_z \geq 7$ [105], however this is still dependent on the choice of the implementation method.

### D.4.2 Generating a Rayleigh/Rician process for frequency non-selective channels

Two independent coloured Gaussian processes form the fundamental building blocks required in order to create either a Rayleigh or Rician process. As the Rayleigh process is a special case ($\rho = 0$) of the Rician process, both processes will be referred to as Rician, unless specifically stated otherwise. In order to ensure that the required statistical properties of the Rician process are achieved, it is necessary to ensure that the coloured Gaussian processes have identical ACFs, i.e. $r_{Ti}(\tau) = r_{Tq}(\tau)$, and zero cross-correlation, $r_{Ti,q}(\tau) = 0$. Using *Eq.* (D.29), a complex deterministic Rician process can be created by summing two independent coloured Gaussian processes as

$$\tilde{T}(t) = \tilde{T}_i(t) + j\tilde{T}_q(t) \tag{D.30}$$

The absolute value of *Eq.* (D.30), given by

$$\begin{aligned} \tilde{\zeta}(t) &= \left|\tilde{T}(t)\right| = \left|\tilde{T}_i(t) + j\tilde{T}_q(t)\right| \\ \tilde{\xi}(t) &= \left|\tilde{T}_\rho(t)\right| = \left|\tilde{T}_i(t) + j\tilde{T}_q(t) + m(t)\right| \end{aligned} \tag{D.31}$$

results in either a Rayleigh or Rician process respectively, with $m(t) = m_1(t) + jm_2(t)$ the LOS component. A deterministic simulation model for a Rician process is illustrated in *Fig.* D.8.

### D.4.3 Generating a Wideband Rayleigh/Rician process for frequency selective channels

The complex Rician process of *Fig.* D.8 may be used as a building block for a wideband Rician fading process. Such a process is used to simulate multipath fading wireless channels, which are typically characterised by a power delay profile describing the relative power level and delay between the $L$ different paths by which the transmitted signal, $t_k(t)$ (of the $k^{th}$ user) has been received. Each of the $L$ complex Rician processes ($CRP_l$) can be characterised by a unique Doppler frequency and LOS component. Every branch is scaled with the average

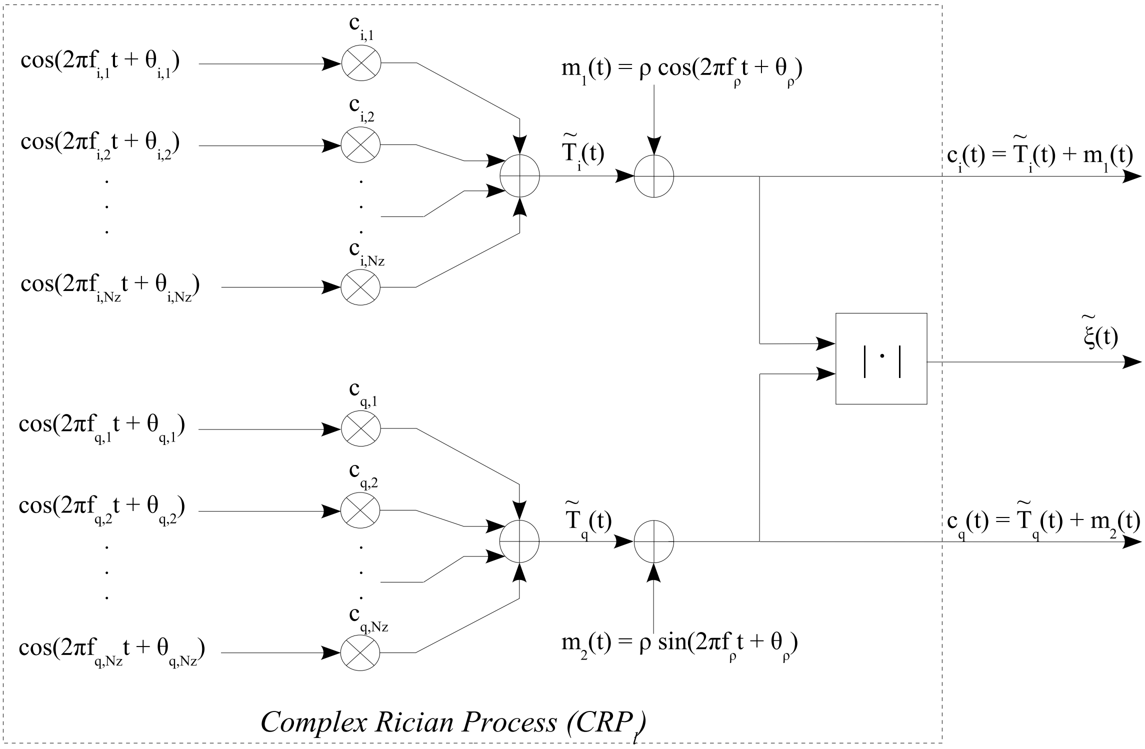

FIGURE D.8: Simulation model for a deterministic Rician process

amplitude and delayed with the time constant associated with that branch as characterised in the power delay profile. All the branches are then linearly combined to form the final output.

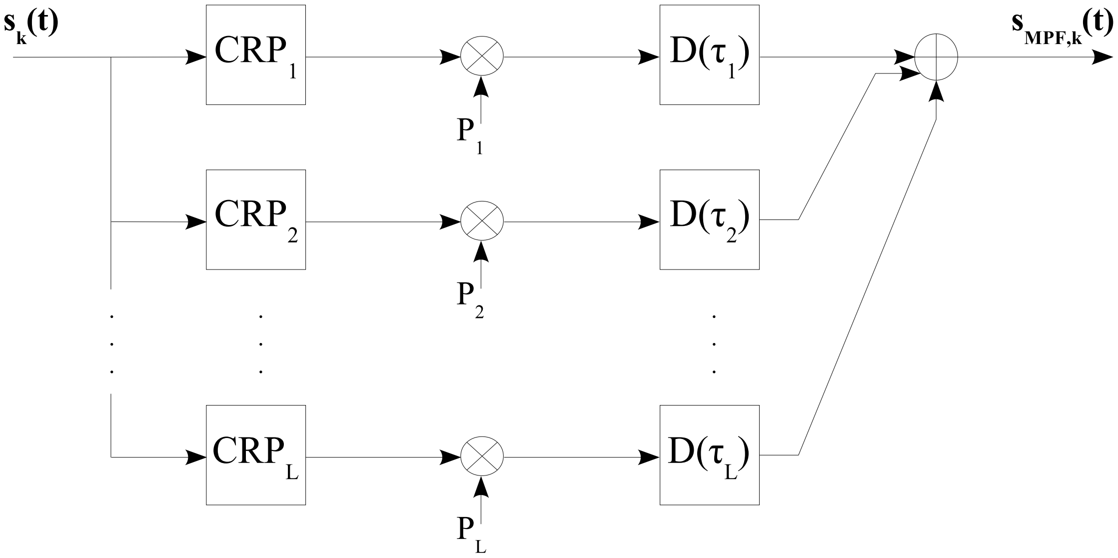

FIGURE D.9: Block diagram of a deterministic wideband Rician process

It should be noted that the linear combination of $L$ versions of the input may increase the power of the output relative to the power of the input, which is not feasible for practical channels. It is, therefore, necessary to scale the power provided by the process such that

$$\sum_{l=1}^{L} P_l^2 = 1 \tag{D.32}$$

### D.4.4 Statistical properties of the deterministic Rician process based on the sum-of-sinusoids method

Many of the elementary and statistical properties described earlier can be related to the Doppler coefficients directly [105]. In the following definitions, it is always assumed that $f_{z,n} \neq 0$ for $n = 1, 2, ..., N_z$ and $z = i, q$.

- The **mean value** of a deterministic Rician process is given by

$$\tilde{m}_{T_z} = 0 \tag{D.33}$$

- The **mean power** of a deterministic Rician process is given by

$$\tilde{\sigma}_{T_z}^2 = \sum_{n=1}^{N_z} \frac{c_{z,n}^2}{2} \tag{D.34}$$

- The **ACF** of a deterministic Rician process is given by

$$\tilde{r}_{T_z T_z}(\tau) = \sum_{n=1}^{N_z} \frac{c_{z,n}^2}{2} \cos\left(2\pi f_{z,n}\tau\right) \tag{D.35}$$

  It is instructive to note that the ACF at $\tau = 0$ is equivalent to the mean power of the process, i.e. $r_{T_z T_z}(0) = \tilde{\sigma}_{T_z}^2$.

- The *Cross-Correlation Function* **(CCF)** of two deterministic processes is given by

$$\tilde{r}_{T_i T_q}(\tau) = \sum_{\substack{n=1 \\ f_{i,n}=\pm f_{q,m}}}^{N} \frac{c_{i,n} c_{q,m}}{2} \cos\left(2\pi f_{i,n}\tau - \theta_{i,n} \pm \theta_{q,m}\right) \tag{D.36}$$

  with N the largest value of $N_i$ and $N_q$. If the two functions are uncorrelated, it follows that $\tilde{r}_{T_i T_q}(\tau) = 0$ if $f_{i,n} \neq \pm f_{q,m}$ holds for all $n = 1, 2, ..., N_i$ and $m = 1, 2, ..., N_q$, a result that implies that the absolute values of the discrete Doppler frequencies are different from each other.

- The **PSD** of a deterministic Rician process is a symmetrical line spectrum given by

$$\tilde{S}_{T_z}(f) = \sum_{n=1}^{N_z} \frac{c_{z,n}^2}{4} \left[\delta(f - f_{z,n}) + \delta(f + f_{z,n})\right] \tag{D.37}$$

- The **cross-PSD** of two deterministic processes is given by

$$\begin{aligned}\tilde{S}_{T_iT_q}(f) = \sum_{\substack{n=1 \\ f_{i,n}=\pm f_{q,m}}}^{N} \tfrac{c_{i,n}c_{q,m}}{4} &[\delta(f - f_{i,n}) \cdot e^{-j(\theta_{i,n}\mp\theta_{q,m})} \\ &+\delta(f + f_{i,n}) \cdot e^{-j(\theta_{i,n}\mp\theta_{q,m})}]\end{aligned} \tag{D.38}$$

  with N the largest value of $N_1$ and $N_2$, $n = 1, 2, ..., N_i$ and $m = 1, 2, ..., N_q$. $\tilde{S}_{T_iT_q}(f) = 0$ if $f_{i,n} \neq \pm f_{q,m}$.

- The **periodicity** of a deterministic process can be determined if the greatest common divisor, given by

$$F_z = \gcd\{f_{z,1}, f_{z,2}, \ldots f_{z,N_z}\} \neq 0 \tag{D.39}$$

  exists. The process is then periodic with period $T_i = 1/F_i$, implying that $\tilde{T}_z(t + T_i) = \tilde{T}_z(t)$ and $\tilde{r}_{Tz}(\tau + T_i) = \tilde{r}_{Tz}(\tau)$.

### D.4.5 Methods to determine the Doppler parameters

A number of different approaches exist to determine the approximate Doppler parameters (the Doppler coefficients $c_{z,n}$, the discrete Doppler frequencies $f_{z,n}$ and the Doppler phases $\theta_{z,n}$) used in the simulation models. This section serves to aid with the design of such simulation models. Each subsection will provide references to additional reading on the derivation of these parameters to the interested reader. The following subsections will mainly focus on the optimal design of the Doppler coefficients $c_{z,n}$ and the discrete Doppler frequencies $f_{z,n}$, as these methods are independent of Doppler phases $\theta_{z,n}$. A number of different approaches have been adopted to initialise the phase condition. These phases can be set to $\theta_{z,n} = 0$ or $\theta_{z,n} = 2\pi n/N_z$ with ($n = 1, 2, ..., N_z$), but both cases result in undesirable initial transient behavior for the Rician process. An alternative approach is to set $\theta_{z,n}$ equal to the outcome of a random uniformly distributed process over $[-\pi,\pi)$ as in [47, 108]. This method has been adopted for the remainder of this study.

### D.4.5.1 Method of equal distances

The *Method of Equal Distances* (MED) is similar to that originally proposed by Rice as the Doppler frequencies $f_{z,n}$ are spaced with equal distances between each neighbouring harmonic. The main difference is in the way that the Doppler coefficients $c_{z,n}$ are matched to the desired Jakes PSD. The desired Doppler parameters may be determined as [59, 60]

$$\begin{aligned} f_{z,n} &= \tfrac{f_{d,max}}{2N_z}\left(2n-1\right) \\ c_{z,n} &= \tfrac{2\sigma_0}{\sqrt{\pi}} \cdot \sqrt{\arcsin\left(\tfrac{n}{N_z}\right) - \arcsin\left(\tfrac{n-1}{N_z}\right)} \end{aligned} \tag{D.40}$$

with $n = 1, 2, ..., N_z$ and $z = i, q$.

The main disadvantage of this method is the relatively short period of the underlying deterministic process $\tilde{T}_z(t)$. This is due to the fact that the Doppler frequencies $f_{z,n}$ are spaced at equal distances from their neighbours, resulting in a small periodicity given by $F_z = \gcd\{f_{z,n}\}_{n=1}^{N_z} = f_{d,max}/(2N_z)$. This unwanted behaviour is easily observed in the periodical behaviour of the ACF.

A complex deterministic process may be generated as $\tilde{T}(t) = \tilde{T}_i(t) + j\tilde{T}_q(t)$. In order to ensure that $\tilde{T}_i(t)$ and $\tilde{T}_q(t)$ are uncorrelated, it is necessary to choose $f_{i,n} \neq f_{q,m}$ with $n = 1, 2, ..., N_i$ and $m = 1, 2, ..., N_q$. This is easily achieved by choosing $N_q = N_i + 1$.

### D.4.5.2 Mean square error method

Similar to the MED, the *Mean Square Error Method* (MSEM) only differs from the Rice method in the way that the Doppler coefficients $c_{z,n}$ are matched to the desired Jakes PSD, as it, too, is based on the summation of equidistance harmonics. In this case, the $c_{z,n}$ values are derived from the mean squared error between the theoretical and model parameter ACFs. The desired Doppler parameters may be determined as [59]

$$\begin{aligned} f_{z,n} &= \tfrac{f_{d,max}}{2N_z}\left(2n-1\right) \\ c_{z,n} &= 2\sigma_0 \cdot \sqrt{\tfrac{1}{\tau_{max}} \int_0^{\tau_{max}} J_0\left(2\pi f_{d,max}\tau\right) \cos\left(2\pi f_{z,n}\tau\right) d\tau} \end{aligned} \tag{D.41}$$

with $\tau_{max} = N_z/(2f_{d,max})$ an appropriate time interval over which the approximation of the ACF is of interest.

As with the MED, the MSEM also suffers from periodical behaviour in the ACF. This is due to the fact that the Doppler frequencies are determined in the same way for both methods. The MSEM, however, does yield a lower relative model error.

### D.4.5.3 Method of exact Doppler spread

The *Method of Exact Doppler Spread* (MEDS) is a quasi-optimal procedure designed specifically to obtain a Jakes shaped PSD. The desired Doppler parameters may be determined as [50]

$$\begin{aligned} f_{z,n} &= f_{d,max} \sin\left[\frac{\pi}{2N_z}\left(n-\frac{1}{2}\right)\right] \\ c_{z,n} &= \sigma_0\sqrt{\frac{2}{N_z}} \end{aligned} \tag{D.42}$$

for all $n = 1, 2, ..., N_z$ and $z = i, q$.

The MEDS has the advantage that $F_z = \gcd\{f_{z,n}\}_{n=1}^{N_z} \approx 0$, resulting in an almost infinite period (recall that $T_z = 1/F_z$).

### D.4.5.4 Jakes method

The *Jakes Method* (JM) was specifically designed to obtain a Jakes shaped PSD and is a very popular method. The desired Doppler parameters may be derived from the original design equations and are given as [49]

$$\begin{aligned} f_{z,n} &= \begin{cases} f_{d,max}\cos\left(\frac{n\pi}{2N_z-1}\right), & n = 1, 2, \ldots, N_z-1, \quad z = \mathrm{i, q} \\ f_{d,max}, \quad n = N_z, & z = \mathrm{i, q} \end{cases} \\ c_{z,n} &= \begin{cases} \frac{2\sigma_0}{\sqrt{N_z-\frac{1}{2}}}\sin\left(\frac{n\pi}{N_z-1}\right), & n = 1, 2, \ldots, N_z-1, \quad z = \mathrm{i} \\ \frac{2\sigma_0}{\sqrt{N_z-\frac{1}{2}}}\cos\left(\frac{n\pi}{N_z-1}\right), & n = 1, 2, \ldots, N_z-1, \quad z = \mathrm{q} \\ \frac{\sigma_0}{\sqrt{N_z-\frac{1}{2}}}, \quad n = N_z, & z = \mathrm{i, q} \end{cases} \end{aligned} \tag{D.43}$$

with the Doppler phases $\theta_{z,n} = 0$. In order to maintain the notation as used thus far, it should be ensured that, for the JM, $N_i = N_q$.

The main disadvantage of the JM is the existence of a large correlation between the real and imaginary parts of the complex Gaussian process due to the high correlation between the $\sin(\cdot)$ and $\cos(\cdot)$ functions. This also results in a non-zero cross-correlation between $\tilde{T}_i(t)$ and $\tilde{T}_q(t)$, indicating that the condition of independent real and imaginary parts are not met. This has resulted in a vigorous investigation by various authors to either motivate or discredit the method [47, 49, 51, 52, 109]. However, this model still remains very popular and the error introduced can be mostly overcome by i) initialising the simulation with $\theta_{z,n}$ equal to the outcome of a random uniformly distributed process over $[-\pi,\pi)$ and ii) increasing the number of harmonics to more than eight [105].

## D.5 PRACTICAL CONSIDERATIONS FOR AWGN CHANNELS

A common benchmark for assessing the performance of digital communication systems is the addition of Gaussian noise to the signal prior to the receiver filter and detection. This may sound like a trivial exercise, but there are a number of important considerations to take into account to ensure that accurate observations can be made.

Shanmugan describes in [110] that a resistor will generate a voltage, $V$, which has a Gaussian distribution with zero mean and variance given by

$$E\left[V^2\right] = \frac{2\left(\pi k T\right)^2}{3h} R \qquad \mathrm{V}^2 \tag{D.44}$$

with $k$ the Boltzman constant and $T$ the temperature in Kelvin. The PSD has also been shown to be equivalent to

$$G_\nu(f) = \frac{2Rh\left|f\right|}{e^{\left(\frac{h|f|}{kT}\right)} - 1} \qquad \mathrm{V}^2/\mathrm{Hz} \tag{D.45}$$

This function is essentially flat at room temperature for frequencies varying from DC to $\mid f \mid < 10^{12}$ Hz. This noise may therefore be modelled as having a constant PSD over all the frequencies of interest for practical communication systems. The available power spectral density at an optimally matched (i.e. maximum power transfer) load is given by

$$G_\nu(f) = \frac{kT}{2} \qquad \mathrm{W}/\mathrm{Hz} \tag{D.46}$$

which is constant for all frequencies at a specific temperature. The implication of this is that zero mean stationary white Gaussian noise can be used as a model for the noise that corrupts the signal at the receiver input. The ACF of a zero mean Gaussian white noise process, $V(t)$, with variance $\sigma_\nu^2$ is given by

$$R_{\nu\nu}\left(\tau\right) = \sigma_\nu^2 \delta\left(\tau\right) \tag{D.47}$$

The PSD can by obtained by applying the Wiener-Khintchine theorem. This yields

$$G_{\nu}(f) = \Im \left\{ R_{\nu\nu}(\tau) \right\} = \sigma_{\nu}^2 \qquad \mathrm{W/Hz} \tag{D.48}$$

Computer based simulation models of real systems are done in the discrete time domain, hence a certain sampling frequency is associated with the system. This results in a sequence of random numbers with a Gaussian amplitude distribution, zero mean and variance given by $\sigma_n^2 = N_0$ to represent the AWGN. This sequence is easily generated by implementing a pseudorandom algorithm like the Wichmann-Hill algorithm [16] for generating uniform data, which can be mapped to a normal distribution with the Marsaglia-Bray mapping algorithm [111]. A scaling factor of 2 is usually used to take the complex baseband notation into account. This leads to complex AWGN with independent real and imaginary parts, both with variance given by $\sigma_n^2 = \frac{N_0}{2}$.

Since the entire simulated system is bandlimited to the sampling frequency, $f_s$, it is necessary to take this limitation into account for the sampled noise. The original wideband noise now becomes bandlimited to $-\frac{f_s}{2} < f_s < \frac{f_s}{2}$ with spectral density given by $\frac{N_0}{2}$ W/Hz. The power of the noise, $N(t)$, or equivalently the variance, is given by $\sigma_n^2 = N_0 B$ W, with $B$ the noise equivalent bandwidth in Hz. Therefore, if the sampling frequency of the system is $f_s$ and the baud rate is 1, i.e. the system is oversampled or interpolated at a factor equal to $f_s$, the variance of the real and imaginary components of the Gaussian random noise source becomes $\sigma_n^2 = \frac{N_0 f_s}{2}$.

Assuming a signal power or the energy per symbol as $S$, the SNR then becomes

$$\frac{E_s}{N_0} = \gamma_s = 10 \log_{10}\left(\frac{S}{N_0}\right) \qquad \mathrm{dB} \tag{D.49}$$

The SNR is an important parameter when communication systems are concerned. However, it is a relatively poor parameter for comparing various systems with different coding and modulation techniques due to certain restrictions of this parameter. This led to the introduction of the bit energy to noise ratio, or $E_b/N_0 = \gamma_b$, since it takes into account the bandwidth at which the system is operating, but more importantly the coderate.

It should be clear by now that, for a simulated system, each noise sample should be scaled properly with respect to the in-band noise power to produce the correct $E_b/N_0$. The SNR can be rewritten as

$$\gamma_s = \frac{\sigma_s^2}{\sigma_n^2} = \frac{E_b \cdot R_b}{N_0 \cdot B} \tag{D.50}$$

with $E_b$ the average energy per bit and $R_b$ the rate at which bits are transferred. It should be clear that $\gamma_s$ is bandwidth dependent. Thus, for any $E_b/N_0$ of rate $R_b$ sampled at frequency $f_s$, the channel noise power can be bandlimited by scaling it appropriately as [112]

$$\sigma_n = \sqrt{\frac{\sigma_s^2 \cdot f_s}{2R_b \cdot 10^{\frac{E_b}{10N_0}}}} \tag{D.51}$$

## D.6 PRACTICAL SIMULATION MODELS FOR COMPLEX FADING CHANNELS

Practical computer simulations are often done with a complex baseband system representative model to remove the need for excessively high sample rates required to digitally represent carrier frequencies that typically exceed the data bandwidth by approximately two to three orders (and sometimes more). The transmitted signal will experience multiplicative fading and AWGN, yielding a received signal expressed in a complex notation as

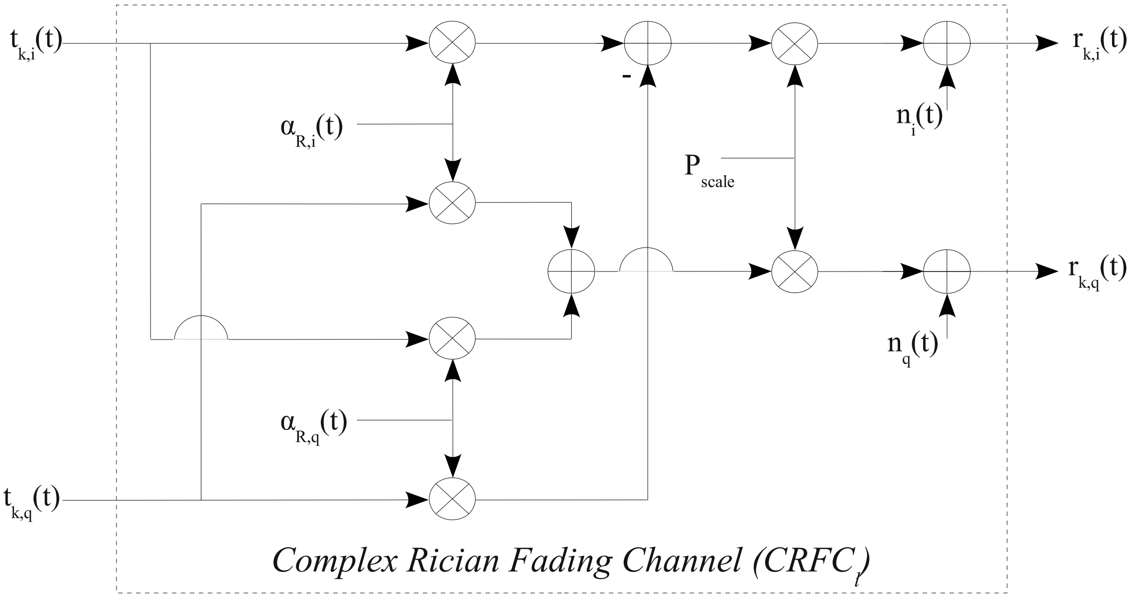

FIGURE D.10: Simulation model for complex Rician fading channel (frequency non-selective channel)

$$\begin{aligned} r_k(t) &= t_k(t)\alpha_R(t) + n_k(t) \\ &= [t_{k,i}(t) + jt_{k,q}(t)][\alpha_{R,i}(t) + j\alpha_{R,q}(t)] + [n_i(t) + jn_q(t)] \\ &= [t_{k,i}\alpha_{R,i} - t_{k,q}\alpha_{R,q} + n_i(t)] + j[t_{k,i}\alpha_{R,q} + t_{k,q}\alpha_{R,i} + n_q(t)] \end{aligned} \tag{D.52}$$

with $\alpha_{R,i}(t)$ and $\alpha_{R,q}(t)$ the output coefficients generated by the complex Rician process as shown in *Fig.* D.8. The output of the Rician process is a function of time and may, therefore, be considered in different ways. It is often necessary to express the instantaneous output of the complex Rician process, which may be done as

$$\begin{aligned} \alpha_R(t) &= \alpha_{R,i} + j\alpha_{R,q} \\ &= \alpha_c(t)cos(\phi_c(t)) + \alpha_c(t)sin(\phi_c(t)) \end{aligned} \tag{D.53}$$

with $\alpha_c(t)$ the instantaneous fading amplitude and $\phi_c(t)$ the instantaneous fading phase of the Rician process. These instantaneous values are often of importance during receiver design and operation, as will become apparent throughout this thesis.

Careful inspection of *Eq.* (D.52) shows that the channel components may be divided into the respective complex and real parts, corresponding to the in-phase and quadrature components. A complex Rician channel model is illustrated in *Fig.* D.10 and was developed directly from *Eq.* (D.52).

It is of importance to note that without proper scaling of the power levels, the output power of this simulator would be equal to $(1+\rho^2)P_{scale}^2 + P_{scale}^2$. Therefore, to ensure unity power, both at the input and the output, it is necessary to set $P_{scale} = \frac{1}{\sqrt{2+\rho^2}}$.

Perfect or near perfect channel state information is of importance during coherent demodulation and the various levels of synchronisation. It is also often used during FEC techniques (especially in serial, parallel and hybrid concatenation schemes) employing decoder metric calculations. The instantaneous fading amplitude may be determined from the complex Rician channel simulator as

$$\alpha_c(t) = \sqrt{\frac{(\alpha_{R,i} + \rho)^2 + \alpha_{R,q}(t)^2}{2+\rho^2}} \tag{D.54}$$

while the instantaneous fading phase is determined as

$$\phi_c(t) = -\tan^{-1}\left(\frac{\alpha_{R,q}}{\alpha_{R,i} + \rho}\right) \tag{D.55}$$

This model may be further expanded to simulate multiple fading channel paths at the receiver, yielding a complex baseband frequency selective fading channel setup. A model performing the functions illustrated in *Fig.* D.9 is given in *Fig.* D.11 and was implemented.

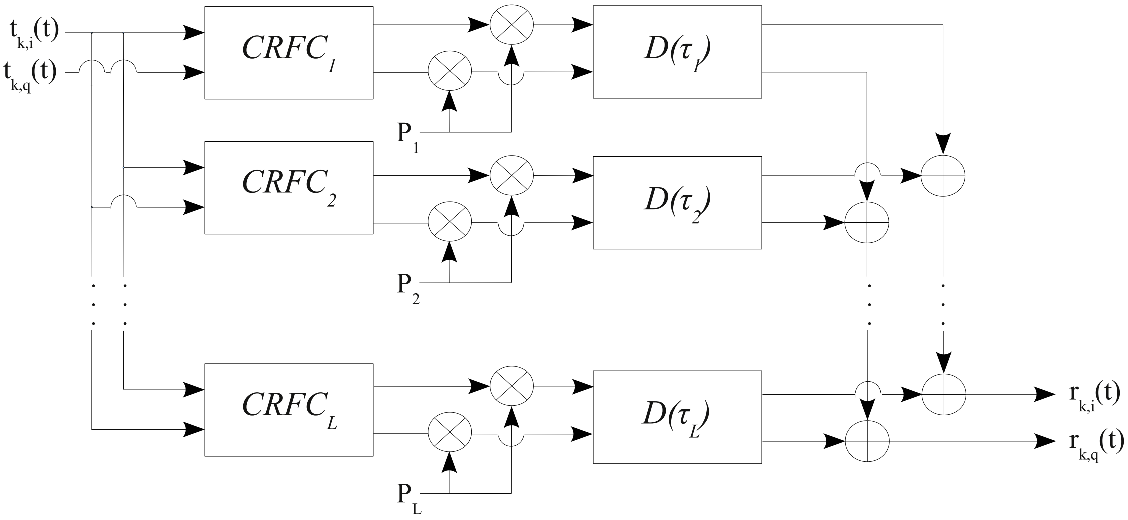

FIGURE D.11: Simulation model for complex wideband Rician fading channel (frequency selective channel)

It should again be noted that the same restrictions apply to power scaling to ensure that the complex baseband multi-path fading channel simulator does not add additional power to the system.

The simulator design was approached in a generic way, and any power and delay profile may be chosen by the user of the software, with the only requirement being that a power vector $(P_1, P_2, ..., P_L)$ and a delay vector $(\tau_1, \tau_2, ..., \tau_L)$, both of length $L$, are available at initialisation. This generic approach makes the simulation of any COST model possible.

# APPENDIX E

# BER PERFORMANCE OVER FREQUENCY NON-SELECTIVE CHANNELS

This section continues the discussion commenced in *Section* 3.1.2.2 regarding the derivation of the BER performance of a BPSK-based communication system over a frequency non-selective channel. It is assumed that the phase shift caused by the channel can be estimated accurately, allowing for coherent detection, but it requires that the channel fading level should be constant over one chip period in the case of a WCDMA implementation. In *Section* 3.1.2.1 a channel with a constant SNR was considered, but this may be generalised to a case where the presented result is a conditional error probability of a random process with a random fading level attenuation, denoted as $\alpha_{fl}$, resulting in

$$P_b(e|\gamma_b) = Q\left[\sqrt{\frac{\alpha_{fl}^2 2E_b}{N_0}}\right] \tag{E.1}$$

with $2\alpha_{fl}^2 E_b/N_0$ the systems SNR per bit, $\gamma_b$, taking the random attenuation factor into account as well. This result should be averaged over the PDF of $\gamma_b$, given as $p(\gamma_b)$ when $\alpha_{fl}$ is random with a specific probability distribution (see for example Proakis [44] or Rappaport [43]).

In the case where $\alpha_{fl}$ has a Rayleigh distribution, $\alpha_{fl}^2$ exhibits a chi-square probability distribution with two degrees of freedom. Therefore, $\gamma_b$ will also be chi-square-distributed with a PDF given by

$$p(\gamma_b) = \frac{1}{\overline{\gamma}_b} e^{-\gamma_b/\overline{\gamma}_b}, \qquad \gamma_b \geq 0 \tag{E.2}$$

with $\overline{\gamma}_b$ the average SNR given by

$$\overline{\gamma}_b = E[\alpha_{fl}^2]\frac{E_b}{N_0} \tag{E.3}$$

and $E[\alpha_{fl}^2]$ is the average value or expectation of $\alpha_{fl}^2$.

The averaging process mentioned earlier may be done as

$$\begin{aligned} P_e &= \int_0^\infty P_b\left(e|\gamma_b\right)p\left(\gamma_b\right)d\gamma_b \\ &= \int_0^\infty Q\left(\sqrt{2\gamma_b}\right)\frac{1}{E_b/N_o}e^{-\gamma_b/(E_b/N_o)}d\gamma_b \end{aligned} \tag{E.4}$$

The resulting integral may be solved by means of an integration by parts process, where it is required to solve

$$\int_a^b f\left(\gamma_b\right)g'\left(\gamma_b\right)d\gamma_b = \left[f\left(\gamma_b\right)g\left(\gamma_b\right)\right]_a^b - \int_a^b f'\left(\gamma_b\right)g\left(\gamma_b\right)d\gamma_b \tag{E.5}$$

with the necessary functions defined as

$$\begin{aligned} f\left(\gamma_b\right) &= Q\left[\sqrt{2\gamma_b}\right] \\ g\left(\gamma_b\right) &= -e^{-\left(\gamma_b/E_b/N_o\right)} \end{aligned} \tag{E.6}$$

and their corresponding derivatives given by

$$\begin{aligned} f'\left(\gamma_b\right) &= \frac{d}{d\gamma_b}\left[Q\left(\sqrt{2\gamma_b}\right)\right] \\ &= \frac{d}{d\gamma_b}\left[\frac{1}{2}\left(1-erf\left(\frac{\sqrt{2\gamma_b}}{\sqrt{2}}\right)\right)\right] \\ &= -\frac{1}{2}\frac{d}{d\gamma_b}\left[erf\left(\sqrt{\gamma_b}\right)\right] \\ &= -\frac{1}{2}\cdot\frac{2}{\sqrt{\pi}}e^{-\left(\sqrt{\gamma_b}\right)^2}\frac{d}{d\gamma_b}\left(\sqrt{\gamma_b}\right), \qquad (chain\ rule) \\ &= -\frac{1}{2}\cdot\frac{2}{\sqrt{\pi}}e^{-\left(\sqrt{\gamma_b}\right)^2}\cdot\frac{1}{2}\gamma_b^{-\frac{1}{2}} \\ &= -\frac{1}{\sqrt{4\pi\gamma_b}}e^{-\gamma_b} \end{aligned} \tag{E.7}$$

and

$$\begin{aligned} g'\left(\gamma_b\right) &= -e^{-\left(\gamma_b/E_b/N_o\right)} \\ &= \frac{d}{d\gamma_b}\left[-e^{-\left(\gamma_b/E_b/N_o\right)}\right] \\ &= -e^{-\left(\gamma_b/E_b/N_o\right)}\frac{d}{d\gamma_b}\left[-\gamma_b/E_b/N_o\right], \qquad (chain\ rule) \\ &= \frac{1}{E_b/N_o}e^{-\left(\gamma_b/E_b/N_o\right)} \end{aligned} \tag{E.8}$$

Now, by inspection of *Eq.* (E.4) through *Eq.* (E.8), we may conclude that

$$\begin{aligned} P_e &= \int\limits_a^b f\left(\gamma_b\right) g'\left(\gamma_b\right) d\gamma_b \\ &= \int\limits_0^\infty Q\left(\sqrt{2\gamma_b}\right) \frac{1}{E_b/N_o} e^{-\gamma_b/\left(E_b/N_o\right)} d\gamma_b \end{aligned} \tag{E.9}$$

which is equivalent to

$$\begin{aligned} P_e &= \left[f\left(\gamma_b\right) g\left(\gamma_b\right)\right]_a^b - \int\limits_a^b f'\left(\gamma_b\right) g\left(\gamma_b\right) d\gamma_b \\ &= -Q\left(\sqrt{2\gamma_b}\right) e^{-\gamma_b/\left(E_b/N_o\right)}\Big|_0^\infty - \int\limits_0^\infty \frac{1}{\sqrt{4\pi\gamma_b}} e^{-\gamma_b} \cdot e^{-\gamma_b/\left(E_b/N_o\right)} d\gamma_b \\ &= 0 - \left(-\tfrac{1}{2}\right) - \int\limits_0^\infty \frac{1}{\sqrt{4\pi\gamma_b}} e^{-\gamma_b\left[1+\frac{1}{E_b/N_o}\right]} d\gamma_b \\ &= \frac{1}{2} - \frac{1}{2\sqrt{\pi}} \int\limits_0^\infty \frac{1}{\left(\gamma_b\right)^{1/2}} e^{-K_C\gamma_b} d\gamma_b \end{aligned} \tag{E.10}$$

The solution to this definite integral may be found from published tables, and is given by

$$\begin{aligned} P_e &= \frac{1}{2}\left[1 - \frac{1}{\sqrt{\pi}} \cdot \left\{\frac{\Gamma\left(-\frac{1}{2}+1\right)}{\left(K_C\right)^{-\frac{1}{2}+1}}\right\}\right], \qquad \Gamma\left(\tfrac{1}{2}\right) = \sqrt{\pi} \\ &= \frac{1}{2}\left[1 - \frac{1}{\sqrt{\pi}} \cdot \left\{\frac{\sqrt{\pi}}{\sqrt{1+\frac{1}{E_b/N_o}}}\right\}\right] \\ &= \frac{1}{2}\left[1 - \sqrt{\frac{E_b/N_o}{1+E_b/N_o}}\right] \end{aligned} \tag{E.11}$$